



Universidade de Aveiro Departamento de Química
2016

**Bruno Reis
Figueiredo**

**Materiais microporosos para a deteção de Cs^+
e sua remoção seletiva de soluções aquosas**

**Microporous materials for Cs^+ sensing and
selective removal from aqueous solutions**



Universidade de Aveiro Departamento de Química
2016

**Bruno Reis
Figueiredo**

**Materiais microporosos para a deteção de Cs⁺
e sua remoção seletiva de soluções aquosas**

**Microporous materials for Cs⁺ sensing and
selective removal from aqueous solutions**

Tese apresentada à Universidade de Aveiro para cumprimento dos requisitos necessários à obtenção do grau de Doutor em Engenharia Química, realizada sob a orientação científica do Doutor Carlos Manuel Santos Silva, Professor Auxiliar do Departamento de Química da Universidade de Aveiro, e co-orientação científica do Doutor João Carlos Matias Celestino Gomes da Rocha, Professor Catedrático do Departamento de Química da Universidade de Aveiro.

Apoio financeiro da FCT e do
FSE no âmbito do III Quadro
Comunitário de Apoio.

This thesis is not the same as any other thesis submitted for a degree or diploma or other qualification at this or any other University. This thesis is the result of my own work and it includes nothing which is the outcome of collaboration unless declared otherwise. Accounts of some of the work reported here have been given or will appear in

Journals

B.R. Figueiredo, D. Ananias, J. Rocha, C.M. Silva, Cs⁺ ion exchange over lanthanide silicate Eu-AV-20: Experimental measurement and modelling, *Chem. Eng. J.* 268 (2015) 208–218.

B.R. Figueiredo, M.M.R. de Melo, I. Portugal, D. Ananias, J. Rocha, C.M. Silva, Cs⁺ removal and optical detection by microporous lanthanide silicate Eu-AV-20 in a fixed-bed column, *Chem. Eng. J.* 286 (2016) 48–58.

B.R. Figueiredo, D. Ananias, I. Portugal, J. Rocha, C.M. Silva, Tb/Eu-AV-9: A lanthanide silicate for the sensing and removal of cesium ions from aqueous solutions, *Chem. Eng. J.* 286 (2016) 679–688.

B.R. Figueiredo, I. Portugal, J. Rocha, C.M. Silva, Batch and fixed-bed removal of Cs⁺ from aqueous solutions using ETS-4: Measurement and modeling of loading-regeneration cycles and equilibrium, *Chem. Eng. J.* 301 (2016) 276–284.

B.R. Figueiredo, I. Portugal, J. Rocha, C.M. Silva, Inorganic ion exchangers for cesium removal from radioactive wastewater, *Sep. Pur. Rev.* (submitted)

B.R. Figueiredo, A.A. Valente, Z. Lin, C.M. Silva, Photoluminescent porous and layered lanthanide silicates: a review, *Micropor. Mesopor. Mat.* (doi:10.1016/j.micromeso.2016.07.004)

"I can't change the direction of the wind, but I can adjust my sails to always reach my destination."

Jimmy Dean

À minha família.

o júri

presidente

Professor Doutor José Carlos Esteves Duarte Pedro
Professor Catedrático do Departamento de Electrónica, Telecomunicações e Informática da Universidade de Aveiro

vogais

Prof. Doutor Carlos Manuel Santos da Silva
Professor Auxiliar do Departamento de Química da Universidade de Aveiro

Professor João Carlos Matias Celestino Gomes da Rocha
Professor Catedrático do Departamento de Química da Universidade de Aveiro

Professor Doutor João Paulo Serejo Goulão Crespo
Professor Catedrático da Faculdade de Ciências e Tecnologia da Universidade Nova de Lisboa

Professor Doutor Armando da Costa Duarte
Professor Catedrático do Departamento de Química da Universidade de Aveiro

Prof. Doutora Maria Filipa Gomes Ribeiro
Professora Associada do Instituto Superior Técnico da Universidade de Lisboa

Prof. Doutor José Miguel Loureiro
Professor Associado do Departamento de Engenharia Química da Faculdade de Engenharia da Universidade do Porto

Prof. Doutor Licínio Manuel Gando de Azevedo Ferreira
Professor Auxiliar da Faculdade de Ciências e Tecnologia da Universidade de Coimbra

agradecimentos

Desejo expressar o meu sincero agradecimento a todas as pessoas que de forma direta, ou indireta, contribuíram para a realização deste trabalho, em especial:

Aos meus orientadores, Doutor Carlos Silva e Professor Doutor João Rocha, pela sua orientação científica, apoio e amizade.

Ao Doutor Duarte Ananias pelos seus diversos ensinamentos nas mais distintas áreas científicas.

À Doutora Teresa Caldeira pela ajuda incansável que deu na espectroscopia de absorção atômica e pela sua simpatia em todos os momentos.

À Doutora Rosário Soares pela simpatia e disponibilidade demonstrada na preparação do equipamento para as análises de raio-X e interpretação de alguns resultados.

À Doutora Cláudia Lopes pela compreensão, paciência e amizade manifestadas em todas as minhas solicitações.

À Doutora Eduarda Pereira pela disponibilidade mostrada quando foi necessária a análise da composição de diversas matrizes por espectroscopia de emissão atômica por plasma acoplado e pelo fornecimento de água ultra pura.

Aos atuais e anteriores membros do grupo EgiChem pelos momentos vividos dentro e fora do laboratório.

Ao Doutor Francisco Avelino Silva e à Doutora Inês Portugal pela amizade, simpatia e ensinamentos científicos.

Aos meus amigos pelo incansável apoio.

Um agradecimento muito especial aos meus pais, à minha irmã e à Soraia pelo apoio incondicional, incentivo, paciência, compreensão e carinho, determinantes para o meu sucesso.

Finalmente, agradeço o apoio financeiro que me foi concedido pela FCT no âmbito QREN (bolsa de investigação com a referência SFRH/BD/75457/2010)

palavras-chave

silicatos microporosos, lantanídeos, permuta iónica, cézio, fotoluminescência, equilíbrio, cinética, caracterização, modelação

resumo

$^{134,137}\text{Cs}$ são dois isótopos de tempo de meia vida longo, produzidos durante a fissão nuclear e que contribuem significativamente para a radioatividade das águas residuais nucleares produzidas em todo o Mundo. Presentemente, assiste-se ao crescimento demográfico e económico de países como a China, Brasil e Índia, o que coloca as centrais nucleares como opções fortes para a geração de energia. Todavia, as águas residuais radioativas são geralmente armazenadas em tanques metálicos soterrados que, ao longo do tempo, padecem de fugas que contaminam os terrenos confinantes, um facto registado atualmente em Hanford Site (pertencente ao Departamento de Energia dos EUA) onde estão armazenados cerca de 250,000 m³ de resíduos.

Estão publicadas várias famílias de materiais para o tratamento de águas residuais nucleares, entre as quais se encontram permutadores inorgânicos como zeólitos, hexacianoferratos e titanossilicatos. Estes materiais podem assumir um papel importante por possuírem elevadas estabilidades térmica e química, mesmo na presença de níveis significativos de radiação. Por outro lado, a síntese de novos materiais siliciosos conheceu, nas últimas décadas, a incorporação de elementos terras raras (em particular lantanídeos), tendo surgido sólidos que combinam microporosidade estrutural com fotoluminescência. Este facto confere aos novos silicatos de terras raras um enorme potencial, uma vez que suas propriedades óticas podem ser exploradas em funções de deteção (*i.e.*, na construção de sensores), sendo que a sua emissão de luz pode ser alterada por modificação da vizinhança do lantanídeo. Por exemplo, a variação da natureza dos contra-íões do sorvente fotoluminescente pode resultar num espectro de emissão diferente.

Esta dissertação tem os seguintes objectivos: estudar a síntese e a caracterização de materiais microporosos de metais de transição e lantanídeos, e avaliar a sua possível aplicação como permutadores de Cs⁺ e em sensores deste ião. Numa primeira fase, o titanossilicato ETS-4 e os lantanossilicatos Eu-AV-20 e Tb/Eu-AV-9 foram sintetizados e caracterizados por microscopia eletrónica de varrimento, difração de raios-X de pós, espectroscopia de emissão atómica por plasma acoplado indutivamente, entre outras. De seguida, foram realizadas experiências de permuta iónica em vaso fechado (descontínuo) com Eu-AV-20 e Tb/Eu-AV-9, e em coluna

de leito fixo (contínuo) com Eu-AV-20 e ETS-4. Os silicatos luminescentes Eu-AV-20 e Tb/Eu-AV-9 foram caracterizados por espectroscopia de fotoluminescência, antes e depois dos ensaios de sorção, por forma a avaliar o seu potencial como sensores de Cs^+ . As isotérmicas de todos os sistemas foram determinadas em vaso fechado, fazendo variar a massa de sólido e fixando a força iónica da solução. No caso dos materiais investigados em descontínuo (Eu-AV-20 e Tb/Eu-AV-9), foram medidas curvas cinéticas de remoção de Cs^+ para diferentes massas de silicato, enquanto que nos ensaios efetuados em coluna de leito fixo (com Eu-AV-20 e ETS-4) se mediram curvas de rutura para diferentes velocidades superficiais. Os resultados experimentais mostram que a capacidade de permuta do Eu-AV-20 é muito inferior à do Tb/Eu-AV-9, como os patamares máximos das suas isotérmicas confirmam: $0,09 \text{ eq}\cdot\text{kg}^{-1}$ vs. $3,47 \text{ eq}\cdot\text{kg}^{-1}$, respetivamente. Para além disto, a cinética de remoção com o Eu-AV-20 é muito mais lenta do que com Tb/Eu-AV-9: 0,5 g do primeiro silicato removeram 1 ppm de cézio em 80 horas, enquanto que o Tb/Eu-AV-9 permutou trinta vezes mais Cs^+ em menos de 2 horas.

As experiências de permuta em leito fixo mostram que os silicatos Eu-AV-20 e ETS-4 podem ser usados em contínuo, tendo-se ainda constatado que o ETS-4 pode ser utilizado em ciclos de sorção-regeneração sem prejuízo estrutural. Em termos de capacidade de permuta iónica, o Eu-AV-20 foi novamente o sólido com o desempenho mais fraco, $0,09 \text{ eq}\cdot\text{kg}^{-1}$ vs. $1,86 \text{ eq}\cdot\text{kg}^{-1}$.

Foram realizados estudos com o intuito de relacionar a concentração de Cs^+ na fase sólida com as variações observadas nos espectros de fotoluminescência do Eu-AV-20 e do Tb/Eu-AV-9. De um modo geral, a permuta iónica diminui a intensidade da emissão. A transição não degenerada $^5\text{D}_0 \rightarrow ^7\text{F}_0$ do ião európio foi a mais relevante neste estudo, dado ser a que melhor testemunha as modificações que ocorrem na vizinhança do lantanídeo. No caso particular do silicato Tb/Eu-AV-9, foram realizadas medições de tempos de vida que confirmaram a existência de uma relação linear entre estes e a concentração de Cs^+ no sólido.

Esta tese compreendeu ainda a modelação de todos os resultados experimentais de equilíbrio e cinética usando modelos baseados nas equações de fluxo de Maxwell-Stefan e Nernst-Planck, e onde se combinaram as limitações internas e externas para a transferência de massa. As difusividades dos contra-íons otimizadas têm valores na gama 10^{-18} – $10^{-15} \text{ m}^2 \text{ s}^{-1}$, típicos de materiais microporosos. Como esperado, a difusividade do par Cs^+ /sólido assumiu um valor mais baixo do que a do par Na^+ /sólido, o que pode ser imputado ao maior raio iónico de Cs^+ . Relativamente ao transporte iónico no filme, o coeficiente de transferência de massa por convecção estimado pela correlação generalizada de Armenante e Kirwan forneceu valores coerentes com os otimizados a partir dos pontos experimentais.

keywords

microporous silicates, lanthanides, ion-exchange, cesium, photoluminescence, equilibrium, kinetics, characterization, modeling

abstract

^{134,137}Cs are two long-lived isotopes produced during nuclear fission and are among the biggest contributors to the radioactivity of nuclear wastewaters produced around the World. At present, the economic and demographic evolution of countries such as China, Brazil and India raises the possibility of nuclear power plants becoming an excellent alternative for clean energy generation. Furthermore, radioactive wastewaters are commonly kept in underground stainless-steel tanks that may leak and contaminate the confining land. Indeed, this is already observed at the Hanford Site (belonging to the Department of Energy, USA) where some of the tanks storing almost 250.000 m³ of radioactive solutions are leaking. The literature reports several good materials for nuclear wastewater treatment, particularly inorganic exchangers, such as zeolites, hexacyanoferrates and titanosilicates, that may play an important role due to their good thermal and chemical properties, preserved even in the presence of high doses of radiation. On the other hand, in the last two decades, the synthesis of new materials incorporating rare-earth elements (in particular lanthanides) enabled the appearance of solids combining microporosity and photoluminescence properties. This fact may be explored for detection purposes (e.g., in sensors) because the material's emission may change upon modification of the lanthanide vicinity. For example, counter-ions composition variation of a luminescent sorbent results in different emission spectra. This thesis aimed at studying the synthesis and characterization of transition metal and rare-earth (lanthanide) microporous materials and applying them as Cs⁺ exchangers and sensors. Firstly, the titanosilicate ETS-4 and the lanthanide silicates Eu-AV-20 and Tb/Eu-AV-9 were synthesized and characterized by scanning electron microscopy, powder X-ray diffraction, inductively coupled plasma mass spectroscopy, among others. Then, the batch ion exchange was performed with Eu-AV-20 and Tb/Eu-AV-9, while the fixed-bed ion exchange was performed with Eu-AV-20 and ETS-4. The parent and Cs⁺-exchanged silicates Eu-AV-20 and Tb/Eu-AV-9 were characterized by photoluminescence spectroscopy, in order to evaluate their capacity for Cs⁺ sensing. All the equilibrium isotherms were determined using batch ion experiments and manipulating the mass of solid with defined solution's ionic strength. For the materials (Eu-AV-20, Tb/Eu-AV-9) tested during the batch ion

exchanges, Cs⁺ removal curves for different masses of solid were measured, while in the fixed-bed assays (with Eu-AV-20 and ETS-4) breakthrough curves were measured varying the superficial velocity. The exchange capacity of Eu-AV-20 is much lower than that of Tb/Eu-AV-9, as the isotherm's thresholds confirmed, 0.09 eq·kg⁻¹ vs. 3.47 eq·kg⁻¹, respectively. Furthermore, the Eu-AV-20 removal kinetics is slower than that of Tb/Eu-AV-9: while 0.5 g of the first removed 1 ppm of cesium in 80 hours, the latter exchanged an amount 30 times higher in less than 2 hours.

The fixed-bed experiments show that Eu-AV-20 and ETS-4 may be used in a continuous mode. Moreover, ETS-4 can perform sorption-regeneration cycles without structural losses. Again, Eu-AV-20 is the weakest performer, 0.09 eq·kg⁻¹ vs. 1.86 eq·kg⁻¹.

Photoluminescence studies were performed in order to relate the Cs⁺ concentration in the solid phase with changes in the Eu-AV-20 and Tb/Eu-AV-9 emission. In general, the ion exchange decreased the emission intensity. In this study, the Eu³⁺ non-degenerated ⁵D₀→⁷F₀ transition was the most informative spectral feature since it is the one that changes most upon modification of the local environment of the emitter lanthanide. In the particular case of Tb/Eu-AV-9, lifetime measurements were also measured and confirmed the existence of a linear relation between the average life time in the solid and the solid's Cs⁺ concentration.

Finally, this thesis also considers the modelling of all the equilibrium and kinetic experimental data. For that, Maxwell-Stefan and Nernst-Planck based models combining internal and external mass transfer limitations were used. The optimized counter-ion diffusivities are in the range 10⁻¹⁸ to 10⁻¹⁵ m²·s⁻¹, values that are typical of microporous materials. As expected the diffusivity of the pair Cs⁺/solid assumed a value lower than the pair Na⁺/solid, which may be ascribed to the larger Cs⁺ ionic radius. Concerning the ionic transport in the film, the convective mass transfer coefficient estimated by the Armenante and Kirwan correlation provided results similar to those optimized from the experimental data.

Index

I. Motivation and structure of this thesis	1
II. Theoretical Introduction	7
II.1. Inorganic ion exchangers for cesium removal from radioactive wastewater	12
II.1.1. Introduction.....	12
II.1.2. Inorganic exchange materials	15
II.1.2.1. Zeolites.....	15
II.1.2.2. Titanosilicates.....	24
II.1.2.3. Hexacyanoferrates	36
II.1.2.4. Other Materials	38
II.1.2.5. Composite Materials	43
II.1.3. Conclusions	53
II.1.4. Nomenclature	54
II.2. Photoluminescent porous and layered lanthanide silicates: a review	58
II.2.1. Introduction.....	58
II.2.1.1. Relevance of the review	60
II.2.2. Lanthanide Materials	66
II.2.2.1. Materials doped with lanthanides <i>via</i> ion exchange	66
II.2.2.2. Lanthanide silicates	73
II.2.2.2.1. <i>Microporous</i> lanthanide silicates.....	73
II.2.2.2.2. <i>Layered</i> lanthanide silicates	96
II.2.3. Conclusions	103
II.3. References	105
III. Optical sensing of Cs⁺ and Na⁺ by Eu-AV-20.....	125
III.1. Optical sensing of Cs ⁺ and Na ⁺ by Eu-AV-20.....	129
III.1.1. Introduction.....	129
III.1.2. Materials and Methods	131
III.1.2.1. Chemicals and materials	131
III.1.2.2. Synthesis procedures	131
III.1.2.3. Batch ion exchange experiments.....	132
III.1.2.4. Equipment and techniques	133
III.1.3. Results and discussion	134
III.1.3.1. Materials characterization	134
III.1.3.2. Photoluminescence studies	137
III.1.4. Conclusions	143
III.2. References	145
IV. Removal of Cs⁺ from aqueous solutions through batch experiments	147
IV.1. Cs ⁺ ion exchange over lanthanide silicate Eu-AV-20: Experimental measurement and modelling	152
IV.1.1. Introduction.....	152

IV.1.2.	Materials and Methods	155
IV.1.2.1.	Chemicals and materials	155
IV.1.2.2.	Synthesis procedures.....	155
IV.1.2.3.	Sorption experiments: isotherm and removal curves	155
IV.1.2.4.	Equipment and techniques	157
IV.1.3.	Modelling.....	158
IV.1.4.	Results and discussion.....	162
IV.1.4.1.	Materials characterization	162
IV.1.4.2.	Photoluminescent spectra of native and Cs ⁺ -exchanged Eu-AV-20..	163
IV.1.4.3.	Ion exchange isotherm.....	164
IV.1.4.4.	Influence of Eu-AV-20 mass upon Cs ⁺ removal.....	165
IV.1.4.5.	Ion exchange kinetics.....	166
IV.1.4.6.	Ion exchange modelling based on Maxwell-Stefan equations.....	169
IV.1.5.	Conclusions	173
IV.1.6.	Nomenclature.....	174
IV.2.	Tb/Eu-AV-9: A lanthanide silicate for the sensing and removal of cesium ions from aqueous solutions	178
IV.2.1.	Introduction	178
IV.2.2.	Materials and Methods	180
IV.2.2.1.	Chemicals and materials	180
IV.2.2.2.	Synthesis procedures.....	180
IV.2.2.3.	Characterization of the Tb/Eu-AV-9 material	181
IV.2.2.4.	Sorption experiments: isotherm and removal curves	181
IV.2.3.	Modelling.....	183
IV.2.4.	Results and discussion.....	187
IV.2.4.1.	Characterization of the Tb/Eu-AV-9 material	187
IV.2.4.2.	Ion exchange isotherm.....	188
IV.2.4.3.	Influence of Tb/Eu-AV-9 mass upon Cs ⁺ removal.....	189
IV.2.4.4.	Ion exchange kinetics.....	191
IV.2.4.5.	Photoluminescence spectra of native and Cs ⁺ -exchanged Tb/Eu-AV-9 192	
IV.2.4.6.	Ion exchange modelling based on Maxwell-Stefan equations.....	196
IV.2.5.	Conclusions	198
IV.2.6.	Nomenclature.....	199
IV.3.	References.....	203

V. Removal of Cs⁺ from aqueous solutions through fixed-bed experiments..... 209

V.1.	Cs ⁺ removal and optical detection by microporous lanthanide silicate Eu-AV-20 in a fixed-bed column	214
V.1.1.	Introduction	214
V.1.2.	Materials and Methods	215
V.1.2.1.	Chemicals and materials	215
V.1.2.2.	Synthesis and characterization of Eu-AV-20	216
V.1.2.3.	Characterization and analytic methods.....	216
V.1.2.4.	Fixed-bed and batch ion experiments.....	217
V.1.3.	Modelling isotherms and breakthrough curves	220

V.1.3.1.	Equilibrium Isotherm	220
V.1.3.2.	Nernst-Planck based model for fixed-bed ion exchange	220
V.1.3.3.	Analytic breakthrough models.....	223
V.1.3.4.	Numerical methods and calculations approach.....	224
V.1.4.	Results and discussion	225
V.1.4.1.	Materials characterization	225
V.1.4.2.	Fixed-bed experimental results and selectivity assessment	227
V.1.4.3.	Fixed-bed modelling results	230
V.1.4.4.	Photoluminescence results	236
V.1.5.	Conclusions	237
V.1.6.	Nomenclature	238
V.2.	Batch and fixed-bed removal of Cs ⁺ from aqueous solutions using ETS-4: Measurement and modeling of loading-regeneration cycles and equilibrium.....	242
V.2.1.	Introduction.....	242
V.2.2.	Modelling	243
V.2.3.	Materials and Methods	247
V.2.3.1.	Chemicals and materials	247
V.2.3.2.	Synthesis and characterization	247
V.2.3.3.	Fixed-bed and batch ion exchange experiments.....	248
V.2.4.	Results and discussion	250
V.2.4.1.	Materials characterization	250
V.2.4.2.	Ion exchange isotherm	251
V.2.4.3.	Fixed-bed experimental results.....	252
V.2.4.4.	Fixed-bed modelling results – Nernst-Planck based model.....	256
V.2.5.	Conclusions	258
V.2.6.	Nomenclature	259
V.3.	References	263
VI.	General conclusions and future work.....	269
VI.1.	General conclusions	271
VI.2.	Future work.....	273
VI.3.	References	276

Figures Index

Figure II.1.1 – Number of scientific publications concerning the use of inorganic exchangers for cesium uptake from water and wastewaters, in the period 1966–2015. Search keywords: cesium AND hexacyanoferrate; cesium AND zeolite; cesium AND titanasilicate (or “titanium silicate” or “silicotitanate”) in the publication title [75].	14
Figure II.1.2 – a) LTA α -cage with aperture diameter of 0.42 nm; b) sodalite and LTA zeolite β -cage with aperture diameter of 0.22 nm and c) cancrinite ε -cage with aperture diameter of 0.59 nm (adapted from [28]).	17
Figure II.1.3 – (a) Natrolite chains running along the c -axis; (b) View down the c -axis, showing the pore structure. Al and Si tetrahedra are depicted in orange and green, respectively, Na^+ cations in grey, and O atoms of water molecules in yellow (adapted from [105]).	20
Figure II.1.4 – Ti_4O_4 cubane-like cluster. Green and red spheres depict titanium and oxygen atoms, respectively (adapted from [118]).	24
Figure II.1.5 – Equilibrium uptake of five monovalent cations (0.05 N MCl–MOH, M = Li^+ , Na^+ , K^+ , Rb^+ and Cs^+) by H-CST as function of pH, at room temperature. The volume to mass ratio was $300 \text{ cm}^3 \text{ g}^{-1}$. (adapted from [124]).	26
Figure II.1.6 – Framework of ivanyukite (and sitinakite) built from TiO_6 octahedra and SiO_4 tetrahedra viewed in the ab plane [135].	29
Figure II.1.7 – Cesium distribution coefficients for K-form of germanium ivanyukites plotted as a function of cubic unit cell dimensions of the final cesium-exchanged materials. $\text{CsGe} - \text{HM}_3(\text{GeO})_4(\text{GeO}_4)_3 \cdot 4\text{H}_2\text{O}$, $\text{CsTiSi} - \text{HM}_3(\text{TiO})_4(\text{SiO}_4)_3 \cdot 4\text{H}_2\text{O}$, $\text{CsTiSiGe} - \text{HM}_3(\text{Ti}_{0.5}\text{Ge}_{0.5}\text{O})_4(\text{Si}_{0.5}\text{Ge}_{0.5}\text{O}_4)_3 \cdot 4\text{H}_2\text{O}$ and $\text{CsTiGe} - \text{HM}_3(\text{TiO})_4(\text{GeO}_4)_3 \cdot 4\text{H}_2\text{O}$ (adapted from [19]).	31
Figure II.1.8 – (a) Zig-zag arrangement of the ETS-4 pore structure comprising 7- and 12-membered rings along c -direction (adapted from [164]). (b) Diagonal arrangement of the ETS-10 pore structure of ETS-10 polytype B comprising 7- and 12-membered rings (adapted from [153]). Green polyhedra are TiO_5 and TiO_6 , and blue tetrahedra are SiO_4 .	36
Figure II.1.9 – Structure of potassium cobalt hexacyanoferrate. Purple spheres depict cobalt and iron atoms, yellow spheres potassium ions, and grey bars cyanide groups (adapted from [64]).	37
Figure II.1.10 – (a) Photoluminescent emission spectra of native (solid black line) and Cs^+ -exchanged Eu-AV-20 excited at 393 nm and (b) expansion of the $^5\text{D}_0 \rightarrow ^7\text{F}_0$ transition (adapted from [183]).	42

Figure II.1.11 – Plot of the average Tb^{3+} emission lifetime as a function of the Cs^+ concentration on the native and Cs^+ -exchanged Tb/Eu-AV-9 samples. Symbols (data); line (linear fitting).	43
Figure II.1.12 – The separation of radioactive cesium (^{137}Cs) using a magnetic Prussian Blue (adapted from [189]). Experiments performed after ion exchange: a) Magnet positioned far away from reservoir; b) Reservoir is placed close to the magnet, which immediately attracts the dispersed cesium-containing magnetic particles, facilitating the separation. .	44
Figure II.2.1 – Photoluminescent emission spectra of native (solid black line) and Cs^+ -exchanged Eu-AV-20 (red dashed line) excited at 393 nm; (b) enlargement of their $^5\text{D}_0 \rightarrow ^7\text{F}_0$ transition [183].....	62
Figure II.2.2 – $^5\text{D}_4 \rightarrow ^7\text{F}_5$ transition of hydrated and calcined Tb-ZT1 (200) excited at 545 nm and recorded at 393 K (data from [226]).....	67
Figure II.2.3 – Pore structure of ETS-10 comprises corner-sharing SiO_4 tetrahedra and TiO_6 octahedra linked through bridging oxygen atoms that forms 12-membered rings [224]. ..	68
Figure II.2.4 – 14 K emission spectra of Eu^{3+} -doped ETS-10 (solid line) and Eu^{3+} -doped narsarsukite (dashed line) excited at 395 nm [28]. The inset shows the $^5\text{D}_0 \rightarrow ^7\text{F}_0$ transition.	69
Figure II.2.5 – 14 K emission spectra of $^5\text{D}_0 \rightarrow ^7\text{F}_0$ transitions of Eu^{3+} -doped umbite (solid line) and Eu^{3+} -doped wadeite (dashed line) excited at 394 nm [31].	70
Figure II.2.6 – $^5\text{D}_0 \rightarrow ^7\text{F}_0$ transitions of Eu^{3+} -doped narsarsukite with different Ti/Eu ratios, excited at 394 nm and recorded at 14 K [65].	71
Figure II.2.7 – a) Emission spectra of Eu^{3+} -doped sitinakite and Eu^{3+} -doped ivanyukite at 14 K for the excitation wavelength 393 and 280 nm, respectively [33,34]. b) Detail of $^5\text{D}_0 \rightarrow ^7\text{F}_0$ transition of the Eu^{3+} -doped sitinakite [33]. c) Detail of $^5\text{D}_0 \rightarrow ^7\text{F}_1$ transition of the Eu^{3+} -doped ivanyukite [34].	73
Figure II.2.8 – Structure of Ln-AV-9 materials: a) alternating octahedral sheet and double-silicate layer where the single silicate sheet is of the apophyllite type with four- and eight-membered rings; b) an open octahedral sheet, composed of two non-equivalent EuO_6 octahedra and two distinct $\text{NaO}_4(\text{H}_2\text{O})_2$ octahedra in the <i>bc</i> plane.....	75
Figure II.2.9 – Emission $^5\text{D}_0 \rightarrow ^7\text{F}_0$ and $^5\text{D}_0 \rightarrow ^7\text{F}_2$ transitions of Eu-AV-9 recorded at 45 K and excited at (a) 394, (b) 466 and (c) 527 nm [37].	75
Figure II.2.10 – EMS-6 polyhedra representation of the 8-membered ring of the single silicate apophyllite-type sheet along the [101] crystallographic direction [38]. The 9-coordinated K^+ cations and the oxygen atoms from water molecules are also shown.....	76
Figure II.2.11 – a) Two wollastonite-type chains lying on the symmetry plane normal to <i>c</i> are condensed through the bridging oxygen O5, forming a double silicate chain and	

originating an 8-membered ring [23]. b) Connection of silicate chains (wollastonite-type) to the calcium polyhedra CaO_7 [23].	78
Figure II.2.12 – Room temperature emission spectrum of Eu-AV-20 excited at 394 nm [23]. The inset shows the $^5\text{D}_0 \rightarrow ^7\text{F}_0$ transition.	79
Figure II.2.13 – Crystal structure of Sm-AV-21 viewed in the crystallographic [010] direction [84].	80
Figure II.2.14 – Room temperature emission spectrum of Eu-AV-21 excited at 392 nm [84].	81
Figure II.2.15 – Representation of the petarasite and AV-3 structure viewed along [001] direction showing the corner-sharing, 6-membered silicate rings and Zr octahedra. In the ring channels exists Na^+ , Cl^- and OH^- ions that stabilize the structures [89].	84
Figure II.2.16 – Emission spectrum of Eu-AV-3 recorded at 14 K and excited at 320 nm [35].	84
Figure II.2.17 – Crystal structure of $\text{K}_7[\text{Sm}_3\text{Si}_{12}\text{O}_{32}] \cdot 4\text{H}_2\text{O}$ viewing along the [100] crystallographic direction [46].	86
Figure II.2.18 – Emission spectrum of $\text{K}_7[\text{Eu}_3\text{Si}_{12}\text{O}_{32}] \cdot 4\text{H}_2\text{O}$ recorded at 12 K and excited at 393 nm [46].	86
Figure II.2.19 – Room temperature emission spectrum of $\text{K}_5\text{Eu}_2\text{FSi}_4\text{O}_{13}$ excited at 532 nm [25].	89
Figure II.2.20 – Polyhedral view of the open-framework structure of $\text{K}_{1.25}\text{Gd}_{1.25}\text{Si}_{2.5}\text{O}_{7.5}$ contains 10-ring channels along [001] direction [59].	90
Figure II.2.21 – Polyhedral view of the open-framework structure of $\text{Cs}_3\text{TbSi}_8\text{O}_{19} \cdot 2\text{H}_2\text{O}$ along [010] direction [59].	91
Figure II.2.22 – Crystal structure of $\text{Cs}_3\text{DySi}_6\text{O}_{15}$ viewed along [001] direction and infinite chain along [001] direction containing cages composed of six SiO_4 and two DyO_6 polyhedra [59].	91
Figure II.2.23 – Room temperature emission spectrum of $\text{Cs}_3\text{TbSi}_8\text{O}_{19} \cdot 2\text{H}_2\text{O}$ excited at 267 nm [59].	92
Figure II.2.24 – a) Framework of a microporous terbium(III) silicate which contains 9-membered ring channels along the [100] directions delimited by four TbO_6 octahedra and five SiO_4 tetrahedra [40]. b) Infinite left-handed helical silicate chain with a period of six tetrahedra following the screw axis running along the [100] direction [40].	94
Figure II.2.25 – Room temperature emission spectrum of $\text{Na}_3\text{TbSi}_3\text{O}_9 \cdot 3\text{H}_2\text{O}$ excited at 266 nm [40].	94

Figure II.2.26 – a) Representation of the unit cell of Tb-AV-22 viewed along the <i>c</i> -axis. O-H...O hydrogen bonds are drawn as yellow dashed lines and K ⁺ ions (K2) as purple circles. (b) Perforated, single [TbSi ₃ O ₈ (OH) ₂] ³⁻ layer showing K1 ions along the <i>b</i> -axis [20].	97
Figure II.2.27 – Schematic representation of the calcination of AV-22 yielding the AV-23 structure [19].	99
Figure II.2.28 – Room temperature emission spectrum of Eu-AV-23 excited at 392 nm. The inset shows the ⁵ D ₀ → ⁷ F ₀ transition [19].	100
Figure II.2.29 – a) Perspective view of the crystal packing along the [001] direction of Eu ₂ (SiO ₄ H)(OH) ₂ (H ₂ O)Cl and b) towards the <i>bc</i> plane showing a top view of the layer.	102
Figure II.2.30 – 10 K emission spectra of Eu ₂ (SiO ₄ H)(OH) ₂ (H ₂ O)Cl (dashed line) and (Eu _{0.125} Gd _{0.875}) ₂ (SiO ₄ H)(OH) ₂ (H ₂ O)Cl (solid line) excited at 394 nm [21].	102
Figure III.1.1 – a) Eu-AV-20 sheets comprising alternating chains of Na ⁺ and Eu ³⁺ polyhedra; b) framework channels running along the [110] direction and housing Na ⁺ and K ⁺ ions and water molecules. Crystal structure drawn using Diamond software.	130
Figure III.1.2. – SEM images of exchanged Eu-AV-20 (see experimental conditions in Table III.1.2).	135
Figure III.1.3 – PXRD patterns of the Cs ⁺ -exchanged Eu-AV-20 (Exps. 1-5, see experimental conditions in Table III.1.2). The asterisks depict impurities.	135
Figure III.1.4 – PXRD patterns of the Na ⁺ -exchanged Eu-AV-20 (Exps. 6-10, see experimental conditions in Table III.1.2).	136
Figure III.1.5 – PXRD patterns of the (Cs ⁺ ,Na ⁺)-exchanged Eu-AV-20 (Exps. 11 to 15, see experimental conditions Table III.1.2). The asterisks depict impurities.	136
Figure III.1.6 – RT emission spectra of native and Cs ⁺ -exchanged Eu-AV-20 materials (excitation at 393 nm). See experimental conditions in Table III.1.2.	137
Figure III.1.7 – ⁵ D ₀ → ⁷ F ₀ transition region of the luminescence spectra of the native and Cs ⁺ -exchanged Eu-AV-20.	138
Figure III.1.8 – RT emission spectra of Cs ⁺ -exchanged Eu-AV-20 materials from Exps. 1-5 (excitation at 393 nm). See experimental conditions in Table III.1.2.	139
Figure III.1.9 – ⁵ D ₀ → ⁷ F ₀ transition region of the luminescence spectra of Exps. 1-5 (see experimental conditions in Table III.1.2).	139
Figure III.1.10 - RT emission spectra of Na ⁺ -exchanged Eu-AV-20 materials from Exps. 6-10 (excitation at 393 nm). See experimental conditions in Table III.1.2.	140

Figure III.1.11 – $^5D_0 \rightarrow ^7F_0$ transition region of the luminescence spectra of Exps. 6-10 (see experimental conditions in Table III.1.2).....	140
Figure III.1.12 - RT emission spectra of (Cs ⁺ ,Na ⁺)-exchanged Eu-AV-20 materials from Exps. 11-15 (excitation at 393 nm). See experimental conditions in Table III.1.2.....	141
Figure III.1.13 – $^5D_0 \rightarrow ^7F_0$ transition region of the luminescence spectra of Exps. 11-15 (see experimental conditions in Table III.1.2).....	142
Figure III.1.14 – Eu1/Eu2 areas ratio as a function of: a) Cs ⁺ /Eu molar ratio (Exps. 1-5); b) Na ⁺ /Eu molar ratio (Exps. 6-10); and c) Cs ⁺ /Eu and Na ⁺ /Eu molar ratios (Exps. 11-16). Red circles depict the Cs ⁺ /Eu molar ratio and blue triangles the Na ⁺ /Eu molar ratio (see experimental conditions in Table III.1.2.).....	143
Figure IV.1.1 – a) Eu-AV-20 sheets comprising alternating chains of Na ⁺ and Eu ³⁺ polyhedral; b) framework channels, running along the [110] direction and housing Na ⁺ and K ⁺ . Crystal structure drawn using Diamond software.....	155
Figure IV.1.2 – Experimental and powder X-ray diffraction patterns of the synthesized EU-AV-20 used in the ion exchange assays and the simulated one in accordance with the crystal data reported by Ferreira <i>et al.</i> [47]. The inset shows a typical SEM image of the sample crystals.	163
Figure IV.1.3 – (a) Photoluminescent emission spectra of native (solid black line) and Cs ⁺ -exchanged Eu-AV-20 (Exp. 12, red dashed line) excited at 393 nm; (b) enlargement of their $^5D_0 \rightarrow ^7F_0$ transition.....	164
Figure IV.1.4 – Measured data and Langmuir isotherm for Cs ⁺ /Na ⁺ ,K ⁺ /Eu-AV-20 system at 298.15 K.	165
Figure IV.1.5 – Influence of Eu-AV-20 mass on the final uptake of Cs ⁺ . Bars, data (experimental conditions in Table IV.1.2); line, calculated results.....	166
Figure IV.1.6 – Experimental data of normalized Cs ⁺ concentration in the solution. Purple Circles, green diamonds and blue squares are Exps. 8, 10 and 11, respectively (experimental conditions in Table IV.1.2); lines are modelling results.	167
Figure IV.1.7 – Experimental data of normalized Cs ⁺ concentration in the solution. Blue triangles and red squares are Exps. 12 and 13, respectively (exp. conditions in Table IV.1.2).....	169
Figure IV.1.8 – Calculated Cs ⁺ concentration inside Eu-AV-20 particles at distinct removal times. See experimental conditions in Table IV.1.2.	171
Figure IV.1.9 – Normalized Cs ⁺ concentration in the Eu-AV-20 particle for r = 0, 12Rp, 34Rp and Rp. Calculations accomplished with MS based model for Exp. 11.....	172

Figure IV.1.10 – Calculated <i>versus</i> experimental normalized Cs ⁺ concentration in solution. Experimental conditions (see Table IV.1.2): Same as Figure IV.1.6.	172
Figure IV.2.1 – Structure of Ln-AV-9 materials: a) alternating octahedral sheet and double-silicate layer where the single silicate sheet is of the apophyllite type with four- and eight-membered rings; b) an open octahedral sheet, composed of two non-equivalent {LnO ₆ } octahedra and two distinct {NaO ₄ (H ₂ O) ₂ } octahedra in the <i>bc</i> plane.	180
Figure IV.2.2 – SEM image of the native Tb/Eu-AV-9.	188
Figure IV.2.3 – Powder X-Ray diffraction patterns of the native Tb/Eu-AV-9 and Cs ⁺ -exchanged Tb/Eu-AV-9 (see experimental conditions of Exps. 5, 7 and 10 in Table IV.2.2).	188
Figure IV.2.4 – Experimental data (black dots: Exps. 1-4, 6, 8 and 9; green squares: Exps. 5, 7 and 10) and Langmuir-Freundlich isotherm for the system Cs ⁺ /K ⁺ / Tb/Eu-AV-9 at 295 K.	189
Figure IV.2.5 – Influence of the ratio between the mass of Tb/Eu-AV-9 and the initial concentration of Cs ⁺ upon the final uptake of Cs ⁺ . circles: experimental data; line: theoretical prediction (AARD = 4.14%).	190
Figure IV.2.6 – Evolution of the normalized concentration of Cs ⁺ in solution along time. Symbols, experimental data; curves, MS-based model which achieves AARD = 8.37%.	192
Figure IV.2.7 – (a) Partial room-temperature emission spectra of native and Cs ⁺ -exchanged Tb/Eu-AV-9 materials (excitation at 393 nm); (b) Enlarged region containing the ⁵ D ₀ → ⁷ F ₀ transition (central peak). Experimental conditions in Table IV.2.2, and equilibrium solid loadings in Table IV.2.3.	193
Figure IV.2.8 – Room-temperature emission spectra of native and Cs ⁺ -exchanged Tb/Eu-AV-9 materials (excitation at 377 nm). Experimental conditions in Table IV.2.2, and equilibrium solid loadings in Table IV.2.3.	195
Figure IV.2.9 – Tb ³⁺ emission decay curves (transition ⁵ D ₄ → ⁷ F _j) of native and Cs ⁺ -exchanged Tb/Eu-AV-9 materials. Spectra were collected at room temperature, with excitation at 377 nm and detection at 541 nm. Experimental conditions in Table IV.2.2, and equilibrium solid loadings in Table IV.2.3.	196
Figure IV.2.10 – Normalized cesium concentration in the Tb/Eu-AV-9 particles as a function of time and radial position, for Exps. 5 (experimental conditions given in Table IV.2.2).	198
Figure V.1.1 – Experimental setup of the ion exchange unit: 1) influent reservoir tank; 2) peristaltic pump; 3) fixed-bed column in up-flow mode; 4) Eu-AV-20 powder bed; 5) membrane disc filter; and 6) sample collecting tube.	219
Figure V.1.2 – SEM image of Eu-AV-20 crystals.	226

Figure V.1.3 – EDS spectra of (a) native and (b) Cs ⁺ -exchanged Eu-AV-20 samples.	226
Figure V.1.4 – PXRD of native and Cs ⁺ -exchanged Eu-AV-20 samples collected after the fixed-bed experiments (Exps. 1–5, see Table V.1.2). Inset: PXRD on an expanded scale in the range 28-31°.	227
Figure V.1.5 – Normalized experimental breakthroughs for Cs ⁺ removal in a fixed-bed of Eu-AV-20. (a) Effect of superficial velocity (<i>via</i> flow rate variation); (b) Effect of the mass of ion exchanger. Symbols: data (experimental conditions in Table V.1.2); lines: NP-based model.	228
Figure V.1.6 – Final uptake of cesium as function of the initial molar ratio of Na ⁺ and Cs ⁺ (experimental conditions in Table V.1.3).	230
Figure V.1.7 – Normalized Cs ⁺ concentration in bulk solution (a) and normalized Cs ⁺ loading in the solid (b) as function of dimensionless time and longitudinal bed position. Simulations were performed for the conditions of Exp. 3 (Table V.1.2).	232
Figure V.1.8 – Comparison of the four conventional analytic models for fixed-bed ion exchange: calculated versus experimental normalized fluid concentrations at column outlet. (Experimental conditions in Table V.1.2).	234
Figure V.1.9 – a) Measured breakthrough curves for two different run times (Exps. 3 and 5; experimental conditions in Table V.1.2); b) Normalized ⁵ D ₀ → ⁷ F ₀ transition of the photoluminescence emission room temperature spectra of the native and Cs ⁺ exchanged Eu-AV-20 with excitation at 393 nm.	237
Figure V.2.1 – Experimental setup for the fixed-bed ion exchange experiments.	249
Figure V.2.2 – Normalized PXRD patterns of native and Cs ⁺ -exchanged ETS-4 (after Exp. 9; see experimental conditions in Table V.2.3).	251
Figure V.2.3 – Measured (solid circles) and calculated (line) Langmuir isotherms of Cs ⁺ /Na ⁺ /ETS-4 system at 295 K.	252
Figure V.2.4 – Effect of the feed flow rate on the normalized breakthrough curves for Cs ⁺ removal in a fixed-bed of ETS-4. Symbols: data (experimental conditions in Table V.2.3); lines: NP-based model (parameters in Table V.2.4).	253
Figure V.2.5 – Normalized cesium concentration at column outlet for Exps. 11, 12 and 13 in a loading-regeneration operation. Symbols: data (experimental conditions in Table V.2.3); lines: NP-based model (parameters in Table V.2.4); A1 = area above the breakthrough of the 1 st ion exchange cycle; AR = area below the regeneration curve of the 1 st cycle; A2 = area above breakthrough of the 2 nd cycle.	255
Figure V.2.6 – Calculated <i>versus</i> experimental normalized Cs ⁺ concentration in solution (experimental conditions in Table V.2.3).	258

Tables Index

Table II.1.1 – Chemical formulae and exchange capacities of the reviewed materials.	47
Table II.2.1 – Rare earth (RE)-silicates and lanthanide (Ln)-silicates reviewed.....	63
Table III.1.1 – Features of the synthesized Eu-AV-20 lanthanide silicate [8].	132
Table III.1.2 – Batch ionexchange experimental conditions; fixed: $V = 1$ L and $T = 294.15$ K.	133
Table III.1.3 – Eu1 and Eu2 peak areas, their respective ratio and standard errors (experimental conditions in Table III.1.2).....	142
Table IV.1.1 – Features of the synthesized Eu-AV-20 lanthanide silicate.....	156
Table IV.1.2 – Experimental conditions of batch ion exchange assays using Eu-AV-20. (Fixed: $T=295$ K \pm 1; $V_{\text{liquid}} = 2 \times 10^{-3}$ m ³ ; pH =4).	158
Table IV.1.3 – Model for batch ion exchange based on the Maxwell-Stefan equations. There are $n = 2$ counter ions (A and B), and the co-ions are the $n + 1$ th = 3rd species.	161
Table IV.1.4 – Optimized parameters and AARD (%) of the Maxwell-Stefan based model.	169
Table IV.2.1 – Features of the synthesized Tb/Eu-AV-9 lanthanide silicate.....	181
Table IV.2.2 – Experimental conditions of batch ion exchange tests using Tb/Eu-AV-9. (Fixed conditions: $T = 295$ K \pm 1 K; $V_L = 2 \times 10^{-3}$ m ³ ; pH 4).....	183
Table IV.2.3 – Average decay lifetimes of the $5D_4 \rightarrow 7F_5$ transition of Tb ³⁺ of the native and Cs ⁺ -exchanged Tb/Eu-AV-9 materials, and corresponding equilibrium solid loading. The experimental conditions in Table IV.2.2	194
Table IV.2.4 – Estimated convective mass transfer coefficient and optimized MS diffusivities for Tb/Eu-AV-9 and Eu-AV-20 materials at $T = 295$ K.....	197
Table V.1.1 – Features of the synthesized Eu-AV-20 lanthanide silicate [28].	216
Table V.1.2 – Eu-AV-20 fixed-bed ion exchange experiments performed at 295 ± 1 K..	219
Table V.1.3 – Eu-AV-20 competitive ion exchange in batch experiments performed at 295 ± 1 K.	219
Table V.1.4 – Optimized parameters and calculated deviations for the Nernst-Planck based model and for the analytic models from literature applied to the fixed-bed experiments. (Exp. conditions in Table V.1.2).	235

Table V.2.1 – Features of the synthesized titanosilicate ETS-4 [66].	247
Table V.2.2 – Experimental conditions for batch ion exchange assays with ETS-4 to obtain isotherm data. (Fixed conditions: $T = 295 \pm 1$ K, $V_{\text{liquid}} = 2 \times 10^{-3}$ m ³ , pH = 4).....	249
Table V.2.3 - Experimental conditions for fixed-bed ion exchange assays using ETS-4. (Fixed conditions: $T = 295 \pm 1$ K, pH 4, $\varepsilon = 0.88$, $L = 0.01$ m).	250
Table V.2.4 – Optimized parameters and calculated deviations for the Nernst-Planck based model applied to the fixed-bed assays. (Experimental conditions in Table V.2.3).	257



Motivation and
structure of this thesis

1) Radionuclide ^{137}Cs (half-life of 30 years) accounts for most of the radioactivity of the nuclear wastewaters produced around the World [1]. These wastes (acidic or alkaline) may be treated by ion exchange using inorganic solids, typically, possessing high thermal, chemical and radiation stability [2,3], such as microporous mixed octahedral-pentahedral-tetrahedral (OPT) silicates, which are inorganic ion exchangers that may offer excellent selectivity. Perhaps more important than their capacity to selectively confine ions in a stable solid matrix is their ability to reduce the volume occupancy of radioactive wastes, from thousands of liters of solutions to a few grams of solids.

OPT materials may be photoluminescent when (stoichiometric) amounts of lanthanides are embedded in their framework, a property endowing them with sensing ability for target ions or molecular species [4–6].

The progress of countries such as China, Brazil and India will require more energy, making nuclear power plants part of the solution for achieving such a demand [1], and increasing radioactive wastewaters. On the other hand, there is also the need for remediation solutions since, for instance, following the Fukushima Daichii disaster tons of radioactive waters have leaked into the Pacific Ocean and surrounding soils, that must be treated [7,8]. Additionally, in Hanford Site (Department of Energy, USA), some stainless-steel underground tanks containing radioactive solutions leaked due to corrosion and contaminated groundwater and confining land.

2) The work reported in this thesis is developed at the interface of Chemistry, Chemical Engineering and Materials Science, encompassing the synthesis, structural characterization, assessment of Cs^+ ion exchange capacity (batch and fixed-bed operations) and sensing ability (based on photoluminescence) of microporous transition-metal and lanthanide silicates. Accordingly, the following specific objectives were accomplished:

- Synthesis of microporous transition metal and lanthanide silicates;
- Characterization of the prepared materials by powder X-ray diffraction (PXRD), scanning electron microscopy (SEM), energy-dispersive X-ray spectroscopy (EDS), inductively coupled plasma mass spectroscopy (ICP-MS). Also, the characterization of the emitting lanthanide silicates by photoluminescence spectroscopy (PLS) and lifetime (LT) measurements aiming at their application as hybrid Cs^+ cation exchangers and sensors;

- Batch and fixed-bed experiments (kinetic and equilibrium measurements) to evaluate the ion exchange capacity of the microporous silicates;
- Modelling ion-exchange equilibrium and uptake kinetic curves.

3) Besides this current chapter, the thesis comprises additionally four main parts.

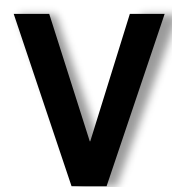
- **Chapter II** ("Theoretical Introduction") consists of two sections reviewing the main materials used in the treatment of radioactive wastewater (in particular for cesium removal) and the family of microporous lanthanides silicates. Thus, the first section informs the reader about the three major families used in the radioactive wastewater treatment domain, namely, zeolites, hexacyanoferrates and titanasilicates. Section two reviews the rare earth and in particular the lanthanides silicates family, mainly relevant structural features, such as the number luminescent sites, framework or layered structure, crystal size (bulk or nanoparticles), and type of lanthanide incorporation (ion exchange or embedment).
- **Chapter III** ("Optical sensing of Cs⁺ and Na⁺ by Eu-AV-20") describes the studies concerning the assessment of the Cs⁺ and Na⁺ sensing ability of Eu-AV-20. The work involves fifteen different batch ion exchange experiments. SEM, PXRD, ICP-MS and PLS fully-characterize the solid after the experiments. The optical properties of the exchanged materials focus mainly on the relationship between the intensity of the non-degenerated $^5D_0 \rightarrow ^7F_0$ Eu³⁺ transition and the cesium and sodium molar ratios in the solid phase.
- **Chapter IV** studies the Cs⁺ removal from aqueous solutions in batch experiments using the Eu-AV-20 and Tb/Eu-AV-9 materials. Results on the influence of the mass of exchanger on the final uptake are presented. Accurate modelling of the obtained experimental data (equilibrium and kinetic) is also described, using Maxwell-Stefan equations to represent intraparticle diffusion. Some photoluminescence results are also reported in this chapter.
- **Chapter V** is devoted to the removal of Cs⁺ from aqueous solutions in fixed-bed experiments. It essentially discusses the bed efficiency on the uptake of cesium in a continuous mode, using microporous titanium silicate ETS-4 and the lanthanide

silicate Eu-AV-20. Among others, the influence of the superficial velocity and mass of exchanger on the removal behaviour (*via* breakthrough curves) are discussed in detail. The experimental data are modelled by two distinct approaches: 1) simplified analytic models taken from the literature, such as Thomas, Bohart-Adams, Clark and Yoon-Nelson; and 2) a Nernst-Planck based model. In order to assess the sensing ability of Eu-AV-20 towards different cesium loadings, two different photoluminescent studies are presented disclosing the potential of the material to be used as Cs⁺ sensor. In the particular case of ETS-4, a loading-regeneration-loading assay was additionally performed, bringing to light its capability to be used in several ion exchange cycles.

- **Chapter VI** brings this thesis to an end, presenting the general conclusions, outlook and future work.

References

- [1] A. Clearfield, Ion-exchange materials: seizing the caesium, *Nat. Chem.* 2 (2010) 161–162.
- [2] K. Popa, C.C. Pavel, Radioactive wastewaters purification using titanosilicates materials: State of the art and perspectives, *Desalination* 293 (2012) 78–86.
- [3] A. Clearfield, Inorganic ion exchangers, past, present, and future, *Solvent Extr. Ion Exch.* 18 (2000) 655–678.
- [4] D. Ananias, M. Kostova, F.A.A. Paz, A. Ferreira, L.D. Carlos, J. Klinowski, J. Rocha, Photoluminescent layered lanthanide silicates, *J. Am. Chem. Soc.* 126 (2004) 10410–10417.
- [5] J. Rocha, Z. Lin, Microporous mixed octahedral-pentahedral-tetrahedral framework silicates, *Micro- Mesoporous Miner. Phases* 57 (2005) 173–201.
- [6] J. Rocha, L.D. Carlos, Microporous materials containing lanthanide metals, *Curr. Opin. Solid State Mater. Sci.* 7 (2003) 199–205.
- [7] G. Brumfiel, Fukushima set for epic clean-up, *Nature* 472 (2011) 146–147.
- [8] M. Ebihara, N. Yoshida, Y. Takahashi, Preface: Migration of radionuclides from the Fukushima Daiichi Nuclear Power Plant accident, *Geochem. J.* 46 (2012) 267–270.



Removal of Cs^+ from aqueous solutions through fixed-bed experiments

This chapter is devoted to the removal of Cs^+ ion from aqueous solution using two different silicates – Eu-AV-20 and ETS-4 – carrying out fixed-bed ion exchange experiments; in the case of ETS-4 a set of batch assays were also performed. The parent and exchanged materials were characterized by several techniques, such as scanning electron microscopy (SEM), energy-dispersive X-ray spectroscopy (EDS), powder X-Ray diffraction (PXRD), inductively coupled plasma mass spectroscopy (ICP-MS) and photoluminescent spectroscopy (PLS). Several breakthrough curves were measured and, in the specific case of ETS-4, a complete loading-regeneration-loading assay was performed in order to assess its ability to be used in ion exchange cycles. The experimental data were modelled using: 1) a Nernst-Planck based model taking into account the internal and external limitations to the mass transfer; and 2) simplified analytic models from the literature such as Thomas, Bohart-Adams, Clark and Yoon-Nelson models. In the particular case of the Eu-AV-20, photoluminescent spectroscopic studies were also performed aiming the evaluation of its sensing ability towards cesium.

Index

V.1. Cs ⁺ removal and optical detection by microporous lanthanide silicate Eu-AV-20 in a fixed-bed column	214
V.1.1. Introduction	214
V.1.2. Materials and Methods	215
V.1.2.1. Chemicals and materials	215
V.1.2.2. Synthesis and characterization of Eu-AV-20	216
V.1.2.3. Characterization and analytic methods.....	216
V.1.2.4. Fixed-bed and batch ion experiments.....	217
V.1.3. Modelling isotherms and breakthrough curves	220
V.1.3.1. Equilibrium Isotherm	220
V.1.3.2. Nernst-Planck based model for fixed-bed ion exchange.....	220
V.1.3.3. Analytic breakthrough models	223
V.1.3.4. Numerical methods and calculations approach	224
V.1.4. Results and discussion.....	225
V.1.4.1. Materials characterization	225
V.1.4.2. Fixed-bed experimental results and selectivity assessment	227
V.1.4.3. Fixed-bed modelling results	230
V.1.4.4. Photoluminescence results	236
V.1.5. Conclusions	237
V.1.6. Nomenclature.....	238
V.2. Batch and fixed-bed removal of Cs ⁺ from aqueous solutions using ETS-4: Measurement and modeling of loading-regeneration cycles and equilibrium.....	242
V.2.1. Introduction	242
V.2.2. Modelling.....	243
V.2.3. Materials and Methods	247
V.2.3.1. Chemicals and materials	247
V.2.3.2. Synthesis and characterization.....	247
V.2.3.3. Fixed-bed and batch ion exchange experiments	248
V.2.4. Results and discussion.....	250
V.2.4.1. Materials characterization	250
V.2.4.2. Ion exchange isotherm.....	251

V.2.4.3.	Fixed-bed experimental results	252
V.2.4.4.	Fixed-bed modelling results – Nernst-Planck based model.....	256
V.2.5.	Conclusions	258
V.2.6.	Nomenclature	259
V.3.	References	263

Work reported in the scientific article

Cs⁺ removal and optical detection by microporous lanthanide silicate Eu-AV-20 in a fixed-bed column

published on Chemical Engineering Journal 286 (2016) 48-58

Abstract

Microporous silicate Eu-AV-20 has recently proved to be a promising ion exchange material for cesium removal from aqueous solutions, and its potential for Cs⁺ photoluminescence sensing was additionally demonstrated. In this work, Cs⁺ removal was performed in a fixed-bed column, and the influence of linear velocity and mass of ion exchanger on the breakthrough curves was analyzed. The experimental data were modelled on the basis of Nernst-Planck (NP) equations and with four well-known analytic models. The analytic expressions provided low errors (root mean square deviation, RMSD, between 3.20% and 6.47%); the 2-parameter NP-based model fitted the data quite well (RMSD = 6.66% for correlation and 6.54% for prediction), yielding crucial information on both the transport mechanism within the Eu-AV-20 particles, and the intrinsic dynamic behaviour of the fixed-bed ion exchange column. Taking into account that Eu-AV-20 samples loaded with different amounts of Cs⁺ exhibited distinct photoluminescence spectra, our results reinforce the potential of AV-20 materials for Cs⁺ sensing, which raises the possibility of online monitoring the ion exchange in a fixed-bed column using an optical fiber and a spectrometer.

V.1. Cs⁺ removal and optical detection by microporous lanthanide silicate Eu-AV-20 in a fixed-bed column

V.1.1. Introduction

Nuclear wastes are complex systems containing fission products including two long-lived cesium isotopes (¹³⁵Cs and ¹³⁷Cs with a half-life of 2.3 million years and 30.17 years, respectively). The negative effects of cesium are well known and encompass medullary dystrophy, disorders of the reproductive function, and adverse effects on the liver and renal functions of mammals [1]. In soil and water environments cesium exists predominantly as a free monovalent ion (Cs⁺) since the formation of organic and inorganic cesium complexes is insignificant [2]. Several approaches may be deployed to eliminate cesium from radioactive aqueous wastes, such as chemical precipitation, evaporation, reverse osmosis, filtration, solvent extraction, ion exchange and adsorption [3]. However, ion exchange is usually preferred for water and wastewater remediation, particularly when high-purity water is required [3–5], since they allow concentrating metal ions to a level where disposal, destruction, or subsequent use are affordable.

Ion exchange can be implemented as a batch process in a stirred tank or in a continuous fixed-bed (column) operation. The last alternative is preferred from an industrial point-of-view because: (i) it is the most effective configuration for cyclic sorption-desorption stages; (ii) a nearly solute-free effluent may be obtained until the exchanger agent in the bed approaches equilibrium; (iii) the removal efficiency is usually better due to higher sorbate concentration gradients between solution and solid. Some examples of ion exchange studies in fixed-beds include the uptake of zinc by NaY zeolite [6], the removal of mercury and lead by titanosilicates ETS-4 and ETS-10, respectively [7,8], and the sorption of cesium by titanosilicate granules [9]. Most recently, the elimination of Hg(II) and Pt(IV) from aqueous solutions have been studied using fixed-beds composed of chelating resins [10–12].

Inorganic ion exchangers are well-known for their chemical, thermal, mechanical and radiation stabilities, and typically exhibit high capacity and selectivity towards a wide variety of monovalent and divalent metal cations [3,4,10–20]. Concerning the specific use of inorganic solids for Cs⁺ removal, three main families have been studied, zeolites [18,19],

hexacyanoferrates [20,21] and titanosilicates [9,22,23]. Nevertheless, their use in fixed-bed experiments is limited [9,24,25].

In the early years of this century, the synthesis of zeolite-type rare-earth or lanthanide-silicate (Ln-silicates) materials was an emerging field due to their interesting optical properties associated to transitions between 4f orbitals, which generate atomic-like emission spectra displaying characteristic sharp lines [26,27]. The existence of other species in the vicinity of the emitter lanthanide may affect the photoluminescence spectra, which raises the possibility of exploring such optical properties for sensing the presence of molecules/ions [27].

The microporous Ln-silicate Eu-AV-20 and the mineral tobermorite 11 Å [28] have a similar crystal structure, encompassing 5.8 Å x 6.8 Å channels and cavities containing exchangeable Na⁺ and K⁺ ions coordinated with framework oxygen atoms and water molecules [29]. Furthermore, the presence of stoichiometric amounts of europium affords photoluminescence properties to Eu-AV-20 [29,30]. Figueiredo et al. [31] assessed the ion-exchange capacity of Eu-AV-20 for Cs⁺ removal from aqueous solutions in a stirred batch tank, and found that indeed the photoluminescence of Eu-AV-20 does change upon Cs⁺ uptake.

Here, we study Cs⁺ removal in a fixed-bed column and evaluate the photoluminescence properties of Cs⁺-exchanged Eu-AV-20. The experimental breakthrough curves were modelled using two distinct approaches: Nernst-Planck (NP) based model, and commonly used analytic models, such as the Thomas, Bohart-Adams, Yoon-Nelson and Clark models.

V.1.2. Materials and Methods

V.1.2.1. Chemicals and materials

Extra pure sodium silicate solution (HS code 2839 19 00), potassium hydroxide (CAS number 1310-58-3) and sodium hydroxide (CAS number 1310-73-2) were supplied by Merck. Europium(III) chloride hexahydrate (CAS number 13759-92-7) and cesium nitrate (CAS number 7789-18-6) were purchased from Sigma-Aldrich. High-purity water (18.2 MΩcm) was produced in a Milli-Q Millipore water purification system and the cellulose acetate membrane disc filters were bought from Sterlitech Corporation.

V.1.2.2. Synthesis and characterization of Eu-AV-20

The hydrothermal synthesis of Eu-AV-20 was performed as previously described [29]. Briefly, an alkaline solution was prepared by mixing a sodium silicate solution ($\text{Na}_2\text{O}(\text{SiO}_2)_x \cdot x\text{H}_2\text{O}$, 5.75 g), with H_2O (16.51 g), KOH (3.25 g) and NaOH (1.07 g) followed by the addition of $\text{EuCl}_3 \cdot 6\text{H}_2\text{O}$ (1.37 g) and stirring the mixture thoroughly. The resulting gel (with molar ratios 0.79 Na_2O : 1.10 K_2O : 1.0 SiO_2 : 0.07 Eu_2O_3 : 35 H_2O) was transferred to a Teflon-lined autoclave and heated at 230 °C under autogenous pressure, during 3 days. After quenching the autoclave in cold water the off-white microcrystalline powder was filtered-off, washed at room temperature with distilled water, and dried overnight at 100 °C [29]. The relevant features of this material are summarized in Table V.1.1.

Table V.1.1 – Features of the synthesized Eu-AV-20 lanthanide silicate [28].

Formula	$\text{Na}_{1.08}\text{K}_{0.5}\text{Eu}_{1.14}\text{Si}_3\text{O}_{8.5} \cdot 1.78\text{H}_2\text{O}$
Density, ρ_s (kg m ⁻³)	3080
Cation exchange capacity, Q (eq. kg ⁻¹)	2.55
Equivalent particle diameter (10 ⁻⁶ m)	23.1
Pore diameter (10 ⁻¹⁰ m)	5.8 x 6.8

V.1.2.3. Characterization and analytic methods*Photoluminescence spectroscopy.*

The photoluminescent spectra of native and Cs⁺-exchanged Eu-AV-20 samples (oven-dried at 353.15 K during 48 h) were recorded in the visible region, at room temperature, using a Jobin Yvon-Spex spectrometer (HR 460) fitted with a 1200 grooves mm⁻¹ grating blazed at 500 nm, coupled to a R928 Hamamatsu photomultiplier. A 150 W Xenon arc lamp coupled to an excitation monochromator Jobin Yvon-Spex (TRIAX 180) fitted with a 1200 grooves mm⁻¹ grating blazed at 330 nm was used as excitation source. All spectra were corrected for the response of the detectors.

Scanning Electron Microscopy (SEM) and Energy-Dispersive X-Ray Spectroscopy (EDS).

Particle dimensions and morphology of native and Cs⁺-exchanged Eu-AV-20 samples were

assessed by SEM analysis using a Hitachi S4100 microscope. EDS was used to confirm the cesium uptake by Eu-AV-20.

Powder X-Ray Diffraction (PXRD).

PXRD was carried out on a PANalytical Empyrean diffractometer (Cu K_{α1,2}X-radiation, $\lambda_1 = 1.540598 \text{ \AA}$; $\lambda_2 = 1.544426 \text{ \AA}$) equipped with an PIXcel 1D detector and a flat-plate sample holder in a Bragg-Brentano para-focusing optics configuration (45 kV, 40 mA). Intensity data were collected by the step-counting method (step 0.04°), in continuous mode, in the range $ca. 5 \leq 2\theta \leq 50^\circ$.

Cesium concentration in solution.

The concentration of Cs⁺ in solution was measured with a Perkin Elmer AAnalyst 100 atomic absorption spectrometer, in the emission mode (with a wavelength of 852.1 nm and a slit of 0.2 nm) and using an air-acetylene flame. The ionization was controlled by the addition of 0.5% (wt.) of potassium chloride to samples and standards. Each sample was

V.1.2.4. Fixed-bed and batch ion experiments

Preparation of the fixed-bed column. The column consisted of a vertical stainless steel tube (length 10.0 cm and internal diameter 1.30 cm) containing a precise amount of Eu-AV-20 (Figure 1). The solid was placed in the tube and confined at both ends by four to six quartz wool discs (from Elemental Microanalysis), followed by one stainless steel net, and the assembly was closed with Swagelok® fittings. The bottom of the column was connected to the influent reservoir and the top of the column was connected to a sampler (Figure V.1.1).

Preparation of solutions. A Cs⁺ stock solution (10.0 mol m⁻³) was prepared by dissolving CsNO₃ (0.0980x10⁻³ kg, 5.03x10⁻⁴ mol) in high-purity water (50.0 mL). Working solutions were prepared by diluting the stock solution to the desired concentration, using high-purity water, immediately before their usage to avoid cation adsorption on the glassware and lab material.

Fixed-bed ion exchange experiments. In a typical experiment a freshly prepared solution containing a known concentration of Cs⁺ was fed to the bottom of the column (up-flow mode) at constant flow rate using a peristaltic pump (Knauer Smartline pump 100). The pH and

temperature were measured at column inlet using a pH meter (Crison Basic 20). Periodically, 15 mL samples were collected at the outlet of the column after passing an acid washed cellulose acetate membrane disc filter (0.45 μm). The concentration of Cs⁺ in the samples was measured by atomic emission spectroscopy. Operation of the column was stopped for equal influent and effluent concentrations of Cs⁺. A control experiment (i.e. without Eu-AV-20 in the column) was run to check that Cs⁺ removal occurred by ion exchange with the solid rather than by adsorption on the lab material.

A set of five experiments (Table V.1.2) was performed to assess the influence of superficial velocity ($0.40\text{--}1.03\times 10^{-3} \text{ m s}^{-1}$) and mass of ion exchanger ($0.42\text{--}0.85\times 10^{-3} \text{ kg}$) on the Cs⁺ removal efficiency. Exps. 1–3 were performed for similar cesium influent concentration (ca. 1.4 ppm) and mass of solid (ca. $0.43\times 10^{-3} \text{ kg}$) to study the influence of the superficial velocity. The effect of exchanger mass can be evaluated from Exps. 2 and 4. The last run (Exp. 5) was carried out for a shorter period, under the same conditions of Exp. 3, to obtain Eu-AV-20 with an intermediate amount of Cs⁺ (ca. 65% of the breakthrough curve, 80% of the exchange capacity) in order to assess reproducibility and the dependence of photoluminescence on the cesium content in the sorbent.

Batch ion experiments. An additional set of four batch experiments (Table V.1.3) was carried out to evaluate the selectivity of Eu-AV-20 towards Cs⁺ in the presence of Na⁺. The initial concentration of cesium was fixed around $5\times 10^{-3} \text{ mol m}^{-3}$ and the initial sodium nitrate concentrations were 0, 1.02, 10.00 and 52.42 mol m^{-3} , which means the molar ratios were 0, 193, 2000 and 9456, respectively. The mass of Eu-AV-20 was always ca. $3\times 10^{-4} \text{ kg}$ and the run time 150 h to ensure system equilibration. Preparation of the solutions and cesium quantification were performed as described above.

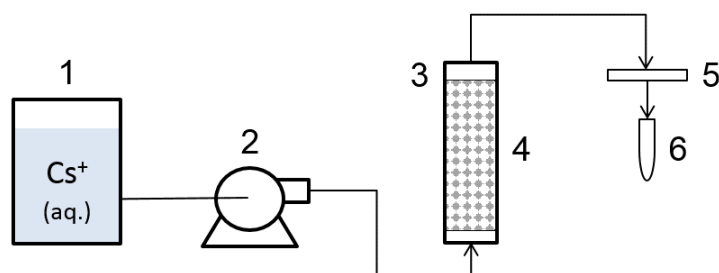


Figure V.1.1 – Experimental setup of the ion exchange unit: 1) influent reservoir tank; 2) peristaltic pump; 3) fixed-bed column in up-flow mode; 4) Eu-AV-20 powder bed; 5) membrane disc filter; and 6) sample collecting tube.

Table V.1.2 – Eu-AV-20 fixed-bed ion exchange experiments performed at 295 ± 1 K.

Experiment number	1	2	3	4	5
Inlet concentration of Cs ⁺ (mol m ⁻³)	0.0107	0.0108	0.0108	0.0111	0.0107
Inlet concentration of Cs ⁺ (ppm)	1.422	1.435	1.435	1.475	1.422
Bed height (m)	0.010	0.010	0.010	0.016	0.010
Mass of Eu-AV-20 (10 ⁻³ kg)	0.424	0.424	0.436	0.853	0.438
Superficial velocity (10 ⁻³ m s ⁻¹)	1.03	0.618	0.399	0.618	0.402
Run time (h)	50	50	50	50	15

Table V.1.3 – Eu-AV-20 competitive ion exchange in batch experiments performed at 295 ± 1 K.

Experiment number	1	2	3	4
Initial concentration of Cs ⁺ (mol m ⁻³)	0.0055	0.0050	0.0053	0.0047
Initial concentration of Na ⁺ (mol m ⁻³)	52.42	10.00	1.02	0
Initial Na ⁺ /Cs ⁺ molar ratio	9456	2000	193	0
Mass of Eu-AV-20 (10 ⁻³ kg)	0.301	0.308	0.306	0.302
Run time (h)	150			

V.1.3. Modelling isotherms and breakthrough curves

V.1.3.1. Equilibrium Isotherm

Ion exchange is often represented as a conventional chemical reaction, since it is a stoichiometric process by which two counter ions, A^{z_A} and B^{z_B} , are exchanged between an electrolyte solution and a solid exchanger [32,33]. Generically, an ion exchange process is represented by:



where z_A and z_B are the electrochemical valences of both counter ions, and the capping bar denotes the exchanger phase. According to Eq. (V.1.1), the exchanger is in B^{z_B} form and is converted into A^{z_A} form. For the particular case in analysis, $A^{z_A} = \text{Cs}^+$, $B^{z_B} = \text{Na}^+, \text{K}^+$, which, for simplicity, will be henceforth designated by A and B.

The isotherm of $\text{Cs}^+(\text{Na}^+, \text{K}^+)/\text{Eu-AV-20}$ system was determined by Figueiredo et al. [31], who represented the equilibrium data with 5.3% of error by the Langmuir equation:

$$q_{A,\text{eq}} = \frac{125048 \times C_{A,\text{eq}}}{1 + 437.5 \times C_{A,\text{eq}}} \quad (V.1.2)$$

where $C_{A,\text{eq}}$ is the equilibrium concentration of A in solution (mol m^{-3}) and $q_{A,\text{eq}}$ is the equilibrium concentration of A in the solid, here expressed in mol m^{-3} .

V.1.3.2. Nernst-Planck based model for fixed-bed ion exchange

The ion-exchange process was modelled using the Nernst-Planck equations, which state that the net intraparticle fluxes (N_i , $\text{mol m}^{-2} \text{s}^{-1}$) result from molar concentration (q_i , mol m^{-3}) gradients and electric potential gradient. For counter ion A, the flux is given by [16,17,32,33]:

$$N_A = -\frac{D_A D_B (z_A^2 q_A + z_B^2 q_B)}{D_A z_A^2 q_A + D_B z_B^2 q_B} \left(\frac{\partial q_A}{\partial r} \right) = -D_{AB} \left(\frac{\partial q_A}{\partial r} \right), \quad D_{AB} \equiv \frac{D_A D_B (z_A^2 q_A + z_B^2 q_B)}{D_A z_A^2 q_A + D_B z_B^2 q_B} \quad (V.1.3)$$

where D_A and D_B ($\text{m}^2 \text{s}^{-1}$) are the self-diffusion coefficients of both counter ions, r (m) is the radial position in the particle, and D_{AB} ($\text{m}^2 \text{s}^{-1}$) is the interdiffusion coefficient. The ion exchanger capacity is given by: $Q(\text{eq m}^{-3}) = q_A z_A + q_B z_B$.

The fixed-bed model encompasses a material balance to the column, Eq. (V.1.4), with an axial dispersion term, a convective term, and two accumulation terms for the fluid and solid phases, whose boundary conditions are given by Eqs. (V.1.5) and (V.1.6):

$$\frac{\partial C_A(l, t)}{\partial t} = D_L \frac{\partial^2 C_A(l, t)}{\partial l^2} - u \frac{\partial C_A(l, t)}{\partial l} - \frac{1 - \varepsilon}{\varepsilon} \frac{\partial \bar{q}_A(l, t)}{\partial t} \quad (\text{V.1.4})$$

$$l = 0, \quad D_L \left. \frac{\partial C_A(l, t)}{\partial l} \right|_{l=0^+} = -u(C_{A,0} - C_A|_{l=0^+}) \quad (\text{V.1.5})$$

$$l = L, \quad \left. \frac{\partial C_A(l, t)}{\partial l} \right|_{l=L} = 0 \quad (\text{V.1.6})$$

Here, C_A is the molar concentration of species A in solution (mol m^{-3}), u is the superficial velocity (m s^{-1}), l is the position along the bed length (m), L is the total length of the bed (m), t is time (s), D_L is the axial dispersion coefficient ($\text{m}^2 \text{s}^{-1}$), ε is the average bed porosity ($\varepsilon = 0.88$), \bar{q}_A is the average concentration of A in the solid (mol m^{-3}), and $C_{A,0}$ is the concentration of A at the column inlet. D_L was estimated using the following correlation [34]:

$$D_L = (20 + 0.5 \times \text{Sc} \times \text{Re}) \times \frac{D_m}{\varepsilon} \quad (\text{V.1.7})$$

where D_m is the diffusivity of Cs⁺ in water ($2.06 \times 10^{-9} \text{ m}^2 \text{s}^{-1}$ at 298.15 K [35]) and Sc and Re are the Schmidt and Reynolds numbers, respectively.

The material balance to the ion exchanger is given by Eq. (V.1.8). Eqs. (V.1.9)-(V.1.11) represent its initial and boundary conditions, and Eq. (V.1.12) translates the equality of fluxes at the interface:

$$\frac{\partial q_A}{\partial t} = -\frac{1}{r^2} \frac{\partial}{\partial r} (r^2 N_A) \quad (\text{V.1.8})$$

$$t = 0, \quad \begin{cases} q_A = 0 \\ C_A = C_{A,0} \end{cases} \quad (\text{V.1.9})$$

$$r = 0, \quad \frac{\partial q_A}{\partial r} = 0 \quad (\text{V.1.10})$$

$$r = R_p, \quad q_A = q_{A,R_p} \quad (\text{V.1.11})$$

$$N_A|_{R_p} = k_f (C_A - C_A|_{R_p}) \quad (\text{V.1.12})$$

R_p is the particle radius (m), $C_A|_{R_p}$ is the concentration at the interface, and k_f is the convective mass transfer coefficient (m s⁻¹) of counter ion A. The value of k_f was estimated by the following correlation involving classical Sherwood (Sh), Reynolds (Re) and Schmidt (Sc) numbers [8]:

$$\text{Sh} = \frac{1.13}{\varepsilon} \text{Re}^{0.21} \text{Sc}^{1/3} \quad (\text{V.1.13})$$

The average loading per unit particle volume needed in Eq. (V.1.4) is calculated by:

$$\bar{q}_A = \frac{3}{R_p^3} \int_0^{R_p} r^2 q_A dr \quad (\text{V.1.14})$$

The stoichiometric time, t_{st} (h), of a breakthrough curve can be calculated by Eq. (V.1.15) using experimental data or estimated on the basis of the solute movement theory by Eq. (V.1.16):

$$t_{st} = \int_0^\infty \left(1 - \frac{C_A(t)}{C_{A,0}} \right) dt \quad (\text{V.1.15})$$

$$t_{st} = \frac{L}{v} \left(1 + \frac{1 - \varepsilon}{\varepsilon} \frac{q_{A,0}}{C_{A,0}} \right) \quad (\text{V.1.16})$$

where $q_{A,0}$ is the solid loading in equilibrium with feed concentration, $C_{A,0}$.

V.1.3.3. Analytic breakthrough models

The equations of Clark [36], Yoon-Nelson [37], Bohart-Adams [38], and Thomas [39] were adopted in this study to model the breakthrough curves along with the Nernst-Planck based model.

The Thomas model [39] assumes Langmuir kinetics for sorption-desorption, negligible axial and radial dispersion, and a second-order reversible kinetics. The most common version of this model in environmental sorption and biosorption literature is given by:

$$\frac{C_A(t)}{C_{A,0}} = \frac{1}{1 + e^{\left[\frac{k_{Th}}{v}(Q_{Th}m - C_{A,0}vt)\right]}} \quad (V.1.17)$$

where k_{Th} is the Thomas rate constant ($m^3 \text{ mol}^{-1} \text{ s}^{-1}$), Q_{Th} is the maximum concentration of the solute in the solid phase (mol kg^{-1}), m is the mass of solid (kg), and v is the volumetric flow rate ($m^3 \text{ s}^{-1}$).

The Bohart-Adams model, initially developed to describe the adsorption of chloride on charcoal [38], assumes that the sorption rate is proportional to the residual capacity of the exchanger and to the concentration of the solute species in solution. Its equation may be expressed as:

$$\frac{C_A(t)}{C_{A,0}} = \frac{1}{1 + e^{[k_{BA}(q_{A,max} \tau - C_{A,0} t)]}} \quad (V.1.18)$$

where k_{BA} is the Bohart-Adams mass transfer coefficient ($m^3 \text{ mol}^{-1} \text{ s}^{-1}$), $q_{A,max}$ is the saturation concentration (mol m^{-3}), and $\tau = L/u$ is the space time (s).

The major difference between the Thomas and Bohart-Adams models lies in the embodied isotherms: the first one uses Langmuir and the latter adopts a rectangular or irreversible isotherm. Therefore, for highly favourable isotherms the Thomas model reduces to the Bohart-Adams equation and their parameters become interchangeable, i.e. $k_{Th} = k_{BA}$ and $Q_{Th}m/v = q_{A,max} \tau$ [40].

The Clark model [36] combines mass transfer concepts and the Freundlich isotherm, and it assumes plug flow and negligible dispersion phenomena. It is mathematically given by:

$$\frac{C_A(t)}{C_{A,0}} = \left[\frac{1}{1 + A_C e^{-\omega t}} \right]^{\frac{1}{n-1}} \quad \text{with} \quad A_C = \left(\frac{C_{A,0}^{n-1}}{C_b^{n-1}} - 1 \right) e^{\omega t_b} \quad (\text{V.1.19})$$

where n is the Freundlich constant, and C_b is the solute concentration (mol m⁻³) at breakthrough time, t_b (h), and ω is a rate parameter (h⁻¹).

The Yoon-Nelson model [37] assumes that the rate of decrease in the probability of sorption for each sorbate molecule is proportional to the probability of sorbate sorption and sorbate breakthrough on the sorbent. The model does not require detailed data concerning solute characteristics, type of sorbent and physical properties of the bed. For a single component system it is expressed by:

$$\frac{C_A(t)}{C_{A,0}} = \frac{e^{[k_{YN}(t-t_{50})]}}{1 + e^{[k_{YN}(t-t_{50})]}} \quad (\text{V.1.20})$$

where k_{YN} denotes the Yoon-Nelson rate constant (h⁻¹), and t_{50} is the time for $C_A/C_{A,0} = 0.5$.

V.1.3.4. Numerical methods and calculations approach

The Method of Lines was applied for the numerical calculation of the concentration profiles of Cs⁺, and their evolution along time in the solution and in the solid phase, for the case of the NP-based model. The required spatial discretization in the particle and bed length was accomplished by Finite Differences. The resulting initial-value problem set of ordinary differential equations was solved numerically using 51 grid points for the particle radius and 31 grid points for the bed length.

Regarding the NP-based model, the self-diffusion coefficients (D_A and D_B) were fitted to the data of Exp. 1 only, while k_f values were estimated by Eq. (V.1.13). Therefore, only two initial guesses were required to model Exp. 1, and the breakthrough curves of Exps. 2–4 were completely predicted.

In what concerns the so-called Thomas and Bohart-Adams models, Eqs. (V.1.17) and (V.1.18), the calculations involved four individual constants (k_{Th} or k_{BA}), one for each run, plus one shared parameter (Q_{Th} or $q_{A,max}$). In turn, the Clark and Yoon-Nelson models (Eqs.

(V.1.19) and (V.1.20)) were adjusted considering one pair of parameters per curve: (ω , A_C) and (k_{YN} , t_{50}). Moreover, for the Clark model the values of A_C and ω were determined by nonlinear regression of breakthrough data, using the Freundlich constant ($n = 2.368$) obtained by fitting the adsorption isotherm to published equilibrium points [31]. Although the Freundlich isotherm is not the best model to represent the Cs⁺/(Na⁺,K⁺)/Eu-AV-20 system, the fitting was acceptable (9.74% error).

The Nelder-Mead and the Marquardt-Levenberg algorithms were adopted in this work for all optimizations using the root mean square deviation (RMSD) as objective functions:

$$\text{RMSD (\%)} = 100 \times \sqrt{\sum_{i=1}^{\text{NDP}} \frac{(C_{A,\text{calc}}|_i - C_{A,\text{exp}}|_i)^2}{\text{NDP}}} \quad (\text{V.1.21})$$

where NDP is the number of data points, and the subscripts 'exp' and 'calc' denote measured and calculated concentrations, respectively. All programs were written and coded in Matlab R2013a®.

V.1.4. Results and discussion

V.1.4.1. Materials characterization

SEM images of native and Cs⁺-exchanged Eu-AV-20 crystals are similar (Figure V.1.2) and reveal microcrystalline pseudo hexagonal thin plates with a lateral dimension lower than 20×10⁻⁶ m, which is consistent with previous reports [31]. With respect to EDS results, Figure 3 confirms that the Cs⁺ was sorbed because cesium is absent in the native material (see Figure V.1.3.a) while it appears in the solid after ion exchange (see Figure V.1.3.b).

The experimental PXRD pattern of native Eu-AV-20 (Figure V.1.4) shows all the characteristic reflections [29] and no impurity phases are detected. The PXRD patterns of the samples collected after the fixed-bed experiments (Exps. 1–5, Table V.1.2) exhibit some changes, such as peak shifts from 14.21° to 14.36°, from 31.25° to 31.38° and from 32.27° to 32.43°, the increment of intensity of the peak at 28.95° and the presence of a new peak at 30.09°. Altogether, these results indicate slight changes in the crystalline structure of Cs⁺-

exchanged Eu-AV-20, which may result in alterations in the local Eu^{3+} environment that impact on the photoluminescence properties (to discuss in Section V.1.4.4).

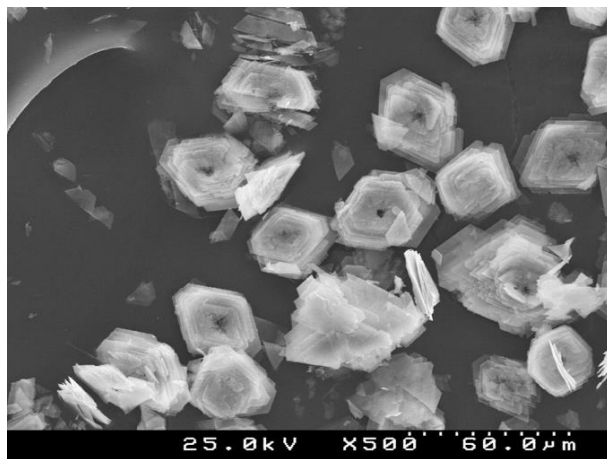


Figure V.1.2 – SEM image of Eu-AV-20 crystals.

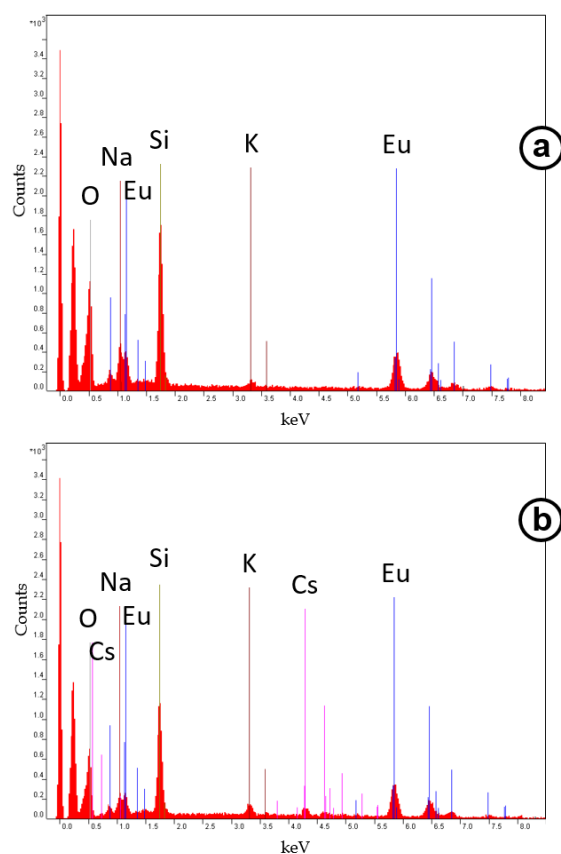


Figure V.1.3 – EDS spectra of (a) native and (b) Cs^+ -exchanged Eu-AV-20 samples.

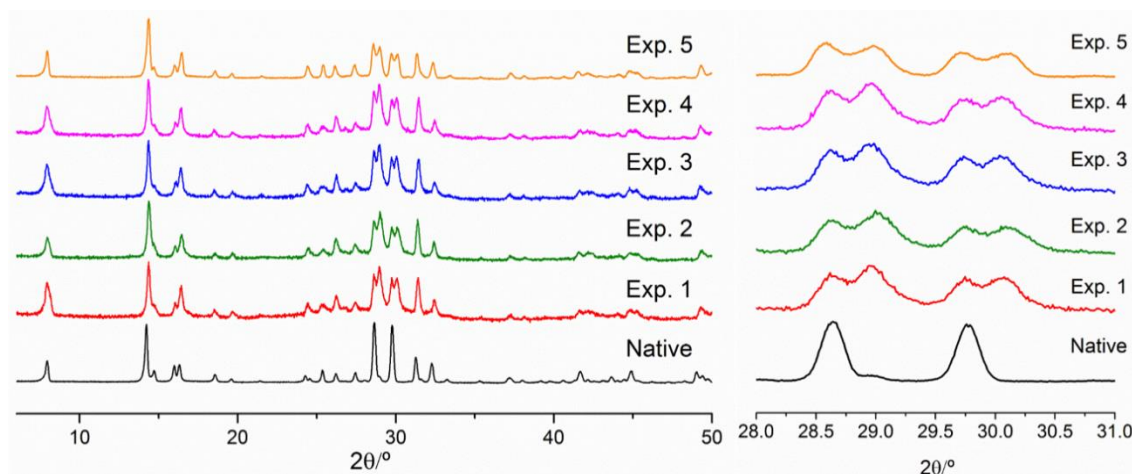


Figure V.1.4 – PXRD of native and Cs⁺-exchanged Eu-AV-20 samples collected after the fixed-bed experiments (Exps. 1–5, see Table V.1.2). Inset: PXRD on an expanded scale in the range 28–31°.

V.1.4.2. Fixed-bed experimental results and selectivity assessment

The breakthrough curves (Exps. 1–4, Table V.1.2) are plotted in Figure 5 grouped according to the different variables under study, namely, the superficial velocity (varied *via* flow rate modification) (Exps. 1–3, Figure V.1.5.a), and the mass of ion exchanger (Exps. 2 and 4, Figure V.1.5.b). The plots illustrate the evolution of the normalized cesium concentration in solution at the column outlet, $C_A(t)/C_{A,0}$.

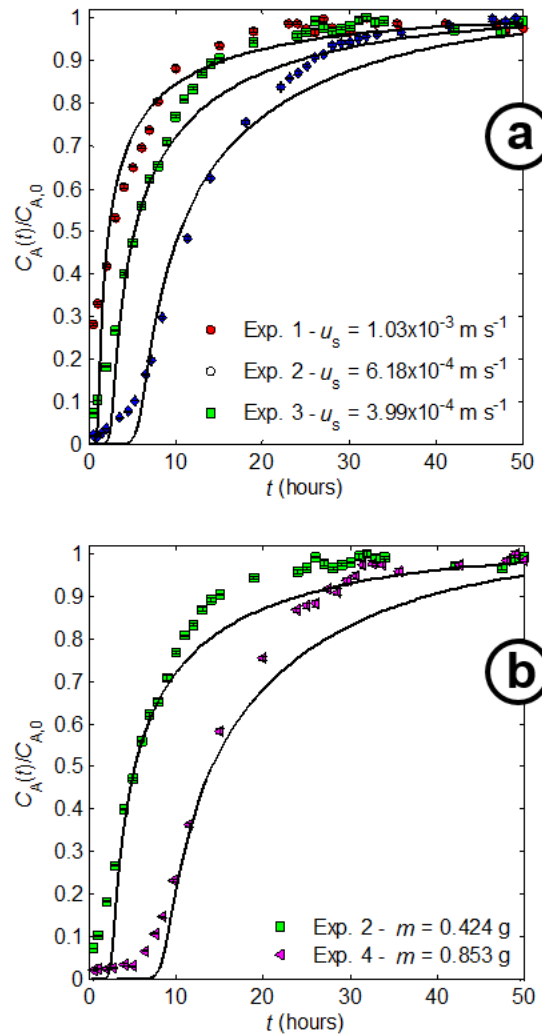


Figure V.1.5 – Normalized experimental breakthroughs for Cs^+ removal in a fixed-bed of Eu-AV-20. (a) Effect of superficial velocity (*via* flow rate variation); (b) Effect of the mass of ion exchanger. Symbols: data (experimental conditions in Table V.1.2); lines: NP-based model.

Considering that the isotherm of the $\text{Cs}^+ / (\text{Na}^+, \text{K}^+) / \text{Eu-AV-20}$ system is favourable, *i.e.*, convex upward (see Eq. (V.1.2)), in the absence of dispersive phenomena (such as axial dispersion and/or film and intraparticle resistances to mass transfer) a step-function would propagate ideally without changes along the fixed-bed and would exit the column at a precise instant, the stoichiometric time (t_{st}) given by Eqs. (V.1.15) or (V.1.16). Hence, the experimental ion exchange breakthrough curves shown in Figure 5 clearly disclose that mass transfer effects prevail in this system.

The influence of axial dispersion is certainly negligible since the calculated axial Peclet numbers ($Pe_L = uL/D_{ax}$) were 174.5, 115.1, 78.7 and 178.6 for Exps. 1–4, and the well-known relation $L > 50 d_p$ was largely obeyed ($d_p = 2.3 \times 10^{-5}$ m and L was 0.010 m (Exps. 1–3) or 0.016 m (Exp. 4)). Regarding external resistance to mass transfer, the width of the breakthrough curves changed with flow rate variation, *i.e.*, they increased with decreasing superficial velocity (Exps. 1–3), which indicates the existence of film diffusion limitations. This observation was also confirmed by simulation (to be further discussed below).

According to the breakthroughs curves (Exps. 1–3, Figure V.1.5.a), lower superficial velocities require higher operating times to exhaust the solid phase, and vice-versa. This result is in agreement with the solute movement theory, Eq. (V.1.16), since the stoichiometric time (t_{st}) is inversely proportional to superficial velocity. The t_{st} values calculated from experimental data were 4.96, 7.53 and 13.80 h (for Exps. 1, 2 and 3, respectively).

To study the impact of ion exchanger mass on the breakthrough curves, the mass of Eu-AV-20 was increased 100% (Exp. 4 *versus* Exp. 2). The two breakthrough curves (Figure V.1.5.b) are considerably different especially in what concerns the 5 h delay period observed in Exp. 4, before the consistent and visible rise of $C_A(t)$. Once again, the solute movement theory provided excellent results, since $t_{st,4}/t_{st,2} = 15.62/7.53 = 2.07$, which is almost equal to the ratio of sorbent masses, $m_4/m_2 = 0.853/0.424 = 2.0$ (calculated by Eq. (V.1.16) considering also that $L \propto m$).

A preliminary study of ion exchange competition was performed in order to analyse the influence of the presence of Na⁺ upon cesium uptake (see experimental conditions in Table V.1.3). The final uptake of Cs⁺ is plotted in Figure V.1.6 against the initial molar ratio of Na⁺ and Cs⁺, being possible to conclude that Eu-AV-20 reached Cs⁺ removals of 76.0, 70.2, 39.5 and 20.0% for 0, 193, 2000 and 9456 ratios, respectively. These values confirmed the exchanger affinity to cesium as 20% uptake was attained even when the initial sodium concentration was three orders of magnitude higher.

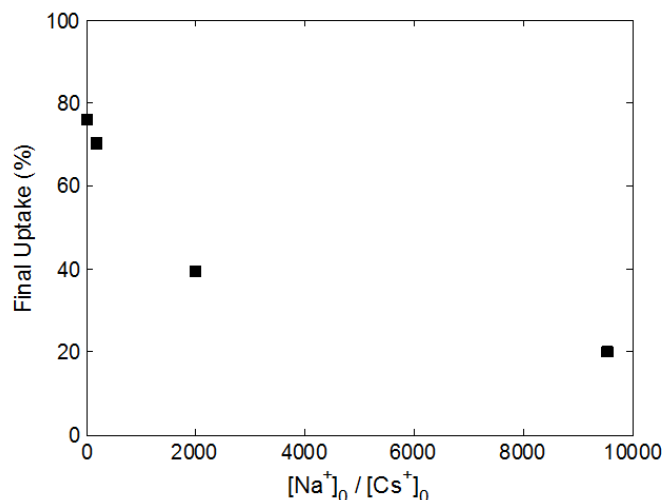


Figure V.1.6 – Final uptake of cesium as function of the initial molar ratio of Na⁺ and Cs⁺ (experimental conditions in Table V.1.3).

V.1.4.3. Fixed-bed modelling results

A model can be validated through the fitting of experimental results, but its usefulness comes mainly from its ability to predict the behaviour of a process under operating conditions different from those used to obtain its parameters [33]. In the present section, the calculated results obtained with NP-based model and by the analytic equations of Thomas, Bohart-Adams, Clark and Yoon-Nelson are presented and discussed, being demonstrated the prediction ability of the NP-based model.

Nernst-Planck based model. The results achieved in this case are plotted in Figure V.1.5 together with the experimental data (Exps. 1–4). The model parameters (D_A and D_B) were obtained by fitting the data of Exp. 1 only, with good correlation (RMSD = 6.66%), while for Exps. 2–4 pure prediction provided deviations of 6.55%, 5.24% and 7.95%, respectively (Table V.1.4) The self-diffusivities ($D_A = 2.324 \times 10^{-16} \text{ m}^2 \text{ s}^{-1}$ and $D_B = 6.134 \times 10^{-15} \text{ m}^2 \text{ s}^{-1}$) are of the same order of magnitude of those reported for the system Cd²⁺/Na⁺/ETS-10 [16], and bigger than those published for Cd²⁺/Na⁺/ETS-4 [14] and Hg²⁺/Na⁺/ETS-4 [41]. Despite the exchanged counter ions are different (Cs⁺ against of Cd²⁺ or Hg²⁺), the diffusion coefficients are consistent with the pore sizes of ETS-4 (3×4 Å), Eu-AV-20 (5.8×6.8 Å) and ETS-10 (4.9×7.6 Å). With respect to the film diffusion coefficients, their values were estimated by Eq. (V.1.13) and gave rise to 4.119×10^{-4} (Exp. 1), 3.700×10^{-4} (Exp. 2 and 4) and 3.381×10^{-4} (Exp. 3) m s⁻¹. During the

course of the simulations it was observed that k_f influences the results, meaning that the external limitation to mass transfer are not negligible.

An advantage of the Nernst-Planck based model is its breadth to understand the kinetic processes governing ion exchange in a fixed-bed column. For instance, the model describes the time evolution of the outlet cesium concentration but, above all, it discloses the concentration profiles of cesium along the column in the bulk and inside the Eu-AV-20 particles. Accordingly, the normalized Cs⁺ concentration in solution, $C_A(t)/C_{A,0}$, and the normalised average solid loading, $\bar{q}_A/q_{A,\max}$, were computed and plotted against time and longitudinal bed position for the conditions of Exp. 3, in Figure V.1.7.a and Figure V.1.7.b, respectively. The independent variables were also normalized, being $Z = l/L$ and $\theta = t/\tau$, where $\tau = L/u$ is the space time (s).

In terms of bulk solution concentration, the surface in Figure V.1.7.a illustrates both the decreasing profiles along the column (as Z goes from 0 to 1) for different exchange times, and the attenuation of these curves as time increases. As a particular case of Figure V.1.7.a, the breakthrough curve previously represented for Exp. 3 in Figure 5.a becomes visible at the column outlet ($Z = 1$).

If the focus is placed on the solid, Figure V.1.7.b evidences that Cs⁺ concentration profiles follow the same tendency as in bulk solution, displaying a delay due to the effect of mass transfer kinetics. Specifically, Cs⁺ load decreases along the column (when Z goes from 0 to 1) and increases with time, reaching 80% of the capacity established by the Langmuir isotherm, Eq. (2), for θ ca. 7000. This is expected because Eu-AV-20 particles positioned at the top of the bed contact with less concentrated solutions throughout the process and, thus, require a longer time to reach equilibrium.

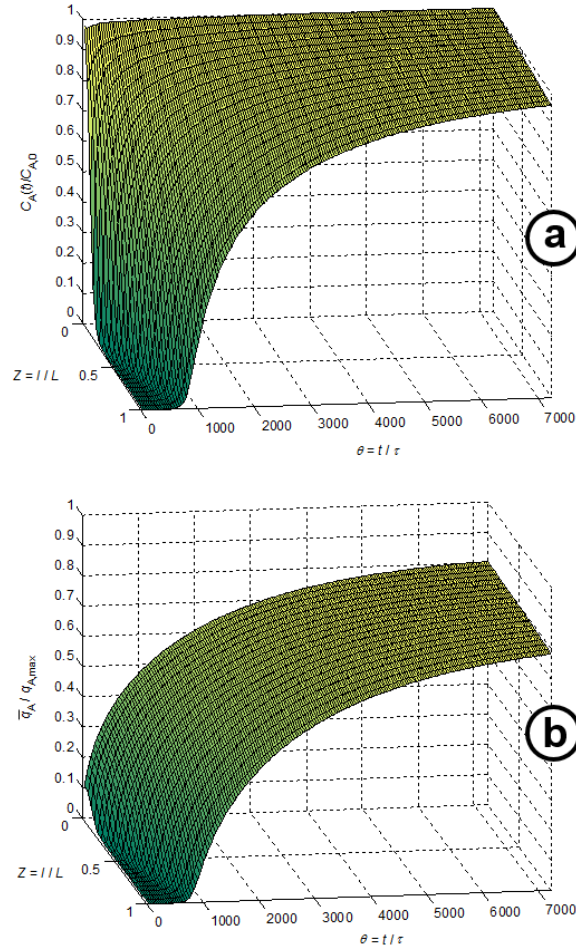


Figure V.1.7 – Normalized Cs⁺ concentration in bulk solution (a) and normalized Cs⁺ loading in the solid (b) as function of dimensionless time and longitudinal bed position. Simulations were performed for the conditions of Exp. 3 (Table V.1.2).

Analytic models. The data from Exps. 1–4 were fitted to four conventional analytic models, Eqs. (17)–(20), with good accuracy: RMSDs in the range 3.20–6.47% and R^2 between 0.962 and 0.985 (Table V.1.3). The fitting quality of the analytic models can also be assessed in Figure 8, which presents calculated *versus* experimental normalized fluid concentrations at the column outlet. In general, the four models fit the data fairly well, but consistently overestimate at low/high outlet concentrations and underestimate for intermediate concentrations, *i.e.*, in the steep rise branches of the breakthrough curves.

The smaller deviations were found for the Clark and Yoon-Nelson models (RMSD 3.64% and 3.20%, respectively) not surprisingly since both models rely on eight regressed parameters. The usefulness of such models is therefore questionable.

The other two models comprise five parameters each, with the Thomas model, which is frequently used in the literature, behaving slightly better than the Bohart-Adams model (RMSD 5.15% and 6.47%, respectively). As discussed in section V.1.3.3, a correlation between the parameters was expected in advance due to the mathematical equivalence of the models, namely $k_{BA} = k_{Th}$ and $Q_{Th}m/v = q_{A,max}L/u$. From Table V.1.3 it is possible to conclude that k_{BA} and k_{Th} are quite similar with an average absolute relative deviation of only 12.4%. Additionally, the average value of the ratio $Q_{Th}mu/(v q_{A,max} L)$ was 0.99, very close to the theoretical value of 1.

In comparison, the 2-parameter Nernst-Planck based model presents higher deviations with a RMSD of 6.53% (Table V.1.3) which is quite similar to the deviations reported in the literature for zeolite-type materials [14,16,17,41]. Despite being less expedite to implement than the four analytic models, the NP-based model presented in this work provides crucial information about the transport mechanisms inside and outside the Eu-AV-20 particles, and predicts the dynamic behaviour of the fixed-bed ion exchange column. Such potential relies on its theoretically sound assumptions.

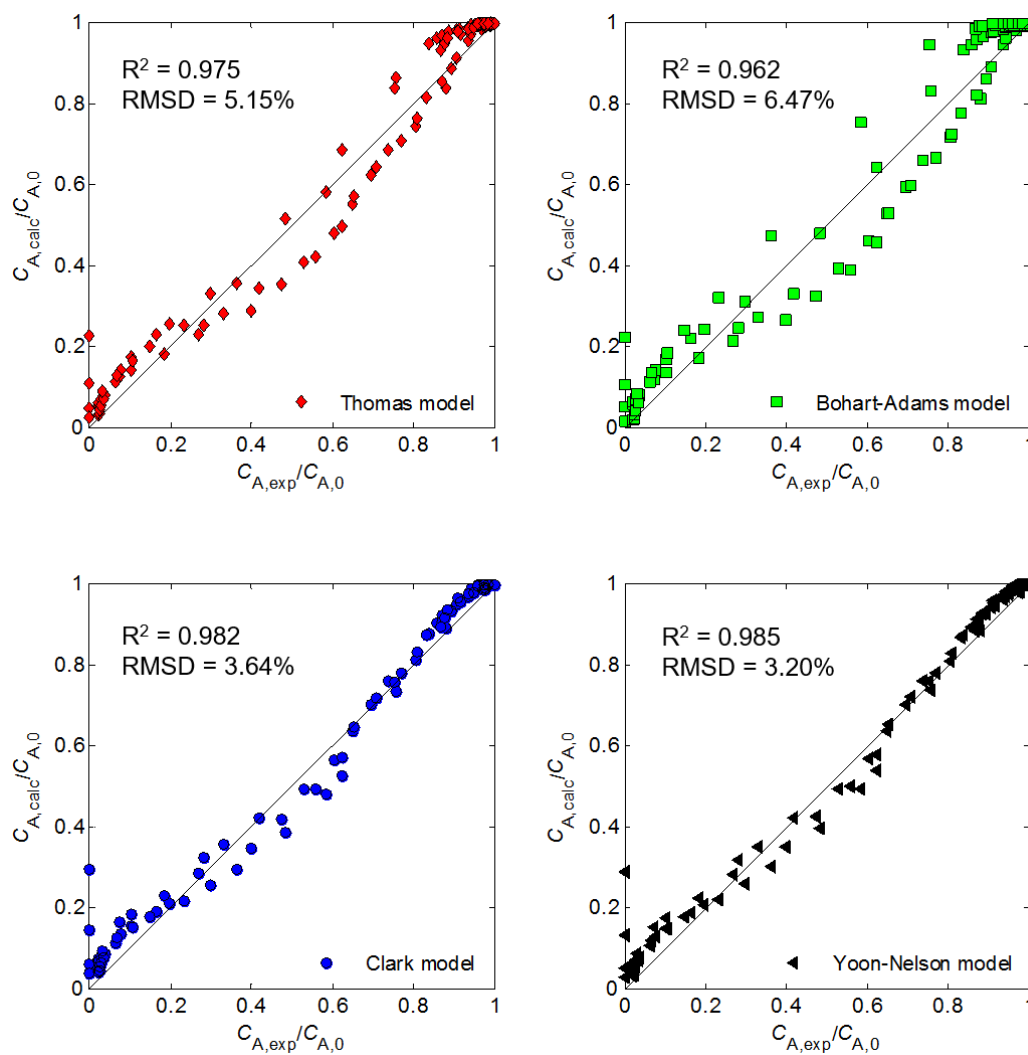


Figure V.1.8 – Comparison of the four conventional analytic models for fixed-bed ion exchange: calculated versus experimental normalized fluid concentrations at column outlet. (Experimental conditions in Table V.1.2).

Table V.1.4 – Optimized parameters and calculated deviations for the Nernst-Planck based model and for the analytic models from literature applied to the fixed-bed experiments. (Exp. conditions in Table V.1.2).

Model	Nernst-Planck based model, Eqs. (V.1.3)-(V.1.6), (V.1.8)-(V.1.12) and (V.1.14)								
Exp.	NDP	Type of calculation	D_A (m ² s ⁻¹)	D_B (m ² s ⁻¹)	RMSD (%)	Global RMSD (%)			
1	29	correlation	2.324x10 ⁻¹⁶	6.134x10 ⁻¹⁵	6.66	6.66 (correlation)			
2	32	prediction	-	-	6.55				
3	31	prediction	-	-	5.24	6.53 (prediction)			
4	28	prediction	-	-	7.95				
Model	Thomas, Eq. (V.1.17)		Bohart-Adams, Eq. (V.1.18)		Clark, Eq. (V.1.19)	Yoon-Nelson, Eq. (V.1.20)			
Exp.	NDP	k_{Th} (m ³ mol ⁻¹ s ⁻¹)	Q_{Th} (mol g ⁻¹)	k_{AB} (m ³ mol ⁻¹ s ⁻¹)	$q_{A,max}$ (mol m ⁻³)	ω (h ⁻¹)	A_C (-)	k_{YN} (s ⁻¹)	t_{50} (h)
1	29	0.0075		0.0071		0.3219	4.30	8.913x10 ⁻⁵	3.07
2	32	0.0077		0.0073		0.3461	12.91	8.708x10 ⁻⁵	5.98
3	31	0.0069	5.293x10 ⁻⁵	0.0065	18.22	0.2463	44.05	6.092x10 ⁻⁵	13.26
4	28	0.0066		0.0088		0.2642	91.14	6.508x10 ⁻⁵	15.09
		RMSD = 5.15%		RMSD = 6.47%		RMSD = 3.64%		RMSD = 3.20%	
		R ² = 0.975		R ² = 0.962		R ² = 0.982		R ² = 0.985	

RMSD = Root Mean Square Deviation; R² = coefficient of determination

V.1.4.4. Photoluminescence results

Three samples were studied, native Eu-AV-20 and two Cs⁺-exchanged materials collected after fixed-bed experiments under similar conditions, except for the time of operation (Exps. 3 and 5, Table V.1.2). Exp. 3 was performed until exhaustion of the solid's exchange capacity (ca. 50 h) while Exp. 5 was run for a shorter period (ca. 15 h) to accomplish only 80% of $q_{A,max}$ (see Figure 9.a). Therefore, in view of the different contact times the three Eu-AV-20 samples have different Cs⁺ contents. Figure V.1.9.b reveals differences in the normalized emission spectra for the non-degenerated $^5D_0 \rightarrow ^7F_0$ transitions. The native washed Eu-AV-20 possesses two distinct europium sites (Eu1 and Eu2), which give peaks at 577.9 nm and 578.9 nm. However, the replacement of sodium and potassium cations by Cs⁺ introduces small modifications in the crystalline structure, as discussed previously (section V.1.4.1 and Figure V.1.4), leading to changes in the vicinity of Eu³⁺ cations and in the photoluminescence spectra: higher Cs⁺ loads decrease the intensity of the Eu1 emission and shift the Eu2 peak to lower wavelengths (Figure V.1.9.b). Even these are preliminary results they suggest that photoluminescence may be an expedite method to assess ion exchange phenomena in Cs⁺/Eu-AV-20 systems, and in addition disclose the potential of microporous Ln-silicate Eu-AV-20 solids for cesium sensing purposes.

The fact that the Eu-AV-20 photoluminescence varies upon Cs ion exchange raises the intriguing possibility of following up this process on-line by coupling to the fixed-bed column an optical fiber and a spectrometer. In this way the solid loading can be assessed online, complementing the usual sampling of the bulk liquid along the column. This combined information is important if one takes into account that mass transfer limitations always exist which means both phases are not in equilibrium. Work along these lines is in progress.

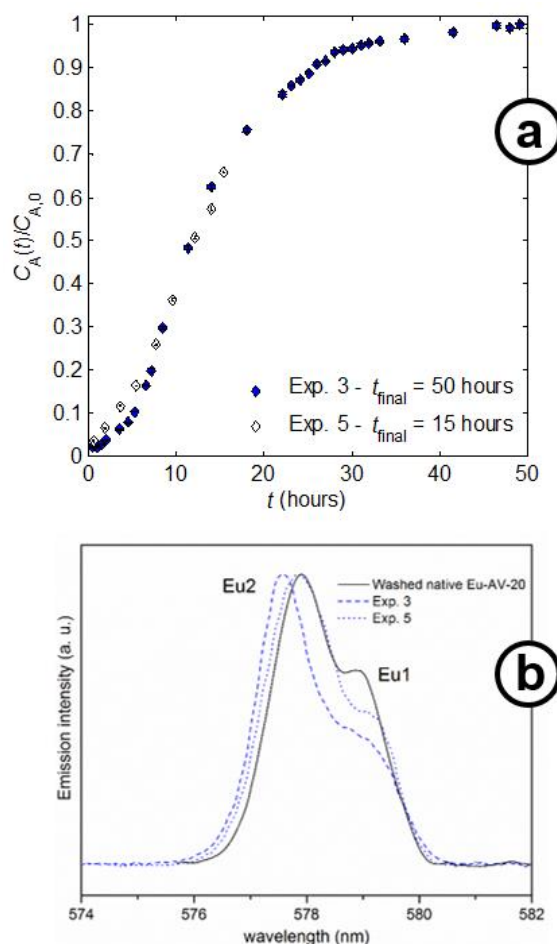


Figure V.1.9 – a) Measured breakthrough curves for two different run times (Exps. 3 and 5; experimental conditions in Table V.1.2); b) Normalized $^5\text{D}_0 \rightarrow ^7\text{F}_0$ transition of the photoluminescence emission room temperature spectra of the native and Cs^+ exchanged Eu-AV-20 with excitation at 393 nm.

V.1.5. Conclusions

The use of Eu-AV-20 for Cs^+ removal from aqueous solutions was studied in a fixed-bed column. The dynamic behaviour of the ion exchange column was in accord with theory, namely, higher solid masses and lower superficial velocities (*via* inferior flow rates) delayed the breakthrough curves. Moreover, the experimental stoichiometric times followed the solute movement theory.

The proposed Nernst-Planck based model (2 parameters) achieved $\text{RMSD} = 6.66\%$ for the correlation of one breakthrough curve, and only 6.54% for the prediction of the others. The optimized self-diffusivities were consistent with data from the literature, and followed essentially the pore size diameter of the solids. The RMSDs of Thomas, Bohart-

Adams, Clark and Yoon-Nelson models ranged between 3.20% (Yoon-Nelson, 10 parameters) and 6.47% (Bohart-Adams, 5 parameters). These reliable results are ascribed to the number of fitting parameters.

Regarding the photoluminescence of native and ion-exchanged Eu-AV-20, the uptake of Cs⁺ modifies the local environment of the Eu³⁺ emitter resulting in changes in the ⁵D₀→⁷F₀ transition intensities and line positions, indicating the potential of Eu-AV-20 for sensing purposes.

V.1.6. Nomenclature

A or A ^{ZA}	Counter ion initially in solution
A _C	Clark model parameter
B or B ^{ZB}	Counter ion initially in the exchanger
C _b	Solute concentration at breakthrough time in Clark model (mol m ⁻³)
C _A	Concentration of counter ion A in solution (mol m ⁻³)
C _{A,0}	Initial concentration of counter ion A in solution (mol m ⁻³)
D _i	Self-diffusion coefficient of counter ion <i>i</i> (m ² s ⁻¹)
D _L	Axial dispersion coefficient (m ² s ⁻¹)
D _{AB}	Interdiffusion coefficient of NP model (m ² s ⁻¹)
D _m	Diffusion coefficient of Cs ⁺ in water (m ² s ⁻¹)
Exp. j	Experiment number j
<i>i</i> and <i>j</i>	Generic counter ions
k _{BA}	Bohart-Adams mass transfer coefficient (m ³ mol ⁻¹ s ⁻¹)
k _f	Convective mass transfer coefficient (m s ⁻¹)
k _{Th}	Thomas rate constant (m ³ mol ⁻¹ s ⁻¹)
k _{YN}	Yoon-Nelson rate constant (h ⁻¹)
<i>l</i>	Column longitudinal coordinate (m)
L	Length of the fixed-bed (m)
Ln-silicate	Lanthanide silicate
<i>m</i>	Mass of ion exchanger (Eu-AV-20) (g)
<i>n</i>	Freundlich isotherm constant
NDP	Number of data points
NP	Nernst-Planck
PXRD	Powder X-ray diffraction

$q_{A,\max}$	Maximum solute concentration in the particle in Bohart-Adams model (mol m ⁻³)
$q_{A,0}$	Solid loading in equilibrium with feed concentration, $C_{A,0}$
q_i	Molar concentration of counter ion i in the particle (mol m ⁻³)
\bar{q}_i	Average concentration of counter ion i in the particle (mol m ⁻³)
Q_{Th}	Thomas model parameter: maximum solute concentration in the solid (mol kg ⁻¹)
r	Radial position in the particle (m)
R^2	Coefficient of determination
R_p	Particle radius (m)
RMSD	Root Mean Square Deviation (%)
SEM	Scanning Electron Microscopy
t_{50}	Yoon-Nelson parameter: time for $C_A/C_{A,0} = 0.5$, (h)
t	time (h or s)
t_{st}	Stoichiometric time (h)
t_b	Breakthrough time (h)
T	Absolute temperature (K)
u	Superficial velocity (m s ⁻¹)
v	Flow rate (m ³ s ⁻¹)
Z	Dimensionless longitudinal coordinate in the column
z_i	Electrochemical valence of counter ion i

Greek letters

ε	Bed void fraction
ρ_s	Density of ion exchanger
θ	Dimensionless time
τ	Space time (s)
ω	Clark model rate parameter (h ⁻¹)

Subscripts

0	Initial conditions
A	Counter ion initially present in the bulk solution (Cs ⁺)

B	Counter ions initially present in the ion exchange (K^+ and Na^+)
BA	Bohart-Adams model
calc	Calculated value
eq	Equilibrium value
exp	Experimental value
Th	Thomas
s	solid
YN	Yoon-Nelson model

Work reported in the scientific article

**Batch and fixed-bed removal of Cs⁺ from aqueous solutions using ETS-4:
Measurement and modeling of loading-regeneration cycles and equilibrium**

published on Chemical Engineering Journal 301 (2016) 276–284

Abstract

ETS-4 was prepared by hydrothermal synthesis and characterized by powder X-ray diffraction in order to assess its ion exchange capacity towards the removal of Cs⁺ from aqueous solutions in both batch and fixed-bed operation modes. Several assays were carried out to measure isotherm (8 experiments) and breakthrough curves (5 experiments); a set of loading-regeneration-loading experiments was also performed highlighting the ability of ETS-4 to be used in cyclic ion exchange. Powder X-ray diffraction showed that parent and Cs⁺-exchanged ETS-4 are isostructural. The Langmuir equation achieved good correlation results (average deviation of 6.58%), while the Nernst-Planck based model proposed for the fixed-bed assays fitted one breakthrough curve with 18.66% error, and was able to predict the remaining four experiments with 9.55% error. The Nernst-Planck parameters are the self-diffusion coefficients of Cs⁺ and Na⁺ in ETS-4, whose values ($D_{\text{Cs}^+} = 3.193 \times 10^{-16} \text{ m}^2 \text{ s}^{-1}$ and $D_{\text{Na}^+} = 6.088 \times 10^{-15} \text{ m}^2 \text{ s}^{-1}$) are consistent with the microporosity of ETS-4 framework and with the size of the counter ions.

V.2. Batch and fixed-bed removal of Cs⁺ from aqueous solutions using ETS-4: Measurement and modeling of loading-regeneration cycles and equilibrium

V.2.1. Introduction

The removal of long-lived radionuclides generated by nuclear power plants represents an important environmental aspect in nuclear waste management. For instance, the medium-lived radioisotopes strontium (⁹⁰Sr) and cesium (¹³⁷Cs), whose decay half-lives are, respectively, 28.9 and 30.1 years are responsible for most of the accumulated radiation on the produced effluents. Therefore, their removal is imperative and can be seen as an effective strategy to minimize such nuclear waste volumes [42,43]. To achieve the desired separation, various physicochemical processes may be applied, namely, co-precipitation, solvent extraction, coagulation, electrochemical, membrane processes, and adsorption/ion exchange [3,44].

In this context, inorganic ion exchangers are widely employed for the removal and safe storage of radionuclides from nuclear wastes due to their high mechanical, thermal and radiation stabilities and potential selectivity. On the other hand, due to the unique pore structure and cation exchange properties of natural and synthetic zeolites, this class of materials has attracted significant attention [33]. For instance, clinoptilolite has been used for cesium and strontium uptake before effluents discharge in the Irish Sea [45]. Mordenite and chabazite also found application in treating hazardous solutions from nuclear power plants [46,47]. Very recently, two microporous lanthanide silicates have been tested for the first time as Cs⁺ exchangers, Eu-AV-20 [31,48] (mineral tobermorite analogue) and Tb/Eu-AV-9 [49] (mineral montregianite analogue), where AV-n stands for Aveiro material number n.

Microporous titanosilicates are also a successful class of zeolite-like materials for the uptake of long- and medium-lived radionuclides from nuclear waste effluents. In this class, sitinakite [50,51] and pharmacosiderite [52,53] stand out, with the former having a synthetic counterpart commercially available from UOP [9,54,55]. Many other such materials deserve mention, such as the ETS (Engelhard Titanosilicates) [56–60] and AM (acronym of Aveiro-Manchester) [2,61–63] families. Titanosilicate ETS-4, in particular, comprises SiO₄ tetrahedra and TiO₅ and TiO₆ polyhedra, exhibiting high ion exchange capacity and, in the parent form, exchangeable Na⁺ and K⁺ cations [64]. ETS-4 has the ideal composition M₈Ti₅Si₁₂O₃₈·nH₂O (M=K,Na), essentially, the structure of zorite, comprising 8-membered rings and an effective pore size of 0.37 nm that may be fine-tuned by

progressive dehydration [64]. The Na-form of ETS-4 collapses at ca. 473 K, a limitation that may be overcome by ion exchange, for example with strontium [64].

Most of articles dealing with ion exchange focuses on batch assays for equilibrium and kinetic studies [15–17,41,45,60,65]. Nonetheless, fixed-bed experiments comprising both loading and regeneration steps are crucial for commercial/industrial applications, as their accurate design requires not only isotherms but also the knowledge of the dynamic behaviour of the system. For instance, the well-known breakthrough experiments are indispensable to measure the length of unused bed for the accurate scale-up of industrial sorption units. To accomplish this, the development of theoretically sound models for the representation of ion exchange data and subsequent simulations is also necessary for reliable optimization and scale-up. Some examples of fixed-bed assays include studies performed with titanosilicates ETS-10 [7,8] and CST [9], NaY zeolite [6], and lanthanide silicate Eu-AV-20 [31].

Here, the removal of Cs⁺ from aqueous solutions by ETS-4 is investigated using batch and fixed-bed experiments. Complete loading-regeneration cycles are performed and they are simulated using Nernst-Planck equations and Langmuir isotherm.

V.2.2. Modelling

Ion exchange is often represented as a chemical reaction because of the stoichiometric nature of the process by which two counter ions, A^{z_A} and B^{z_B} , are exchanged between an electrolyte solution and a solid sorbent according to:



where z_A and z_B are the electrochemical valences of counter ions, and the capping bar denotes the exchanger phase. In this study, A^{z_A} is Cs⁺, B^{z_B} is Na⁺, $z_A = z_B = +1$, and the exchanger (ETS-4) is converted from the $\overline{B^{z_B}}$ to the $\overline{A^{z_A}}$ form. For simplicity, A^{z_A} and B^{z_B} will be henceforth designated as A and B. To describe the fixed-bed ion exchange of the Cs⁺/Na⁺/ETS-4 system, a Nernst-Planck (NP) based model was written and coded in Matlab R2013a®.

The following equations were used successfully to represent the intraparticle mass transport of Hg²⁺/Na⁺ and Cd²⁺/Na⁺ pairs through ETS-4 [16,17]. Briefly, the NP equations state that the fluxes (N_i , mol m⁻² s⁻¹) of counter ions result from both concentration (q_i , mol

m⁻³) and electric potential gradients. For a binary A/B system, the internal flux of A is given by [16,17,32,33]:

$$N_A = -\frac{D_A D_B (z_A^2 q_A + z_B^2 q_B)}{D_A z_A^2 q_A + D_B z_B^2 q_B} \left(\frac{\partial q_A}{\partial r} \right) = -D_{AB} \left(\frac{\partial q_A}{\partial r} \right) \quad (\text{V.2.2})$$

$$D_{AB} \equiv \frac{D_A D_B (z_A^2 q_A + z_B^2 q_B)}{D_A z_A^2 q_A + D_B z_B^2 q_B} \quad (\text{V.2.3})$$

where D_A and D_B (m² s⁻¹) are the self-diffusion coefficients of A and B, r (m) is the radial coordinate in the particle, and D_{AB} (m² s⁻¹) is taken as an interdiffusion coefficient. The exchange capacity of the sorbent is calculated by Q (eq m⁻³) = $q_A z_A + q_B z_B$.

The fixed-bed model encompasses the material balance to the column (Eq. (V.2.4)), which contains the accumulation contributions in the fluid and solid phases, an axial dispersion term and a convective term. The appropriate initial and boundary conditions are given by Eqs. (V.2.5) and (V.2.6).

$$\frac{\partial C_A(l, t)}{\partial t} + \frac{1 - \varepsilon}{\varepsilon} \frac{\partial \langle q_A \rangle(l, t)}{\partial t} = D_L \frac{\partial^2 C_A(l, t)}{\partial l^2} - u \frac{\partial C_A(l, t)}{\partial l} \quad (\text{V.2.4})$$

$$t = 0, \quad C_A = C_{A, \text{in}} = 0 \quad (\text{V.2.5})$$

$$l = 0, \quad D_L \frac{\partial C_A}{\partial l} = -u(C_{A,0} - C_A) \quad (\text{V.2.6})$$

$$l = L, \quad \frac{\partial C_A}{\partial l} = 0$$

In Eqs. (V.2.4)-(V.2.6), C_A (mol m⁻³) is the molar concentration of species A in solution, u (m s⁻¹) the superficial velocity, l (m) the position along the bed, L (m) the bed length, t (s) time, ε the bed porosity ($\varepsilon = 0.88$), $\langle q_A \rangle$ (mol m⁻³) the average concentration of A in the solid, $C_{A, \text{in}}$ the initial concentration of A in the fluid inside the bed, and $C_{A,0}$ the concentration of A in the feed. The axial dispersion coefficient D_L (m² s⁻¹) was estimated here using the following correlation [34]:

$$D_L = (20 + 0.5 \times Sc \times Re) \times \frac{D_m}{\varepsilon} \quad (\text{V.2.7})$$

where D_m is the diffusivity of Cs⁺ in water ($2.06 \times 10^{-9} \text{ m}^2 \text{ s}^{-1}$ at 298.15 K [35]), and Sc and Re are the well known Schmidt and Reynolds numbers, respectively.

The material balance to the exchanger particle is given by Eq. (V.2.8), and the initial and boundary conditions for the ion exchange experiment are represented by Eqs. (V.2.9)-(V.2.11).

$$\frac{\partial q_A}{\partial t} = -\frac{1}{r^2} \frac{\partial}{\partial r} (r^2 N_A) \quad (\text{V.2.8})$$

$$t = 0, \quad q_A = q_{A,\text{in}} = 0 \quad (\text{V.2.9})$$

$$r = 0, \quad \frac{\partial q_A}{\partial r} = 0 \quad (\text{V.2.10})$$

$$r = R_p, \quad q_A = q_{A,R_p} \quad (\text{V.2.11})$$

where R_p (m) is the particle radius, $q_{A,\text{in}}$ (mol m⁻³) the initial concentration of A in the solid along the bed, and q_{A,R_p} (mol m⁻³) the concentration of A in the solid at the interface, which is in equilibrium with fluid concentration C_{A,R_p} (*i.e.*, they are related by the isotherm).

In consecutive loading-regeneration operations, the initial conditions of step n , ($C_{A,\text{in}}|_n$ and $q_{A,\text{in}}|_n$) must equal the final concentration profiles of step $n - 1$, ($C_{A,\text{final}}|_{n-1}$ and $q_{A,\text{final}}|_{n-1}$). Accordingly, Eqs. (V.2.5) and (V.2.9) should be substituted by the following conditions:

$$t = t_{\text{in}}|_n, \quad \begin{cases} C_{A,\text{in}}|_n = C_{A,\text{final}}|_{n-1} \\ q_{A,\text{in}}|_n = q_{A,\text{final}}|_{n-1} \end{cases}, \quad 2 \leq n < \infty, \quad (\text{V.2.12})$$

The equality of fluxes at the surface of the particle is expressed by Eq. (V.2.13), which involves the convective mass transfer coefficient of counter ion A, k_f (m s⁻¹), estimated here by Eq. (V.2.14) in terms of Sherwood (Sh), Reynolds and Schmidt numbers, and $d_p = 2R_p$ is the equivalent particle diameter (m) [8].

$$N_{A,R_p} = k_f (C_A - C_{A,R_p}) \quad (\text{V.2.13})$$

$$\text{Sh} = \frac{k_f d_p}{D_m} = \frac{1.13}{\varepsilon} \text{Re}^{0.21} \text{Sc}^{1/3} \quad (\text{V.2.14})$$

The average loading per unit particle volume, included in the material balance to the column, Eq. (V.2.4), is calculated by:

$$\langle q_A \rangle = \frac{3}{R_p^3} \int_0^{R_p} r^2 q_A dr \quad (\text{V.2.15})$$

The equilibrium isotherm of the system Cs⁺/Na⁺/ETS-4 is given by the Langmuir equation:

$$q_{A,\text{eq}} = q_{A,\text{max}} \frac{K_L C_{A,\text{eq}}}{1 + K_L C_{A,\text{eq}}} \quad (\text{V.2.16})$$

where $q_{A,\text{max}}$ (mol m⁻³) and K_L (mol⁻¹ m³) are parameters to fit the experimental data.

The Method of Lines was selected to solve the concentration profiles of Cs⁺ and their evolution along time, in solution and in the solid phase, and the spatial discretization was accomplished by finite differences of second order. The resulting ordinary differential equations of the initial-value type were solved applying numerical differentiation formulas using 31 grid points for particle radius and bed length.

Concerning the methodology, the self-diffusion coefficients (D_A and D_B) of the NP-based model were adjusted to the experimental data (section V.2.4.4), the Nelder-Mead and the Marquardt-Levenberg algorithms were adopted for the optimizations, and the root mean square deviation (RMSD) was the objective function:

$$\text{RMSD (\%)} = 100 \times \sqrt{\frac{\sum_i^{\text{NDP}} (C_{A,\text{calc}}|_i - C_{A,\text{exp}}|_i)^2}{\text{NDP}}} \quad (\text{V.2.17})$$

Here NDP is the number of data points, and subscripts 'exp' and 'calc' denote measured and calculated cesium concentrations, respectively.

V.2.3. Materials and Methods

V.2.3.1. Chemicals and materials

Sodium hydroxide (CAS number 1310-73-2), potassium chloride (CAS number 7447-40-7) and titanium(III) chloride (15 wt% TiCl₃ and 10 wt% HCl) were supplied by Merck. Sodium metasilicate (CAS Number 13517-24-3) was purchased from BDH Chemicals. Cesium nitrate (CAS number 7789-18-6) and sodium nitrate (CAS Number 7631-99-4) were acquired from Sigma-Aldrich. Cellulose acetate membrane disc filters were bought from Sterlitech Corporation, and quartz wool discs were purchased from Elemental Microanalysis. The high-purity water (18.2 MΩ cm) was generated in a Milli-Q Millipore water purification system.

V.2.3.2. Synthesis and characterization

ETS-4 synthesis was performed as follows [13,15]. An alkaline solution was prepared by dissolving sodium metasilicate, NaOH and KCl in high-purity water (18.2 MΩcm). Then, TiCl₃ was added to this solution and stirred thoroughly. The resulting gel, with molar composition 5.9 Na₂O : 0.7 K₂O : 5.0 SiO₂ : 1.0 TiO₂ : 114 H₂O, was transferred to a Teflon-lined autoclave and heated at 230 °C for 17 h under autogenous pressure without agitation. The product was filtered off, washed at room temperature with distilled water, and dried at 70 °C overnight. *The sample crystallinity and purity were ascertained by powder X-Ray Diffraction (PXRD) collected on a PANalytical Empyrean diffractometer (CuK_{α1,2} X-radiation, λ₁ = 1.540598 Å; λ₂ = 1.544426 Å), equipped with an PIXcel 1D detector and a transmission-spinner sample holder in a Bragg-Brentano para-focusing optics configuration (45 kV, 40 mA). Intensity data were collected by the step-counting method (step 0.04°), in continuous mode, in the range ca. 5 ≤ 2θ ≤ 50°. Table V.2.1 summarizes the important features of this material.*

Table V.2.1 – Features of the synthesized titanosilicate ETS-4 [66].

Formula	M ₈ Ti ₅ Si ₁₂ O ₃₈ ·nH ₂ O (M=K,Na)
Density (kg m ⁻³)	2200
Theoretical cation exchange capacity (eq kg ⁻¹)	6.39
Measured equivalent particle diameter (10 ⁻⁶ m)	12
Pore diameter (10 ⁻¹⁰ m)	3.7

V.2.3.3. Fixed-bed and batch ion exchange experiments

Preparation of solutions. Measurement of Cs^+ concentration.

A 0.01 mol L^{-1} Cs^+ stock solution was prepared by dissolving 0.098 g of CsNO_3 in 50 mL of high-purity water ($18.2 \text{ M}\Omega \text{ cm}$). The Cs^+ operational solutions were obtained by diluting the stock solution to the desired concentration with high-purity water, prepared immediately before use in order to reduce cation adsorption on the vessel walls and remaining glassware and lab material.

The cesium concentration of the solutions was measured by atomic emission spectroscopy (AES) with a Perkin Elmer AAnalyst 100 atomic absorption spectrometer, in the emission mode (with a wavelength of 852.1 nm and a slit of 0.2 nm) and using an air-acetylene flame. The ionization was controlled by the addition of a potassium chloride solution to all samples and standards until they all contained 0.5 wt.% of such alkali. Each sample was analysed in triplicate and the results are the average of concordant values (less than 5% variation between measurements of the same sample).

Batch ion exchange experiments

Batch experiments were performed contacting cesium solutions with known masses of powdered ETS-4 in volumetric flasks (2 dm^3) under agitation (*ca.*, 300 rpm) at room temperature (295 K) and initial pH 4. The initial cesium concentrations were fixed at *ca.* 40 ppm in order to maintain constant the ionic strength of the solutions, while the masses of ETS-4 were varied as shown in Table V.2.2. The assays started when the exchanger was added to the solution and the stirring initiated. Aliquots (10 mL) were collected, (before adding the solid and at the end of the experiment), filtered through an acid washed cellulose acetate membrane disc filter of $0.45 \mu\text{m}$, and the cesium concentration was measured by AES. A blank experiment (without ETS-4) was always run as a control to check that the removal of Cs^+ occurred by ion exchange with the solid and not by adsorption on the lab material.

Fixed-bed ion exchange experiments

A stainless steel fixed-bed column was mounted on a support and filled with a precise amount of ETS-4 confined by four to six quartz wool discs plus two stainless steel nets, one at the bottom and other on top. Swagelock fittings were used to close the assembly and to connect the bottom and the top of the column to an influent reservoir and to a sample collector, respectively (Figure V.2.1).

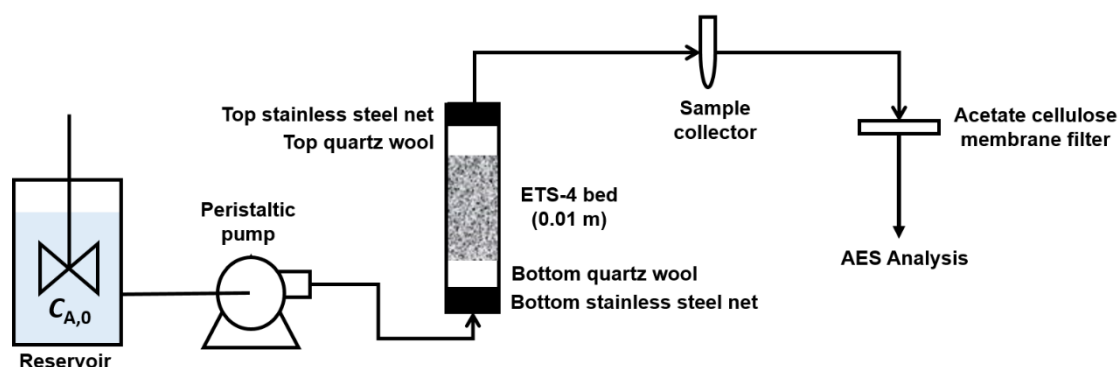


Figure V.2.1 – Experimental setup for the fixed-bed ion exchange experiments.

Three fixed-bed experiments (Exps. 9, 10 and 11 of Table V.2.3) were performed isothermally at 295 ± 1 K to study the influence of the flow rate on cesium exchange over ETS-4. The influent solution containing *ca.* 40 ppm Cs⁺ was continuously fed to the column in the up-flow mode. The pH was measured at the column inlet using a pH meter Crison Basic 20. The volumetric flow rate was regulated with a variable peristaltic pump (Knauer Smartline pump 100). Aliquots of 10 mL were collected periodically at column outlet, filtered through acid washed cellulose acetate membrane (0.45 μ m) disc filters, and then analysed for Cs⁺ concentration by AES. The experiments were stopped when the effluent and the influent Cs⁺ concentrations were equal.

To assess the regeneration capacity of ETS-4, an additional experiment was performed after Exp. 11 (Table V.2.3) using a solution of Na⁺ ($1.72 \text{ mol} \cdot \text{m}^{-3}$) continuously fed to the column for 75 hours (Exp. 12 in Table V.2.3). Then, a second cycle began using a cesium solution and operating conditions equivalent to those of Exp. 11 (Exp. 13 in Table V.2.3). The ion exchange process was always controlled through Cs⁺ measurement by AES as described above.

Table V.2.2 – Experimental conditions for batch ion exchange assays with ETS-4 to obtain isotherm data. (Fixed conditions: $T = 295 \pm 1$ K, $V_{\text{liquid}} = 2 \times 10^{-3} \text{ m}^3$, pH = 4).

Experiment No.	1	2	3	4	5	6	7	8
Mass of ETS-4 (10^{-6} kg)	8	60	157	206	314	418	524	804
Initial Cs ⁺ conc. (mol m^{-3})	0.288	0.295	0.308	0.285	0.295	0.291	0.294	0.303

Table V.2.3 - Experimental conditions for fixed-bed ion exchange assays using ETS-4. (Fixed conditions: $T = 295 \pm 1$ K, pH 4, $\varepsilon = 0.88$, $L = 0.01$ m).

Experiment No.	9	10	11	12	13
Type of experiment / cycle	Loading	Loading	Loading 1 st cycle	Regeneration 1 st cycle	Loading 2 nd cycle
Mass of ETS-4 (10^{-6} kg)	501	509	503	503	503
Initial Cs ⁺ conc. (mol m^{-3})	0.311	0.305	0.301	-	0.293
Initial Na ⁺ conc. (mol m^{-3})	-	-	-	1.720	-
Superficial velocity (m s^{-1}) 1)	6.366×10^{-4}	3.893×10^{-4}	2.567×10^{-4}	2.567×10^{-4}	2.567×10^{-4}
D_L ($\text{m}^2 \text{s}^{-1}$) by Eq. (7)	5.895×10^{-8}	5.556×10^{-8}	5.350×10^{-8}	5.350×10^{-8}	5.350×10^{-8}

V.2.4. Results and discussion

This section starts with the characterization of the synthesised ETS-4 by PXRD, before and after ion exchange. Then, the measured and modelled isotherms of the Cs⁺/Na⁺/ETS-4 system are analysed, followed by the breakthrough curves obtained under fixed-bed operation. The regeneration and the second cycle of ion exchange are also examined. Finally, the results achieved with the Nernst-Planck based model (developed in Section V.2.2) are presented and discussed in detail.

V.2.4.1. Materials characterization

The PXRD pattern of the parent sample is characteristic of ETS-4 providing no evidence for the presence of any additional impurities (Figure V.2.2). Cs⁺-exchanged ETS-4 reveals some modifications in the peaks intensities and positions, which may be ascribed not only to crystal orientation effects but also to the introduction of cesium in its framework. The major differences are found at 23.21° , where a new peak appears, and at 30.37° and 31.17° , where two peaks substituted the native 30.79° peak. Despite these differences, parent ETS-4 and the Cs⁺-exchanged solid are isostructural.

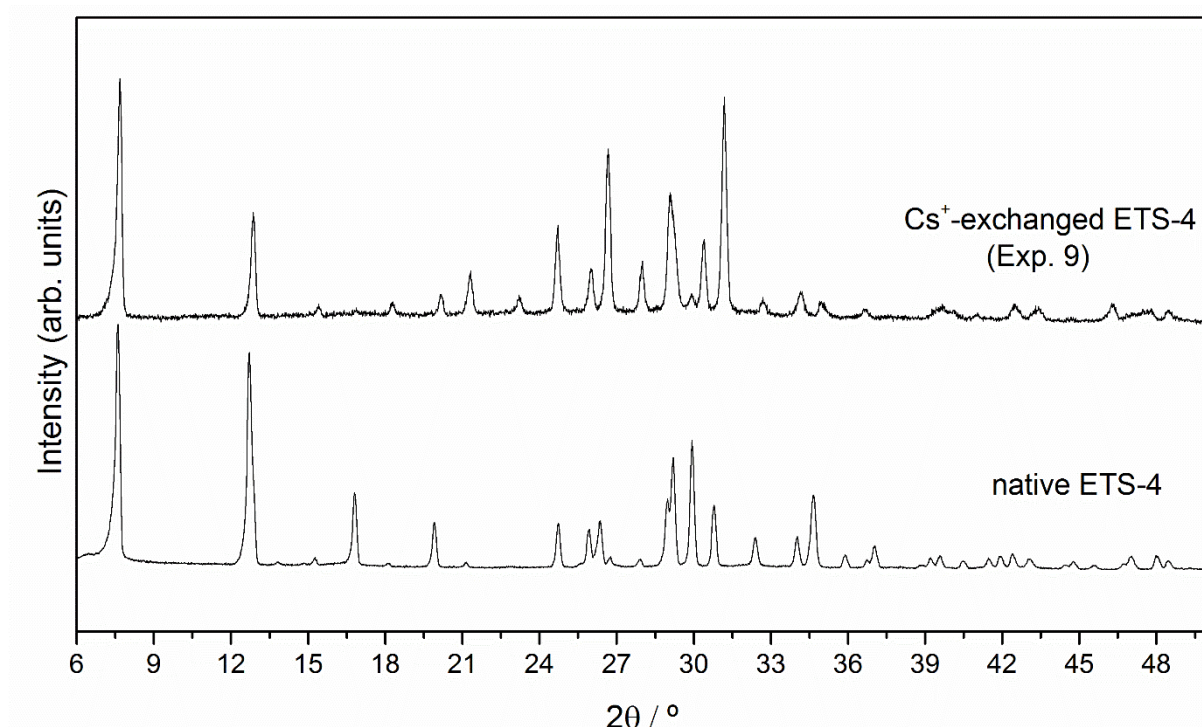


Figure V.2.2 – Normalized PXRD patterns of native and Cs⁺-exchanged ETS-4 (after Exp. 9; see experimental conditions in Table V.2.3).

V.2.4.2. Ion exchange isotherm

The equilibrium data were obtained from batch Exps. 1-8 (Table V.2.2) and fitted with the Langmuir isotherm, Eq. (V.2.16), with an average absolute relative deviation (AARD) of 6.58%. The analytical equation is depicted in Figure V.2.3 and exhibits the Langmuir parameters $q_{A,\max} = 1.86 \text{ mol kg}^{-1}$ and $K_L = 43.46 \text{ m}^3 \text{ mol}^{-1}$, similar to previously published data [57]. Freundlich and Langmuir-Freundlich isotherms were also considered, but the former fails to represent the experimental points, while the latter adds an additional parameter but no substantial gain.

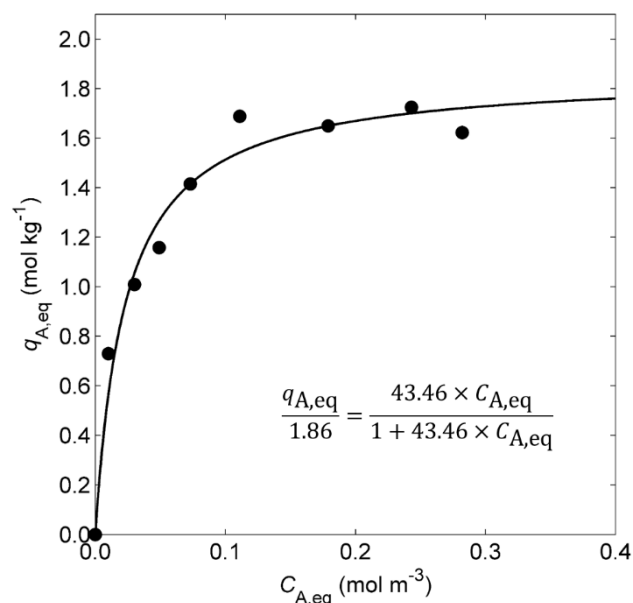


Figure V.2.3 – Measured (solid circles) and calculated (line) Langmuir isotherms of Cs⁺/Na⁺/ETS-4 system at 295 K.

V.2.4.3. Fixed-bed experimental results

The breakthrough curves obtained from Exps. 9-11 were evaluated at different superficial velocities in the range $(2.5\text{--}6.4) \times 10^{-4}$ m s⁻¹ for 75 hours (Table V.2.3). The experimental data plotted in Figure V.2.4 represent the time evolution of the normalized cesium concentration in solution at column outlet, *i.e.*, $C_A(t, L)/C_{A,0}$. Because the three breakthrough curves deviate significantly from (displaced) Heaviside functions, these results reveal mass transfer limitations in the system.

When equilibrium is favourable (which is the case for the Langmuir isotherm) and dispersive phenomena (*e.g.*, axial dispersion, film and intraparticle resistances to mass transfer) are negligible, an ideal wave front propagates unchanged along the bed and exits the column at the stoichiometric time, t_{st} . On the other hand, the occurrence of transport-rate resistances broadens the traveling wave front, which reaches a constant pattern flow due to the simultaneous effect of the self-sharpening favourable isotherm [67,68]. The stoichiometric time can be calculated from the experimental breakthrough curve using Eq. (V.2.18) or estimated from Eq. (V.2.19) on the basis of the solute movement theory:

$$t_{st} = \int_0^\infty \left(1 - \frac{C_A(t)}{C_{A,0}} \right) dt \quad (V.2.1)$$

$$t_{st} = \frac{L}{u} \left(1 + \frac{1 - \varepsilon}{\varepsilon} \frac{q_{A,0}}{C_{A,0}} \right) \quad (V.2.2)$$

where $q_{A,0}$ is the solid loading in equilibrium with feed concentration, $C_{A,0}$. For the regeneration step, the concept of stoichiometric time was extended with the objective of computing the process efficiency using:

$$t_{st} = \int_0^\infty \frac{C_A(t)}{C_{A,0}} dt \quad (V.2.3)$$

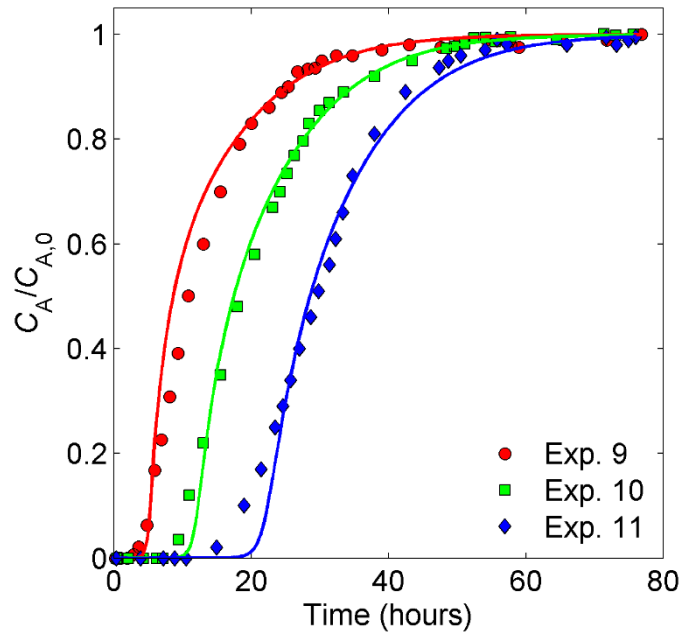


Figure V.2.4 – Effect of the feed flow rate on the normalized breakthrough curves for Cs⁺ removal in a fixed-bed of ETS-4. Symbols: data (experimental conditions in Table V.2.3); lines: NP-based model (parameters in Table V.2.4).

According to the breakthrough curves (Exps. 9, 10 and 11 in Figure 4), lower superficial velocities require higher operating times to deplete the solid phase, and vice-versa, in agreement with the solute movement theory, Eq. (V.2.19), since t_{st} is inversely proportional to the superficial velocity, u . The experimental values obtained were $t_{st} = 13.9$, 21.9 and 30.8 h, for $u = 6.366 \times 10^{-4}$ (Exp. 9), 3.893×10^{-4} (Exp. 10) and $2.567 \times 10^{-4} \text{ m s}^{-1}$ (Exp. 11), respectively.

Concerning axial dispersion, its influence was negligible because the L/d_p ratio was 833, clearly obeying the well-known relation $L > 50 d_p$, and the axial Peclet numbers ($Pe = uL/D_L$) attained were 108.0, 70.1 and 48.0, for Exps. 9, 10 and 11, respectively. Nonetheless, external mass transfer limitations were confirmed, experimentally and theoretically (further discussion in Section V.2.4.4) because the spreading of the breakthrough curves increased with decreasing superficial velocities. For example, the widths of the mass transfer zone (MTZ) based on 0.01 and 0.99 limits (*i.e.*, $0.01 \leq C_A(t, L)/C_{A,0} \leq 0.99$) were 42.4, 46.3 and 48.1 h for Exps. 9, 10 and 11, respectively; for the more flexible limits 0.05 and 0.95, the corresponding MTZ widths were 27.2, 30.1 and 31.5 h.

The regeneration experiment (Exp. 12) was subsequently performed using a Na^+ solution (*ca.* 40 ppm) to convert the ETS-4 bed at the end of Exp. 11 into its original Na -form, in order to evaluate the Cs^+ uptake capacity after regeneration (Exp. 13). The results for the normalized cesium concentration at column outlet are shown in Figure V.2.5, where time was measured continuously, without interruption, with the successive regeneration and loading experiments (Exps. 12 and 13, respectively) having the same time extension of Exp. 11. As expected, the regeneration curve is highly dispersed ($75 < t(\text{h}) < 150$) because a favourable isotherm broadens the wave front during a desorbing step and the mass transfer limitations reinforces even more this thermodynamic behaviour along the bed.

Since all experimental conditions were preserved during Exps. 11, 12 and 13, except the Cs^+ concentration of the feed, the efficiency of the regeneration and second loading steps may be unveiled by the ratio between their stoichiometric times and that of Exp. 11. With respect to this, Figure V.2.5 encompasses three different areas (A1, AR and A2) whose values correspond to the experimental stoichiometric times, $t_{\text{st}} = 31.0, 23.8$ and 23.0 h, respectively. Thus, the ratio $\text{AR}/\text{A1}$ indicates that the regeneration process (Exp. 12) attained *ca.* 76.8% of efficiency, a value confirmed by the experimental $\text{A2}/\text{A1}$ ratio that attained 74.2%. It is worth mentioning that after *ca.* 150 h (*i.e.*, at the end of *ca.* 75 h of regeneration) the Cs^+ concentration of the effluent was *ca.* 20% of its initial concentration, *i.e.*, the regeneration was incomplete. To convert all ETS-4 in its Na -form, long ion exchange runs would be necessary under the same experimental conditions. Alternatively, to accelerate the regeneration process, the inlet counter ion (Na^+) concentration and flow rate could be increased. In both cases, the mass transfer driving force would be increased, while the second possibility would also to reduce the external film thickness with advantage. In industrial applications the residual loading after regeneration is usually finite and frequently non-uniform, constituting the well-known delta loading of steady state cyclic processes.

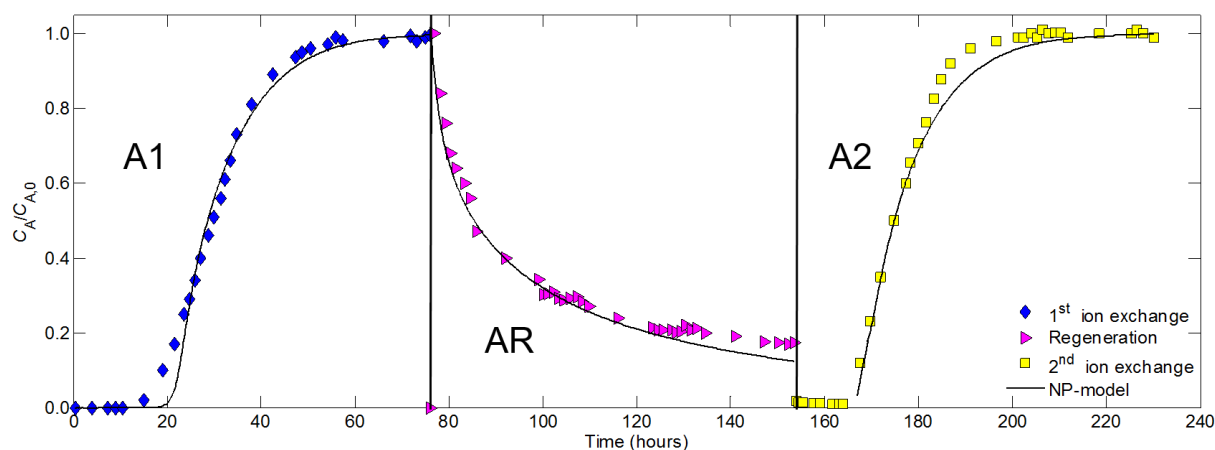


Figure V.2.5 – Normalized cesium concentration at column outlet for Exps. 11, 12 and 13 in a loading-regeneration operation. Symbols: data (experimental conditions in Table V.2.3); lines: NP-based model (parameters in Table V.2.4); A1 = area above the breakthrough of the 1st ion exchange cycle; AR = area below the regeneration curve of the 1st cycle; A2 = area above breakthrough of the 2nd cycle.

The ability of spent ETS-4 to enter a second ion exchange cycle after intermediate regeneration is a valuable outcome of this essay. ETS materials have been much studied for the removal of several hazardous metals [4] but their regeneration and utilization in subsequent ion exchange cycles is scarcely assessed. Lopes *et al.*, [7] studied the uptake of Hg²⁺ from aqueous solutions on a packed-bed of ETS-4, and the regeneration was carried out with a chelating agent, namely a concentration gradient EDTA-Na₂ solution (0.05–0.25 mol dm⁻³), attaining an elution efficiency of 98% only after 50 hours. If, alternatively, a simple aqueous solution of a counter ion had been used the fixed-bed cleaning would be impractical. This is in accord with the large selectivity of titanosilicates towards divalent cations such as Hg²⁺ and Cd²⁺ [13–15,41,65,69]. In our case the counter ions Cs⁺ and Na⁺ possess the same valence (+1) and, as mentioned above, the PXRD patterns of parent and Cs⁺-exchanged ETS-4 show that the solids are isostructural. Hence, both loading and regeneration steps were expected in advance to be essentially and effectively reversible despite the differences imparted by the distinct ionic radius of Cs⁺ and Na⁺ (170 *versus* 102 pm [70], respectively).

V.2.4.4. Fixed-bed modelling results – Nernst-Planck based model

Modelling results for the fixed-bed operation are plotted together with data for Exps. 9-11 in Figure V.2.4, and Exps. 11 (loading, 1st cycle), 12 (regeneration, 1st cycle) and 13 (loading, 2nd cycle) in Figure V.2.5. The axial dispersion (D_L) and convective mass transfer coefficients (k_f) were estimated by Eqs. (7) and (14), respectively, and the model parameters (D_A and D_B) were fitted to the data of Exp. 11 only, with RMSD = 18.66 %. The remaining four curves were predicted, providing deviations of 15.20% (Exp. 9), 13.27% (Exp. 10), 4.17% (Exp. 12) and 5.88% (Exp.13), and global RMSD of 9.55% (see Table V.2.4). Globally, these are reliable results for an ion exchange process embodying several runs with different operating conditions and distinct cycle steps.

Considering that the system's counter ions are monoatomic and monovalent, the adjusted self-diffusivities for Cs⁺ ($D_A = 3.193 \times 10^{-16} \text{ m}^2 \text{ s}^{-1}$) and Na⁺ ($D_B = 6.088 \times 10^{-15} \text{ m}^2 \text{ s}^{-1}$) must reflect their ionic radius, *i.e.*, $D_A < D_B$ because $r_{\text{ion}}(\text{Cs}^+) = 170 \text{ pm} > r_{\text{ion}}(\text{Na}^+) = 102 \text{ pm}$ [70]. Furthermore, D_A and D_B are of the same order of magnitude of those published recently for the system Cs⁺/Na⁺/Eu-AV-20 [48] and three times larger than the values for Cd²⁺/Na⁺/ETS-4 [14] and Hg²⁺/Na⁺/ETS-4 [41] systems. In all cases, the small magnitudes of the diffusion coefficients are consistent with the presence of small micropores [14,71–73], since the cations never escape from the force field of the matrix co-ions, mainly due to the strong and long-range nature of the electrostatic interactions, which imply the intraparticle transport mechanism is surface diffusion.

As mentioned above, the self-diffusivity found for Cs⁺ is approximately three times higher than those reported for Cd²⁺ and Hg²⁺ in ETS-4 [14,41]. Despite the ionic radius of cadmium(II) and mercury(II), respectively, 95 and 102 pm [70], their double charge originates stronger interactions with the solid surface, increasing their activation energy for diffusing through the channels (remember that the ionic radius of Cs⁺ is 170 pm). An additional feature that penalizes Cd²⁺ and Hg²⁺ in comparison to Cs⁺ is the magnitude of their molar Gibbs free energy of dehydration: $\Delta_{\text{dehyd}}G = 1755, 1760$ and 250 kJ mol^{-1} [70], respectively, which means the energy required by the divalent cations for accessing the microporosity of ETS-4 is *ca.*, seven times higher than that of monovalent cesium ion, just for the dehydration step.

The convective mass transfer coefficients estimated by Eq. (V.2.14) are $3.775 \times 10^{-4} \text{ m s}^{-1}$ (Exp. 9), $3.416 \times 10^{-4} \text{ m s}^{-1}$ (Exp. 10) and $3.122 \times 10^{-4} \text{ m s}^{-1}$ (Exps. 11-13), following the decreasing superficial velocity of the fluid (*i.e.*, 6.366×10^{-4} , 3.893×10^{-4} and $2.567 \times 10^{-4} \text{ m s}^{-1}$, respectively). These values are consistent with the increasing widths of the mass transfer

zones (cited in Section V.2.4.3) for Exps. 9-11, because the film contribution to the second moment (*i.e.*, dispersion) of a pulse response of a chromatographic model is proportional to R_p/k_f [67,68]. It is interesting to confront the following ratios for qualitative but theoretically sound purposes: $k_f(\text{Exp. 10})/k_f(\text{Exp. 9})=0.905$ and $k_f(\text{Exp. 11})/k_f(\text{Exp. 10})=0.914$, *versus* $\text{MTZ}(\text{Exp. 9})/\text{MTZ}(\text{Exp. 10})=0.904$ and $\text{MTZ}(\text{Exp. 10})/\text{MTZ}(\text{Exp. 11})=0.956$.

To access the performance of the NP-based model, the calculated *versus* experimental normalized cesium concentrations at column outlet are plotted in Figure V.2.6. As expected from the RMSD values listed in Table V.2.4, the rough linearity observed between both sets of data highlights the model's ability to correlate and predict the ion exchange behaviour of the Cs⁺/Na⁺/ETS-4 system under the various experimental conditions, in particular, different superficial velocities and loading-regeneration steps. Despite the reliable results achieved, the model overestimates Exp. 9, while the points of the remaining experiments are well distributed near the diagonal. Figure V.2.6 also reveals that the proposed model is less reliable at the beginning of the breakthrough curves, where errors are more likely to occur due to the detection limits of the analytical method (AES). The fact that the proposed NP-based model can be used to study the different stages of a cyclic ion exchange operation is of major importance, since it is a fundamental tool for the accurate scale-up and optimization of a fixed-bed unit.

Table V.2.4 – Optimized parameters and calculated deviations for the Nernst-Planck based model applied to the fixed-bed assays. (Experimental conditions in Table V.2.3).

Exp.	NDP	Type of calculation	D_A (m ² s ⁻¹)	D_B (m ² s ⁻¹)	RMSD (%)	Global RMSD (%)
9	35	Prediction	-	-	15.20	9.55 (prediction)*
10	34	Prediction	-	-	13.27	
11	31	Correlation	3.193x10 ⁻¹⁶	6.088x10 ⁻¹⁵	18.66	18.66 (correlation)
12	35	Prediction	-	-	4.17	
13	35	Prediction	-	-	5.88	

* 9.55% is the calculated RMSD for the set of Exps. 9,10,12 and 13.

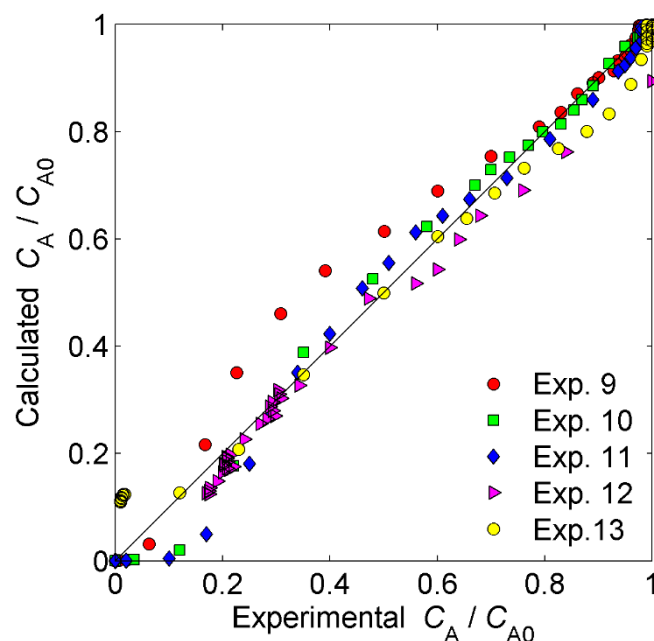


Figure V.2.6 – Calculated *versus* experimental normalized Cs^+ concentration in solution (experimental conditions in Table V.2.3).

V.2.5. Conclusions

The cesium exchange capacity of ETS-4 was assessed in batch and fixed-bed experiments aiming at: measuring the isotherm of the system $\text{Cs}^+/\text{Na}^+/\text{ETS-4}$, assessing the influence of the superficial velocity on the fixed-bed operation (*via* breakthrough curves), and evaluating the regeneration ability of ETS-4 for future cyclic operation. The Langmuir isotherm fitted the equilibrium data reliably (AARD = 6.58%), while the experimental breakthrough curves exhibited the expected trend characterized by a sigmoidal shape. The proposed Nernst-Planck based model achieved global deviations of 18.66% and 9.55%, respectively, for correlation (1 curve) and prediction (4 curves) of cesium concentration in the fluid at column outlet. The correlated parameters were the NP self-diffusivities of Cs^+ and Na^+ in ETS-4, and the determined values ($D_{\text{Cs}^+} = 3.193 \times 10^{-16} \text{ m}^2 \text{ s}^{-1}$ and $D_{\text{Na}^+} = 6.088 \times 10^{-15} \text{ m}^2 \text{ s}^{-1}$) were consistent with the microporosity of ETS-4 and the size of the exchanged cations. The embodied axial dispersion and convective mass transfer coefficients (estimated by dimensionless correlations) confirmed external limitations and ruled out axial dispersion phenomena. The good results obtained in consecutive loading-regeneration steps evidence the ability of ETS-4 to be used in cyclic ion exchange operations, while the NP-based model proved to be reliable for process design and optimization.

V.2.6. Nomenclature

A^{Z_A}	Counter ion initially in solution (Cs ⁺)
A1, A2	Areas above breakthrough curves in Figure V.2.5 (h)
AARD	$= \frac{100}{\text{NDP}} \sum_{i=1}^{\text{NDP}} C_{A,i,\text{calc}} - C_{A,i,\text{exp}} / C_{A,i,\text{exp}}$, Average absolute relative deviation (%)
AES	Atomic emission spectroscopy
AR	Area below regeneration curve in Figure V.2.5 (h)
B^{Z_B}	Counter ion initially in the exchanger (Na ⁺)
C_A	Concentration of counter ion A in solution (mol m ⁻³)
$C_{A,0}$	Concentration of counter ion A in the feed (mol m ⁻³)
$C_{A,\text{in}}$	Initial concentration of counter ion A in solution (mol m ⁻³)
$C_{A,\text{eq}}$	Concentration of counter ion A in solution in equilibrium with solid loading concentration, $q_{A,\text{eq}}$ (mol m ⁻³)
C_{A,R_p}	Concentration of counter ion A in solution at the interface (mol m ⁻³)
d_p	Equivalent particle diameter (m)
D_i	Nernst-Planck self-diffusion coefficient of counter ion i in the exchanger (m ² s ⁻¹)
D_L	Axial dispersion coefficient (m ² s ⁻¹)
D_{AB}	Interdiffusion coefficient of Nernst-Planck model (m ² s ⁻¹)
D_m	Diffusion coefficient of Cs ⁺ in water (m ² s ⁻¹)
ETS-4	Engelhard titanosilicate number 4
Exp. n	Experiment number n
i and j	Generic counter ions
k_f	Convective mass transfer coefficient (m s ⁻¹)
K_L	Langmuir parameter (m ³ mol ⁻¹)
l	Column longitudinal coordinate (m)
L	Length of the fixed-bed (m)
MTZ	Mass transfer zone
N_{A,R_p}	Net intraparticle flux of counter ion A at the interface (mol m ⁻² s ⁻¹)
NDP	Number of data points
N_i	Intraparticle flux of counter ion i (mol m ⁻² s ⁻¹)
NP	Nernst-Planck
Pe	Peclet number

PXRD	Powder X-ray diffraction
q_{\max}	Langmuir parameter (mol kg ⁻¹)
$q_{A,0}$	Solid loading in equilibrium with feed concentration, $C_{A,0}$
$q_{A,\text{eq}}$	Solid loading in equilibrium with concentration of counter ion A in solution, $C_{A,\text{eq}}$ (mol kg ⁻¹)
q_i	Molar concentration of counter ion i in the particle (mol m ⁻³)
$\langle q \rangle_i$	Average concentration of counter ion i in the particle (mol m ⁻³)
Q	Total amount of sorbed species per unit mass of exchanger (eq m ⁻³)
r	Radial coordinate in the particle (m)
Re	Reynolds number
RMSD	Root mean square deviation (%)
R_p	Particle radius (m)
Sc	Schmidt number
Sh	Sherwood number
t	Time (h or s)
t_{st}	Stoichiometric time (h)
T	Absolute temperature (K)
u	Superficial velocity (m s ⁻¹)
V_s	Volume of exchanger (m ³)
z_i	Electrochemical valence of counter ion i

Greek letters

$\Delta_{\text{dehyd}}G$	Molar Gibbs free energy of dehydration (kcal mol ⁻¹)
ε	Bed void fraction

Subscripts

0	Feed condition
A	Counter ion initially present in the bulk solution (Cs ⁺)
B	Counter ion initially present in the exchanger particle (Na ⁺)
calc	Calculated
eq	Equilibrium
exp	Experimental

- in Initial condition
- n Step n in a loading-regeneration setup

V.3. References

- [1] X. Liu, G.R. Chen, D.J. Lee, T. Kawamoto, H. Tanaka, M.L. Chen, Y.K. Luo, Adsorption removal of cesium from drinking waters: A mini review on use of biosorbents and other adsorbents, *Bioresour. Technol.* 160 (2014) 142–149.
- [2] G. Lujaniene, J. Šapolaite, A. Amulevičius, K. Mažeika, S. Motiejunas, Retention of cesium, plutonium and americium by engineered and natural barriers, *Czechoslov. J. Phys.* 56 (2006) D103–D110.
- [3] K. Popa, C.C. Pavel, Radioactive wastewaters purification using titanosilicates materials: State of the art and perspectives, *Desalination* 293 (2012) 78–86.
- [4] C.B. Lopes, P.F. Lito, S.P. Cardoso, E. Pereira, A.C. Duarte, C.M. Silva, Metal Recovery, Separation and/or Pre-concentration, in: Inamuddin, M. Luqman (Eds.), *Ion Exchange Technology II - Applications*, Springer Netherlands, Dordrecht, 2012.
- [5] P.F. Lito, J.P.S. Aniceto, C.M. Silva, Removal of Anionic Pollutants from Waters and Wastewaters and Materials Perspective for Their Selective Sorption, *Water, Air, Soil Pollut.* 223 (2012) 6133–6155.
- [6] I.C. Ostroski, C.E. Borba, E.A. Silva, P.A. Arroyo, R. Guirardello, M.A.S.D. Barros, Mass Transfer Mechanism of Ion Exchange in Fixed Bed Columns, *J. Chem. Eng. Data* 56 (2011) 375–382.
- [7] C.B. Lopes, E. Pereira, Z. Lin, P. Pato, M. Otero, C.M. Silva, J. Rocha, A.C. Duarte, Fixed-bed removal of Hg²⁺ from contaminated water by microporous titanosilicate ETS-4: Experimental and theoretical breakthrough curves, *Microporous Mesoporous Mater.* 145 (2011) 32–40.
- [8] L. Lv, Y. Zhang, K. Wang, A.K. Ray, X.S. Zhao, Modeling of the adsorption breakthrough behaviors of Pb²⁺ in a fixed bed of ETS-10 adsorbent, *J. Colloid Interface Sci.* 325 (2008) 57–63.
- [9] I.M. Latheef, M.E. Huckman, R.G. Anthony, Modeling Cesium Ion Exchange on Fixed-Bed Columns of Crystalline Silicotitanate Granules, *Ind. Eng. Chem. Res.* 39 (2000) 1356–1363.
- [10] C. Xiong, Q. Jia, X. Chen, G. Wang, C. Yao, Optimization of Polyacrylonitrile-2-aminothiazole Resin Synthesis, Characterization, and Its Adsorption Performance and Mechanism for Removal of Hg(II) from Aqueous Solutions, *Ind. Eng. Chem. Res.* 52 (2013) 4978–4986.
- [11] C. Xiong, Y. Zheng, Y. Feng, C. Yao, C. Ma, X. Zheng, J. Jiang, Preparation of a novel chloromethylated polystyrene-2-amino-1,3,4-thiadiazole chelating resin and its adsorption properties and mechanism for separation and recovery of Pt(IV) from aqueous solutions, *J. Mater. Chem. A* 2 (2014) 5379–5386.
- [12] C. Xiong, Y. Li, G. Wang, L. Fang, S. Zhou, C. Yao, Q. Chen, X. Zheng, D. Qi, Y. Fu, Y. Zhu, Selective removal of Hg(II) with polyacrylonitrile-2-amino-1,3,4-thiadiazole chelating resin: Batch and column study, *Chem. Eng. J.* 259 (2015) 257–265.

- [13] S.P. Cardoso, C.B. Lopes, E. Pereira, A.C. Duarte, C.M. Silva, Competitive Removal of Cd²⁺ and Hg²⁺ Ions from Water Using Titanosilicate ETS-4: Kinetic Behaviour and Selectivity, *Water, Air, Soil Pollut.* 224 (2013) 1535–1541.
- [14] T.R. Ferreira, C.B. Lopes, P.F. Lito, M. Otero, Z. Lin, J. Rocha, E. Pereira, C.M. Silva, A. Duarte, Cadmium(II) removal from aqueous solution using microporous titanosilicate ETS-4, *Chem. Eng. J.* 147 (2009) 173–179.
- [15] C.B. Lopes, M. Otero, Z. Lin, C.M. Silva, J. Rocha, E. Pereira, A.C. Duarte, Removal of Hg²⁺ ions from aqueous solution by ETS-4 microporous titanosilicate - Kinetic and equilibrium studies, *Chem. Eng. J.* 151 (2009) 247–254.
- [16] E.D. Camarinha, P.F. Lito, B.M. Antunes, M. Otero, Z. Lin, J. Rocha, E. Pereira, A.C. Duarte, C.M. Silva, Cadmium(II) removal from aqueous solution using microporous titanosilicate ETS-10, *Chem. Eng. J.* 155 (2009) 108–114.
- [17] L.D. Barreira, P.F. Lito, B.M. Antunes, M. Otero, Z. Lin, J. Rocha, E. Pereira, A.C. Duarte, C.M. Silva, Effect of pH on cadmium (II) removal from aqueous solution using titanosilicate ETS-4, *Chem. Eng. J.* 155 (2009) 728–735.
- [18] M. Endo, E. Yoshikawa, N. Muramatsu, N. Takizawa, T. Kawai, H. Unuma, A. Sasaki, A. Masano, Y. Takeyama, T. Kahara, The removal of cesium ion with natural Itaya zeolite and the ion exchange characteristics, *J. Chem. Technol. Biotechnol.* 88 (2013) 1597–1602.
- [19] J. Mon, Y. Deng, M. Flury, J.B. Harsh, Cesium incorporation and diffusion in cancrinite, sodalite, zeolite, and allophane, *Microporous Mesoporous Mater.* 86 (2005) 277–286.
- [20] Z. Du, M. Jia, X. Wang, Cesium removal from solution using PAN-based potassium nickel hexacyanoferrate(II) composite spheres, *J. Radioanal. Nucl. Chem.* 298 (2012) 167–177.
- [21] J. Lehto, S. Haukka, R. Harjula, M. Blomberg, Mechanism of caesium ion exchange on potassium cobalt hexacyanoferrates(II), *J. Chem. Soc. Dalt. Trans.* (1990) 1007–1011.
- [22] A.J. Celestian, J.D. Kubicki, J. Hanson, A. Clearfield, J.B. Parise, The mechanism responsible for extraordinary Cs ion selectivity in crystalline silicotitanate, *J. Am. Chem. Soc.* 130 (2008) 11689–11694.
- [23] A. Clearfield, D.G. Medvedev, S. Kerlegon, T. Bosser, J.D. Burns, M. Jackson, Rates of Exchange of Cs⁺ and Sr²⁺ for Poorly Crystalline Sodium Titanium Silicate (CST) in Nuclear Waste Systems, *Solvent Extr. Ion Exch.* 30 (2012) 229–243.
- [24] A.M. El-Kamash, Evaluation of zeolite A for the sorptive removal of Cs⁺ and Sr²⁺ ions from aqueous solutions using batch and fixed bed column operations, *J. Hazard. Mater.* 151 (2008) 432–445.
- [25] R. Cortés-Martínez, M.T. Olguín, M. Solache-Ríos, Cesium sorption by clinoptilolite-rich tuffs in batch and fixed-bed systems, *Desalination* 258 (2010) 164–170.
- [26] J. Rocha, Z. Lin, Microporous mixed octahedral-pentahedral-tetrahedral framework

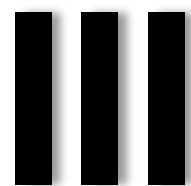
- silicates, *Micro- Mesoporous Miner. Phases* 57 (2005) 173–201.
- [27] J. Rocha, L.D. Carlos, Microporous materials containing lanthanide metals, *Curr. Opin. Solid State Mater. Sci.* 7 (2003) 199–205.
 - [28] S. Komarneni, D.M. Roy, Tobermorites - A New Family of Cation Exchangers, *Sci. Class.* 221 (1983) 647–648.
 - [29] A. Ferreira, D. Ananias, L.D. Carlos, C.M. Morais, J. Rocha, Novel microporous lanthanide silicates with tobermorite-like structure, *J. Am. Chem. Soc.* 125 (2003) 14573–14579.
 - [30] R.C. Evans, L.D. Carlos, P. Douglas, J. Rocha, Tuning the emission colour in mixed lanthanide microporous silicates: energy transfer, composition and chromaticity, *J. Mater. Chem.* 18 (2008) 1100–1107.
 - [31] B.R. Figueiredo, D. Ananias, J. Rocha, C.M. Silva, Cs⁺ ion exchange over lanthanide silicate Eu-AV-20: Experimental measurement and modelling, *Chem. Eng. J.* 268 (2015) 208–218.
 - [32] F. Helfferich, *Ion Exchange*, Courier Dover Publications, New York, 1995.
 - [33] P.F. Lito, S.P. Cardoso, J.M. Loureiro, C.M. Silva, Ion Exchange Equilibria and Kinetics, in: Inamuddin, M. Luqman (Eds.), *Ion Exchange Technology I - Theory and Materials*, Springer Netherlands, Dordrecht, 2012.
 - [34] N. Wakao, T. Funazkri, Effect of fluid dispersion coefficients on particle-to-fluid mass transfer coefficients in packed beds, *Chem. Eng. Sci.* 33 (1978) 1375–1384.
 - [35] H. Sato, M. Yui, H. Yoshikawa, Ionic Diffusion Coefficients of Cs⁺, Pb²⁺, Sm³⁺, Ni²⁺, SeO₂⁻⁴ and TcO₂⁻⁴ in Free Water Determined from Conductivity Measurements, *J. Nucl. Sci. Technol.* 33 (1996) 950–955.
 - [36] R.M. Clark, Evaluating the cost and performance of field-scale granular activated carbon systems, *Environ. Sci. Technol.* 21 (1987) 573–580.
 - [37] Y.H. Yoon, J.H. Nelson, Application of Gas Adsorption Kinetics I. A Theoretical Model for Respirator Cartridge Service Life, *Am. Ind. Hyg. Assoc. J.* 45 (1984) 509–510.
 - [38] G.S. Bohart, E.Q. Adams, Some aspects of the behavior of charcoal with respect to chlorine, *J. Am. Chem. Soc.* 42 (1920) 523–544.
 - [39] H.C. Thomas, Heterogeneous ion exchange in a flowing system, *J. Am. Chem. Soc.* 66 (1944) 1664–1666.
 - [40] K.H. Chu, Fixed bed sorption: setting the record straight on the Bohart-Adams and Thomas models., *J. Hazard. Mater.* 177 (2010) 1006–1012.
 - [41] C.B. Lopes, P.F. Lito, M. Otero, Z. Lin, J. Rocha, C.M. Silva, E. Pereira, A.C. Duarte, Mercury removal with titanasilicate ETS-4: Batch experiments and modelling, *Microporous Mesoporous Mater.* 115 (2008) 98–105.
 - [42] E.A. Behrens, P. Sylvester, A. Clearfield, Assessment of a sodium nonatitanate and

- pharmacosiderite-type ion exchangers for strontium and cesium removal from DOE waste simulants, *Environ. Sci. Technol.* 32 (1998) 101–107.
- [43] A. Clearfield, Ion-exchange materials: seizing the caesium, *Nat. Chem.* 2 (2010) 161–162.
- [44] R.O.A. Rahman, H.A. Ibrahim, Y.T. Hung, Liquid Radioactive Wastes Treatment: A Review, *Water* 3 (2011) 551–565.
- [45] C.C. Pavel, M. Walter, P. Pöml, D. Bouëxière, K. Popa, Contrasting immobilization behavior of Cs⁺ and Sr²⁺ cations in a titanosilicate matrix, *J. Mater. Chem.* 21 (2011) 3831–3837.
- [46] H. Mimura, T. Kobayashi, K. Akiba, Chromatographic Separation of Strontium and Cesium with Mixed Zeolite, Column, *J. Nucl. Sci. Technol.* 32 (1995) 60–67.
- [47] E.H. Borai, R. Harjula, L. Malinen, A. Paajanen, Efficient removal of cesium from low-level radioactive liquid waste using natural and impregnated zeolite minerals, *J. Hazard. Mater.* 172 (2009) 416–422.
- [48] B.R. Figueiredo, M.M.R. de Melo, I. Portugal, D. Ananias, J. Rocha, C.M. Silva, Cs⁺ removal and optical detection by microporous lanthanide silicate Eu-AV-20 in a fixed-bed column, *Chem. Eng. J.* 286 (2016) 48–58.
- [49] B.R. Figueiredo, D. Ananias, I. Portugal, J. Rocha, C.M. Silva, Tb/Eu-AV-9: A lanthanide silicate for the sensing and removal of cesium ions from aqueous solutions, *Chem. Eng. J.* 286 (2016) 679–688.
- [50] A.I. Bortun, L.N. Bortun, A. Clearfield, Ion exchange properties of a cesium ion selective titanosilicate, *Solvent Extr. Ion Exch.* 14 (1996) 341–354.
- [51] D.M. Poojary, R.A. Cahill, A. Clearfield, Synthesis, Crystal-Structures, and Ion-Exchange Properties of a Novel Porous Titanosilicate, *Chem. Mater.* 6 (1994) 2364–2368.
- [52] A.M. Puziy, Cesium and strontium exchange by the framework potassium titanium silicate K₃HTi₄O₄(SiO₄)₃·4H₂O, *J. Radioanal. Nucl. Chem.* 237 (1998) 73–79.
- [53] E.A. Behrens, A. Clearfield, Titanium silicates, M₃HTi₄O₄(SiO₄)₃·4H₂O (M=Na⁺,K⁺), with three-dimensional tunnel structures for the selective removal of strontium and cesium from wastewater, *Microporous Mater.* 11 (1997) 65–75.
- [54] C. V. Philip, S.H. Kim, M. Philip, R.G. Anthony, The Effect of Hydrogen Peroxide on a CST Under Cesium Ion Exchange Conditions, *Sep. Sci. Technol.* 38 (2003) 3009–3029.
- [55] T.A. Todd, K.N. Brewer, D.J. Wood, P.A. Tullock, N.R. Mann, L.G. Olson, Evaluation and testing of inorganic ion exchange sorbents for the removal of cesium-137 from actual Idaho nuclear technology and engineering center acidic tank waste, *Sep. Sci. Technol.* 36 (2001) 999–1016.
- [56] K.P. C. Borcia, Sorption of thallos ion from acidic aqueous solutions onto as-made and modified ETS-10, *J. Radioanal. Nucl. Chem.* 288 (2011) 25–30.

- [57] H. Liu, A. Yonezawa, K. Kumagai, M. Sano, T. Miyake, Cs and Sr removal over highly effective adsorbents ETS-1 and ETS-2, *J. Mater. Chem. A* 3 (2015) 1562–1568.
- [58] K. Popa, C.C. Pavel, N. Bilba, A. Cecal, Purification of waste waters containing ⁶⁰Co²⁺, ^{115m}Cd²⁺ and ²⁰³Hg²⁺ radioactive ions by ETS-4 titanasilicate, *J. Radioanal. Nucl. Chem.* 269 (2006) 155–160.
- [59] L. Al-Attar, A. Dyer, R. Blackburn, Uptake of Uranium on ETS-10 Microporous Titanosilicate, *J. Radioanal. Nucl. Chem.* 246 (2000) 451–455.
- [60] C.C. Pavel, K. Popa, Investigations on the ion exchange process of Cs⁺ and Sr²⁺ cations by ETS materials, *Chem. Eng. J.* 245 (2014) 288–294.
- [61] N. Döbelin, T. Armbruster, N. Dobelin, T. Armbruster, Microporous titanosilicate AM-2: Rb-exchange and thermal behaviour, *Mater. Res. Bull.* 42 (2007) 113–125.
- [62] N. Dobelin, T. Armbruster, Microporous titanosilicate AM-2: Ion-exchange and thermal stability, *Microporous Mesoporous Mater.* 99 (2007) 279–287.
- [63] L. Al-Attar, A. Dyer, R. Harjula, Uptake of radionuclides on microporous and layered ion exchange materials, *J. Mater. Chem.* 13 (2003) 2963–2968.
- [64] S.M. Kuznicki, V.A. Bell, S. Nair, H.W. Hillhouse, R.M. Jacubinas, C.M. Braunbarth, B.H. Toby, M. Tsapatsis, A titanosilicate molecular sieve with adjustable pores for size-selective adsorption of molecules, *Nature* 412 (2001) 720–724.
- [65] M. Otero, C.B. Lopes, J. Coimbra, T.R. Ferreira, C.M. Silva, Z. Lin, J. Rocha, E. Pereira, A.C. Duarte, Priority pollutants (Hg²⁺ and Cd²⁺) removal from water by ETS-4 titanosilicate, *Desalination* 249 (2009) 742–747.
- [66] L. Liu, W. Tan, P. Xiao, Y. Zhai, A novel synthesis process of ETS-4 titanosilicate using commercial anatase in the absence of fluoride ions, *Int. J. Miner. Metall. Mater.* 19 (2012) 675–678.
- [67] D.M. Ruthven, *Principles of Adsorption and Adsorption Processes*, John Wiley & Sons, New York, 1984.
- [68] J.P.S. Aniceto, C.M. Silva, Preparative Chromatography: Batch and Continuous, In: J. L. Anderson, A. Berthod, V. Pino, A. Stalcup (Eds.), *Analytical Separation Science* (Vol. 5) Wiley-VCH, 2015.
- [69] C.B. Lopes, M. Otero, Z. Lin, C.M. Silva, E. Pereira, J. Rocha, A.C. Duarte, Effect of pH and temperature on Hg²⁺ water decontamination using ETS-4 titanosilicate, *J. Hazard. Mater.* 175 (2010) 439–444.
- [70] Y. Marcus, Thermodynamics of solvation of ions. Part 5.-Gibbs free energy of hydration at 298.15 K, *J. Chem. Soc. Faraday Trans.* 87 (1991) 2995–2999.
- [71] P.F. Lito, J.P.S. Aniceto, C.M. Silva, Modelling ion exchange kinetics in zeolyte-type materials using Maxwell-Stefan approach, *Desalin. Water Treat.* (2013) 1–10.
- [72] C.M. Silva, P.F. Lito, Application of the Maxwell–Stefan approach to ion exchange in microporous materials. Batch process modelling, *Chem. Eng. Sci.* 62 (2007) 6939–

6946.

- [73] P.F. Lito, J.P.S. Aniceto, C.M. Silva, Maxwell–Stefan based modelling of ion exchange systems containing common species (Cd²⁺, Na⁺) and distinct sorbents (ETS-4, ETS-10), *Int. J. Environ. Sci. Technol.* 12 (2015) 183–192.



Optical sensing of Cs^+ and Na^+ by Eu-AV-20

This chapter is devoted to the assessment of the Cs^+ and Na^+ sensing ability of Eu-AV-20. Fifteen different batch ion experiments were performed in order to relate the non-degenerated $^5\text{D}_0 \rightarrow ^7\text{F}_0$ Eu^{3+} transition with cesium and sodium molar ratios of the exchanged and fully-characterized materials.

Index

III.1. Optical sensing of Cs ⁺ and Na ⁺ by Eu-AV-20	129
III.1.1. Introduction	129
III.1.2. Materials and Methods	131
III.1.2.1. Chemicals and materials	131
III.1.2.2. Synthesis procedures.....	131
III.1.2.3. Batch ion exchange experiments	132
III.1.2.4. Equipment and techniques	133
III.1.3. Results and discussion.....	134
III.1.3.1. Materials characterization	134
III.1.3.2. Photoluminescence studies.....	137
III.1.4. Conclusions	143
III.2. References.....	145

Abstract

The ability of Eu-AV-20 to sense the Cs⁺ and Na⁺ ions based on photoluminescence was assessed. Eu-AV-20 was prepared by hydrothermal synthesis and characterized by Scanning Electron Microscopy (SEM), Energy-dispersive X-ray spectroscopy (EDS), Powder X-Ray Diffraction (PXRD), Inductively Coupled Plasma – Mass Spectrometry (ICP-MS) and Photoluminescent Spectroscopy (PLS). Fifteen batch ion exchange experiments were carried out with cesium, sodium and equimolar cesium and sodium solutions until reaching the equilibrium (5 different concentration experiments each). The emission photoluminescence spectra of native and ion exchanged Eu-AV-20 samples were collected at room temperature and significant changes were detected and correlated with the cations molar ratio in solid Eu-AV-20. Concerning the non-degenerated transition $^5D_0 \rightarrow ^7F_0$ of the Eu³⁺ septet, the intensity of the emissions attributed to Eu1 and Eu2 were reversed upon increasing the cesium concentration in the solid.

III.1. Optical sensing of Cs⁺ and Na⁺ by Eu-AV-20

III.1.1. Introduction

The synthesis of zeolite-type rare-earth or Ln-silicates was initiated in the beginning of the century, aiming at their use as phosphors and as probes for the structure and the environment of the guest cations in the cages [1,2]. Such materials exhibit interesting optical properties and have the possibility of emitting over the entire spectral range. The electronic transitions of the Ln-solids take place between 4f orbitals which are well shielded from their chemical environment by 5s² and 5p⁶ electrons, [3] resulting in atomic-like emission spectra displaying characteristic sharp lines. Since the emission spectra of a given material depend on the presence of chemical species such as molecules and ions in the vicinity of the emitter lanthanide, the possibility of sensing the presence of the former may be explored [3,4]. An interesting recent development has been the use of a lanthanide silicate as the first ratiometric luminescent thermometer operative at cryogenic temperatures (<100 K) [5].

In this context, AV-n (Aveiro microporous silicates) solids may play an important role in the development of sensors for future use in wastewater control because they combine in a single and stable solid microporosity and tuneable optical properties [6]. During the synthesis of the AV-9 materials [7], a new crystalline microporous lanthanide silicate, AV-20, appears. This material is formulated as Na_{1.08}K_{0.5}Ln_{1.14}Si₃O_{8.5}·1.78H₂O, with Ln = Eu, Ce, Nd, Sm, Gd or Tb [8]. The structure of AV-20 is amenable to the incorporation of a

second type of Ln³⁺ ion [6] and presents optical properties characteristic of the incorporated lanthanide, *i.e.*, red (Eu³⁺) and green (Tb³⁺) and infrared (Nd³⁺) emissions. Interestingly, when the crystal structure of AV-20 was solved, Ferreira *et al.*, [8] found that it was related to the structure of a fascinating group of calcium hydrated silicate minerals known as tobermorites. Special attention has been paid to the ion exchange properties of these minerals [9] and their potential application in the decontamination of waters containing metals, such as cesium [10]. Some studies showed that their exchange capacity may be enhanced by increasing the number of exchangeable cations by insertion of Na⁺ and Al³⁺ [10,11]. The structure of AV-20 is related with the structure of “normal” tobermorite 11 Å [8,12]. However, in the dense layers of Eu-AV-20 (Figure III.1.1.a) there are heptacoordinated europium and sodium instead of the calcium present in tobermorites (Ca²⁺ ↔ Eu³⁺ + Na⁺). Additionally, *ca.* 10% of the Na⁺ present in the dense AV-20 layers is substituted by disordered Eu³⁺. The layers are connected through double silicate chains of 8-membered rings forming the framework channels, running along the [110] direction (Figure III.1.1.b). The 5.8 Å x 6.8 Å channels contain K⁺ ions coordinated by four oxygen framework atoms and three water molecules, and Na⁺ ions coordinated by three framework cations and three water molecules. Both sites, particularly the sodium site, may be partially occupied by water molecules. The sodium population ratio in the layer/channels cavities is *ca.* 4 [8].

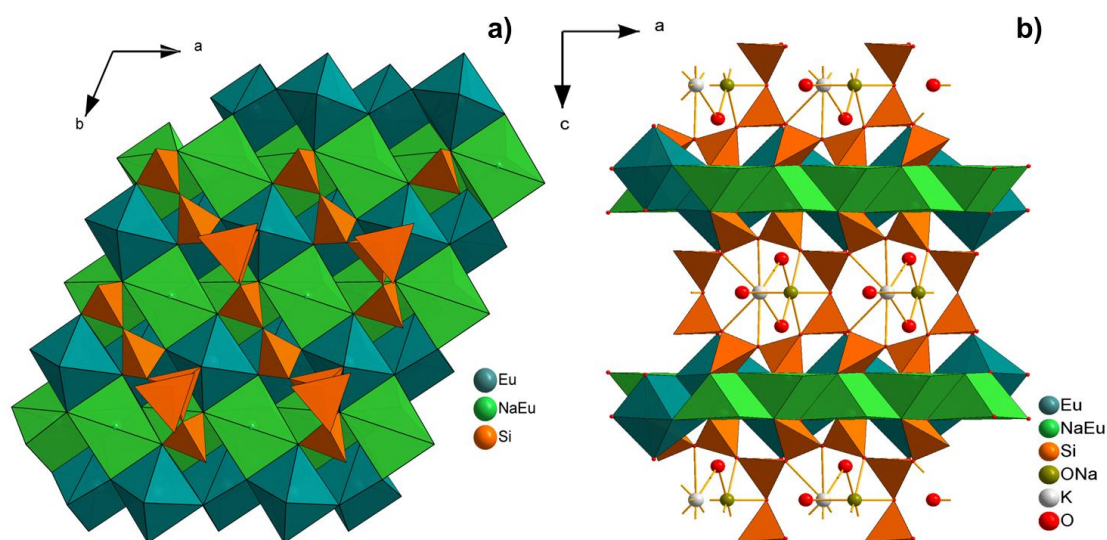


Figure III.1.1 – a) Eu-AV-20 sheets comprising alternating chains of Na⁺ and Eu³⁺ polyhedra; b) framework channels running along the [110] direction and housing Na⁺ and K⁺ ions and water molecules. Crystal structure drawn using Diamond software.

Assessing the potential use of AV-20 materials in wastewater treatment by ion exchange is of interest because they may allow swiftly detecting and quantifying the presence of contaminants by photoluminescence. In the nuclear energy field such applications are of particular importance because this type of sensing materials does not require direct contact with the radioactive samples. A case in point is Cs⁺ sensing: ¹³⁷Cs, is a long-lived isotope produced during the nuclear fission and is the main responsible for the majority of the radioactivity of nuclear wastewaters produced around the World. However, some of the radioactive wastewaters are in extreme conditions (acidic or alkaline) and in the present of large quantities of salinity which creates the necessity to have high selective exchangers/sensor.

In this chapter, I report my studies on the Cs⁺ and Na⁺ sensing ability of Eu-AV-20 based on photoluminescence was assessed in order to evaluate its potential as both a decontaminating agent and a sensor. Eu-AV-20 was, thus, synthesized and characterized in detail, and batch ion exchange experiments were carried out until reaching the equilibrium. After ion exchange, the solids were characterized again and underwent a microwaved-assisted acid digestion to determine their composition. Photoluminescence studies gave particular attention to the non-degenerated transition ⁵D₀→⁷F₀ of the Eu³⁺ septet, the transition that changed most with the modifications in the vicinity of the emitter lanthanide.

III.1.2. Materials and Methods

III.1.2.1. Chemicals and materials

High-purity water (18.2 MΩcm) was generated from a Milli-Q Millipore water purification system. Extra pure sodium silicate solution (HS code 2839 19 00), potassium hydroxide (CAS number 1310-58-3) and sodium hydroxide (CAS number 1310-73-2) were supplied from Merck. Europium(III) chloride hexahydrate (CAS number 13759-92-7), sodium nitrate (CAS number 7631-99-4) and cesium nitrate (CAS number 7789-18-6) were purchased from Sigma-Aldrich.

III.1.2.2. Synthesis procedures

The synthesis of the native Eu-AV-20 [8] comprised the preparation of an alkaline solution obtained by mixing 5.75 g of sodium silicate solution, 16.51 g of H₂O, 3.25 g of KOH, and 1.07 g of NaOH. The gel, with composition 0.79 Na₂O : 1.10 K₂O : 1.0 SiO₂ : 0.07 Eu₂O₃ :

35 H₂O was autoclaved under autogenous pressure for 3 days at 230 °C. After the synthesis, the autoclave was removed and quenched in cold water. The off-white microcrystalline powder was filtered, washed at room temperature with distilled water, and dried at 100 °C. Table III.1.1 summarizes the relevant features of this material.

Table III.1.1 – Features of the synthesized Eu-AV-20 lanthanide silicate [8].

Formula	Na _{1.08} K _{0.5} Eu _{1.14} Si ₃ O _{8.5} ·1.78H ₂ O
Density, ρ_{solid} (kg m ⁻³)	3080
Cation exchange capacity, q_s (eq kg ⁻¹)	2.55
Equivalent particle diameter (10 ⁻⁶ m)	23.1
Pore diameter (10 ⁻¹⁰ m)	5.8 x 6.8

III.1.2.3. Batch ion exchange experiments

The batch ion exchange experiments were performed contacting, under stirring, the prepared Cs⁺ solutions (Exps. 1 to 5, Table III.1.2), Na⁺ (Exps. 6 to 10, Table III.1.2) and equimolar Na⁺ and Cs⁺ (Exps. 11 to 15, Table III.1.2), with the powdered (ca. 250 mg) Eu-AV-20 in volumetric flasks of 1 L, at room temperature. The stirring velocity was maintained at ca. 300 rpm and the initial pH of the solution was 4.

The experiments started when Eu-AV-20 was added to the prepared solutions and the stirring initiated. After the sorption experiments, the solids were separated from the solution by sedimentation and washed with high-purity water in order to avoid remaining impurities from the solution.

The chemical formulae of the native and exchanged Eu-AV-20 samples were determined by ICP-MS and EDS. The solids underwent a microwave-assisted digestion (with sequences of 3 minutes at 70% of 600 W for 30 minutes) with the use of strong acids, *i.e.*, 150 mg of solid was dissolved in 100 mg of high purity water and 2 mL of nitric acid (65%) and 0.15 mL of fluoride acid.

Table III.1.2 – Batch ionexchange experimental conditions; fixed: V = 1 L and T = 294.15 K.

Experiment number	1	2	3	4	5
Exchanged cation(s)	Cs ⁺				
Mass of Eu-AV-20 (g)	0.253	0.254	0.253	0.252	0.255
Mass of CsNO ₃ (g)	0.201	0.976	1.953	4.877	9.751
Concentration of CsNO ₃ (mol dm ⁻³)	0.001	0.005	0.010	0.025	0.050

Experiment number	6	7	8	9	10
Exchanged cation(s)	Na ⁺				
Mass of Eu-AV-20 (g)	0.248	0.256	0.254	0.244	0.256
Mass of NaNO ₃ (g)	0.088	0.429	0.847	2.124	4.248
Concentration of NaNO ₃ (mol dm ⁻³)	0.001	0.005	0.010	0.025	0.050

Experiment number	11	12	13	14	15
Exchanged cation(s)	Cs ⁺ and Na ⁺				
Mass of Eu-AV-20 (g)	0.246	0.246	0.249	0.241	0.251
Mass of CsNO ₃ (g)	0.098	0.490	0.975	2.495	4.870
Mass of NaNO ₃ (g)	0.046	0.217	0.427	1.064	2.128
Concentration of CsNO ₃ (mol dm ⁻³)	0.0005	0.0025	0.0050	0.0128	0.0250
Concentration of NaNO ₃ (mol dm ⁻³)	0.0005	0.0026	0.0050	0.0125	0.0250

III.1.2.4. Equipment and techniques

SEM and EDS

The crystal phase and chemical purity of the Cs⁺- and Na⁺-exchanged samples were assessed using SEM and EDS. The SEM microscope used was a SEM Hitachi S-4100. The EDS coupled Römteck system with a polymeric window was also used to establish the chemical formula of Eu-AV-20 and Cs⁺-exchanged samples.

PXRD

The crystallinity and purity of the cesium exchanged samples was also unveiled by PXRD collected at ambient temperature on a PANalytical Empyrean diffractometer (Cu K_{α1,2}X-radiation, $\lambda_1 = 1.540598 \text{ \AA}$; $\lambda_2 = 1.544426 \text{ \AA}$), equipped with an PIXcel 1D detector and a flat-plate sample holder in a Bragg-Brentano para-focusing optics configuration (45 kV, 40 mA). Intensity data were collected by the step-counting method (step 0.04°), in continuous mode, in the ca. $5 \leq 2\theta \leq 50^\circ$ range.

ICP-MS

The chemical formula of the Eu-AV-20 and Cs⁺- and Na⁺-exchanged samples were determined by ICP-MS on a Jobin-Yvon JY70 Plus Spectrometer.

PLS

The photoluminescent spectra in the visible region were recorded at room temperature on a Jobin Yvon-Spex spectrometer (HR 460) fitted with a 1200 grooves mm⁻¹ grating blazed at 500 nm-coupled to a R928 Hamamatsu photomultiplier. A 150 W Xe arc lamp coupled to an excitation monochromator Jobin Yvon-Spex (TRIAX 180) fitted with a 1200 grooves mm⁻¹ grating blazed at 330 nm was used as excitation source. All spectra were corrected for the response of the detectors.

III.1.3. Results and discussion

This section starts with the crystallinity and purity characterization of the native and exchanged Eu-AV-20 samples by SEM and PXRD, after which it presents and discusses the PLS results. Finally it discusses the relation between the cation molar ratio in the Eu-AV-20 solid (after ion exchange) and the ratio of the areas of the Eu1 and Eu2 ⁵D₀→⁷F₀ transitions.

III.1.3.1. Materials characterization

Figure III.1.2 shows the SEM images of the exchanged Eu-AV-20 samples (experimental conditions in Table III.1.2). The results indicate that material preserves its crystallographic pseudo hexagonal habit after ion exchange. Negligible amounts of nitric salts impurities were confirmed by PXRD (asterisks on Figure III.1.3, Figure III.1.4 and Figure III.1.5). PXRD confirmed that the crystallinity of the samples is also preserved after ion exchange. Relatively to the impurities observed by SEM, PXRD allowed their estimation at less than 5% (wt/wt) and revealed that the solids exchanged with cesium nitrate had the highest amounts.

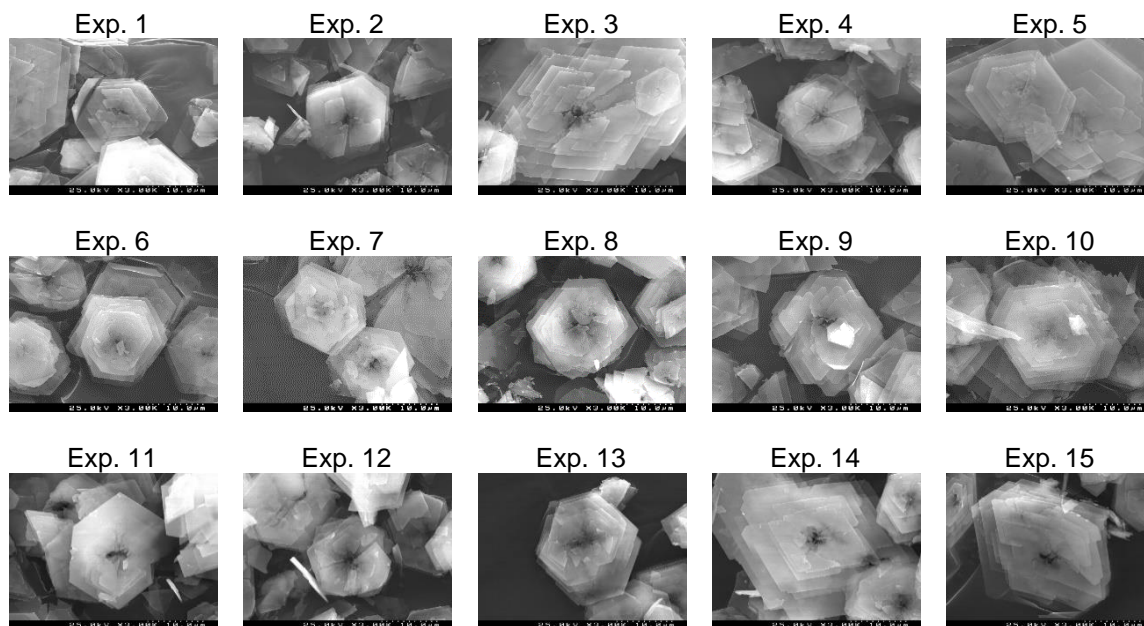


Figure III.1.2. – SEM images of exchanged Eu-AV-20 (see experimental conditions in Table III.1.2).

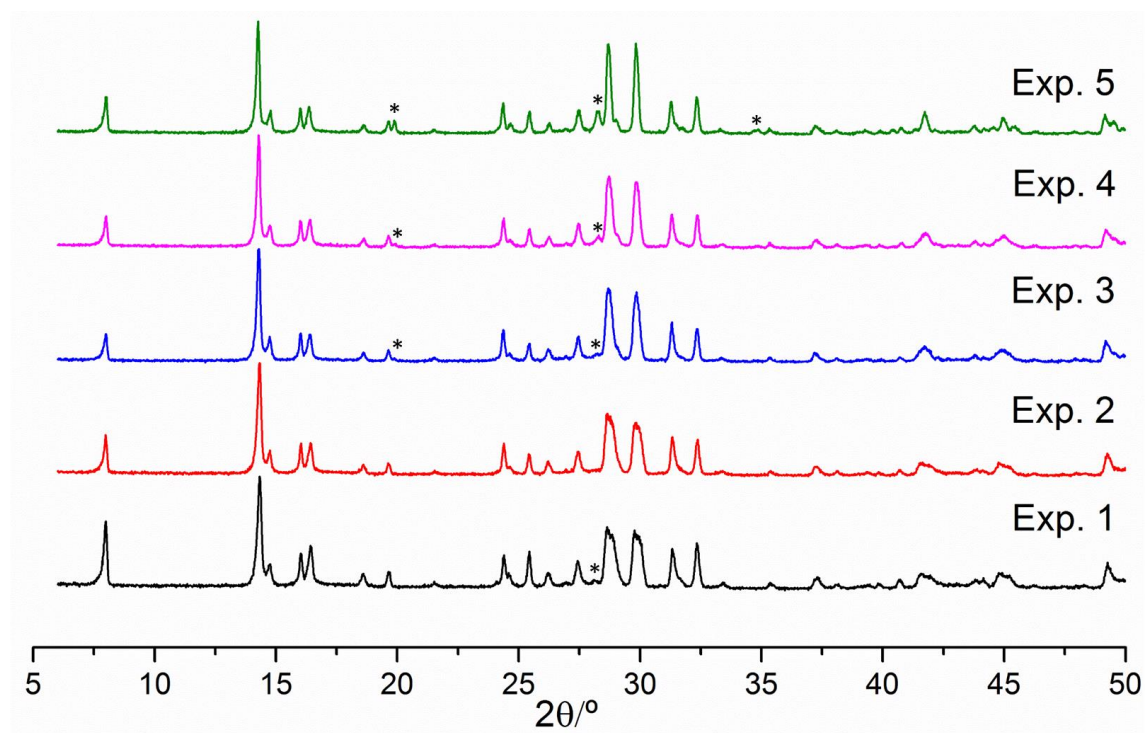


Figure III.1.3 – PXRD patterns of the Cs⁺-exchanged Eu-AV-20 (Exps. 1-5, see experimental conditions in Table III.1.2). The asterisks depict impurities.

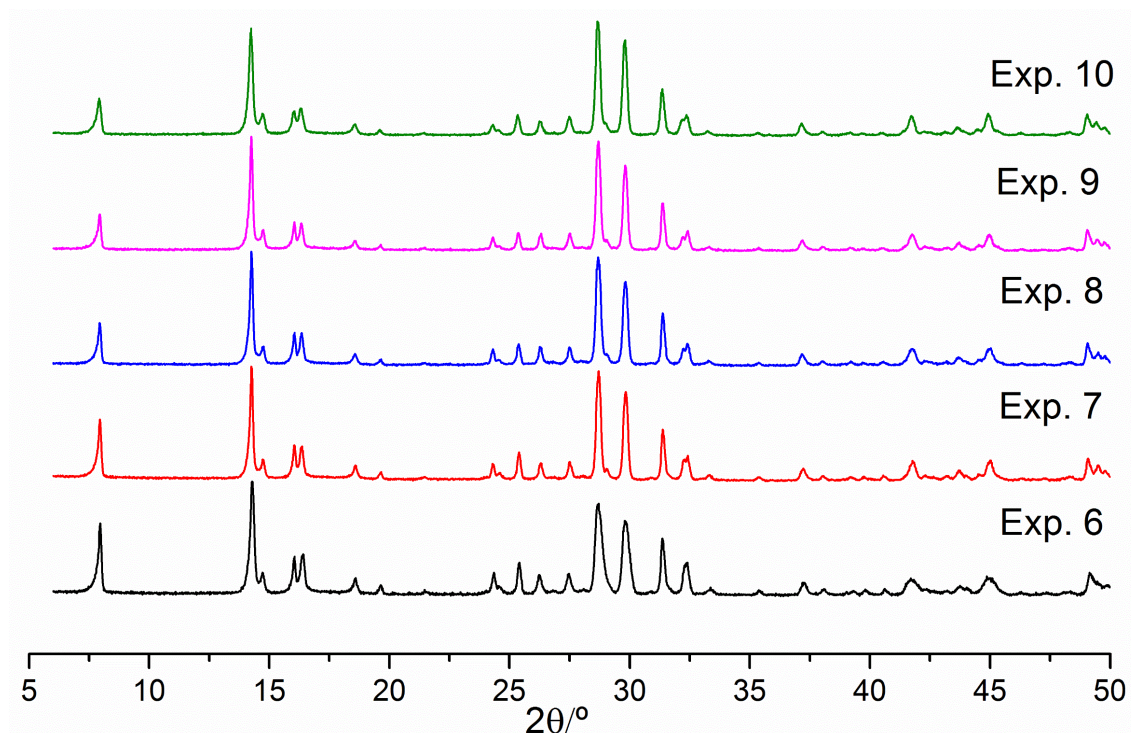


Figure III.1.4 – PXR D patterns of the Na⁺-exchanged Eu-AV-20 (Exps. 6-10, see experimental conditions in Table III.1.2).

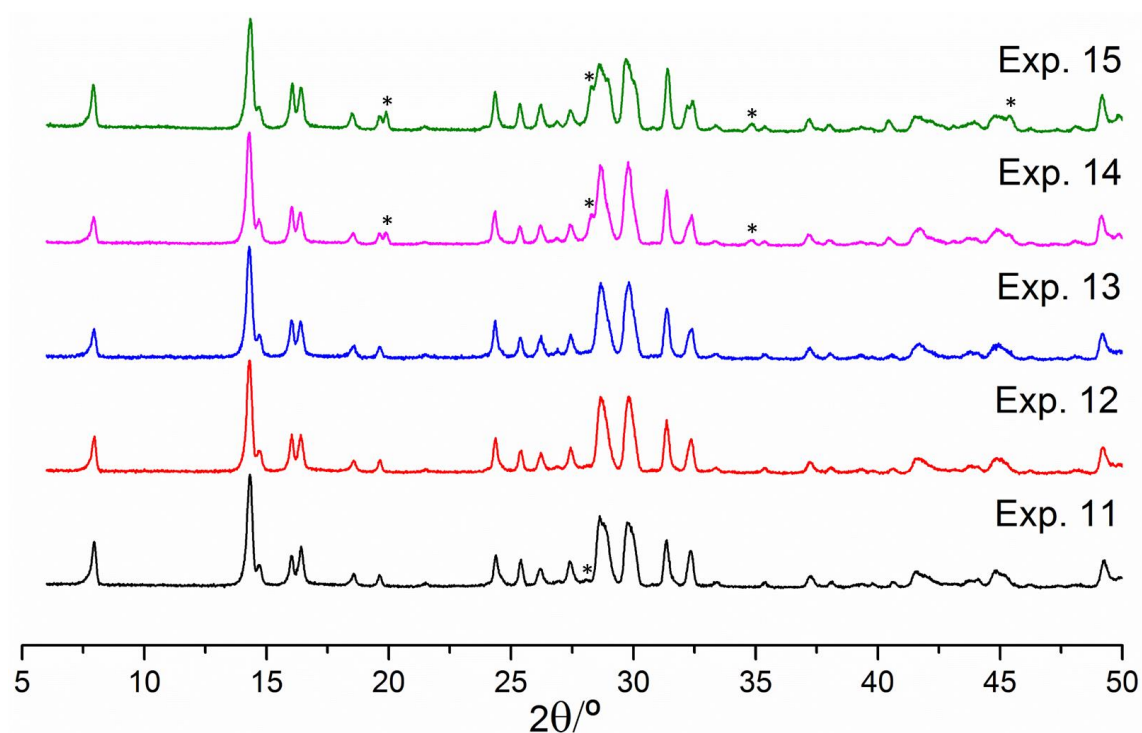


Figure III.1.5 – PXR D patterns of the (Cs⁺,Na⁺)-exchanged Eu-AV-20 (Exps. 11 to 15, see experimental conditions Table III.1.2). The asterisks depict impurities.

III.1.3.2. Photoluminescence studies

The full room-temperature (RT) photoluminescence emission spectra of the native and Cs⁺-exchanged Eu-AV-20 materials recorded with excitation at 393 nm are qualitatively compared in Figure III.1.6, where five of the transitions ascribed to the Eu³⁺ septet ($^5D_0 \rightarrow ^7F_j$, $j = 0-4$), due to its relevance, are identified. All the spectra were measured keeping the experimental set-up fixed (slits width, irradiated area, and optics geometry) and using the same amount of sample in the form of pellets pressed at a constant pressure of ca. 2 Ton cm⁻². Figure III.1.6 shows the RT emission spectra of the native and Cs⁺-exchanged Eu-AV-20 (from Exp. 1) and reveals a high sensitivity of the europium(III) emission to the Cs⁺ incorporation into the solid since big differences in all transitions are observable.

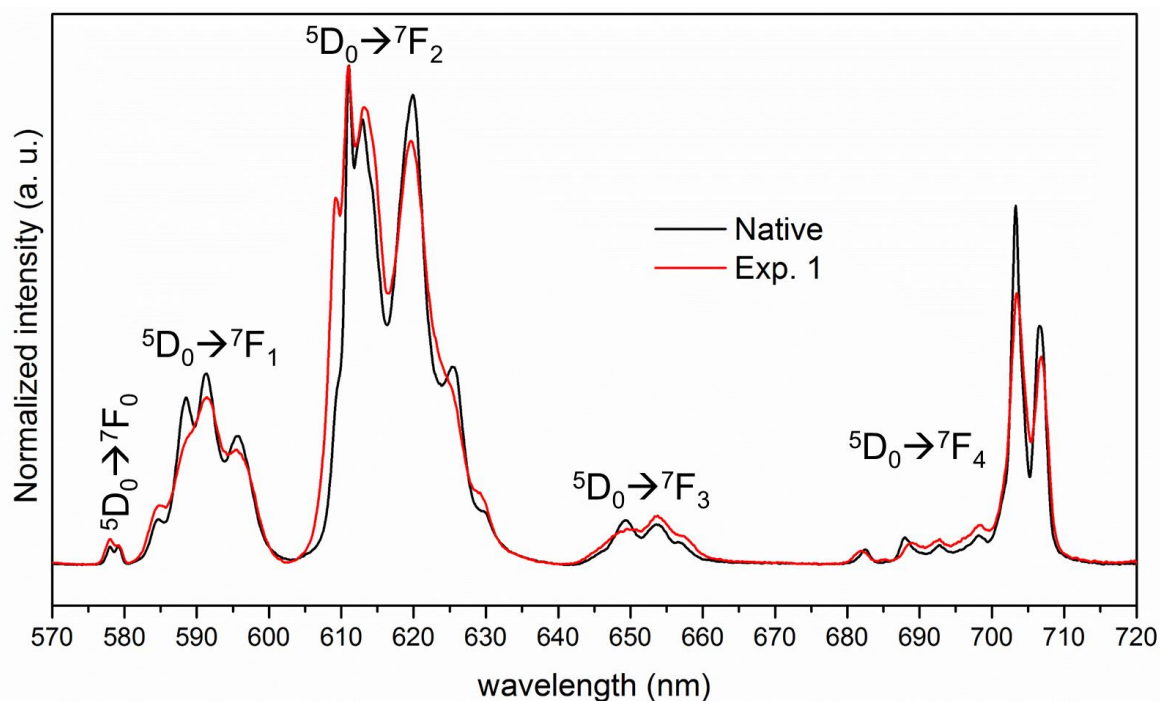


Figure III.1.6 – RT emission spectra of native and Cs⁺-exchanged Eu-AV-20 materials (excitation at 393 nm). See experimental conditions in Table III.1.2.

Figure III.1.7 shows the non-degenerated $^5D_0 \rightarrow ^7F_0$ transition of the emission spectra of the native and Cs⁺-exchanged Eu-AV-20 (Exp. 1) from which two local Eu³⁺ environments are clearly inferred by the presence of two lines. The native Eu-AV-20 and Cs⁺-exchanged are distinct because of the presence of this ion and some quenching effects provoked by the presence of additional sorbed water molecules. The intensity of Eu1 peak decreases, while the Eu2 band broadens and slightly shifts. Similar features were observed by Ferreira *et al.*

[8], when the native Eu-AV-20 was exposed to vacuum. In this case, the unit cell shrunk upon sample dehydration, inducing slight changes in the local environments of Eu1 and Eu2.

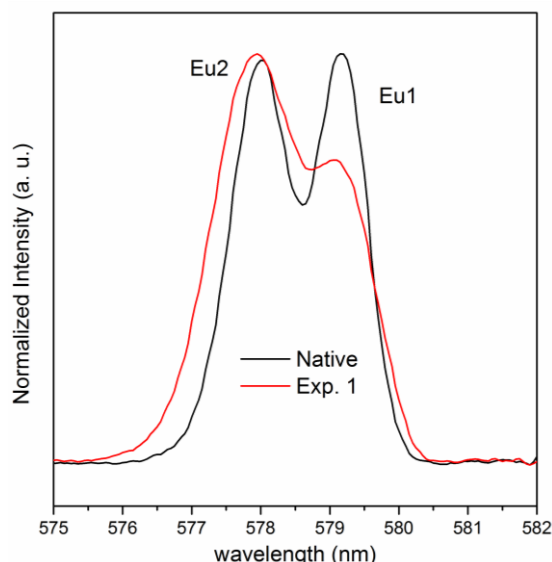


Figure III.1.7 – $^5D_0 \rightarrow ^7F_0$ transition region of the luminescence spectra of the native and Cs⁺-exchanged Eu-AV-20.

The full RT emission spectra (with excitation at 393 nm) of Cs⁺-exchanged Eu-AV-20 from Exps. 1-5 are shown in Figure III.1.8. The spectra unveil an emission increase in $^5D_0 \rightarrow ^7F_1$, $^5D_0 \rightarrow ^7F_2$ and $^5D_0 \rightarrow ^7F_4$ transitions (identified by arrows) as consequence of higher Cs⁺ exchanged concentration. This event is better observable in the $^5D_0 \rightarrow ^7F_0$ region of the photoluminescence spectra of Cs⁺-exchanged Eu-AV-20 presented in Figure III.1.9: the ratio Eu1/Eu2 increases (the area of the Eu1 band increases) with the cesium solid concentration (Exps. 1-5, Table III.1.2). This is also perceived in Figure III.1.12 where the Eu1/Eu2 areas ratio plotted as function of the Cs⁺/Eu molar ratio is almost linear (coefficient of determination $R^2=0.83$).

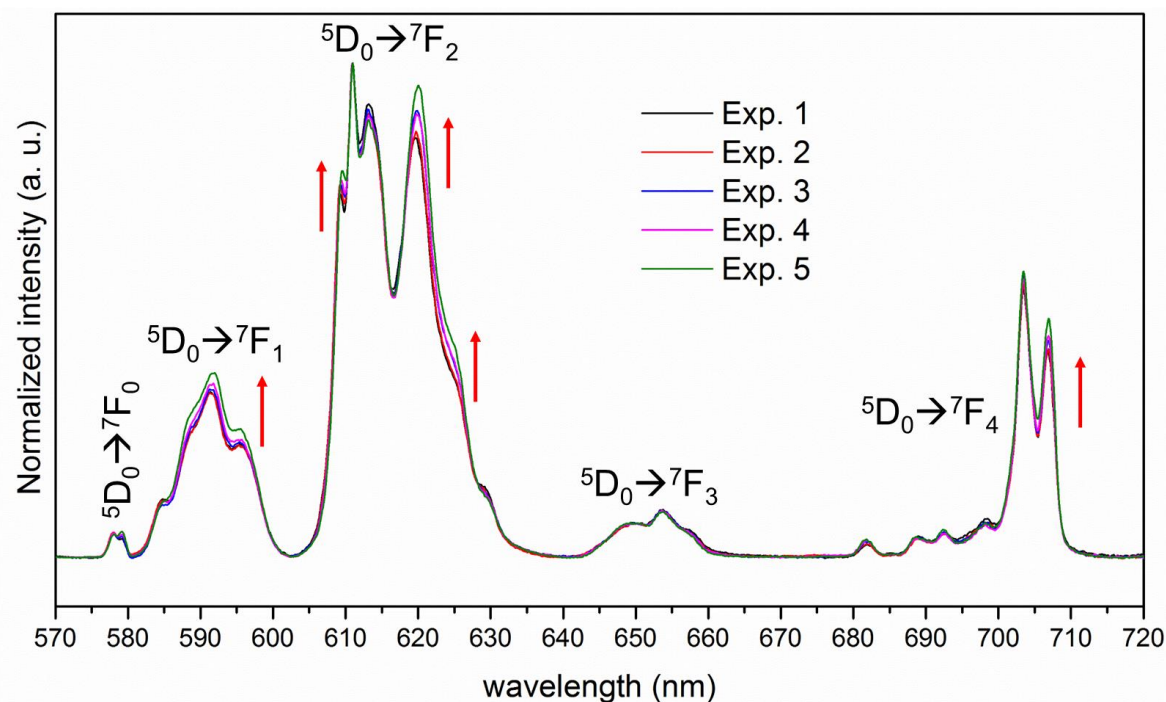


Figure III.1.8 – RT emission spectra of Cs⁺-exchanged Eu-AV-20 materials from Exps. 1-5 (excitation at 393 nm). See experimental conditions in Table III.1.2.

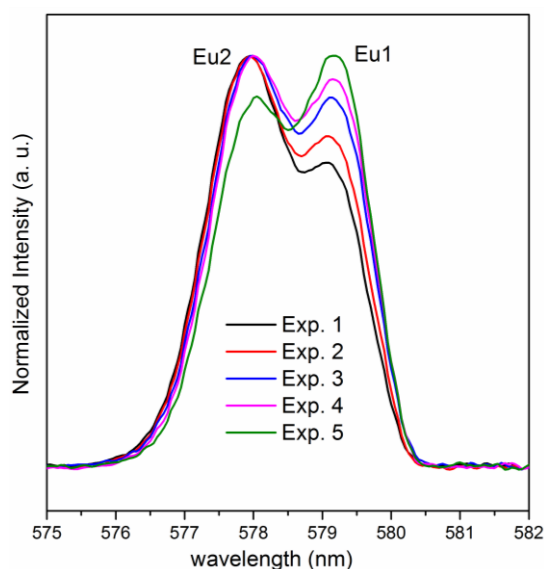


Figure III.1.9 – $^5D_0 \rightarrow ^7F_0$ transition region of the luminescence spectra of Exps. 1-5 (see experimental conditions in Table III.1.2).

Similar results were observed for the Na⁺-exchanged Eu-AV-20 (Exps. 6-10). For instance, the full RT emission spectra (with excitation at 393 nm) shown in Figure III.1.10 unveils a slight increase (identified by arrows) in the emission of $^5D_0 \rightarrow ^7F_1$ and $^5D_0 \rightarrow ^7F_2$ transitions.

Figure III.1.11 discloses a weaker Eu1 band and smaller Eu1/Eu2 ratios for the Na⁺-exchanged Eu-AV-20 (see Exps. 6-10, Table III.1.2). In this case, a linear trend is also observed but with a higher coefficient of determination ($R^2=0.94$, see Figure III.1.12) than that achieved for the Cs⁺-exchanged materials from Exps. 1-5.

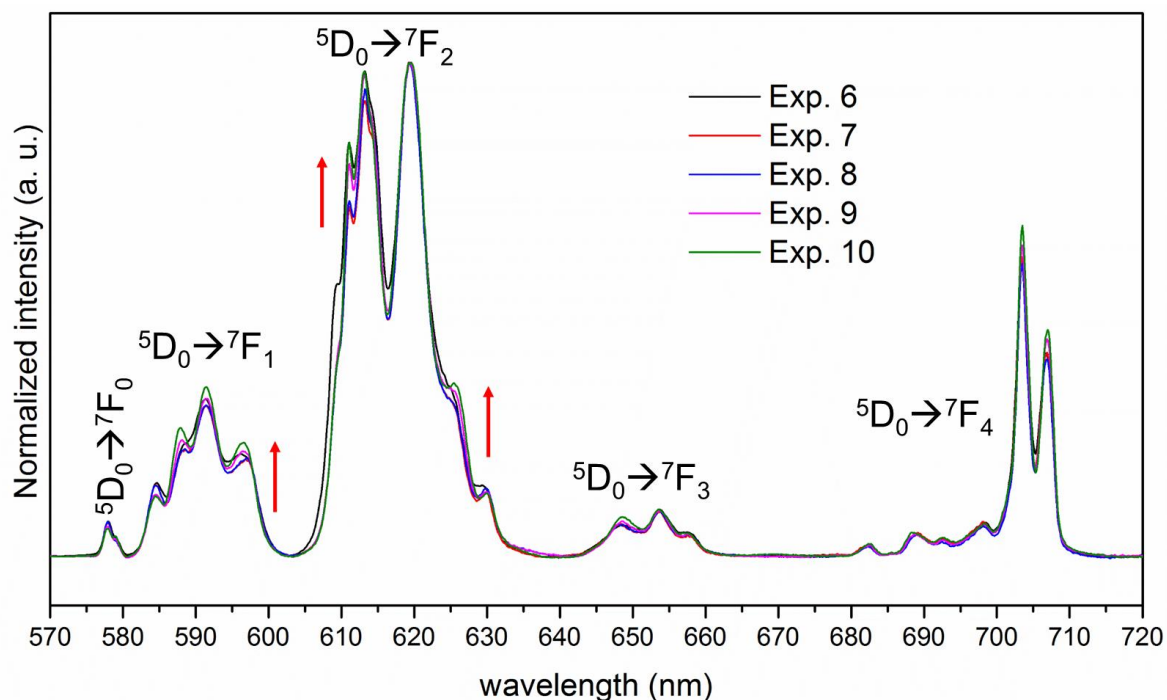


Figure III.1.10 - RT emission spectra of Na⁺-exchanged Eu-AV-20 materials from Exps. 6-10 (excitation at 393 nm). See experimental conditions in Table III.1.2.

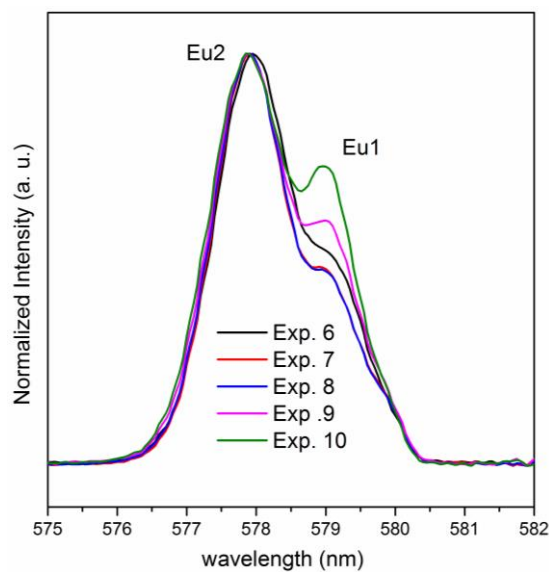


Figure III.1.11 – $^5D_0 \rightarrow ^7F_0$ transition region of the luminescence spectra of Exps. 6-10 (see experimental conditions in Table III.1.2).

Concerning Exps. 11-15, the results obtained with the equimolar Na⁺, Cs⁺ solutions are very interesting because increasing both concentrations decreases the emission intensity of the $^5D_0 \rightarrow ^7D_0$, $^5D_0 \rightarrow ^7F_1$ and $^5D_0 \rightarrow ^7F_2$ transitions (identified by arrows), as can be seen in Figure III.1.12. In fact, Eu1 and Eu2 bands decrease and the Eu1/Eu2 ratio changes little in the range ca. 0.32-0.37 (Table III.1.3 and Figure III.1.14, excluding Exp. 14). These results are probably ascribed to the competition of sodium and cesium during ion exchange, resulting in the absence of a clear trend. Indeed, the ionic radius of the involved cations ($r_{Cs^+} = 170$ pm $>$ $r_{Na^+} = 102$ pm [13]) indicates the sodium higher accessibility to the porous structure of Eu-AV-20 while the magnitude of the molar Gibbs free energy of dehydration ($\Delta_{dehyd}G$) of Cs⁺ and Na⁺, 365 and 250 kJ mol⁻¹ [13], respectively, shows that the energy required by the sodium for accessing the microporosity of Eu-AV-20 is ca. 1.5 times higher than that of cesium.

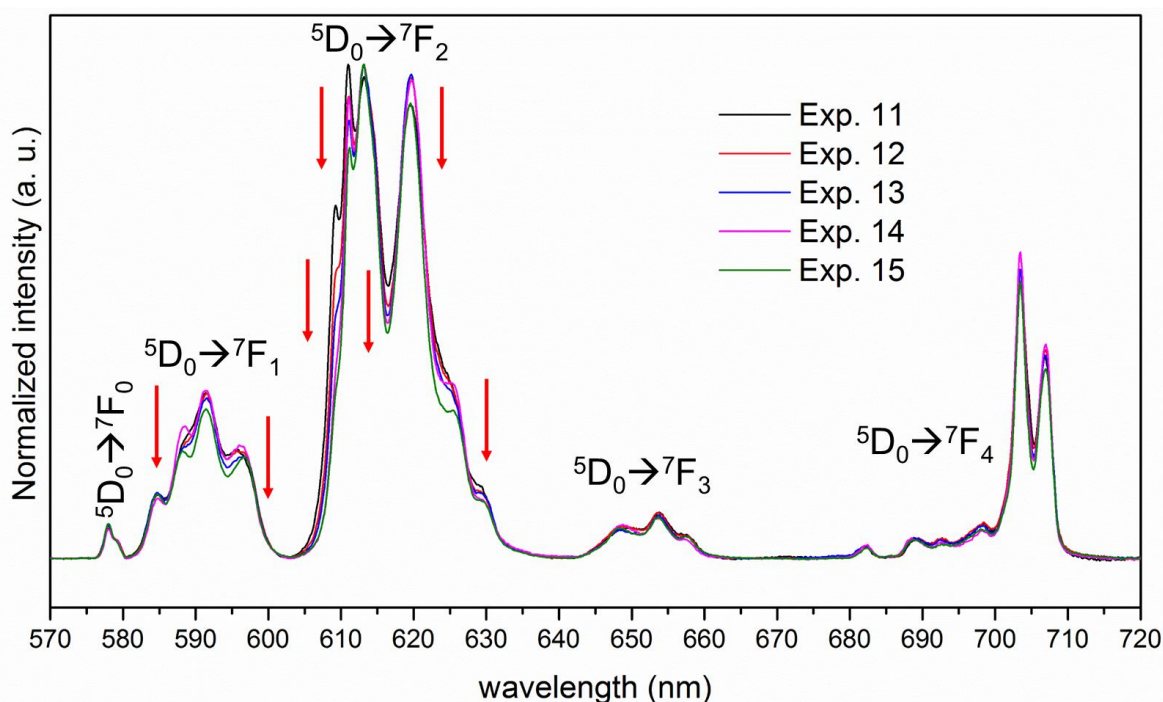


Figure III.1.12 - RT emission spectra of (Cs⁺,Na⁺)-exchanged Eu-AV-20 materials from Exps. 11-15 (excitation at 393 nm). See experimental conditions in Table III.1.2.

Figure III.1.14 reveals a higher sensitivity of the Eu-AV-20's emission to Cs⁺ incorporation since a difference of 52% in its solid molar ratio (Exps. 1-5) caused a ca. 60% increase of the Eu1/Eu2 ratio, while an increment of 67% on the sodium molar ratio (Exps. 6-10) caused an increase of ca. 64% on the Eu1/Eu2 ratio. This is evident by considering the data slopes

in Figure III.1.14.a and Figure III.1.14.b, whose values are *ca.* of 2.03 and 0.28, for cesium and sodium exchange, respectively.

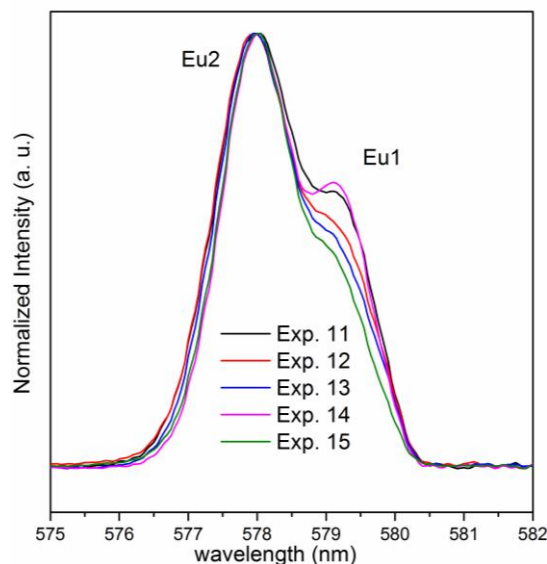


Figure III.1.13 – $^5D_0 \rightarrow ^7F_0$ transition region of the luminescence spectra of Exps. 11-15 (see experimental conditions in Table III.1.2).

Table III.1.3 – Eu1 and Eu2 peak areas, their respective ratio and standard errors (experimental conditions in Table III.1.2).

Exp. number	1	2	3	4	5
Eu1	19.616 ± 0.182	22.435 ± 0.242	25.399 ± 0.244	26.973 ± 0.284	28.845 ± 0.320
Eu2	45.990 ± 0.200	45.707 ± 0.264	45.955 ± 0.265	46.085 ± 0.307	40.875 ± 0.344
Eu1 / Eu2	0.427 ± 0.004	0.491 ± 0.006	0.553 ± 0.006	0.585 ± 0.007	0.706 ± 0.010
Cs ⁺ / Eu	0.12 ± 0.01	0.16 ± 0.02	0.19 ± 0.03	0.23 ± 0.01	0.23 ± 0.02

Exp. number	6	7	8	9	10
Eu1	13.541 ± 0.224	14.755 ± 0.379	14.096 ± 0.346	17.651 ± 0.370	20.564 ± 0.401
Eu2	39.819 ± 0.234	36.229 ± 0.377	37.488 ± 0.349	38.209 ± 0.378	39.156 ± 0.419
Eu1 / Eu2	0.340 ± 0.006	0.407 ± 0.011	0.376 ± 0.010	0.462 ± 0.011	0.525 ± 0.012
Na ⁺ / Eu	1.09 ± 0.40	1.25 ± 0.44	1.15 ± 0.31	1.57 ± 0.77	1.64 ± 0.44

Exp. number	11	12	13	14	15
Eu1	16.605 ± 0.157	15.672 ± 0.220	15.109 ± 0.219	18.533 ± 0.171	12.585 ± 0.211
Eu2	45.546 ± 0.172	43.127 ± 0.235	41.551 ± 0.229	38.841 ± 0.182	39.421 ± 0.222
Eu1 / Eu2	0.365 ± 0.004	0.363 ± 0.005	0.364 ± 0.006	0.477 ± 0.005	0.319 ± 0.006
Cs ⁺ / Eu	0.12 ± 0.02	0.18 ± 0.02	0.20 ± 0.02	0.24 ± 0.03	0.27 ± 0.03
Na ⁺ / Eu	0.93 ± 0.19	1.26 ± 0.19	1.20 ± 0.50	1.47 ± 0.16	1.25 ± 0.25

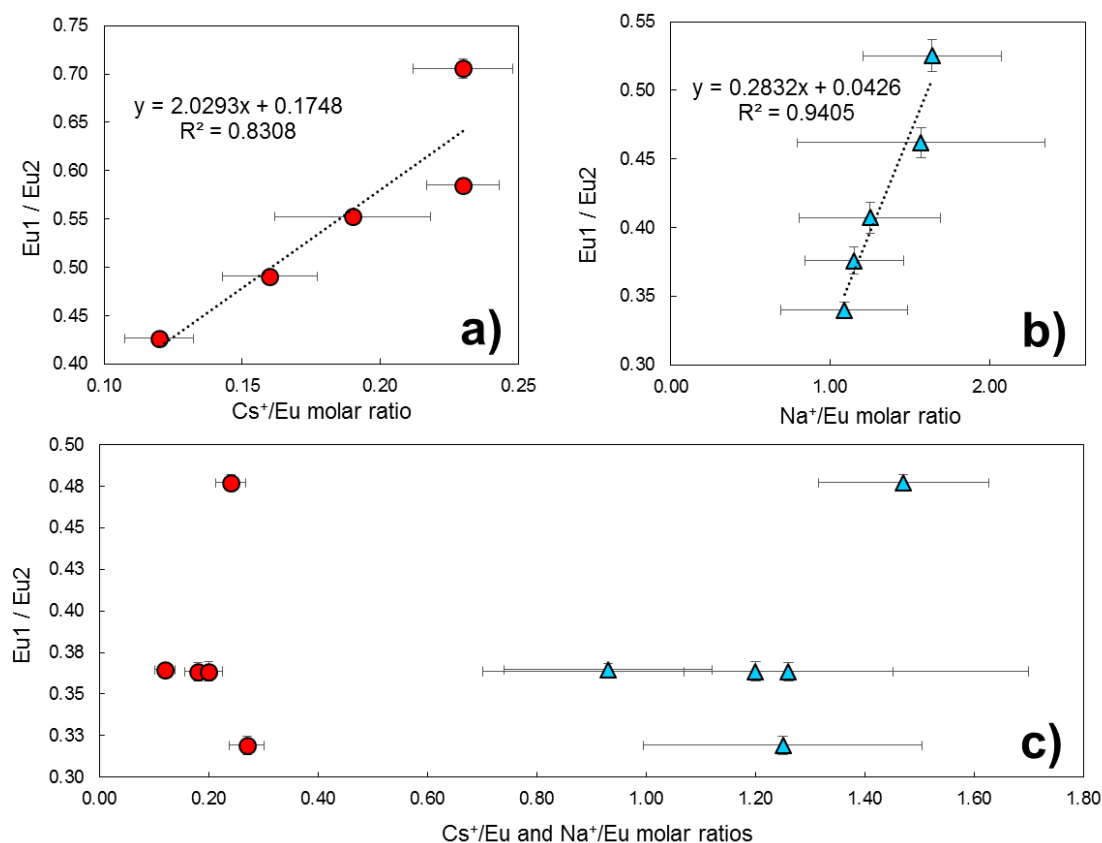


Figure III.1.14 – Eu1/Eu2 areas ratio as a function of: a) Cs⁺/Eu molar ratio (Exps. 1-5); b) Na⁺/Eu molar ratio (Exps. 6-10); and c) Cs⁺/Eu and Na⁺/Eu molar ratios (Exps. 11-16). Red circles depict the Cs⁺/Eu molar ratio and blue triangles the Na⁺/Eu molar ratio (see experimental conditions in Table III.1.2.)

III.1.4. Conclusions

In this chapter, the Cs⁺ and Na⁺ sensing ability of Eu-AV-20 materials, based on photoluminescence, was assessed. Fifteen batch ion exchange experiments were carried out until equilibrium was reached using cesium, sodium and equimolar solutions of both. After ion exchange the solids were characterized by several techniques. SEM, EDS and PXRD results revealed negligible amounts of impurities. Uptake of cesium and sodium resulted in changes in the emission spectrum of native Eu-AV-20, due to slight changes in the local environment of the Eu³⁺ emitter. Intriguingly, when the materials are ion exchanged with only sodium or cesium, the Eu1/Eu2 intensity ratio of the non-degenerated $^5D_0 \rightarrow ^7F_0$ transition increases, whereas when an equimolar solution of both cations is used this ratio remains essentially the same. These results suggest that AV-20 materials have potential

for being used as luminescence sensors for Cs^+ (and Na^+) cations in aqueous solutions. However, further work is needed, as witnessed by the results in Figure III.1.14.

III.2. References

- [1] G. Yang, Y. Wang, D.H. Zhou, J.Q. Zhuang, X.C. Liu, X.W. Han, X.H. Bao, On configuration of exchanged La³⁺ on ZSM-5: A theoretical approach to the improvement in hydrothermal stability of La-modified ZSM-5 zeolite, *J. Chem. Phys.* 119 (2003) 9765–9770.
- [2] G. Yang, Y. Wang, D.H. Zhou, J.Q. Zhuang, X.C. Liu, X.W. Han, X.H. Bao, Investigation on the thermal stability of La/ZSM-5 zeolite and the La³⁺ species, *Acta Physico-Chimica Sin.* 20 (2004) 60–64.
- [3] J. Rocha, L.D. Carlos, Microporous materials containing lanthanide metals, *Curr. Opin. Solid State Mater. Sci.* 7 (2003) 199–205.
- [4] J. Rocha, Z. Lin, Microporous mixed octahedral-pentahedral-tetrahedral framework silicates, *Micro- Mesoporous Miner. Phases* 57 (2005) 173–201.
- [5] D. Ananias, F.A.A. Paz, D.S. Yufit, L.D. Carlos, J. Rocha, Photoluminescent thermometer based on a phase-transition lanthanide silicate with unusual structural disorder, *J. Am. Chem. Soc.* 137 (2015) 3051–3058.
- [6] R.C. Evans, L.D. Carlos, P. Douglas, J. Rocha, Tuning the emission colour in mixed lanthanide microporous silicates: energy transfer, composition and chromaticity, *J. Mater. Chem.* 18 (2008) 1100–1107.
- [7] D. Ananias, J.P. Rainho, A. Ferreira, J. Rocha, L.D. Carlos, The first examples of X-ray phosphors, and C-band infrared emitters based on microporous lanthanide silicates, *J. Alloys Compd.* 374 (2004) 219–222.
- [8] A. Ferreira, D. Ananias, L.D. Carlos, C.M. Morais, J. Rocha, Novel microporous lanthanide silicates with tobermorite-like structure, *J. Am. Chem. Soc.* 125 (2003) 14573–14579.
- [9] S. Komarneni, D.M. Roy, Tobermorites - A New Family of Cation Exchangers, *Sci. Class.* 221 (1983) 647–648.
- [10] O.P. Shrivastava, R. Shrivastava, Cation exchange applications of synthetic tobermorite for the immobilization and solidification of cesium and strontium in cement matrix, *Bull. Mater. Sci.* 23 (2000) 515–520.
- [11] R. Siauciunas, V. Janickis, D. Palubinskaite, R. Ivanauskas, The sorption properties of tobermorite modified with Na⁺ and Al³⁺ ions, *Ceramics-Silikáty* 48 (2004) 76–82.
- [12] S. Merlino, E. Bonaccorsi, T. Armbruster, The real structure of tobermorite 11 angstrom: normal and anomalous forms, OD character and polytypic modifications, *Eur. J. Mineral.* 13 (2001) 577–590.
- [13] Y. Marcus, Thermodynamics of solvation of ions. Part 5.-Gibbs free energy of hydration at 298.15 K, *J. Chem. Soc. Faraday Trans.* 87 (1991) 2995–2999.

IV

Removal of Cs⁺ from aqueous solutions through batch experiments

This chapter concerns the study of two lanthanide silicates, Eu-AV-20 and Tb/Eu-AV-9, for the removal of Cs⁺ ion from aqueous solution performing batch ion exchange experiments. Both materials were synthesized and characterized by several techniques such as scanning electron microscopy (SEM), energy-dispersive X-ray spectroscopy (EDS), powder X-Ray diffraction (PXRD), inductively coupled plasma mass spectroscopy (ICP-MS) and photoluminescent spectroscopy (PLS). Several experiments were carried out to measure isotherm and kinetic removal curves. The kinetic data were modelled using a Maxwell-Stefan based model taking into account internal and external limitations to mass transfer. The photoluminescent spectra of the parent and Cs⁺-ion exchanged solids were obtained in order to evaluate their sensing ability towards cesium.

Index

IV.1. Cs ⁺ ion exchange over lanthanide silicate Eu-AV-20: Experimental measurement and modelling	152
IV.1.1. Introduction	152
IV.1.2. Materials and Methods	155
IV.1.2.1. Chemicals and materials	155
IV.1.2.2. Synthesis procedures.....	155
IV.1.2.3. Sorption experiments: isotherm and removal curves	155
IV.1.2.4. Equipment and techniques	157
IV.1.3. Modelling.....	158
IV.1.4. Results and discussion.....	162
IV.1.4.1. Materials characterization	162
IV.1.4.2. Photoluminescent spectra of native and Cs ⁺ –exchanged Eu-AV-20.....	163
IV.1.4.3. Ion exchange isotherm.....	164
IV.1.4.4. Influence of Eu-AV-20 mass upon Cs ⁺ removal.....	165
IV.1.4.5. Ion exchange kinetics.....	166
IV.1.4.6. Ion exchange modelling based on Maxwell-Stefan equations	169
IV.1.5. Conclusions	173
IV.1.6. Nomenclature.....	174
IV.2. Tb/Eu-AV-9: A lanthanide silicate for the sensing and removal of cesium ions from aqueous solutions.....	178
IV.2.1. Introduction	178
IV.2.2. Materials and Methods	180
IV.2.2.1. Chemicals and materials	180
IV.2.2.2. Synthesis procedures.....	180
IV.2.2.3. Characterization of the Tb/Eu-AV-9 material	181
IV.2.2.4. Sorption experiments: isotherm and removal curves	181
IV.2.3. Modelling.....	183
IV.2.4. Results and discussion.....	187
IV.2.4.1. Characterization of the Tb/Eu-AV-9 material	187
IV.2.4.2. Ion exchange isotherm.....	188
IV.2.4.3. Influence of Tb/Eu-AV-9 mass upon Cs ⁺ removal.....	189
IV.2.4.4. Ion exchange kinetics.....	191
IV.2.4.5. Photoluminescence spectra of native and Cs ⁺ –exchanged Tb/Eu-AV-9.....	192

IV.2.4.6. Ion exchange modelling based on Maxwell-Stefan equations	196
IV.2.5. Conclusions	198
IV.2.6. Nomenclature	199
IV.3. References.....	203

Work reported in the scientific article

Cs⁺ ion exchange over lanthanide silicate Eu-AV-20: Experimental measurement and modelling

published on Chemical Engineering Journal 268 (2015) 208–218

Abstract

The ion exchange of Cs⁺ from aqueous solutions was studied using for the first time a microporous lanthanide silicate with photoluminescence properties, Eu-AV-20. It was prepared by hydrothermal synthesis, characterized by SEM, PLS, PXRD and ICP-MS, and several batch ion exchange experiments were performed to measure isotherm and removal curves. Additional curves were measured to evaluate the competition with Na⁺. The results evidenced the great selectivity of Eu-AV-20 towards Cs⁺ since cesium removal was slightly modified even for Na⁺/Cs⁺ concentrations ratio of 190. The emission photoluminescent spectra of native and Cs⁺-exchanged Eu-AV-20 were also determined for the first time, and significant modifications were detected, which discloses the potential of Eu-AV-20 for Cs⁺ sensing purposes.

The Langmuir equation provided a good fit to the equilibrium data, with average error of 5.3%, and the Maxwell-Stefan based model adopted to represent the kinetic curves (*i.e.*, concentration *versus* time) achieved a deviation of 19.0%. An analysis of variance confirmed that the model was statistically significant to represent the uptake curves.

The Maxwell-Stefan based model comprises three parameters, namely, the diffusion coefficients associated to the interactions of Cs⁺ and Eu-AV-20, Na⁺/K⁺ and Eu-AV-20, and Cs⁺ and Na⁺/K⁺, whose fitted values were 2.706x10⁻¹⁵, 5.713x10⁻¹⁵ and 9.446x10⁻¹⁷ m² s⁻¹. Such low values evidenced that the intraparticle mass transport mechanism is surface diffusion. This fact is ascribed to the small pores of the Eu-AV-20 crystal, 5.8x6.8 Å, because the counter ions never escape from the force field of the framework co-ions, mainly due to the strong and long range nature of the electrostatic interactions.

IV.1. Cs⁺ ion exchange over lanthanide silicate Eu-AV-20: Experimental measurement and modelling

IV.1.1. Introduction

The World, particularly the United States of America, inherited a massive amount of highly radioactive wastes generated in the weapon and electrical power production [1], which have been stored in large underground tanks filled with a complex triphasic system containing a metal hydroxide sludge, a high concentrated alkaline supernatant, and a salt cake where cesium (^{135,137}Cs), strontium (⁹⁰Sr) and technetium (⁹⁹Tc) are the predominant radioactive elements [2–4]. Due to corrosion associated to such high salinity, these tanks suffered leakage allowing the radionuclides to enter the surrounding soils and groundwater [1,2].

The undesirable effect of the radiation associated with these wastes raised the awareness towards its secure management, protecting the human health and environment. Furthermore, the reduction of the volume of these wastes with the purpose to enhance safety and/or decrease their supervision cost makes treatment processes imperative. Several approaches may be adopted like ion exchange/sorption, chemical precipitation, evaporation, reverse osmosis, filtration, and solvent extraction [5,6].

When dealing with the requirement of high purity water for several applications and water/wastewater remediation in general, ion exchange may be recommended [6–8]. It is well known in the nuclear industry field [2,6,7,9,10] as, for example, in the separation of zirconium and hafnium [9] (the former is essentially transparent to free neutrons while the latter is a very strong absorber of neutrons used in reactor control rods).

The utilization of inorganic exchangers is well established due to their advantageous properties [6–8,11]. When compared with conventional resins, they present higher chemical, thermal, and radiation stabilities. Furthermore, inorganic sorbents typically exhibit high capacities and selectivities for a wide variety of monovalent and divalent metal cations [11–18].

Concerning the specific removal of radioactive cesium and strontium, many classes of inorganic materials have been proposed: zeolites [19], zeolite-like materials [2,11,20–25], titanates [26,27], zirconium phosphates [28,29], phyllosilicates [30–32] and pillared clays [33]. Among zeolite-like sorbents, microporous mixed octahedral-pentahedral-tetrahedral (OPT) materials offer great opportunities for selective ion exchangers.

Much attention was focused on two structurally-related titanosilicates: synthetic sitinakite has great affinity for Cs⁺ [20,34], while the synthetic pharmacosiderite is only

selective in very dilute solutions (ppm) at pH 7 [2,23,35]. Dyer *et al.* [36] reported the removal of traces of ¹³⁷Cs and ⁹⁰Sr by different cationic forms of synthetic pharmacosiderite. Later, germanate forms of pharmacosiderite (Ge, TiSi, TiSiGe, TiGe) were also investigated, and such modification caused drastic changes on the Cs⁺ distribution coefficient (from 0 to ~46000) [11,37]. Tripathi and co-workers [38] improved the Cs⁺ exchange using titanosilicate with pharmacosiderite topology with germanium or niobium framework substitution. The incorporation of niobium in the sitinakite structure increased significantly the Cs⁺ selectivity, particularly at high pH [39].

Titanosilicates, such as ETS-10 and ETS-4, were also studied as inorganic ion exchangers for the remediation of waters containing Cs⁺ and Sr²⁺. Pavel *et al.* [22] studied their sorption properties, while Popa *et al.* [6,40] accomplished a deep analysis of cesium and strontium uptake by ETS-10. AM-2 silicates (K₂M'Si₃O₉·2H₂O with M'=Ti, Zr) were described as good exchangers for Rb⁺, Cs⁺ and K⁺, whose selectivities are tailored by varying the Ti/Zr ratio [41].

Although the above-mentioned studies were focused essentially on titanosilicates there is much scope for new Cs⁺ ion exchangers among other transition metal, rare-earth and lanthanide (Ln) silicates. In fact, in the early years of this century, the preparation of zeolite-type rare-earth or Ln-silicates was an emerging field, though they were mainly investigated as phosphors and probes to obtain information about the structure and cations environment inside the cages [42,43].

The Ln-containing materials exhibit interesting optical properties, emitting over the entire spectral range. The associated optical transitions take place only between 4f orbitals which are well shielded from their chemical environment by 5s² and 5p⁶ electrons [44]. Therefore, atomic-like emission spectra displaying characteristic sharp lines may be observed. Since the emission spectra of a given material depend on the existence of other molecules/ions in the vicinity of the emitter lanthanide, the possibility of sensing their presence in the matrix may be explored with interest. In fact, the change of the photoluminescence spectrum of Ln-containing materials induced by ion exchange opens opportunities in this field of research. More information may be found elsewhere [45,44].

Recently, much attention was given to AV (acronym of Aveiro) materials because they combine in a single and stable solid microporosity and tuneable optical properties [46]. This makes them potential materials for applications in devices such as cathode ray tubes, projection televisions, fluorescent tubes and X-ray detectors, photonics and optical communication, and may also play an important role in the development of sensors for future use in wastewater control. A case in point is the microporous Ln-silicate AV-20,

whose structure is closely related to that of Tobermorite 11 Å [47]. The Tobermorite family of materials has already been applied as cation exchangers [48]. Until now only two papers concerning Ln-AV-20 were published, namely focusing the energy transfer and the emission decay kinetic of mixed Ln-AV-20 silicates [46,49].

The structure of Ln-AV-20 has stoichiometric amounts of the Ln³⁺ cation embedded in the framework and does not suffer any transformation upon calcination up to 800 °C [47]. In brief, the Ln-AV-20 framework consists of a series of sheets built up of alternating chains of Na⁺ and Ln³⁺ polyhedra (Figure IV.1.1.a). The layers are connected through double silicate chains of 8-membered rings forming framework channel, running along the [110] direction (Figure IV.1.1.b). The 5.8 Å by 6.8 Å channels contain Na⁺ ions, six-coordinated to three water molecules, and K⁺ ions seven-coordinated to four framework oxygen atoms and three water molecules. Both sites (particularly the Na⁺ site) may be partially occupied by water molecules. The sodium population ratio Na⁺ ions in the layer/channels is *ca.* 4 [47]. The structure of AV-20 is amenable to the incorporation of a second type of Ln³⁺ cation [46].

In this work we assessed the ion exchange capability of Eu-AV-20 to uptake Cs⁺ from aqueous solutions, in order to evaluate its potential as decontaminating agent, and future sensing ability since the presence of different cations and/or molecules inside the pores may change its emission spectra. The material was synthesised and characterized in detail, and batch experiments were performed to obtain equilibrium and removal curves. Modelling was accomplished using Langmuir isotherm and a kinetic model based on Maxwell-Stefan equations.

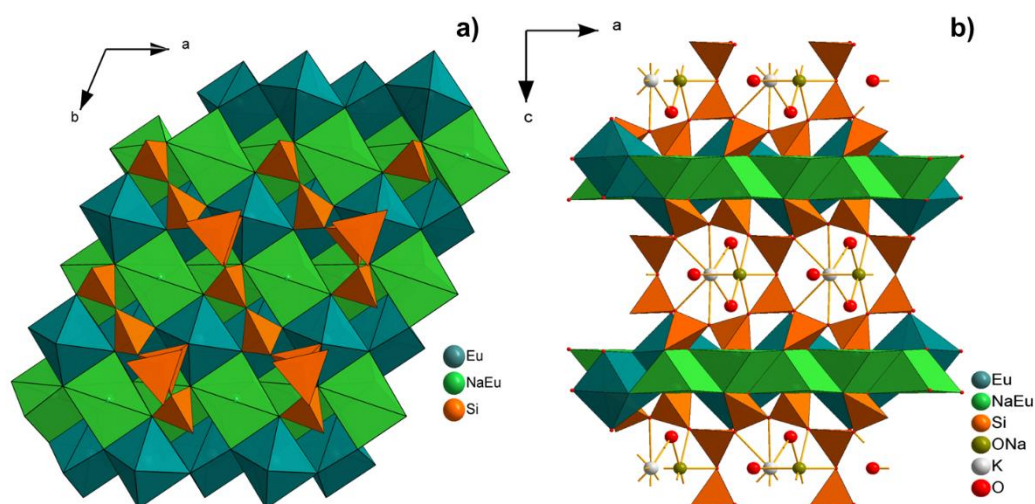


Figure IV.1.1 – a) Eu-AV-20 sheets comprising alternating chains of Na⁺ and Eu³⁺ polyhedral; b) framework channels, running along the [110] direction and housing Na⁺ and K⁺. Crystal structure drawn using Diamond software.

IV.1.2. Materials and Methods

IV.1.2.1. Chemicals and materials

Extra pure sodium silicate solution (HS code 2839 19 00), potassium hydroxide (CAS number 1310-58-3) and sodium hydroxide (CAS number 1310-73-2) were supplied from Merck. Europium(III) chloride hexahydrate (CAS number 13759-92-7) and cesium nitrate (CAS number 7789-18-6) were purchased from Sigma-Aldrich. High-purity water (18.2 MΩcm) was generated from a Milli-Q Millipore water purification system and the cellulose acetate membrane disc filters were bought from Sterlitech Corporation.

IV.1.2.2. Synthesis procedures

The synthesis of Eu-AV-20 was performed as follows [46]: An alkaline solution was prepared by mixing 5.75 g of sodium silicate solution, 16.51 g of H₂O, 3.25 g of KOH, and 1.07 g of NaOH. An amount of 1.37 g of EuCl₃ · 6H₂O was added to this solution, and the mixture was stirred thoroughly. Alternatively Eu₂O₃ (combined with HNO₃) may be utilized as Eu³⁺ source since it is much cheaper, mainly for higher scale applications. The gel, with composition 0.79 Na₂O : 1.10 K₂O : 1.0 SiO₂ : 0.07 Eu₂O₃ : 35 H₂O was autoclaved under autogenous pressure for 3 days at 230 °C. After the synthesis, the autoclave was removed and quenched in cold water. The off-white microcrystalline powder was filtered, washed at room temperature with distilled water, and dried at 100 °C. Table IV.1.1 summarizes the relevant features of this material.

Table IV.1.1 – Features of the synthesized Eu-AV-20 lanthanide silicate.

Formula	Na _{1.08} K _{0.5} Eu _{1.14} Si ₃ O _{8.5} · 1.78H ₂ O
Density, ρ_{solid} (kg m ⁻³)	3080
Cation exchange capacity, q_s (eq kg ⁻¹)	2.55
Equivalent particle diameter (10 ⁻⁶ m)	23.1
Pore diameter (10 ⁻¹⁰ m)	5.8 x 6.8

IV.1.2.3. Sorption experiments: isotherm and removal curves

Batch experiments were performed contacting under agitation the Cs⁺ solution with powdered Eu-AV-20 in volumetric flasks of 2 L, at room temperature. The initial pH was

always 4, and the stirring velocity 300 rpm. In order to evaluate the time necessary for attaining the solid-liquid equilibrium, various aliquots were withdrawn along time until the solution concentration remained constant.

The 0.01 mol L⁻¹ Cs⁺ stock solution was prepared by dissolving 0.098 g CsNO₃ in 50 mL of high-purity water (18.2 MΩcm). The remaining Cs⁺ solutions were obtained by diluting the stock solution to the desired concentration with high-purity water. They were only prepared when necessary for immediate use in order to reduce cation adsorption on the vessel walls and remaining glassware and lab material.

The experiments started when fixed masses of the exchanger were added to the Cs⁺ solutions and stirring was initiated. 10 mL aliquots were collected along time, and filtered through an acid washed cellulose acetate membrane disc filter of 0.45 µm for measuring the cesium concentration in solution by atomic emission. A blank experiment (without Eu-AV-20) was always run as a control to check that the removal of Cs⁺ occurred by ion exchange onto the solid and not by adsorption on the lab material. Besides, a complete experiment was replicated and analysed by ICP-MS in order to validate simultaneously the experimental and analytical procedure.

For assessing the influence of the Eu-AV-20 mass upon the Cs⁺ removal, 10 different masses were studied (5, 12, 16, 31, 103, 104, 105, 149, 350 and 616 mg) and the initial concentrations of the cesium solutions ranged from 0.8 to 1 ppm (Table IV.1.2). These concentrations were fixed around 0.9 ppm in order to maintain constant the ionic strength of the solutions; the masses of the solid were varied, instead. Exps. 1-7 and 9 of Table IV.1.2 were carried out to measure equilibrium data (*i.e.*, isotherm points), while the remaining three (Exps. 8, 10, 11) were used to determine removal curves (from which one equilibrium point per curve was also taken). An additional experiment (Exp. 4) was performed using regenerated Eu-AV-20 with the objective to evaluate the ion exchange performance in second cycles. The regeneration was accomplished with concentrated K⁺/Na⁺ fresh solutions.

The presence of sodium cation as competitor during the cesium uptake was evaluated with two additional experiments (Exps. 12 and 13 of Table IV.1.2). Their kinetic curves were determined for the same mass of exchanger and initial cesium concentration, but Exp.13 includes 0.001 mol L⁻¹ of sodium nitrate since beginning (a value 190 times higher than the initial Cs⁺ concentration).

The average concentration of sorbed metal at time t (s or h), $\overline{q_A}$ (mol kg⁻¹), was computed by material balance:

$$\overline{q_A} = \frac{V_{\text{liquid}}}{V_{\text{solid}} \cdot \rho_{\text{solid}}} (C_{A0} - C_A) \quad (\text{IV.1.1})$$

where C_{A0} and C_A are the initial and instantaneous concentrations of cesium in solution (mol m⁻³), respectively, V_{liq} is the solution volume (m³), $V_{\text{solid}} = m/\rho_{\text{solid}}$ is the volume of solid exchanger (m³), m is the mass of solid exchanger (kg), and ρ_{solid} is the solid's density (kg m⁻³).

Table IV.1.2 – Experimental conditions of batch ion exchange assays using Eu-AV-20. (Fixed: T=295 K ± 1; $V_{\text{liquid}} = 2 \times 10^{-3} \text{ m}^3$; pH=4).

Experiment No.	Mass of Eu-AV-20 (10 ⁻⁶ kg)	Initial Cs ⁺ conc. (eq m ⁻³)	Type of data measured *
1	5	5.906×10 ⁻³	isoth.
2	12	8.457×10 ⁻³	isoth.
3	16	6.124×10 ⁻³	isoth.
4	18	6.160×10 ⁻³	isoth.
5	31	7.855×10 ⁻³	isoth.
6	103	6.290×10 ⁻³	isoth.
7	104	6.230×10 ⁻³	isoth.
8	105	6.335×10 ⁻³	kin. & isoth.
9	149	6.252×10 ⁻³	isoth.
10	350	8.449×10 ⁻³	kin. & isoth.
11	616	5.718×10 ⁻³	kin. & isoth.
12	302	4.693×10 ⁻³ 5.275×10 ⁻³	kin. & isoth. & phot.
13	305	(Initial Na ⁺ conc. = 1 eq m ⁻³)	kin. & phot

* isoth = measurement of isotherm point; kin = determination of removal curve; phot = determination of photoluminescent spectrum

IV.1.2.4. Equipment and techniques

Crystal dimensions and morphology were determined by microscopy on a Scanning Electron Microscope (SEM) Hitachi SU-70. *The sample crystallinity and purity was*

uncertain by Powder X-Ray Diffraction (PXRD) collected at ambient temperature on a PANalytical Empyrean diffractometer (Cu K_{α1,2}X-radiation, λ₁ = 1.540598 Å; λ₂ = 1.544426 Å), equipped with an PIXcel 1D detector and a flat-plate sample holder in a Bragg-Brentano para-focusing optics configuration (45 kV, 40 mA). Intensity data were collected by the step-counting method (step 0.04°), in continuous mode, in the ca. 5 ≤ 2θ ≤ 50° range. The total cation exchange capacity (as sum of Na⁺ and K⁺) of Eu-AV-20 was determined by ICP-MS on a Jobin-Yvon JY70 Plus Spectrometer.

All cesium solution concentrations were measured with a Perkin Elmer AAnalyst 100 atomic absorption spectrometer, in the emission mode (with a wavelength of 852.1 nm and a slit of 0.2 nm) and using an air-acetylene flame. The ionization was controlled by the addition of 0.5% (wt.) of potassium chloride to samples and standards. Each sample was analysed in triplicate. Results are average of concordant values obtained for each sample (less than 5% variation between measurements of the same sample).

The photoluminescent spectra in the visible region were recorded at room temperature on a Jobin Yvon-Spex spectrometer (HR 460) fitted with a 1200 grooves mm⁻¹ grating blazed at 500 nm-coupled to a R928 Hamamatsu photomultiplier. A 150 W Xe arc lamp coupled to an excitation monochromator Jobin Yvon-Spex (TRIAX 180) fitted with a 1200 grooves mm⁻¹ grating blazed at 330 nm was used as excitation source. All spectra were corrected for the response of the detectors.

IV.1.3. Modelling

Ion exchange may be considered a conventional chemical equilibrium [50,51] represented by:



where z_A and z_B are their electrochemical valences, and the top bar denotes the exchanger phase. In this case, A = Cs⁺, B = Na⁺ and K⁺, and thus $z_A = z_B = +1$. The co-ions are the third component, S, of the system for which the valence is $z_S = -1$. Eq. (IV.1.2) implies that the ion exchanger is initially in B-form.

A model based on the Maxwell-Stefan (MS) equations to describe the batch ion exchange [52–54] was written and coded in Matlab R2012a®. This model embodies the following hypothesis: i) film and intraparticle mass transfer resistances; ii) spherical solid particles; iii) perfectly stirred tank; iv) isothermal operation; v) solution co-ions are excluded

from the exchanger particles due to Donnan exclusion; and vi) ideal solution behaviour. Because the model was previously described [52,54] in publications dealing with mercury removal from aqueous solutions using microporous titanosilicate ETS-4, only the final set of equations is compiled in Table IV.1.3. The nomenclature adopted is the following: $n = 2$ is the number of counter ions (A and B); the co-ions are the $(n + 1)^{\text{th}} = 3^{\text{rd}}$ species, being represented by S; q_A , q_B and q_S are individual concentrations (mol kg⁻¹) of counter ions A and B, and co-ions S in the solid; $q_t = q_A + q_B + q_S$ is the total concentration (mol kg⁻¹) in the solid; $y_j = q_j/q_t$ is the molar fraction of species j in the solid; $q_{A,\text{eq}}$ is the equilibrium concentration of A (mol kg⁻¹) in the solid; r is the radial position in the particle (m); t is time (s); C_A is the molar concentration of A in solution (mol m⁻³); V_{liq} and V_{solid} are the solution and solid volumes (m³); R_p is the particle radius (m); $\overline{q_A}$ is the average concentration of A in the solid; k_f is the convective mass transfer coefficient (m s⁻¹) of species A. The generalized Maxwell-Stefan equations (Eq. ((IV.1.13))) are expressed in matrix notation, where N_i is the molar flux of ionic species i (mol m⁻² s⁻¹), $\nabla\phi$ is the electrostatic potential gradient (V m⁻¹), $F = 96485.34 \text{ C mol}^{-1}$ is Faraday constant, $\mathcal{R} = 8.314472 \text{ J K}^{-1} \text{ mol}^{-1}$ is the ideal gas constant, T is absolute temperature (K), \mathcal{D}_{ij} is the MS surface diffusivity of the pair $i - j$ (m² s⁻¹), \mathcal{D}_{is} is the MS surface diffusivity for the interaction between ion i and co-ions s (m² s⁻¹), $\gamma_{i,\text{liq}}$ and x_i are the activity coefficient and the molar fraction of counter ion i in solution, respectively.

The conservation of species A, B and S is established by the material balances given by Eqs. (IV.1.3) and (IV.1.5), the electroneutrality restriction (Eq. (IV.1.6)), and cation exchange capacity (q_S). The molar fluxes of A, S and B are computed by Eqs. ((IV.1.13)-(IV.1.15), respectively. Concerning the equilibrium, only the Langmuir isotherm (Eq. (IV.1.12)), with parameters K_L and q_m , is indicated. Langmuir, Freundlich and Langmuir-Freundlich were examined in this work, though the second one did not fit reliably the equilibrium data and the last one (with one parameter more) provided equivalent results to Langmuir.

The concentration profiles of Cs⁺ and their evolution along time in solution and in the solid phase were numerically calculated using the Method of Lines (MOL) [55] with spatial discretization in the particle by Finite-Differences. The resulting ordinary differential equations (ODEs) of the initial-value type were solved applying numerical differentiation formulas (ode15s function of Matlab R2012a®) using 31 grid points. An odd number of points is required when the average loading given by Eq. ((IV.1.7)) is numerically evaluated by the 1/3 Simpson's Rule.

The MS surface diffusivities are the model parameters to fit to the experimental data. Three initial guesses were provided: D_{As} , D_{Bs} and $D_{AB} = D_{BA}$. The correlation of Armenante and Kirwan [56] (Eq. (IV.1.16)) was adopted to estimate the convective mass transfer coefficient. The size of our particles is in the range of validity of the correlation: $(6 - 420) \times 10^{-6}$ m. The Nelder-Mead algorithm was used to optimize D_{As} , D_{Bs} and D_{AB} , by minimizing the average absolute relative deviation (AARD):

$$AARD(\%) = \frac{100}{NDP} \sum_{i=1}^{NDP} \left| \frac{C_{A,calc} - C_{A,exp}}{C_{A,exp}} \right|_i \quad (IV.1.3)$$

where NDP is the number of data points, and subscripts 'exp' and 'calc' refer to experimental and calculated cesium concentrations in solution, respectively.

Table IV.1.3 – Model for batch ion exchange based on the Maxwell-Stefan equations. There are $n = 2$ counter ions (A and B), and the co-ions are the $(n + 1)^{\text{th}} = 3^{\text{rd}}$ species.

Material balance to the particle	$\rho_{\text{solid}} \frac{\partial q_A}{\partial t} = -\frac{1}{r^2} \frac{\partial}{\partial r} (r^2 N_A)$	(IV.1.4)
Material balance to the vessel	$\frac{dC_A}{dt} = -\frac{V_s \times \rho_{\text{solid}}}{V_L} \frac{d\bar{q}_A}{dt}$	(IV.1.5)
Electroneutrality	$\sum_{i=1}^{n+1} q_i z_i = 0$	(IV.1.6)
Average solid concentration	$\bar{q}_A = \frac{3}{R_p^3} \int_0^{R_p} r^2 q_A dr$	(IV.1.7)
Initial and boundary conditions	$t = 0, \begin{cases} q_A = 0 \\ C_A = C_{A0} \end{cases}$	(IV.1.8)
	$r = R_p, \quad q_A = q_{A,R_p}$	(IV.1.9)
	$r = 0, \quad \frac{\partial q_A}{\partial r} = 0$	(IV.1.10)
Equality of internal and external fluxes at particles surface	$N_A _{R_p} = k_f (C_A - C_A _{R_p})$	(IV.1.11)
Equilibrium (Langmuir isotherm; see parameters in Figure IV.1.4)	$q_{A,\text{eq}} = q_m \frac{K_L C_{A,\text{eq}}}{1 + K_L C_{A,\text{eq}}}$	(IV.1.12)
	$(N) = -q_t \rho_{\text{solid}} [B]^{-1} [\Gamma] (\nabla y) - [B]^{-1} (\nabla \zeta)$ with	
Maxwell-Stefan equations	$B_{ii} = \frac{y_s}{\bar{D}_{is}} + \sum_{\substack{j=1 \\ j \neq i}}^n \frac{y_j}{\bar{D}_{ij}}, B_{ij} = -\frac{y_i}{\bar{D}_{ij}}$ $\nabla \zeta = y_i z_i \frac{F}{RT} \nabla \phi \text{ and } \Gamma_{ij} \equiv y_i \frac{\partial \ln(y_{i,\text{liq}} x_i)}{\partial y_j}$	(IV.1.13)
Null co-ions flux (bootstrap relation)	$N_{n+1} = 0$	(IV.1.14)
Null electric current	$\sum_{i=1}^{n+1} N_i z_i = 0$	(IV.1.15)
Armenante and Kirwan correlation [56]	$Sh = 2 + 0.52 Re^{0.52} Sc^{1/3}$	(IV.1.16)

IV.1.4. Results and discussion

This section starts with the Eu-AV-20 characterization, encompassing the morphological description, powder crystallinity and total cation capacity. Two room temperature emission photoluminescent spectra of native and Cs⁺-exchanged Eu-AV-20 are presented and discussed. Next, the measured and modelled isotherms of our sorption system are analysed, and the ion exchange kinetics (removal curves) evaluated in terms of the contact time between solid and Cs⁺ solution, and the effect of the mass of Ln-silicate on the removal performance examined. The presence of competitors on the removal of cesium is studied by introducing both sodium and cesium cations in the initial solution. Modelling results achieved with MS based equations (Table IV.1.4) are also discussed in detail. The system will be hereafter denoted by Cs⁺/Na⁺,K⁺/Eu-AV-20, where the first symbols identify the counter ions in solution and solid, respectively, and the last one is the ion exchanger.

IV.1.4.1. Materials characterization

SEM showed that the habit of Eu-AV-20 consists of microcrystalline pseudo-hexagonal thin plates with a lateral dimension lower than 20×10^{-6} m (see Figure IV.1.2), which is consistent with a previous report [47]. The experimental PXRD pattern of the prepared sample (see Figure IV.1.2) is characteristic of Eu-AV-20 [47] and provides no evidence for the presence of additional impurities or significant changes in the unit cell parameters. Note that some peaks intensity differences were found between the simulated and the experimental diffractograms, which are simply due to the well-known preferential orientation of crystals during these assays. Both SEM and PXRD confirmed that the studied sample was Eu-AV-20 of good purity and crystallinity. The total cation exchange capacity of 2.55 eq kg⁻¹ was determined by ICP-MS, corresponding to the sum of 0.52 eq kg⁻¹ of Na⁺ and 2.03 eq kg⁻¹ of K⁺.

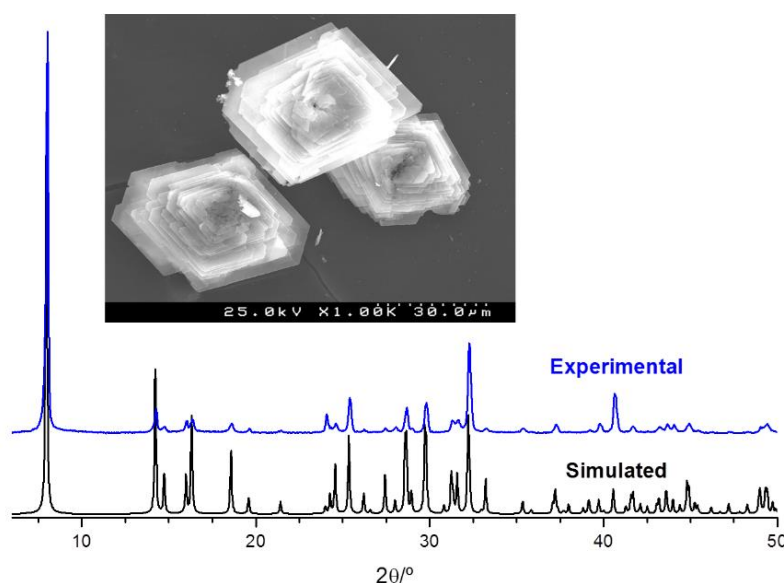


Figure IV.1.2 – Experimental and powder X-ray diffraction patterns of the synthesized EU-AV-20 used in the ion exchange assays and the simulated one in accordance with the crystal data reported by Ferreira *et al.* [47]. The inset shows a typical SEM image of the sample crystals.

IV.1.4.2. Photoluminescent spectra of native and Cs⁺-exchanged Eu-AV-20

Photoluminescent emission spectra of native (solid black line) and Cs⁺-exchanged Eu-AV-20 (Exp. 12, red dashed line) are represented in Figure IV.1.3, where the five transitions ascribable to the Eu³⁺ septet are identified: $^5D_0 \rightarrow ^7F_0$, $^5D_0 \rightarrow ^7F_1$, $^5D_0 \rightarrow ^7F_2$, $^5D_0 \rightarrow ^7F_3$ and $^5D_0 \rightarrow ^7F_4$ (Figure IV.1.3.a). Due to its relevance the transition $^5D_0 \rightarrow ^7F_0$ is detached in Figure IV.1.3.b.

Typical room temperature emission spectrum of native Eu-AV-20 was obtained since there are two distinct peaks in the transition $^5D_0 \rightarrow ^7F_0$ and the intensity of the $^5D_0 \rightarrow ^7F_2$ transition is the highest and characteristic from a low symmetric environment. The principal emission state, 5D_0 , and the fundamental state, 7F_0 , are non-degenerated and should lead to only one transition $^5D_0 \rightarrow ^7F_0$. Thus, the existence of only one place to the emitter, Eu³⁺, is indicated by the presence of one peak referent to that transition. In the Eu-AV-20 case, the appearance of two peaks revealed the presence of two distinct environments (Eu2 and Eu1) [47].

The spectrum obtained with the Cs⁺-exchanged Eu-AV-20 is overlapped in Figure IV.1.3.a, being possible to detect differences in the various transitions, mainly in the first three: $^5D_0 \rightarrow ^7F_0$ (see also Figure IV.1.3.b), $^5D_0 \rightarrow ^7F_1$ and $^5D_0 \rightarrow ^7F_2$. These observations prove

that our material emit differently depending on the vicinity of the Eu³⁺, which discloses the potential of this class of materials (AV solids) for Cs⁺ sensing purposes. These results are reported in this work for the first time. As the concentration in the solid phase influences the emission spectra, a previous and detailed study of the system Cs⁺/Na⁺,K⁺/Eu-AV-20 must be carried out, which is presented in the next sections.

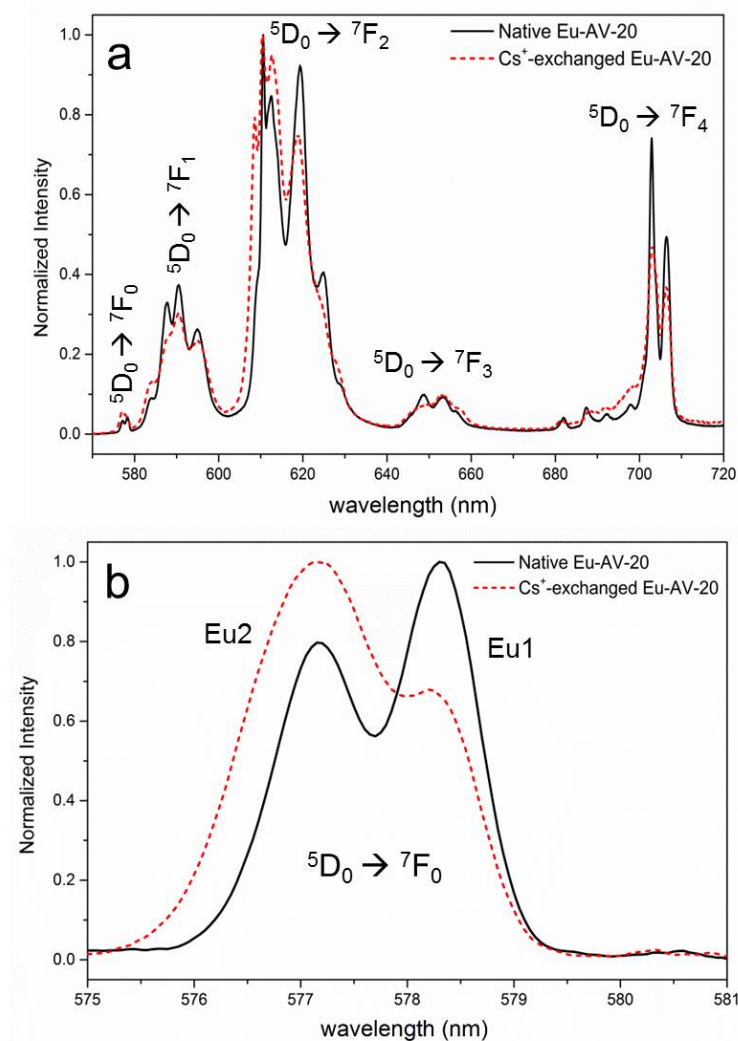


Figure IV.1.3 – (a) Photoluminescent emission spectra of native (solid black line) and Cs⁺-exchanged Eu-AV-20 (Exp. 12, red dashed line) excited at 393 nm; (b) enlargement of their $^5D_0 \rightarrow ^7F_0$ transition.

IV.1.4.3. Ion exchange isotherm

The Cs⁺/Na⁺,K⁺/Eu-AV-20 isotherm and the experimental data are shown in Figure IV.1.4. One data point (square; Exp. 4) was obtained using regenerated Eu-AV-20, being possible

to observe it exhibited an equivalent ion exchange performance. The result of Exp. 4 was very similar to that of Exp. 3 where native Eu-AV-20 was used. Though Langmuir, Freundlich and Langmuir-Freundlich models have been examined, the experimental equilibrium data were best fitted by Langmuir, with an average absolute relative deviation (AARD) of 5.3%, yielding the analytical equation superimposed on Figure IV.1.4. The Langmuir model assumes that the surface of the pores is homogeneous, finite capacity, and negligible interaction between sorbed species. Despite the first assumption, it was able to provide good results in this work, though Eu-AV-20 contains two distinct sites. This eliminated the need of the bi-Langmuir isotherm which would involve the double of the parameters without fitting advantage.

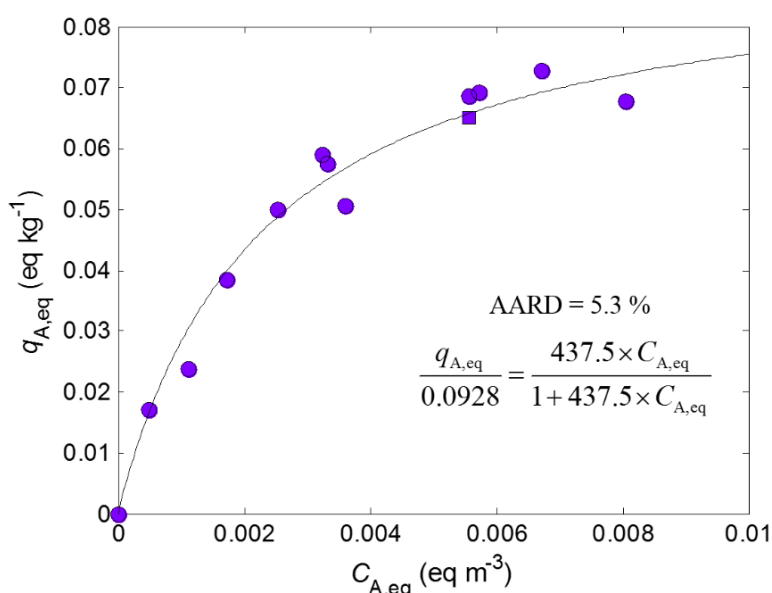


Figure IV.1.4 – Measured data and Langmuir isotherm for Cs⁺/Na⁺, K⁺/Eu-AV-20 system at 298.15 K.

IV.1.4.4. Influence of Eu-AV-20 mass upon Cs⁺ removal

The effect of the Eu-AV-20 mass upon the Cs⁺ removal was evaluated by carrying out experiments with 10 different masses of exchanger (5×10^{-6} – 660×10^{-6} kg) and solution concentrations between 5.718×10^{-3} and 8.457×10^{-3} eq m⁻³ (see Table IV.1.2). Figure IV.1.5 plots the mass of material (and associated solution concentration) *versus* final Cs⁺ removal. As expected, the Cs⁺ uptake increased with increasing mass of exchanger, jumping in our case from 2.9% to 91.4% when the Eu-AV-20 mass increased from 5 to 616

mg. In addition, Figure IV.1.5 superimposes the calculated results (see the solid line), which are in good agreement with the experimental data, and their trend. These predictions were accomplished by combining the material balance to the vessel (Eq. (IV.1.1)) with the isotherm of the system (Eq. (IV.1.11)), giving rise to the following second-order polynomial in the final (equilibrium) concentration, $C_{A,eq}$:

$$C_{A,eq}^2 + \left(\frac{V_{solid}}{V_{liq}} \cdot q_{max} + \frac{1}{K_L} - C_{A0} \right) \cdot C_{A,eq} - \frac{C_{A0}}{K_L} = 0 \quad (IV.1.17)$$

The root of interest is the positive one, from which the desired final uptake can be computed after substitution into Eq. (IV.1.5). The necessary constants may be found in Tables IV.1.1 and IV.1.2, and the Langmuir parameters shown in Figure IV.1.4.

$$\text{Final Uptake (\%)} = 100 \times \left(1 - \frac{C_{A,eq}}{C_{A0}} \right) \quad (IV.1.18)$$

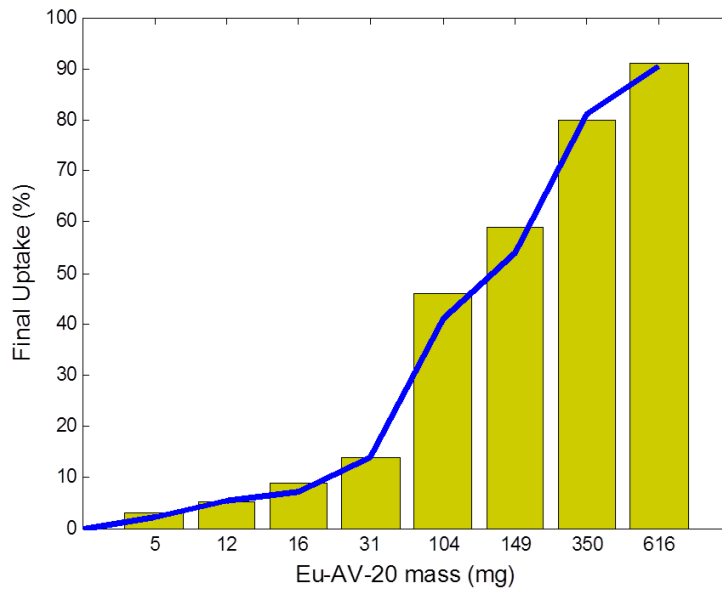


Figure IV.1.5 – Influence of Eu-AV-20 mass on the final uptake of Cs⁺. Bars, data (experimental conditions in Table IV.1.2); line, calculated results.

IV.1.4.5. Ion exchange kinetics

The kinetics of cesium ion removal was evaluated carrying out assays with well-known solution concentrations around 1 ppm and three different masses (105, 350 and 616 mg) of

Eu-AV-20 (see conditions in Table IV.1.2), which correspond to ratios of $C_{A0}/(V_{\text{solid}} \cdot \rho_{\text{solid}})$ equal to 60.3, 24.1 and $9.28 \text{ eq m}^{-3} \text{ kg}^{-1}$. The experimental data measured are shown in Figure IV.1.6, where the evolution of the normalized cesium concentration in solution along time (C_A/C_{A0} vs. t) are plotted. The results point out that the amounts of solid exchanger removed 47.6%, 79.6% and 91.4% of Cs^+ from solution, and attained solid loadings of 0.057, 0.036 and 0.017 eq kg^{-1} , respectively.

The kinetics of ion exchange (Figure IV.1.6) is characterized by a sharp slope in the first hours, followed by a transition zone and then a plateau. For the three cases, the uptake process is complete after approximately 80 hours, and the largest C_A variations occur in the first 10 hours. These observations are consistent with the small diffusivities found (see next section) in agreement with other publications dealing with microporous materials like Analcite, Chabazite, semi-crystalline Zeolite-NaA, titanosilicate ETS-4, and beryllophosphate-G [12–14,57–60].

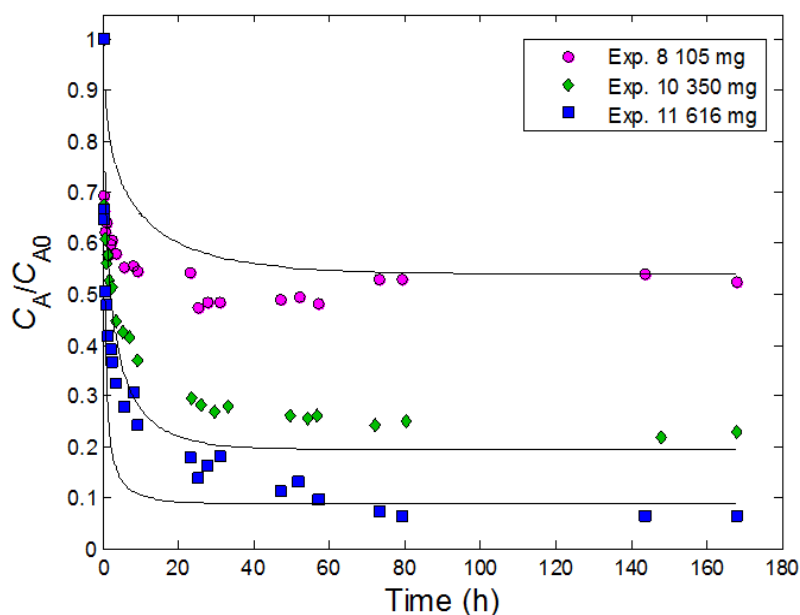


Figure IV.1.6 – Experimental data of normalized Cs^+ concentration in the solution. Purple Circles, green diamonds and blue squares are Exps. 8, 10 and 11, respectively (experimental conditions in Table IV.1.2); lines are modelling results.

It should be noted that Eu-AV-20 has only two possible diffusion directions which penalizes intraparticle mass transport. In fact, the direction $[001]$ is forbidden to diffusion due to the framework layer of $\text{Eu}^{3+}/\text{Na}^+$ polyhedra (see Figure IV.1.1.a). Furthermore, the diameters of the Cs^+ ion and Eu-AV-20 pores, 1.7 \AA and $5.8 \times 6.8 \text{ \AA}$, respectively, impose

an additional restriction to cation exchange, because they probably imply a surface ionic diffusion mechanism, for which the activation energy is an important process parameter.

As mentioned in the Introduction, the radioactive wastes contain several competing cations in solution that may interfere with the removal of Cs⁺. In general the selectivity depends upon pH and on the relative abundances of alkali and alkaline earth metals cations in solution. For instance, Bortun *et al.* [20] reported that the selectivity of the proton form of crystalline silicotitanate decreases significantly for low concentrations of Cs⁺ in the presence of sodium content of nuclear waste solutions, *i.e.* 5-6 M NaNO₃, 1-3 M NaOH. Clearfield *et al.* [61] found that a niobium phase of this material (Nb replaces Ti) performs better in Cs⁺ uptake from a strong base and high Na⁺ concentrations.

In this essay, a preliminary study to evaluate the competition between Cs⁺ and Na⁺ cations in the initial solution was also carried out (Exps. 12 and 13; Table IV.1.2). A sodium nitrate concentration of 1 eq m⁻³ was added to the Cs⁺ solution (Exp. 13) and its removal curve was measured and compared with an experiment performed in the same conditions but in the absence of competitor (Exp. 12) – see Figure IV.1.9. The cesium uptake is similar in both cases (80% in Exp. 13 *versus* 85% in Exp. 12), which emphasizes the selectivity of Eu-AV-20 towards Cs⁺ mainly if one takes into account that the initial concentration of Na⁺ was 190 times higher than Cs⁺ (*i.e.*, two orders of magnitude). It is worth noting that the equilibrium selectivity of the solid to Cs⁺ increased *ca.* 210 times when passing from a solution initially free of Na⁺ (Exp. 12) to the solution of Exp. 13 (with 1 eq m⁻³ of Na⁺ at the beginning).

In terms of trend, the ion exchange kinetics of Exp. 13 is slower than Exp. 12 due to the ion concentration of competing Na⁺ in solution. In fact, the equilibrium in Exp. 13 is attained in approximately 80 hours while in Exp. 12 *ca.* 30 hours are sufficient.

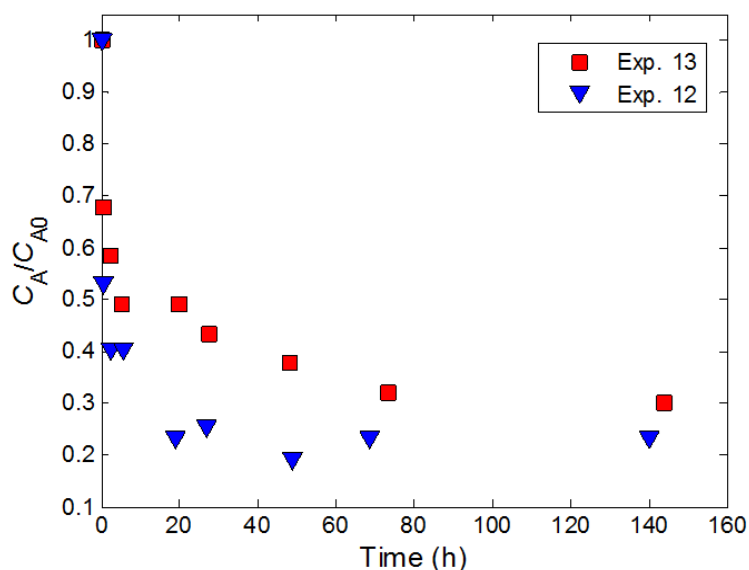


Figure IV.1.7 – Experimental data of normalized Cs⁺ concentration in the solution. Blue triangles and red squares are Exps. 12 and 13, respectively (exp. conditions in Table IV.1.2).

IV.1.4.6. Ion exchange modelling based on Maxwell-Stefan equations

The results obtained with the Maxwell-Stefan based model are plotted in Figure IV.1.6 together with the data measured for the three kinetic experiments (Exp. 8, 10, 11). The model fits simultaneously the three curves with AARD = 19.0%, highlighting the typical difficulty of representing the kinetic curves in the transition from the steep descent branch to the horizontal plateau [13,16,62]. In this work the mass transfer coefficient was not fitted to data, but estimated by the correlation of Armenante and Kirwan in order to reduce the number of parameters, which also contributed to increase the calculated deviation. The optimized diffusivities and estimated k_f are listed in Table IV.1.4.

Table IV.1.4 – Optimized parameters and AARD (%) of the Maxwell-Stefan based model.

D_{As} (m ² s ⁻¹)	D_{Bs} (m ² s ⁻¹)	D_{AB} (m ² s ⁻¹)	k_f (m s ⁻¹)	AARD (%)
2.706x10 ⁻¹⁵	5.713x10 ⁻¹⁵	9.446x10 ⁻¹⁷	2.327x10 ⁻⁴	19.0

Concerning the convective mass transfer coefficient, the Armenante and Kirwan correlation estimated $k_f = 2.327 \times 10^{-4} \text{ m s}^{-1}$. The Eu-AV-20 particles possess higher equivalent diameters in comparison to materials studied elsewhere, such as ETS-4 [17] and ETS-10 [16], respectively. The corresponding sizes are 23.1×10^{-6} , 0.7×10^{-6} and $5.0 \times 10^{-6} \text{ m}$, justifying mass transfer coefficients of 2.327×10^{-4} , 1.281×10^{-3} and $1.930 \times 10^{-4} \text{ m s}^{-1}$, taking into account the diffusivities of the counter ions involved in the process (Cs⁺, $2.06 \times 10^{-9} \text{ m}^2 \text{ s}^{-1}$ [63], and Cd²⁺ in the other two cases, $7.19 \times 10^{-10} \text{ m}^2 \text{ s}^{-1}$ [64]).

The adjusted diffusivities D_{As} , D_{Bs} and D_{AB} were 2.706×10^{-15} , 5.713×10^{-15} and $9.446 \times 10^{-17} \text{ m}^2 \text{ s}^{-1}$ (see Table IV.1.4), respectively, consistent with the small pore diameters of Eu-AV-20. Values of similar magnitude were reported for other materials [13,16,17,57,58,60]. The diffusivities of the pairs Cs⁺/co-ions of Eu-AV-20 and Na⁺,K⁺/co-ions of Eu-AV-20 differ by ca. 2.1 times, indicating distinct interactions between each cation and the Ln-silicate. The value of D_{As} is the lowest, which is in accordance with the ionic radius: 0.170 nm for Cs⁺, 0.102 nm for Na⁺ and 0.138 nm for K⁺. Taking into account these radius and that all ions possess the same valence (+1) it is expected that Cs⁺ diffuses slower through the microporous framework of Eu-AV-20 (pores between 5.8 and 6.8 Å).

The calculated Cs⁺ concentration in Eu-AV-20 at distinct removal times, plotted in Figure IV.1.8, (red and blue identify the highest and lowest concentrations) witnesses the propagation of the concentration wave from the surface to the centre of the exchanger particle. In the experiment using 105 mg (*i.e.* the lowest mass), the final solid loading is the highest and the uniform distribution inside the exchanger is achieved later, relatively to the other essays.

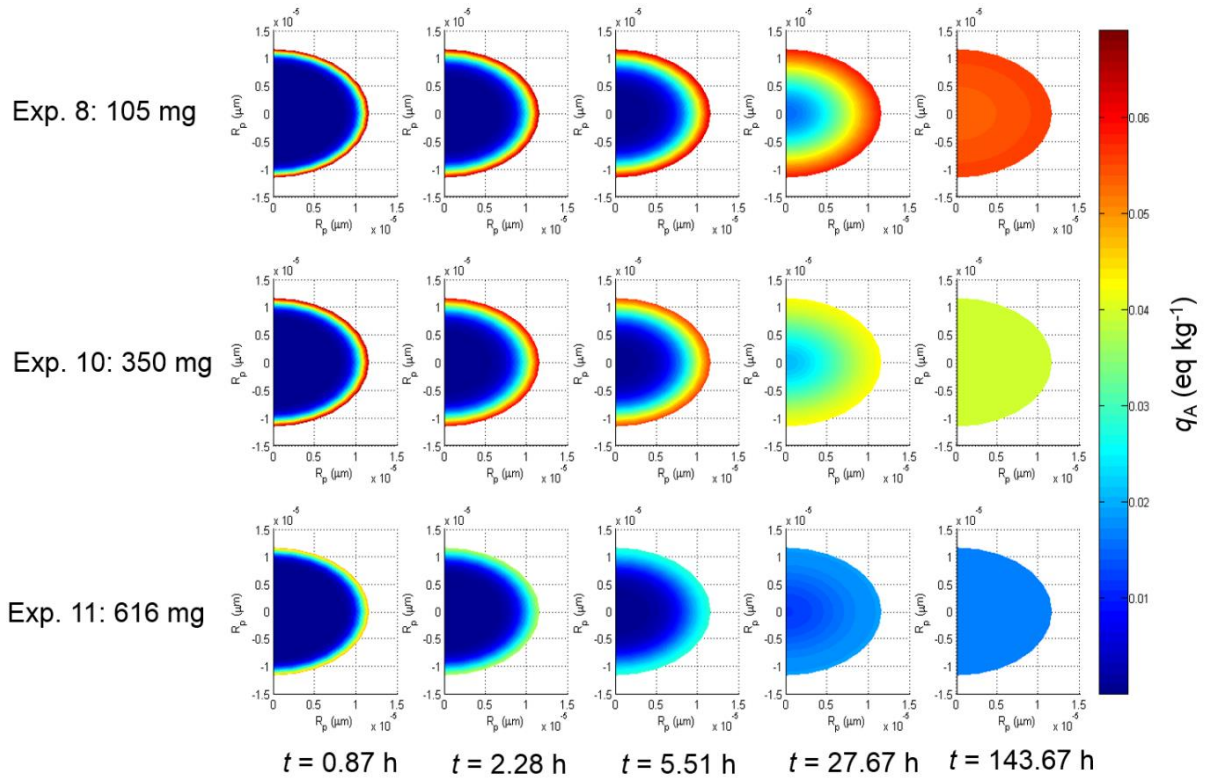


Figure IV.1.8 – Calculated Cs^+ concentration inside Eu-AV-20 particles at distinct removal times. See experimental conditions in Table IV.1.2.

It is interesting to note in Figure IV.1.8 that the surface concentration for $t = 0.87$ h of Exps.. 10 and 11 are higher than the surface concentrations calculated near equilibrium ($t \geq 27.67$ h). This apparently abnormal behaviour may be explained by analysing the evolution of the particle concentration for $r = 0, \frac{1}{2}R_p, \frac{3}{4}R_p$ and R_p , which is shown, without loss of generality, in Figure IV.1.9 for the case of Exp. 11. The initial jump of $q_{A,R_p}(t)/q_{A,\text{eq}}$ is very pronounced and passes through a maximum (much larger than 1.0) and then decreases gradually until equilibrium. In the absence of film resistance, the initial particle concentration at the surface would suddenly increase from 0.0 to $q_{A,\text{eq}}(C_{A0})$, which is the solid concentration in equilibrium with the bulk solution. Then, $q_{A,R_p}(t)$ would decrease monotonously until the final equilibrium, *i.e.* $q_{A,R_p}(t) \rightarrow q_{A,\text{eq}} = q_{A,R_p}(t = \infty)$. Nonetheless, the introduction of mass transfer limitations in the film smoothens this initial step increase, as Figure IV.1.9 shows. In contrast, far from the surface the concentration increases monotonously, as the three curves for $r = 0, \frac{1}{2}R_p$, and $\frac{3}{4}R_p$ point out. These curves vary between the same boundary values (beginning at 0.0 and tending to 1.0), but

$q_{A,0}(t)/q_{A,eq} < q_{A,R_p/2}(t)/q_{A,eq} < q_{A,\frac{3}{4}R_p}(t)/q_{A,eq}$ because the diffusion path increases in the same order, delaying the concentration increase.

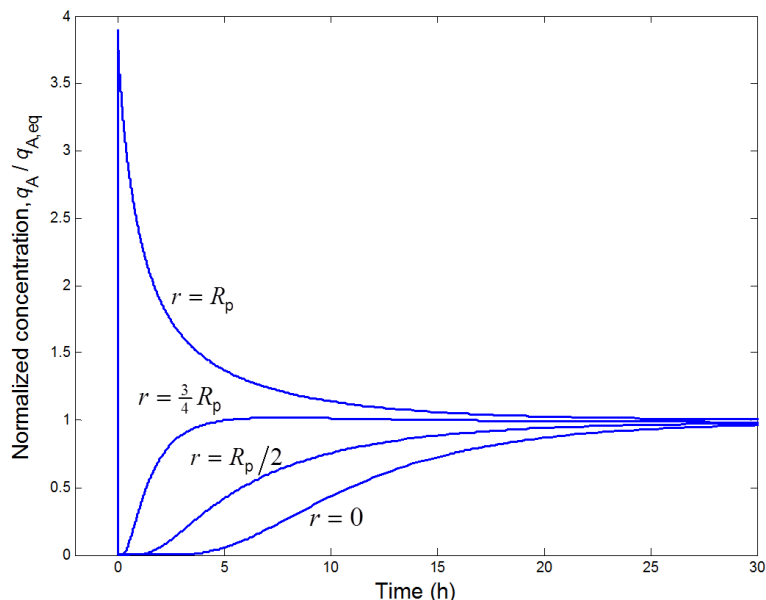


Figure IV.1.9 – Normalized Cs⁺ concentration in the Eu-AV-20 particle for $r = 0, \frac{1}{2}R_p, \frac{3}{4}R_p$ and R_p . Calculations accomplished with MS based model for Exp. 11.

To assess the performance of the proposed model, the calculated *versus* experimental normalized Cs⁺ concentration in solution curves were plotted in Figure IV.1.10. The points are distributed near the diagonal, though the model overestimates Exp. 8 and essentially underestimates Exps. 10 and 11. The results are consistent with the literature [16,62,17].

A variance analysis (ANOVA) proved that the MS based model accounts for the variability in the experimental data. The calculated ratio between the mean squares due to model and residuals was 86.3, which is clearly higher than the tabulated F for 95% with 2 and 65 degrees of freedom (3.138); here, 2 is the number of parameters minus 1, and 65 is the number of data points decreased by the number of fitted parameters. Therefore, the model is statistically significant to represent the experimental ion exchange uptake curves.

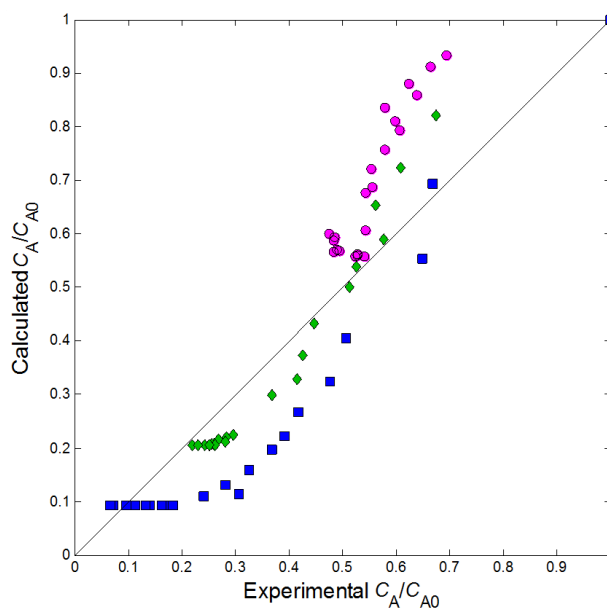


Figure IV.1.10 – Calculated *versus* experimental normalized Cs⁺ concentration in solution. Experimental conditions (see Table IV.1.2): Same as Figure IV.1.6.

IV.1.5. Conclusions

In this work, the cesium ion exchange capacity of Eu-AV-20 was studied by performing equilibrium and kinetic batch experiments. The cation exchange capacity measured by ICP-MS was 2.55 eq. kg⁻¹, corresponding to the sum of 0.52 eq kg⁻¹ of Na⁺ and 2.03 eq kg⁻¹ of K⁺.

The isotherm of the Cs⁺/Na⁺,K⁺/Eu-AV-20 system was determined carrying out eleven experiments. The Langmuir equation provided good results, namely an average absolute relative deviation (AARD) of only 5.3%. Concerning the kinetic experiments, three batch assays were performed to study the influence of Eu-AV-20 mass upon the removal efficiency. The uptake curves exhibited the usual trend of a steep descent branch, followed by a transition zone and a horizontal region. The sharp variation of the Cs⁺ concentration in solution lied between 0 and 10 h, and the final equilibrium was reached after ca. 80 h. This slow process is in accord with reports for other zeolite-type systems, and is ascribed to the presence of small pores imposing a surface diffusion mechanism for the mass transport. Additionally, two batch assays were carried out to study the effect of competing Na⁺ in the initial Cs⁺ solution upon ion exchange. The results proved that Eu-AV-20 is highly selective to Cs⁺, since similar removals were achieved for an initial Na⁺ concentration 190 times higher than that of cesium. However, the existence of Na⁺ slowed the Cs⁺ sorption along time.

Furthermore, it was observed for the first time in this work that the cesium uptake modified the photoluminescent spectrum of Eu-AV-20 as a consequence of changing the vicinity of the Eu³⁺ emitter, which may be explored in the future for Cs⁺ sensing purposes. This relevant property of Eu-AV-20 emphasizes its potential application independently of its absolute ion exchange capacity.

The kinetic curves were modelled using the Maxwell-Stefan equations, which yielded the diffusion coefficients $\mathcal{D}_{As} = 2.706 \times 10^{-15}$, $\mathcal{D}_{Bs} = 5.713 \times 10^{-15}$ and $\mathcal{D}_{AB} = 9.446 \times 10^{-17} \text{ m}^2 \text{ s}^{-1}$. The calculated error was 19.0%, and the orders of magnitude of the adjusted diffusivities were consistent with those found for other microporous materials like titanosilicates ETS-4 and ETS-10. The small Maxwell-Stefan diffusivities confirm the surface mechanism of mass transfer inside the Eu-AV-20 particles. An analysis of variance confirmed that the model is able to take the variability of the experimental data into account, *i.e.*, the model is statistically significant to represent the experimental data of the ion exchange uptake curves.

IV.1.6. Nomenclature

A	External particle surface area (m)
AV-20	Aveiro material number 20
AARD	Average absolute relative deviation (%)
$[B]$	Matrix with MS diffusivities
C	Concentration in bulk solution (mol m ⁻³)
\mathcal{D}_{AB}	MS surface diffusivity of pair A-B (m ² s ⁻¹)
\mathcal{D}_{As}	MS surface diffusivity of pair A-fixed ionic charges (m ² s ⁻¹)
\mathcal{D}_{Bs}	MS surface diffusivity of pair B-fixed ionic charges (m ² s ⁻¹)
F	Faraday constant (C mol ⁻¹)
ICP-MS	Inductively coupled plasma mass spectrometry
k_f	Film mass transfer coefficient (m s ⁻¹)
K_L	Langmuir parameter
Ln-silicate	Lanthanide silicate
MS	Maxwell-Stefan
n	Number of diffusing species
NDP	Number of data points

N_j	Molar flux of the counter ion j (mol m ⁻² s ⁻¹)
PLS	Photoluminescence Spectroscopy
PXRD	Powder X-ray diffraction
q	Molar concentration of ionic species in the particle (mol kg ⁻¹)
q_{\max}	Langmuir parameter (mol kg ⁻¹)
q_S	Ion exchanger molar capacity (mol kg ⁻¹)
q_t	Total concentration of ionic species in the particle (mol kg ⁻¹)
\bar{q}	Average concentration of ionic specie in the particle (mol kg ⁻¹)
r	Radial position in the particle (m)
\Re	Gas constant (J mol ⁻¹ K ⁻¹)
R_p	Particle radius (m)
SEM	Scanning Electron Microscopy
t	Time (h or s)
T	Absolute temperature (K)
V_{liq}	Volume of fluid phase (m ³)
V_{solid}	Volume of solid phase (m ³)
x_i	Molar fraction of i in bulk solution
y_j	Molar fraction of counter ion j in the particle
z_i	Charge of component i

Greek letters

$\gamma_{i,\text{liq}}$	Activity coefficient of counter ion i in a solution in equilibrium with particle
ϕ	Electrostatic potential (V)
$[\Gamma]$	Thermodynamic factors matrix
ξ	Related with the electrostatic potential gradient
ρ_{solid}	Density of ion exchanger

Subscripts

A	Counter ion initially present in the bulk solution (Cs^+)
B	Counter ions initially present in the solid particle (Na^+ and K^+)
calc	Calculated
eq	Equilibrium
exp	Experimental
s	Fixed charged groups of the particle

Work reported in the scientific article

Tb/Eu-AV-9: A lanthanide silicate for the sensing and removal of cesium ions from aqueous solutions

published on Chemical Engineering Journal 286 (2016) 679–688

Abstract

The ion exchange of Cs⁺ from aqueous solutions was studied using a novel microporous lanthanide silicate with photoluminescence properties, Tb/Eu-AV-9. This mixed lanthanide silicate was prepared by hydrothermal synthesis, characterized by scanning electron microscopy, powder X-ray diffraction, and photoluminescence spectroscopy.

Batch ion exchange experiments were performed at room temperature (295 K) to measure isotherm and removal curves. The Langmuir-Freundlich equation provided a good fit to the equilibrium data. A kinetic model based on the Maxwell-Stefan equations was implemented and adjusted to the cesium removal curves, and achieved average deviation of 8.37%. The model parameters were the diffusion coefficients, while the convective mass transfer coefficient was purely estimated. The Maxwell-Stefan diffusivities for the interaction of the counter ions Cs⁺ and K⁺ with the solid exchanger were $D_{As} = 8.373 \times 10^{-15} \text{ m}^2 \text{ s}^{-1}$ and $D_{Bs} = 2.795 \times 10^{-14} \text{ m}^2 \text{ s}^{-1}$, respectively, being consistent with other values in the literature.

With respect to photoluminescence studies, the differences found between the emission spectra of native and Cs⁺-exchanged Tb/Eu-AV-9 disclosed the potential of this sorbent for qualitative/quantitative Cs⁺ sensing purposes.

IV.2. Tb/Eu-AV-9: A lanthanide silicate for the sensing and removal of cesium ions from aqueous solutions

IV.2.1. Introduction

Cesium-137 is a by-product of the nuclear energy production and a slow-decaying element, taking 30 years to lose half of its radioactivity. Recent events have drawn the attention to environmental contamination by cesium. In fact, it has been reported that the tsunami induced Fukushima Daiichi nuclear disaster released large amounts of cesium into the atmosphere and water (Pacific sea) [3]. Furthermore, severe soil and groundwater contamination with several radionuclides (including cesium) has been reported at the Hanford Site due to the corrosion of underground storage tanks [1,2]. Currently, the main concerns with cesium are related to its secure management, and the reduction of its waste volume and processing cost is imperative.

Nevertheless, growing water demand and declining supplies increase the need for rapid and efficient water purification processes. Among the various separation alternatives, ion exchange appears as the most suitable for high purity water production mostly because it is simple to implement and levels of contamination below ppb (parts *per* billion) are easily attained [65,11]. Concerning the ion exchangers, inorganic type materials are well established especially due to their high chemical, thermal, mechanical and radiation stabilities [11,6–8]. Moreover, these materials possess high capacities and selectivities for a wide range of mono- and divalent metal cations, thus being more attractive than the conventional ion exchange resins [17,3,65,6,7,14,15,66–68].

Zeolite-type rare-earth or lanthanide-silicate (Ln-silicates) materials exhibit interesting optical properties associated to transitions between 4f orbitals, which are well shielded from their chemical environment, and thus atomic-like emission spectra displaying characteristic sharp lines are obtained [44,69]. Taking into account that the presence of other ions or molecules near an emitter lanthanide may affect its optical behaviour, the possibility of sensing their presence in the matrix may be accomplished by photoluminescence spectroscopy. Initially, Ln³⁺ ions in zeotype silicates were mainly investigated as probes for the structure and location of extra-framework cations within the material's voids [44,42,43]. The comprehensive study of the photoluminescence spectra of ion-exchanged Ln-silicates deserves much more attention [44,45,70].

The use of Ln-containing materials for the removal of metal cations from aqueous solutions is an emerging field. In particular, AV (acronym for Aveiro) materials, which

combine microporosity and tuneable optical properties in a single and stable solid [46], were tested for the first time by Figueiredo *et al.* [70]. Auspicious results obtained for Cs⁺ removal from water with Eu-AV-20 in batch-ion exchange tests (equilibrium and removal curves) prompted the assessment of other AV materials, such as AV-9.

AV-9 belongs to a group of microporous Eu(III) and Tb(III) silicates ($\text{Na}_4\text{K}_2\text{Ln}_2\text{Si}_{16}\text{O}_{38}\cdot x\text{H}_2\text{O}$, Ln = Eu, Tb) analogues of mineral montregianite [71]. Their structure consists of two different types of layers alternating along the [1 0 0] direction (Figure IV.2.1) namely: i) a double silicate sheet, where the single silicate sheet is of the apophyllite type with four- and eight-membered rings (Figure IV.2.1.a), and ii) an open octahedral sheet, composed of two non-equivalent $\{\text{LnO}_6\}$ octahedra and two distinct $\{\text{NaO}_4(\text{H}_2\text{O})_2\}$ octahedra (Figure IV.2.1.b). Coordinated potassium cations and water molecules are located within the large channels formed by the planar eight-membered silicate rings. Like AV-20, the framework of AV-9 is amenable to the incorporation of a second type of Ln³⁺ cation.

The present work describes the use of the mixed Ln-silicate Tb/Eu-AV-9 for the removal of Cs⁺ from solution. The main objective is to study its efficiency as a decontaminating agent and sensor. The material was synthesized and fully characterized, ion exchange batch experiments were performed to measure equilibrium and removal curves, and photoluminescence spectroscopy was used to assess its potential as a cesium sensor. Modelling was accomplished using the Langmuir-Freundlich isotherm and a kinetic model based on the Maxwell-Stefan equations.

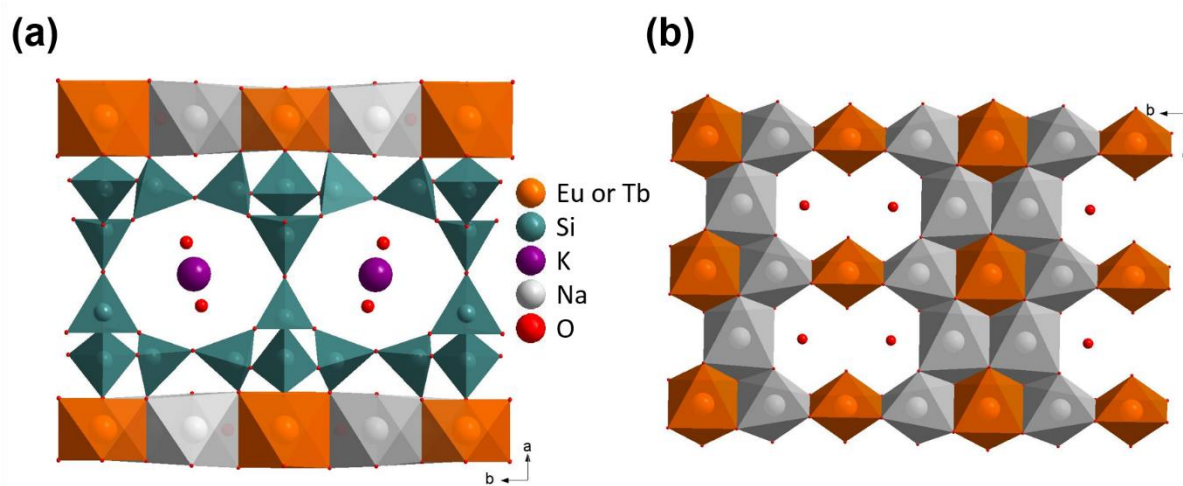


Figure IV.2.1 – Structure of Ln-AV-9 materials: a) alternating octahedral sheet and double-silicate layer where the single silicate sheet is of the apophyllite type with four- and eight-membered rings; b) an open octahedral sheet, composed of two non-equivalent $\{\text{LnO}_6\}$ octahedra and two distinct $\{\text{NaO}_4(\text{H}_2\text{O})_2\}$ octahedra in the bc plane.

IV.2.2. Materials and Methods

IV.2.2.1. Chemicals and materials

Sodium silicate solution (HS code 2839 19 00), potassium chloride (CAS number 7447-40-7) and sodium chloride (CAS number 7647-14-5) were supplied by Merck. Potassium hydroxide (CAS number 1310-58-3) was provided by VWR Prolabo. Cesium nitrate (CAS number 7789-18-6), europium(III) nitrate (CAS number 63026-01-7) and terbium(III) nitrate (CAS number 57584-27-7) were purchased from Sigma-Aldrich. High-purity water (18.2 MΩcm) was generated using a Milli-Q Millipore water purification system. Cellulose acetate membrane disc filters (0.45 μm) were bought from Sterlitech Corporation.

IV.2.2.2. Synthesis procedures

In a typical synthesis, an alkaline solution was prepared by sequentially mixing 11.89 g of a sodium silicate solution (27% SiO₂ and 8.5% Na₂O), 63.42 g of water, 1.48 g of KOH, 1.76 g of NaCl and 0.49 g of KCl, followed by dropwise addition of 2.54 mL Eu(NO₃)₃ solution (0.4 mol L⁻¹) and 10.16 mL Tb(NO₃)₃ solution (0.4 mol L⁻¹). The resultant gel, with composition 0.57Na₂O:0.37K₂O:1.0SiO₂:0.05Eu₂O₃:76H₂O, was left to react in Teflon lined autoclaves (volume 160 mL) at 503 K for 6 days. The autoclave was removed from the

oven, and quenched in cold water after an appropriate time. At the end of the synthesis the supernatant solution pH was ca. 11.1. The off-white microcrystalline powder was filtered, washed at room temperature with distilled water, and dried at 373 K overnight. Table IV.2.1 summarizes the important features of the prepared material.

Table IV.2.1 – Features of the synthesized Tb/Eu-AV-9 lanthanide silicate

Formula	Na ₄ K ₂ Eu _{0.4} Tb _{1.6} Si ₁₆ O ₃₈ ·xH ₂ O
Density (kg m ⁻³)	2542
Equivalent particle diameter (10 ⁻⁶ m)	12
Pore sizes (10 ⁻¹⁰ m)	3.3 x 4.3 in [0 0 1] direction 3.4 x 3.8 in [0 1 0] direction

IV.2.2.3. Characterization of the Tb/Eu-AV-9 material

Powder X-Ray Diffraction (PXRD) data were collected at room temperature on a PANalytical Empyrean diffractometer (Cu K_{α1,2}X-radiation, λ₁ = 1.540598 Å; λ₂ = 1.544426 Å), equipped with an PIXcel 1D detector and a flat-plate sample holder in a Bragg-Brentano para-focusing optics configuration (45 kV, 40 mA). Intensity data were collected by the step-counting method (step 0.04°), in continuous mode, in the ca. 5 ≤ 2θ ≤ 50° range. Crystallographic structure refinement was used to obtain the chemical formula, density and pore sizes (see Table IV.2.1).

Scanning Electron Microscopy (SEM) images were obtained in a Hitachi SU-70 microscope to assess crystal dimensions (equivalent particle diameter) and morphology.

The visible photoluminescence spectra were recorded at room temperature on a Jobin Yvon-Spex spectrometer (HR 460) fitted with a 1200 grooves mm⁻¹ grating blazed at 500 nm, coupled to a R928 Hamamatsu photomultiplier. A 150 W Xenon arc lamp coupled to an excitation monochromator Jobin Yvon-Spex (TRIAx 180) fitted with a 1200 grooves mm⁻¹ grating blazed at 330 nm was used as excitation source. All spectra were corrected for the response of the detectors. All samples were oven-dried at 353.15 K, during 48 hours.

IV.2.2.4. Sorption experiments: isotherm and removal curves

A Cs⁺ stock solution (0.01 mol L⁻¹) was prepared by dissolving 0.098 g CsNO₃ in 50 mL of high-purity water (18.2 MΩcm). Working solutions were prepared by diluting the stock solution to the desired concentration, in high-purity water, immediately before use to avoid cation adsorption on the vessel walls and on the remaining glassware lab material.

The batch experiments were performed by contacting Cs⁺ solutions (fixed at ca. 0.248 mol m⁻³, *i.e.* 33 ppm, to maintain the ionic strength constant) with powdered Tb/Eu-AV-9 (15 to 509 mg), in 2 L volumetric flasks, under constant stirring (300 rpm) at room temperature and initial pH equal to 4. Aliquots (10 mL) were withdrawn along time, filtered through an acid washed cellulose acetate membrane (0.45 µm), and analysed by atomic absorption spectrometry to evaluate the concentration of cesium in solution. Aliquots were collected and analysed until the solution concentration remained constant, *i.e.* until the system reached solid-liquid equilibrium. Seven experiments (Exps. 1-4, 6, 8 and 9 of Table IV.2.2) were carried out to measure only equilibrium data (*i.e.*, isotherm points) and three experiments (Exps. 5, 7 and 10 of Table IV.2.2) were used to determine removal curves (from which one equilibrium point per curve was also taken at the end). A blank experiment (without Tb/Eu-AV-9) was always run to confirm that the removal of Cs⁺ occurred by ion exchange and not by adsorption onto the lab material.

The cesium concentration in solution was analysed in a Perkin Elmer AAnalyst 100 atomic absorption spectrometer, in the emission mode (with a wavelength of 852.1 nm and a slit of 0.2 nm) and using an air-acetylene flame. The ionization was controlled by the addition of 0.5 wt.% of potassium chloride to the samples and standards. Each sample was analysed in triplicate and the concordant values were averaged (less than 5% variation between measurements of the same sample).

The average concentration of cesium adsorbed at time t (s or h), \bar{q}_A (mol kg⁻¹), was computed by material balance to the vessel:

$$\bar{q}_A = \frac{V_L}{V_s \cdot \rho_s} (C_{A,0} - C_A) \quad (\text{IV.2.1})$$

where $C_{A,0}$ and C_A are the initial and instantaneous concentrations of cesium in solution (mol m⁻³), respectively, V_L is the solution volume (m³), ρ_s is the ion exchanger density (kg m⁻³), $V_s = m_s/\rho_s$ is its volume (m³) and m_s its mass (kg).

Table IV.2.2 – Experimental conditions of batch ion exchange tests using Tb/Eu-AV-9. (Fixed conditions: $T = 295 \text{ K} \pm 1 \text{ K}$; $V_L = 2 \times 10^{-3} \text{ m}^3$; pH 4).

Exp.	Mass of solid (m_s , 10^{-6} kg)	Initial Cs ⁺ conc. ($C_{A,0}$, mol m^{-3})	$m_s / C_{A,0}$ ($10^{-4} \text{ kg mol}^{-1} \text{m}^3$)	Type of data measured *
1	15	0.243	0.62	iso.
2	32	0.244	1.31	iso.
3	61	0.249	2.45	iso.
4	125	0.235	5.32	iso.
5	178	0.237	7.51	kin. & iso. & phot.
6	243	0.254	9.57	iso.
7	310	0.259	11.97	kin. & iso. & phot.
8	361	0.257	14.05	iso.
9	479	0.260	18.42	iso.
10	509	0.236	21.58	kin. & iso. & phot.

*iso. = isotherm data point; kin. = kinetic curve; phot. = photoluminescence spectrum

IV.2.3. Modelling

Ion exchange is conventionally represented as a chemical reaction, because it is a stoichiometric process by which two counter ions, A^{z_A} and B^{z_B} , are exchanged between an electrolyte solution and a solid exchanger:



In this equation z_A and z_B are the electrochemical valences, the capping bar denotes the solid phase, and the exchanger initially in B^{z_B} form is converted into A^{z_A} form. In the particular case of our study, $A^{z_A} = \text{Cs}^+$, $B^{z_B} = \text{K}^+$, and thus $z_A = z_B = +1$. The co-ions are the third component, S, of the system for which the valence is $z_S = -1$. For simplicity, the counter ions will be henceforth represented by A and B solely.

A Maxwell-Stefan (MS) based model was written and coded in Matlab R2013a® to describe the discontinuous ion exchange and embodies the following hypothesis: (1) film and intraparticle mass transfer resistances are both present; (2) the particles of the solid exchanger are spherical; (3) the solution is perfectly stirred; (4) operation is isothermal. This model was previously used to study the kinetic behaviour of mercury and cadmium removal from aqueous solutions using microporous titanosilicate ETS-4 [52,54,62], and more recently to model the uptake of cesium by the lanthanide silicate Eu-AV-20 [70].

The mass balances to the counter ion A, in the particle and in solution, are given by:

$$\rho_s \frac{\partial q_A}{\partial t} = -\frac{1}{r^2} \frac{\partial}{\partial r} (r^2 N_A) \quad (\text{IV.2.3})$$

$$\frac{\partial C_A}{\partial t} = -\frac{\rho_s V_s}{V_L} \frac{\partial \bar{q}_A}{\partial t} \quad (\text{IV.2.4})$$

where r represents the radial position in the particle (m), t is time (s or h), q_A is the local concentration (mol kg⁻¹) of counter ion A in the particle, and N_A is the intraparticle diffusional flux of A (mol m⁻² s⁻¹). Note that the integrated form of Eq. (IV.2.4) corresponds to Eq. (IV.2.1). The average load of A per unit particle mass is calculated by:

$$\bar{q}_A = \frac{3}{R_p^3} \int_0^{R_p} r^2 q_A dr \quad (\text{IV.2.5})$$

where R_p represents the particle radius (m). The initial conditions (no A in the solid, no B in solution) and the boundary conditions (interface concentration and symmetry condition at the centre of the exchanger) necessary to solve Eqs. (IV.2.3) and (IV.2.4) can be written as:

$$t = 0, \quad \begin{cases} q_A = 0 \\ C_A = C_{A,0} \end{cases} \quad (\text{IV.2.6})$$

$$r = 0, \quad \frac{\partial q_A}{\partial r} = 0 \quad (\text{IV.2.7})$$

$$r = R_p, \quad q_A = q_{A,R_p} \quad (\text{IV.2.8})$$

The concentration at the interface, $C_A|_{R_p}$, is determined by setting the internal diffusion flux equal to the film convective flux at the boundary, *i.e.*:

$$N_A|_{R_p} = k_f (C_A - C_A|_{R_p}) \quad (\text{IV.2.9})$$

where k_f is the convective mass transfer coefficient (m s⁻¹) of species A. In this work k_f was estimated by the Armenante and Kirwan correlation [56] for particles in stirred vessels:

$$\text{Sh} = 2 + 0.52 \text{Re}^{0.52} \text{Sc}^{1/3} \quad (\text{IV.2.10})$$

where $Sh = k_f \times d_p / D_{Aw}$ is the Sherwood number, $Sc = \nu / D_{Aw}$ is the Schmidt number, and $Re = \varepsilon^{1/3} d_p^{4/3} / \nu$ is the Reynolds number; d_p is the particle diameter (m), D_{Aw} is the diffusivity of counter ion A in solution (m² s⁻¹), ν is the kinematic viscosity (m² s⁻¹) and ε is the power input per unit mass of fluid (m² s⁻³). For Cs⁺ in water at 295 K, $D_{Cs^+,w} = 2.06 \times 10^{-9}$ m² s⁻¹ [63].

The intraparticle counter ion transport can be described by the generalized Maxwell-Stefan (MS) equations expressed in matrix notation [51]:

$$(N) = -q_t \rho_s [B]^{-1} [\Gamma] (\nabla y) - [B]^{-1} (\nabla \zeta) \quad (IV.2.11)$$

where (N) is the vector of the molar fluxes of ionic species i (N_i , mol m⁻² s⁻¹), q_t is the total concentration (mol kg⁻¹) of counter ions A and B and co-ions S in the solid ($q_t = q_A + q_B + q_S$), (∇y) is the vector of gradients of the molar fractions of species i in the solid ($y_i = q_i / q_t$), and $(\nabla \zeta)$ is the vector of gradients defined by:

$$\nabla \zeta_i = y_i z_i \frac{F}{\Re T} \nabla \phi \quad (IV.2.12)$$

where $\nabla \phi$ is the electric potential gradient (V m⁻¹), F is the Faraday constant (96485.34 C mol⁻¹), \Re is the ideal gas constant (8.314472 J mol⁻¹ K⁻¹). The elements of the thermodynamic factors matrix $[\Gamma]$ and of matrix $[B]$ are defined by:

$$\Gamma_{ij} \equiv y_i \frac{\partial \ln(\gamma_{i,L} x_i)}{\partial y_j} \quad (IV.2.13)$$

$$B_{ii} = \frac{y_s}{\mathfrak{D}_{is}} + \sum_{\substack{j=1 \\ j \neq i}}^n \frac{y_j}{\mathfrak{D}_{ij}}, B_{ij} = -\frac{y_i}{\mathfrak{D}_{ij}} \quad (IV.2.14)$$

where $\gamma_{i,L}$ and x_i are the activity coefficient and the molar fraction of counter ion i in solution, respectively, \mathfrak{D}_{ij} is the MS diffusivity of the pair $i - j$ (m² s⁻¹), \mathfrak{D}_{is} is the MS surface diffusivity for the interaction between counter ion i and co-ions S (m² s⁻¹), and n is the number of counter ions ($n = 2$ with the co-ion S being the $(n + 1)^{th}$ species, *i.e.* the 3rd species). Under conditions of electroneutrality and no electric current, the following relations must be obeyed:

$$\sum_{i=1}^{n+1} q_i z_i = 0 \quad \text{and} \quad \sum_{i=1}^{n+1} N_i z_i = 0 \quad (\text{IV.2.15})$$

while the null co-ions flux is established by the bootstrap relation $N_{n+1} = 0$.

The equilibrium isotherm, which relates the fluid and solid concentrations at the interface, is given in the Langmuir-Freundlich equation

$$q_{A,\text{eq}} = \frac{q_{A,\text{max}} K_{\text{LF}} C_{A,\text{eq}}^{1/n_{\text{LF}}}}{1 + K_{\text{LF}} C_{A,\text{eq}}^{1/n_{\text{LF}}}} \quad (\text{IV.2.16})$$

where $q_{A,\text{max}}$, K_{LF} and n_{LF} are the parameters to fit the experimental data, namely the equilibrium concentrations of counter ion A in the solid, $q_{A,\text{eq}}$ (mol kg⁻¹), and in solution, $C_{A,\text{eq}}$ (mol m⁻³); in particular, $q_{A,\text{max}}$ is the ion exchanger capacity (mol kg⁻¹).

The conservation of species A, B and S is established by the material balance equations (Eqs. (IV.2.3) and (IV.2.4)), the electroneutrality restriction (Eq. (IV.2.15)), and the cation exchange capacity ($q_{A,\text{max}}$). The molar fluxes of A, S and B are computed by Eqs. (IV.2.11)–(IV.2.15).

The concentration of Cs⁺ in solution, its concentration profile in the solid phase, and evolution along time, were calculated numerically using the Method of Lines (MoL) with spatial discretization in the particle (71 grid points) using Finite Differences followed by numerical integration of the semi-discrete initial-value type problem defined by the resulting set of ordinary differential equations (ODEs). The Nelder-Mead algorithm was used to optimize the MS diffusivities \mathfrak{D}_{As} , \mathfrak{D}_{Bs} and \mathfrak{D}_{AB} , by minimizing the average absolute relative deviation, AARD:

$$\text{AARD}(\%) = \frac{100}{\text{NDP}} \sum_{i=1}^{\text{NDP}} \left| \frac{C_{A,\text{calc}} - C_{A,\text{exp}}}{C_{A,\text{exp}}} \right|_i \quad (\text{IV.2.17})$$

where NDP is the number of data points, and subscripts ‘exp’ and ‘calc’ refer to experimental and calculated concentrations of cesium in solution, respectively.

IV.2.4. Results and discussion

This section starts with the discussion of the morphology and crystallinity of the synthesised mixed lanthanide silicate Tb/Eu-AV-9. Then the equilibrium isotherm, the ion exchange kinetics (removal curves) and the removal efficiency are discussed, followed by the analysis of the emission photoluminescence spectra of the native and Cs^+ -exchanged samples. Finally, the results achieved with the Maxwell-Stefan (MS) based model are examined.

IV.2.4.1. Characterization of the Tb/Eu-AV-9 material

Native Tb/Eu-AV-9 consists of microcrystalline plates (Figure IV.2.2). The PXRD patterns (Figure IV.2.3) display the main AV-9 reflections [71] and only negligible amounts of impurities may be detected. The results indicate that all the samples are isostructural. Furthermore, the PXRD patterns of the Cs^+ -exchanged samples (Exps. 5, 7 and 10; Figure IV.2.3) indicate slight changes in the unit cell of the solid ascribed to the introduction of cesium in the structure. As expected, the solid containing less cesium (Exp. 5, Table IV.2.2) is the one with the closest pattern to that of the native sample, a result also confirmed by the photoluminescence studies.

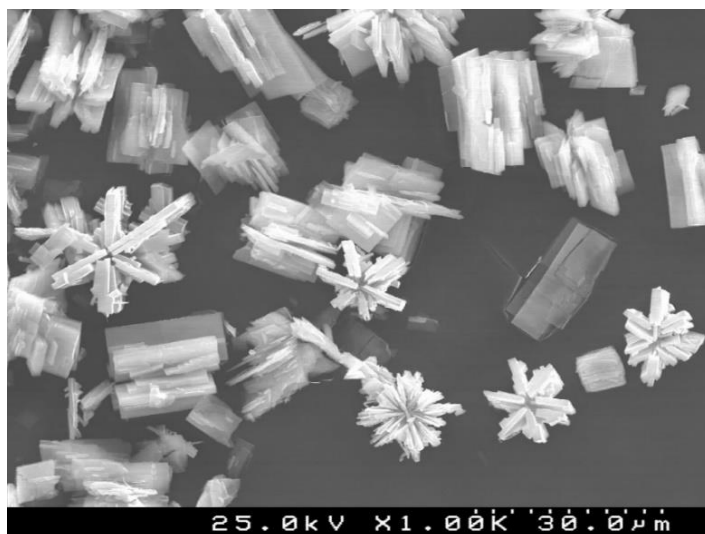


Figure IV.2.2 – SEM image of the native Tb/Eu-AV-9.

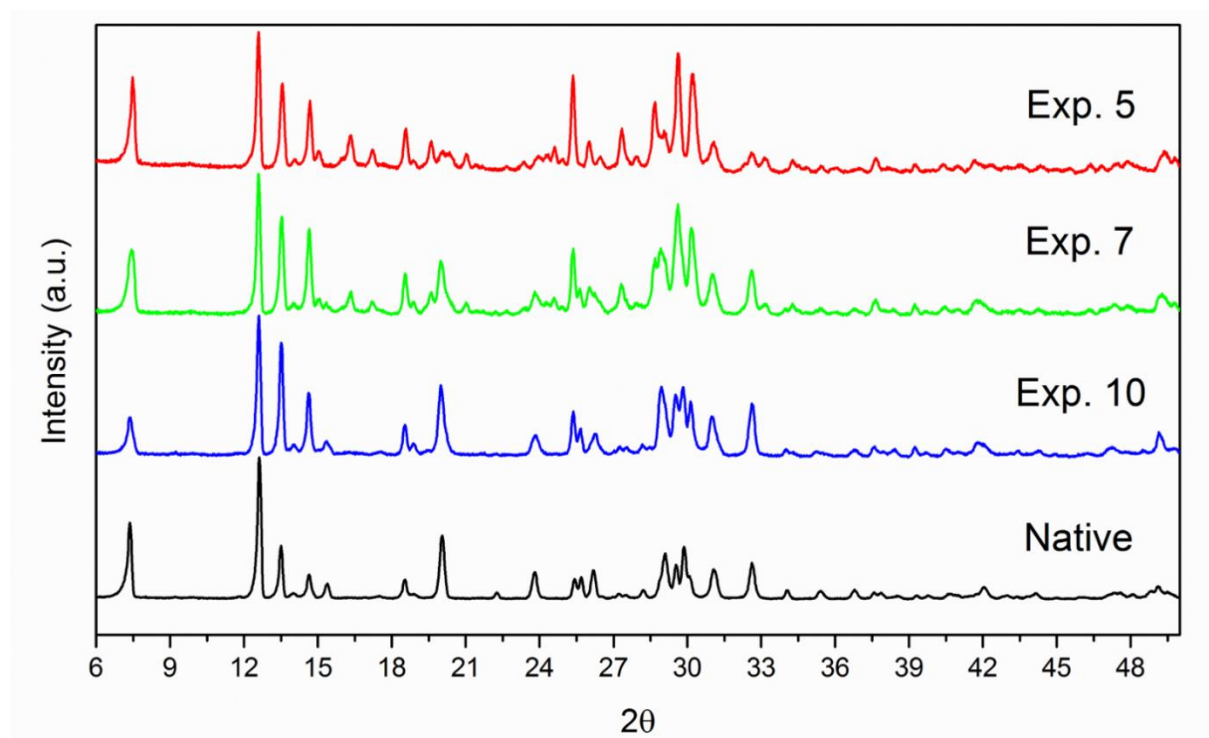


Figure IV.2.3 – Powder X-Ray diffraction patterns of the native Tb/Eu-AV-9 and Cs^+ -exchanged Tb/Eu-AV-9 (see experimental conditions of Exps. 5, 7 and 10 in Table IV.2.2).

IV.2.4.2. Ion exchange isotherm

The experimental ion exchange equilibrium data and the best-fit isotherm are presented in Figure IV.2.4. The Langmuir-Freundlich model provided better fitting than the Langmuir and Freundlich equations, with an average absolute relative deviation (AARD) of 13.06%.

Accordingly, the equilibrium isotherm is given by Eq. (IV.2.18) when concentrations are in mol m⁻³ and mol kg⁻¹.

$$q_{A,eq} = \frac{397.25 C_{A,eq}^{1/0.498}}{1 + 114.48 C_{A,eq}^{1/0.498}} \quad (IV.2.18)$$

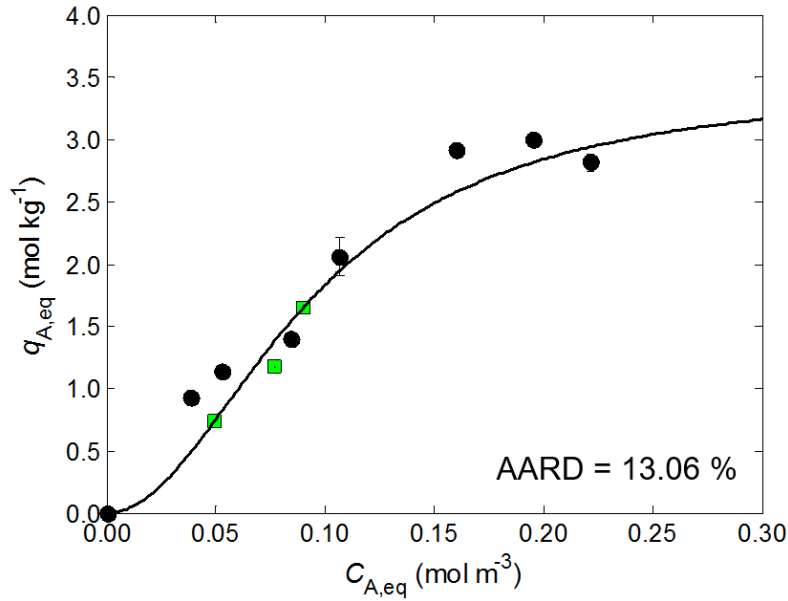


Figure IV.2.4 – Experimental data (black dots: Exps. 1-4, 6, 8 and 9; green squares: Exps. 5, 7 and 10) and Langmuir-Freundlich isotherm for the system Cs⁺/K⁺ / Tb/Eu-AV-9 at 295 K.

IV.2.4.3. Influence of Tb/Eu-AV-9 mass upon Cs⁺ removal

The effect of the mass of ion exchanger upon Cs⁺ removal can be evaluated from the ten experiments (Exps. 1–10, Table IV.2.2) carried out using a fixed initial concentration of cesium in solution (ca. 0.248 mol m⁻³) and amounts of solid in the range 15–509 mg. The results, expressed as final uptake of Cs⁺ (calculated by Eq. (IV.2.19)) against the ratio $m_s/C_{A,0}$ are presented in Figure IV.2.5. As expected, cesium removal increases with the mass of solid, from 7% to 60%, almost linearly up to 125 mg, and then attains a plateau at ca. 80% using higher masses of exchanger.

$$\text{Final Uptake (\%)} = 100 \times \left(1 - \frac{C_{A,eq}}{C_{A,0}} \right) \quad (IV.2.19)$$

The associated theoretical prediction can be calculated by combining the steady state material balance to the vessel (*i.e.*, Eq. (IV.2.1) written for final equilibrium) and the isotherm of the system (Eq. (IV.2.18)). The resulting equation is not solvable for $C_{A,eq}$ due to the exponent $1/n_{LF}$ of isotherm. For the particular case of Langmuir ($n_{LF} \rightarrow 1$), an analytic expression exists, but in our case the $C_{A,eq}$ values have to be numerically determined from:

$$\rho_s V_s q_{A,max} K_{LF} C_{A,eq}^{1/n_{LF}} - V_L (C_{A,0} - C_{A,eq}) (1 + K_{LF} C_{A,eq}^{1/n_{LF}}) = 0 \quad (IV.2.20)$$

The final uptake can be calculated after substitution of $C_{A,eq}$ into Eq. (IV.2.19). A good agreement between data and our calculated results is evident from Figure IV.2.5, for which the average deviation was only AARD = 4.14%.

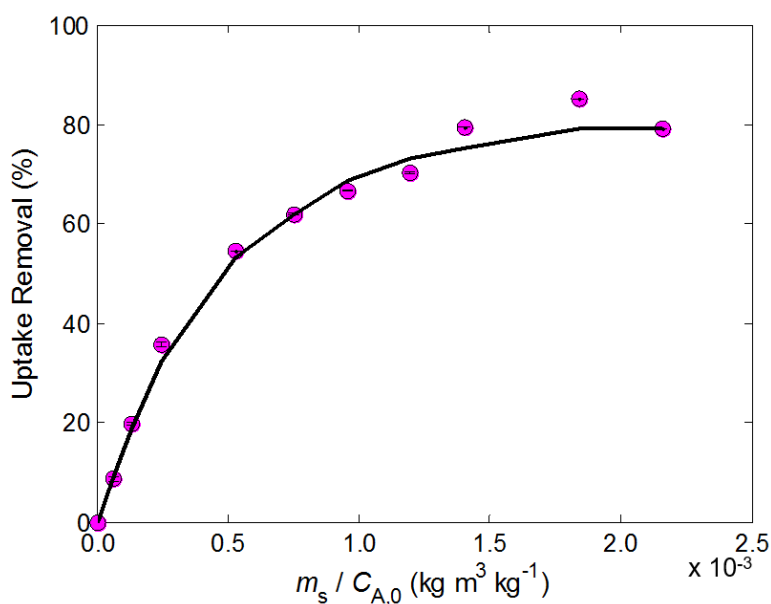


Figure IV.2.5 – Influence of the ratio between the mass of Tb/Eu-AV-9 and the initial concentration of Cs⁺ upon the final uptake of Cs⁺. circles: experimental data; line: theoretical prediction (AARD = 4.14%).

IV.2.4.4. Ion exchange kinetics

The kinetics of Cs⁺ removal was evaluated by carrying out assays with cesium solutions with similar initial concentration ($C_{A,0}$ around 0.248 mol m^{-3}) and using three different masses of Tb/Eu-AV-9 (Table IV.2.2), which correspond to $m_s/C_{A,0} = 7.51 \times 10^{-4}$, 11.97×10^{-4} and $21.57 \times 10^{-4} \text{ kg mol}^{-1} \text{ m}^3$ for Exps. 5, 7 and 10, respectively. The experimental data are plotted in Figure IV.2.6 as normalized concentration of cesium in bulk solution ($C_A/C_{A,0}$) along time.

The ion exchange kinetics is characterized by a very sharp slope descent followed by an almost instantaneous plateau. As discussed above, the results follow expected trends, *i.e.*, cesium removal increases with increasing mass of Tb/Eu-AV-9 since the extensive ion-exchange capacity is proportional to the mass of solid. The fast metal uptake at the beginning is due to the large mass transfer driving forces observed, since the Tb/Eu-AV-9 particles are initially free of Cs⁺.

For the three curves in Figure IV.2.6, the equilibrium uptake process is complete after ca. 1 hour, reaching 62.0, 70.3 and 79.2% removal of Cs⁺ from solution. This outcome places the Tb/Eu-AV-9 material in the class of the fastest zeolite-type ion exchangers. Similar behaviour was encountered for the system Cd²⁺/ETS-10 [16] where 5-160 mg of ETS-10 were contacted with 2 L of an aqueous solution of initial concentration $0.85 \times 10^{-3} \text{ kg m}^{-3}$. In that essay, the time required to reach equilibrium was 1-2 hours. In a distinct work, Zhao *et al.* [72] demonstrated that the sorption rate of Pb²⁺ on ETS-10 was also extremely rapid, as less than 1 minute was needed for attaining equilibrium with a 10 mol m^{-3} solution with batch factor of 0.2 mol kg^{-1} . We note that, in comparison with our essay, Zhao *et al.* utilized 4-10 times more mass of ion exchanger.

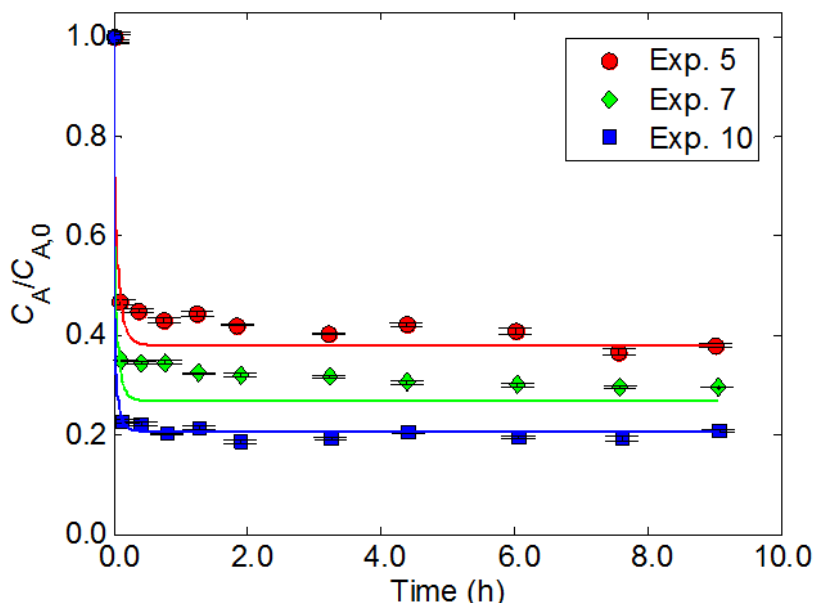


Figure IV.2.6 – Evolution of the normalized concentration of Cs⁺ in solution along time. Symbols, experimental data; curves, MS-based model which achieves AARD = 8.37%.

As a first approximation, these similar trends should be associated to the average pore diameters of the silicates under study. In fact Tb/Eu-AV-9 possesses pore sizes of 3.3 Å x 4.3 Å and 3.4 Å x 3.8 Å (Table IV.2.1) [71] while ETS-10 has pores of 4.9 to 7.6 Å [73], which justifies the better mass transport properties of the latter. We note that this comparison is not strictly rigorous, as the counter ions under analysis have distinct valences and diameters. In order to emphasize even more the interrelation between structure features and kinetics, it is interesting to compare the results obtained by Camarinha *et al.* [16] for Cd²⁺/ETS-10 with those of Barreira *et al.* [74] for Cd²⁺/ETS-4, that were investigated under similar operating conditions: $m_s = 1.5 - 50$ mg, $V_L = 2$ L, $C_{A0} = 0.85 \times 10^{-3}$ kg m⁻³, pH 6 and $T = 295$ K. The time for equilibrium was 1-2 hours for ETS-10 and 10 hours for ETS-4, which can be easily interpreted on the basis of the respective pore sizes, namely, 4.9 Å x 7.6 Å for ETS-10 [73] and 3 Å x 4 Å for ETS-4 [75].

IV.2.4.5. Photoluminescence spectra of native and Cs⁺-exchanged Tb/Eu-AV-9

The room-temperature photoluminescence emission spectra of the native and Cs⁺-exchanged Tb/Eu-AV-9 materials recorded with excitation at 393 nm and 377 nm are shown in Figures IV.2.7 and IV.2.8, respectively. Four of the transitions ascribed to the Eu³⁺ septet (⁵D₀→⁷F_j, j=0–3) are identified in Figure IV.2.7.a and, due to its relevance, the region of the transition ⁵D₀→⁷F₀ is enlarged in Figures IV.2.7.b. The main transitions ascribed to Tb³⁺

(⁵D₄→⁷F_j, j=3–6) are identified in Figure IV.2.8. It is worth noting the spectra obtained for excitation at 377 nm are essentially due to Eu³⁺ emission caused by Tb³⁺-to-Eu³⁺ energy transfer.

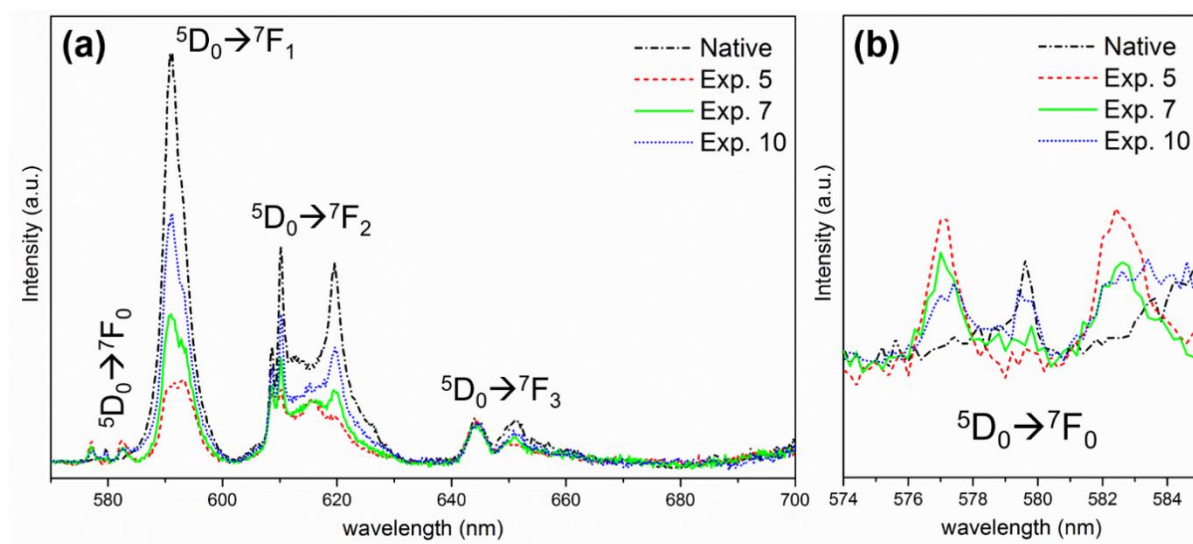


Figure IV.2.7 – (a) Partial room-temperature emission spectra of native and Cs⁺-exchanged Tb/Eu-AV-9 materials (excitation at 393 nm); (b) Enlarged region containing the ⁵D₀→⁷F₀ transition (central peak). Experimental conditions in Table IV.2.2, and equilibrium solid loadings in Table IV.2.3.

For 393 nm the spectrum of native Tb/Eu-AV-9 shown in Figure IV.2.7 is similar to the one reported for Eu-AV-9 by Ananias *et al.* [71]. Figure IV.2.7.a shows that the Eu³⁺ emission intensity decreases with the increasing amount of cesium in the solid, with the Exp. 10 spectrum ($q_{A,eq} = 0.73 \text{ mol kg}^{-1}$, the lowest cesium loading; Table IV.2.3) being closest to the spectrum of the native material. Figure IV.2.7.b shows that the Eu³⁺ transition ⁵D₀→⁷F₀ of the native Tb/Eu-AV-9 material (at 580 nm) becomes attenuated in the case of the Cs⁺-exchanged samples, and two new peaks are increasingly detected at 577 nm and 583 nm, which correspond to the ⁵D₄→⁷F₄ transition of Tb³⁺ shown in Figure IV.2.8.c.

Similarly, the concentration of cesium in the solid influences the emission intensity of the Tb³⁺ transitions (Figure IV.2.8). Again, the spectrum of the Cs⁺-exchanged Exp. 10 (lowest load of Cs⁺) is the closest to that of native material. Although two Tb sites were expected in advance from crystallography, the ⁵D₄→⁷F₅ decay curves (Figure IV.2.9) of the samples are well fitted by tri-exponential functions, which evidences the additional decay effect of the Tb³⁺-to-Eu³⁺ energy transfer cited above. The photoluminescence decay lifetimes are listed in Table IV.2.3, and corroborate the influence of Cs⁺ on the emission

capacity of the solids, namely, higher metal loads lead to lower decay lifetimes. In fact, the linear relation $\langle \tau \rangle = -0.61 q_{A,eq} + 5.73$ was found.

Altogether, the emission photoluminescence spectra of the Cs⁺-exchanged samples obtained in this work discloses the potential of Tb/Eu-AV-9 materials for qualitative or even quantitative sensing purposes, since emission intensities and peak areas may be related to the concentration of cesium in the solid. Work along these lines is still in progress due to the novelty of these materials and very recent investigation towards potential applications.

Table IV.2.3 – Average decay lifetimes of the 5D4→7F5 transition of Tb³⁺ of the native and Cs⁺-exchanged Tb/Eu-AV-9 materials, and corresponding equilibrium solid loading. The experimental conditions in Table IV.2.2

Tb/Eu-AV-9 materials	Average decay lifetimes, $\langle \tau \rangle$ (ms)	$q_{A,eq}$ (mol kg ⁻¹)
Native	5.75	0.00
Exp. 10	5.22	0.73
Exp. 7	5.04	1.18
Exp. 5	4.72	1.65

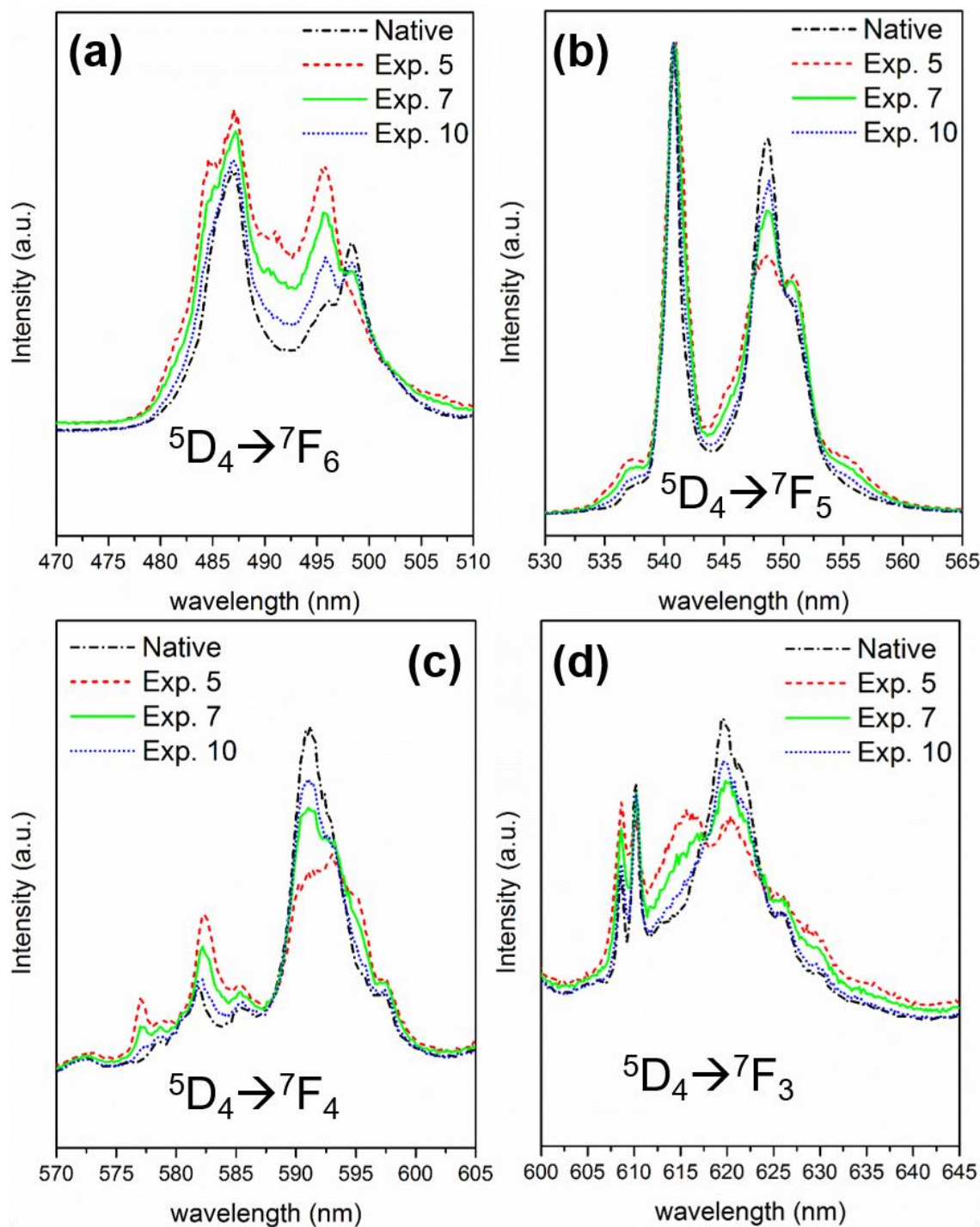


Figure IV.2.8 – Room-temperature emission spectra of native and Cs⁺-exchanged Tb/Eu-AV-9 materials (excitation at 377 nm). Experimental conditions in Table IV.2.2, and equilibrium solid loadings in Table IV.2.3.

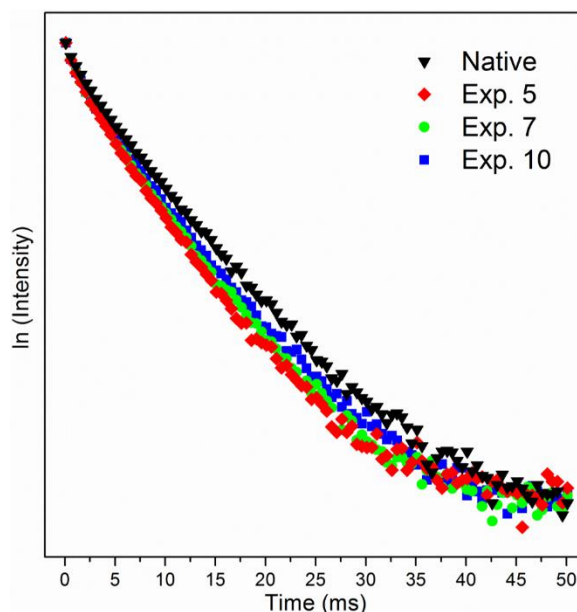


Figure IV.2.9 – Tb³⁺ emission decay curves (transition $^5D_4 \rightarrow ^7F_j$) of native and Cs⁺-exchanged Tb/Eu-AV-9 materials. Spectra were collected at room temperature, with excitation at 377 nm and detection at 541 nm. Experimental conditions in Table IV.2.2, and equilibrium solid loadings in Table IV.2.3.

IV.2.4.6. Ion exchange modelling based on Maxwell-Stefan equations

The MS-based model was fitted to the experimental data from the three kinetic experiments (Exps. 5, 7 and 10) simultaneously with an AARD of 8.37% (see Figure IV.2.6). The convective mass transfer coefficient (k_f) was estimated by the Armenante and Kirwan correlation [56], thus reducing the number of parameters to be optimized. For a particle size of 12×10^{-6} m, the estimated value was $k_f = 4.127 \times 10^{-4} \text{ m s}^{-1}$, which is in agreement with published results for similar setups and run conditions, namely 2.327×10^{-4} , 1.281×10^{-3} and $1.930 \times 10^{-4} \text{ m s}^{-1}$ for Cs⁺/Eu-AV-20 [70], Hg²⁺/ETS-4 [17] and Cd²⁺/ETS-10 [13], respectively, with corresponding particle average diameters of 23.1×10^{-6} , 0.7×10^{-6} and 5×10^{-6} m.

The adjusted MS diffusivities D_{As} , D_{Bs} and D_{AB} (see Table IV.2.4) are five to six orders of magnitude smaller than the Cs⁺ diffusion coefficient in aqueous solution ($2.06 \times 10^{-9} \text{ m}^2 \text{ s}^{-1}$, [63]). These small values are consistent with the small pore diameters of Tb/Eu-AV-9 (3.3×4.3 and $3.4 \times 3.8 \text{ Å}$, Table IV.2.1) and are roughly of the order of those reported by Figueiredo *et al.* [70] for Eu-AV-20 (Table IV.2.4), and the effective diffusivities published by Mon *et al.* [76] for cancrinite ($D_{\text{eff,Cs}^+} = 2.04 \times 10^{-14} \text{ m}^2 \text{ s}^{-1}$), sodalite ($D_{\text{eff,Cs}^+} = 0.47 \times 10^{-14} \text{ m}^2 \text{ s}^{-1}$) and allophane ($D_{\text{eff,Cs}^+} = 0.49 \times 10^{-16} \text{ m}^2 \text{ s}^{-1}$). D_{As} is lower than D_{Bs} ($8.373 \times 10^{-15} <$

$2.795 \times 10^{-14} \text{ m}^2 \text{ s}^{-1}$), which is in accord with the ionic radius of the counter ions: 0.170 nm for Cs⁺ and 0.138 nm for K⁺ (remember that A = Cs⁺ and B = K⁺).

Table IV.2.4 – Estimated convective mass transfer coefficient and optimized MS diffusivities for Tb/Eu-AV-9 and Eu-AV-20 materials at $T = 295 \text{ K}$.

Material	$k_f (\text{m s}^{-1})^\dagger$	$D_{As} (\text{m}^2 \text{s}^{-1})$	$D_{Bs} (\text{m}^2 \text{s}^{-1})$	$D_{AB} (\text{m}^2 \text{s}^{-1})$	AARD (%)	Ref.
Tb/Eu-AV-9	4.127×10^{-4}	8.373×10^{-15}	2.795×10^{-14}	6.037×10^{-15}	8.37	This work
Eu-AV-20	2.327×10^{-4}	2.706×10^{-15}	5.713×10^{-15}	9.446×10^{-16}	19.00	[70]

[†] Estimated using the Armenante and Kirwan correlation [56], Eq. (IV.2.10).

Even if the Tb/Eu-AV-9 pore sizes are smaller than those of Eu-AV-20 (3.3×4.3 & 3.4×3.8 versus $5.8 \times 6.8 \text{ \AA}$, respectively), the MS Cs⁺ and K⁺ diffusivities are both higher in the former. In addition to the influence of the different structures of the material, another factor may explain this apparent contradiction. The Eu-AV-20 framework consists of a series of sheets built up of alternating chains of Na⁺ and Eu³⁺ polyhedra. The layers are connected through double silicate chains of 8-membered rings forming channels [47,70] rendering the intraparticle two-dimensional counter ion traffic in Eu-AV-20, while it is 3D in the case of Tb/Eu-AV-9.

Figure IV.2.10 illustrates the normalized concentration of cesium in the Tb/Eu-AV-9 particles ($q_A/q_{A,\text{eq}}$) as a function of the time and radial position, calculated with the MS-based model for the conditions of Exp. 5 (Table IV.2.2). For the other kinetic experiments (Exps. 7 and 10) the results were similar and are not presented. The plot confirms the expected behaviour, *i.e.*, the concentration of cesium in the solid increases along time until it reaches the equilibrium. Nevertheless, the normalized concentration at the surface, $q_A(t, r = R_p)$, evidences a remarkable behaviour. Inside the particle, far from the surface ($r/R_p \rightarrow 0$), the cesium concentration increases monotonously while at the surface ($r/R_p \rightarrow 1$) it rises abruptly going through a maximum and then gradually decreasing until equilibrium. Without film resistance, the concentration at the particle surface would jump suddenly from 0 to $q_{A,\text{eq}}(C_{A,0})$, which is the concentration in equilibrium with the bulk solution (*i.e.*, for $r = R_p$, $q_{A,t=0^-} = 0$ and $q_{A,t=0^+} = q_{A,\text{eq}}(C_{A,0})$); afterwards, for $t > 0$, the concentration would decrease monotonously until system equilibration. The existence of the external film slows the steep increase in concentration, as shown in Figure IV.2.10. The simulation results also indicate that 0.5 hour is sufficient to exchange 62% of the cesium present in a $C_{A,0} = 0.237 \text{ mol m}^{-3}$ aqueous solution.

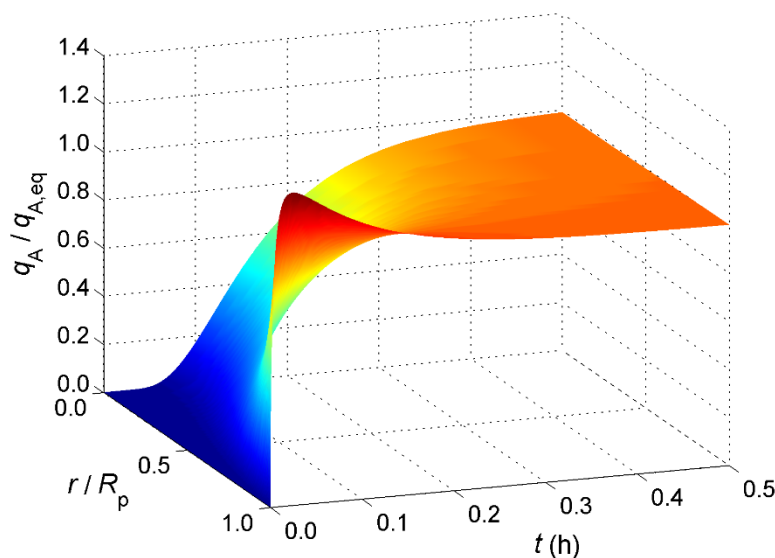


Figure IV.2.10 – Normalized cesium concentration in the Tb/Eu-AV-9 particles as a function of time and radial position, for Exps. 5 (experimental conditions given in Table IV.2.2).

IV.2.5. Conclusions

A mixed lanthanide silicate Tb/Eu-AV-9 material was synthesised and its cesium uptake capacity was assessed by performing ion-exchange equilibrium assays and kinetic studies (removal curves) in stirred-flasks at room temperature (295 K). Ion-exchange equilibrium data were well fitted by the Langmuir-Freundlich isotherm with an average absolute relative deviation (AARD) of 13.06%. The cesium uptake curves exhibited the usual trend with a steep descend of concentration in the first minutes followed by a slow transition zone towards the equilibrium, reached after *ca.* 2 h. The kinetic curves were modelled using the Maxwell-Stefan approach (AARD = 8.37%) and the convective mass transfer coefficient estimated by the Armenante and Kirwan correlation ($k_f = 4.127 \times 10^{-4} \text{ m s}^{-1}$). The model parameters were the MS diffusion coefficients ($D_{As} = 8.373 \times 10^{-15}$, $D_{Bs} = 2.795 \times 10^{-14}$ and $D_{AB} = 6.037 \times 10^{-15} \text{ m}^2 \text{ s}^{-1}$), whose small values were consistent with other results in the literature and confirm the surface mechanism of ion exchange inside the Tb/Eu-AV-9 particles.

The photoluminescence spectra of native and Cs⁺-exchanged Tb/Eu-AV-9 materials revealed that the observed emission intensity and peak areas depend on the concentration

of cesium in the solid. Furthermore, the average lifetime calculated from tri-exponential emission decay curves is linearly interlinked with solid loading, $q_{A,eq}$. Altogether these results are very promising and envision the application of Tb/Eu-AV-9 materials as qualitative or even quantitative cesium sensors.

IV.2.6. Nomenclature

A or A ^{z_A}	Counter ion initially in solution
AARD	Average absolute relative deviation (%)
B or B ^{z_B}	Counter ion initially in the exchanger
[B]	Matrix with MS diffusivities, Eq. (14)
C _A	Concentration of A in bulk solution (mol m ⁻³ or eq m ⁻³)
C _{A,0}	Initial concentration of A in bulk solution (mol m ⁻³ or eq m ⁻³)
Đ _{ij}	MS diffusivity of pair i-j (m ² s ⁻¹)
Đ _{is}	MS surface diffusivity of pair i-fixed ionic charges (m ² s ⁻¹)
D _{Aw}	Diffusivity of counter ion A in solution (m ² s ⁻¹)
d _p	Particle diameter (m)
F	Faraday constant (96485.34 C mol ⁻¹)
<i>i</i> and <i>j</i>	Generic counter ions
k _f	Convective mass transfer coefficient (m s ⁻¹)
K _{LF}	Langmuir-Freundlich parameter, Eqs. (16) and (18)
m _s	Mass of ion exchanger (kg)
MoL	Method of Lines
MS	Maxwell-Stefan
<i>n</i>	Number of diffusing species in MS equations
n _{LF}	Langmuir-Freundlich parameter, Eqs. (16) and (18)
N _{<i>i</i>}	Molar flux of counter ion <i>i</i> (mol m ⁻² s ⁻¹)
NDP	Number of data points
PXRD	Powder X-ray diffraction
q _{<i>i</i>}	Local concentration of counter ion <i>i</i> in the particle (mol kg ⁻¹)
\bar{q}_i	Average concentration of counter ion <i>i</i> in the particle (mol kg ⁻¹)
q _{A,max}	Langmuir-Freundlich parameter (mol kg ⁻¹); ion exchanger capacity
q _s	Ion exchanger (co-ions) molar capacity (mol kg ⁻¹)

q_t	Total concentration of ionic species in the particle (mol kg ⁻¹)
r	Radial position in the particle (m)
\mathfrak{R}	Ideal gas constant (8.314462 J mol ⁻¹ K ⁻¹)
R_p	Particle radius (m)
Re	$= \varepsilon^{1/3} d_p^{1/3} / \nu$, Reynold number
S	Co-ions of the ion exchanger
SEM	Scanning Electron Microscopy
Sc	$= \nu / D_{Aw}$, Schmidt number
Sh	$= k_f \times d_p / D_{Aw}$, Sherwood number
t	Time (h or s)
T	Absolute temperature (K)
V_L	Solution volume (m ³)
V_s	Ion exchanger volume (m ³)
x_i	Molar fraction of counter ion i in bulk solution
y_i	Local molar fraction of counter ion i in the particle
z_i	Electrochemical valence of counter ion i

Greek letters

ε	Stirring power input per unit mass of fluid (m ² s ⁻³)
$\gamma_{i,L}$	Activity coefficient of counter ion i in a solution in equilibrium with exchanger
ν	Kinematic viscosity (m ² s ⁻¹)
ϕ	Electric potential (V)
$[\Gamma]$	Thermodynamics factors matrix
ζ_i	Related with the electric potential gradient, Eq. (11)
ρ_s	Density of ion exchanger (kg m ⁻³),
τ_j	Decay lifetime (ms)

Subscripts

0	Initial condition
A	Counter ion initially present in the bulk solution (Cs ⁺)
B	Counter ion initially present in the solid particle (Na ⁺ and K ⁺)
calc	Calculated value

eq	Equilibrium
exp	Experimental value
i and j	Generic diffusing species
s	Solid

IV.3. References

- [1] J.F. Ahearne, Radioactive waste: The size of the problem, *Phys. Today* 50 (1997) 24–29.
- [2] E.A. Behrens, P. Sylvester, A. Clearfield, Assessment of a sodium nonatitanate and pharmacosiderite-type ion exchangers for strontium and cesium removal from DOE waste simulants, *Environ. Sci. Technol.* 32 (1998) 101–107.
- [3] A. Clearfield, Ion-exchange materials: seizing the caesium, *Nat. Chem.* 2 (2010) 161–162.
- [4] S. Ferdov, Z. Lin, Selective Detection of Cs + in Water Solutions via One-Step Formation of a New Type of Struvite-Like Phosphate, *Chem. Mater.* 22 (2010) 5345–5349.
- [5] R.O.A. Rahman, H.A. Ibrahim, Y.T. Hung, Liquid Radioactive Wastes Treatment: A Review, *Water* 3 (2011) 551–565.
- [6] K. Popa, C.C. Pavel, Radioactive wastewaters purification using titanosilicates materials: State of the art and perspectives, *Desalination* 293 (2012) 78–86.
- [7] C.B. Lopes, P.F. Lito, S.P. Cardoso, E. Pereira, A.C. Duarte, C.M. Silva, Metal Recovery, Separation and/or Pre-concentration, in: Inamuddin, M. Luqman (Eds.), *Ion Exchange Technology II - Applications*, Springer Netherlands, Dordrecht, 2012.
- [8] P.F. Lito, J.P.S. Aniceto, C.M. Silva, Removal of Anionic Pollutants from Waters and Wastewaters and Materials Perspective for Their Selective Sorption, *Water, Air, Soil Pollut.* 223 (2012) 6133–6155.
- [9] M. Smolik, A. Jakóbk-Kolon, M. Porański, Separation of zirconium and hafnium using Diphonix® chelating ion-exchange resin, *Hydrometallurgy* 95 (2009) 350–353.
- [10] A. Clearfield, P. Sylvester, E. Bluhm, A. Bortun, L. Bortun, Use of inorganic ion exchangers for nuclear waste remediation and industrial separations, *Abstr. Pap. Am. Chem. Soc.* 218 (1999) U1061–U1061.
- [11] A. Clearfield, Inorganic ion exchangers, past, present, and future, *Solvent Extr. Ion Exch.* 18 (2000) 655–678.
- [12] S.P. Cardoso, C.B. Lopes, E. Pereira, A.C. Duarte, C.M. Silva, Competitive Removal of Cd²⁺ and Hg²⁺ Ions from Water Using Titanosilicate ETS-4: Kinetic Behaviour and Selectivity, *Water, Air, Soil Pollut.* 224 (2013) 1535–1541.
- [13] T.R. Ferreira, C.B. Lopes, P.F. Lito, M. Otero, Z. Lin, J. Rocha, E. Pereira, C.M. Silva, A. Duarte, Cadmium(II) removal from aqueous solution using microporous titanosilicate ETS-4, *Chem. Eng. J.* 147 (2009) 173–179.
- [14] C.B. Lopes, M. Otero, Z. Lin, C.M. Silva, J. Rocha, E. Pereira, A.C. Duarte, Removal of Hg²⁺ ions from aqueous solution by ETS-4 microporous titanosilicate - Kinetic and equilibrium studies, *Chem. Eng. J.* 151 (2009) 247–254.

- [15] M. Otero, C.B. Lopes, J. Coimbra, T.R. Ferreira, C.M. Silva, Z. Lin, J. Rocha, E. Pereira, A.C. Duarte, Priority pollutants (Hg²⁺ and Cd²⁺) removal from water by ETS-4 titanasilicate, *Desalination* 249 (2009) 742–747.
- [16] E.D. Camarinha, P.F. Lito, B.M. Antunes, M. Otero, Z. Lin, J. Rocha, E. Pereira, A.C. Duarte, C.M. Silva, Cadmium(II) removal from aqueous solution using microporous titanasilicate ETS-10, *Chem. Eng. J.* 155 (2009) 108–114.
- [17] C.B. Lopes, E. Pereira, Z. Lin, P. Pato, M. Otero, C.M. Silva, J. Rocha, A.C. Duarte, Fixed-bed removal of Hg²⁺ from contaminated water by microporous titanasilicate ETS-4: Experimental and theoretical breakthrough curves, *Microporous Mesoporous Mater.* 145 (2011) 32–40.
- [18] C.B. Lopes, P.F. Lito, M. Otero, Z. Lin, J. Rocha, C.M. Silva, E. Pereira, A.C. Duarte, Mercury removal with titanasilicate ETS-4: Batch experiments and modelling, *Microporous Mesoporous Mater.* 115 (2008) 98–105.
- [19] B.W. Mercer, L.L. Ames, P.W. Smith, Cesium Purification by Zeolite Ion Exchange, *Nucl. Appl. Technol.* 8 (1970) 62–69.
- [20] A.I. Bortun, L.N. Bortun, A. Clearfield, Ion Exchange Properties of a Cesium Ion Selective Titanasilicate, *Solvent Extr. Ion Exch.* 14 (1996) 341–354.
- [21] A.J. Celestian, J.D. Kubicki, J. Hanson, A. Clearfield, J.B. Parise, The mechanism responsible for extraordinary Cs ion selectivity in crystalline silicotitanate, *J. Am. Chem. Soc.* 130 (2008) 11689–11694.
- [22] C.C. Pavel, D. Vuono, A. Nastro, J.B. Nagy, N. Bilba, Synthesis and ion exchange properties of the ETS-4 and ETS-10 microporous crystalline titanosilicates, *Impact Zeolites Other Porous Mater. New Technol. Begin. New Millenn.* 142 (2002) 295–302.
- [23] A.M. Puziy, Cesium and strontium exchange by the framework potassium titanium silicate K₃HTi₄O₄(SiO₄)₃ 4H₂O, *J. Radioanal. Nucl. Chem.* 237 (1998) 73–79.
- [24] P. Sylvester, A. Clearfield, Removal of strontium and cesium from simulated hanford groundwater using inorganic ion exchange materials, *Solvent Extr. Ion Exch.* 17 (1999) 1385.
- [25] A. Tripathi, D.G. Medvedev, A. Clearfield, The crystal structures of strontium exchanged sodium titanosilicates in relation to selectivity for nuclear waste treatment, *J. Solid State Chem.* 178 (2005) 253–261.
- [26] T.M. Nenoff, S.G. Thoma, J.E. Miller, D.E. Trudell, S.G. Thoma, D.E. Trudell, Highly selective inorganic crystalline ion exchange material for Sr²⁺ in acidic solutions, *Environ. Sci. Technol.* 412 (1996) 3630–3633.
- [27] T.M. Nenoff, S.G. Thoma, J.E. Miller, D.E. Trudell, SNL-1, a Highly Selective Inorganic Crystalline Ion Exchange Material for Sr²⁺ in Acidic Solutions, *MRS Proc.* 412 (2011) 659–661.
- [28] C.B. Amphlett, P. Eaton, L.A. McDonald, A.J. Miller, Synthetic Inorganic Ion-Exchange Materials - 4 - Equilibrium Studies with Monovalent Cations and Zirconium

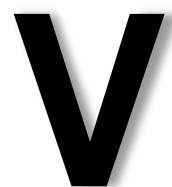
- Phosphate, J. Inorg. Nucl. Chem. 26 (1964) 297–304.
- [29] S. Komarneni, R. Roy, Use of Gamma-Zirconium Phosphate for Cs Removal from Radioactive-Waste, *Nature* 299 (1982) 707–708.
 - [30] S. Komarneni, R. Roy, A Cesium-Selective Ion Sieve Made by Topotactic Leaching of Phlogopite Mica, *Science* 239 (1988) 1286–1288.
 - [31] M. Miyake, S. Komarneni, R. Roy, Immobilization of Pb²⁺, Cd²⁺, Sr²⁺ and Ba²⁺ Ions Using Calcite and Aragonite, *Cem. Concr. Res.* 18 (1988) 485–490.
 - [32] N. Suzuki, D. Yamamoto, N. Anaguchi, H. Tsuchiya, K. Aoki, Y. Kanzaki, The ion-exchange property of some layered inorganic materials with potassium ion, rubidium ion and cesium ion, and selective cesium ion-exchange of synthetic mica, *Bull. Chem. Soc. Jpn.* 73 (2000) 2599–2603.
 - [33] P. Sylvester, A. Clearfield, R.J. Diaz, Pillared montmorillonites: Cesium-selective ion-exchange materials, *Sep. Sci. Technol.* 34 (1999) 2293–2305.
 - [34] D.M. Poojary, R.A. Cahill, A. Clearfield, Synthesis, Crystal-Structures, and Ion-Exchange Properties of a Novel Porous Titanosilicate, *Chem. Mater.* 6 (1994) 2364–2368.
 - [35] E.A. Behrens, A. Clearfield, Titanium silicates, M₃HTi₄O₄(SiO₄)₃·4H₂O (M=Na⁺,K⁺), with three-dimensional tunnel structures for the selective removal of strontium and cesium from wastewat, *Microporous Mater.* 11 (1997) 65–75.
 - [36] A. Dyer, M. Pillinger, S. Amin, Ion exchange of caesium and strontium on a titanosilicate analogue of the mineral pharmacosiderite, *J. Mater. Chem.* 9 (1999) 2481–2487.
 - [37] A. Clearfield, Structure and ion exchange properties of tunnel type titanium silicates, *Solid State Sci.* 3 (2001) 103–112.
 - [38] A. Tripathi, D.G. Medvedev, M. Nyman, A. Clearfield, Selectivity for Cs and Sr in Nb-substituted titanosilicate with sitinakite topology, *J. Solid State Chem.* 175 (2003) 72–83.
 - [39] V. Luca, J. V. Hanna, M.E. Smith, M. James, D.R.G. Mitchell, J.R. Bartlett, Nb-substitution and Cs⁺ ion-exchange in the titanosilicate sitinakite, *Microporous Mesoporous Mater.* 55 (2002) 1–13.
 - [40] C.C. Pavel, M. Walter, P. Pöml, D. Bouëxière, K. Popa, Contrasting immobilization behavior of Cs⁺ and Sr²⁺ cations in a titanosilicate matrix, *J. Mater. Chem.* 21 (2011) 3831–3837.
 - [41] N. Döbelin, T. Armbruster, Microporous titanosilicate AM-2: Ion-exchange and thermal stability, *Microporous Mesoporous Mater.* 99 (2007) 279–287.
 - [42] G. Yang, Y. Wang, D.H. Zhou, J.Q. Zhuang, X.C. Liu, X.W. Han, X.H. Bao, Investigation on the thermal stability of La/ZSM-5 zeolite and the La³⁺ species, *Acta Physico-Chimica Sin.* 20 (2004) 60–64.
-

- [43] G. Yang, Y. Wang, D.H. Zhou, J.Q. Zhuang, X.C. Liu, X.W. Han, X.H. Bao, On configuration of exchanged La³⁺ on ZSM-5: A theoretical approach to the improvement in hydrothermal stability of La-modified ZSM-5 zeolite, *J. Chem. Phys.* 119 (2003) 9765–9770.
- [44] J. Rocha, L.D. Carlos, Microporous materials containing lanthanide metals, *Curr. Opin. Solid State Mater. Sci.* 7 (2003) 199–205.
- [45] J. Rocha, Z. Lin, Microporous mixed octahedral-pentahedral-tetrahedral framework silicates, *Micro- Mesoporous Miner. Phases* 57 (2005) 173–201.
- [46] R.C. Evans, L.D. Carlos, P. Douglas, J. Rocha, Tuning the emission colour in mixed lanthanide microporous silicates: energy transfer, composition and chromaticity, *J. Mater. Chem.* 18 (2008) 1100–1107.
- [47] A. Ferreira, D. Ananias, L.D. Carlos, C.M. Morais, J. Rocha, Novel microporous lanthanide silicates with tobermorite-like structure, *J. Am. Chem. Soc.* 125 (2003) 14573–14579.
- [48] S. Komarneni, D.M. Roy, Tobermorites - A New Family of Cation Exchangers, *Sci. Class.* 221 (1983) 647–648.
- [49] R.C. Evans, D. Ananias, A. Douglas, P. Douglas, L.D. Carlos, J. Rocha, Energy transfer and emission decay kinetics in mixed microporous lanthanide silicates with unusual dimensionality, *J. Phys. Chem. C* 112 (2008) 260–268.
- [50] F. Helfferich, *Ion Exchange*, Courier Dover Publications, New York, 1995.
- [51] P.F. Lito, S.P. Cardoso, J.M. Loureiro, C.M. Silva, Ion Exchange Equilibria and Kinetics, in: Inamuddin, M. Luqman (Eds.), *Ion Exchange Technology I - Theory and Materials*, Springer Netherlands, Dordrecht, 2012.
- [52] C.M. Silva, P.F. Lito, Application of the Maxwell–Stefan approach to ion exchange in microporous materials. Batch process modelling, *Chem. Eng. Sci.* 62 (2007) 6939–6946.
- [53] P.F. Lito, C.M. Silva, Comparison between Maxwell-Stefan and Nernst-Planck Equations to Describe Ion Exchange in Microporous Materials, *Defect Diffus. Forum* 273-276 (2008) 776–781.
- [54] P.F. Lito, J.P.S. Aniceto, C.M. Silva, Modelling ion exchange kinetics in zeolyte-type materials using Maxwell-Stefan approach, *Desalin. Water Treat.* (2013) 1–10.
- [55] W.E. Schiesser, *The Numerical Method of Lines*, Academic Press, USA, 1991.
- [56] P.M. Armenante, D.J. Kirwan, Mass transfer to microparticles in agitated systems, *Chem. Eng. Sci.* 44 (1989) 2781–2796.
- [57] E.N. Coker, L.V.C. Rees, Ion exchange in beryllphosphate-G. Part I - Ion-exchange equilibria, *J. Chem. Soc. Faraday Trans.* 88 (1992) 263–272.
- [58] E.N. Coker, L.V.C. Rees, Kinetics of ion exchange in quasi-crystalline aluminosilicate zeolite precursors, *Microporous Mesoporous Mater.* 84 (2005) 171–

178.

- [59] N.M. Brooke, L.V.C. Rees, Kinetics of ion-exchange, *Trans. Faraday Soc.* 65 (1969) 2728–2739.
- [60] R.M. Barrer, L.V.C. Rees, Self-diffusion of alkali metal ions in analcite, *Trans. Faraday Soc.* 56 (1960) 709.
- [61] A. Clearfield, D.G. Medvedev, S. Kerlegon, T. Bosser, J.D. Burns, M. Jackson, Rates of Exchange of Cs⁺ and Sr²⁺ for Poorly Crystalline Sodium Titanium Silicate (CST) in Nuclear Waste Systems, *Solvent Extr. Ion Exch.* 30 (2012) 229–243.
- [62] P.F. Lito, J.P.S. Aniceto, C.M. Silva, Maxwell–Stefan based modelling of ion exchange systems containing common species (Cd²⁺, Na⁺) and distinct sorbents (ETS-4, ETS-10), *Int. J. Environ. Sci. Technol.* 12 (2015) 183–192.
- [63] H. Sato, M. Yui, H. Yoshikawa, Ionic Diffusion Coefficients of Cs⁺, Pb²⁺, Sm³⁺, Ni²⁺, SeO₂⁻⁴ and TcO⁻⁴ in Free Water Determined from Conductivity Measurements, *J. Nucl. Sci. Technol.* 33 (1996) 950–955.
- [64] I.A.M. Ahmed, S.D. Young, N.M.J. Crout, Time-dependent sorption of Cd²⁺ on CaX zeolite: Experimental observations and model predictions, *Geochim. Cosmochim. Acta* 70 (2006) 4850–4861.
- [65] K. Popa, C.C. Pavel, N. Bilba, A. Cecal, Purification of waste waters containing ⁶⁰Co²⁺, ^{115m}Cd²⁺ and ²⁰³Hg²⁺ radioactive ions by ETS-4 titanasilicate, *J. Radioanal. Nucl. Chem.* 269 (2006) 155–160.
- [66] I.C. Ostroski, C.E. Borba, E.A. Silva, P.A. Arroyo, R. Guirardello, M.A.S.D. Barros, Mass Transfer Mechanism of Ion Exchange in Fixed Bed Columns, *J. Chem. Eng. Data* 56 (2011) 375–382.
- [67] A.I. Bortun, L.N. Bortun, S.A. Khainakov, A. Clearfield, Ion exchange properties of the sulfur-modified biotite, *Solvent Extr. Ion Exch.* 16 (1998) 1541–1558.
- [68] F. Pepe, B. de Gennaro, P. Aprea, D. Caputo, Natural zeolites for heavy metals removal from aqueous solutions: Modeling of the fixed bed Ba²⁺/Na⁺ ion-exchange process using a mixed phillipsite/chabazite-rich tuff, *Chem. Eng. J.* 219 (2013) 37–42.
- [69] J. Rocha, D. Ananias, F.A.A. Paz, Photoluminescent zeolite-type lanthanide silicates, in: J. Reedijk, K. Poeppelmeier (Eds.), *Comprehensive Inorganic Chemistry II*, Elsevier, 2013.
- [70] B.R. Figueiredo, D. Ananias, J. Rocha, C.M. Silva, Cs⁺ ion exchange over lanthanide silicate Eu-AV-20: Experimental measurement and modelling, *Chem. Eng. J.* 268 (2015) 208–218.
- [71] D. Ananias, A. Ferreira, J. Rocha, P. Ferreira, J.P. Rainho, C. Morais, L.D. Carlos, Novel microporous europium and terbium silicates, *J. Am. Chem. Soc.* 123 (2001) 5735–5742.
- [72] G.X.S. Zhao, J.L. Lee, P.A. Chia, Unusual Adsorption Properties of Microporous

- Titanosilicate ETS-10 toward Heavy Metal Lead, *Langmuir* 19 (2003) 1977–1979.
- [73] M.W. Anderson, O. Terasaki, T. Ohsuna, P.J.O. Malley, A. Philippou, S.P. Mackay, A. Ferreira, J. Rocha, S. Lidin, Microporous Titanosilicate ETS-10 - A Structural Survey, *Philos. Mag. B-Physics Condens. Matter Stat. Mech. Electron. Opt. Magn. Prop.* 71 (1995) 813–841.
- [74] L.D. Barreira, P.F. Lito, B.M. Antunes, M. Otero, Z. Lin, J. Rocha, E. Pereira, A.C. Duarte, C.M. Silva, Effect of pH on cadmium (II) removal from aqueous solution using titanosilicate ETS-4, *Chem. Eng. J.* 155 (2009) 728–735.
- [75] S.M. Kuznicki, Large-pored crystalline titanium molecular sieve zeolites, US4853202 A, 1989.
- [76] J. Mon, Y. Deng, M. Flury, J.B. Harsh, Cesium incorporation and diffusion in cancrinite, sodalite, zeolite, and allophane, *Microporous Mesoporous Mater.* 86 (2005) 277–286.



Removal of Cs^+ from aqueous solutions through fixed-bed experiments

This chapter is devoted to the removal of Cs^+ ion from aqueous solution using two different silicates – Eu-AV-20 and ETS-4 – carrying out fixed-bed ion exchange experiments; in the case of ETS-4 a set of batch assays were also performed. The parent and exchanged materials were characterized by several techniques, such as scanning electron microscopy (SEM), energy-dispersive X-ray spectroscopy (EDS), powder X-Ray diffraction (PXRD), inductively coupled plasma mass spectroscopy (ICP-MS) and photoluminescent spectroscopy (PLS). Several breakthrough curves were measured and, in the specific case of ETS-4, a complete loading-regeneration-loading assay was performed in order to assess its ability to be used in ion exchange cycles. The experimental data were modelled using: 1) a Nernst-Planck based model taking into account the internal and external limitations to the mass transfer; and 2) simplified analytic models from the literature such as Thomas, Bohart-Adams, Clark and Yoon-Nelson models. In the particular case of the Eu-AV-20, photoluminescent spectroscopic studies were also performed aiming the evaluation of its sensing ability towards cesium.

Index

V.1. Cs ⁺ removal and optical detection by microporous lanthanide silicate Eu-AV-20 in a fixed-bed column	214
V.1.1. Introduction	214
V.1.2. Materials and Methods	215
V.1.2.1. Chemicals and materials	215
V.1.2.2. Synthesis and characterization of Eu-AV-20	216
V.1.2.3. Characterization and analytic methods.....	216
V.1.2.4. Fixed-bed and batch ion experiments.....	217
V.1.3. Modelling isotherms and breakthrough curves	220
V.1.3.1. Equilibrium Isotherm	220
V.1.3.2. Nernst-Planck based model for fixed-bed ion exchange.....	220
V.1.3.3. Analytic breakthrough models	223
V.1.3.4. Numerical methods and calculations approach	224
V.1.4. Results and discussion.....	225
V.1.4.1. Materials characterization	225
V.1.4.2. Fixed-bed experimental results and selectivity assessment	227
V.1.4.3. Fixed-bed modelling results	230
V.1.4.4. Photoluminescence results	236
V.1.5. Conclusions	237
V.1.6. Nomenclature.....	238
V.2. Batch and fixed-bed removal of Cs ⁺ from aqueous solutions using ETS-4: Measurement and modeling of loading-regeneration cycles and equilibrium.....	242
V.2.1. Introduction	242
V.2.2. Modelling.....	243
V.2.3. Materials and Methods	247
V.2.3.1. Chemicals and materials	247
V.2.3.2. Synthesis and characterization.....	247
V.2.3.3. Fixed-bed and batch ion exchange experiments	248
V.2.4. Results and discussion.....	250
V.2.4.1. Materials characterization	250
V.2.4.2. Ion exchange isotherm.....	251

V.2.4.3.	Fixed-bed experimental results	252
V.2.4.4.	Fixed-bed modelling results – Nernst-Planck based model.....	256
V.2.5.	Conclusions	258
V.2.6.	Nomenclature	259
V.3.	References	263

Work reported in the scientific article

Cs⁺ removal and optical detection by microporous lanthanide silicate Eu-AV-20 in a fixed-bed column

published on Chemical Engineering Journal 286 (2016) 48-58

Abstract

Microporous silicate Eu-AV-20 has recently proved to be a promising ion exchange material for cesium removal from aqueous solutions, and its potential for Cs⁺ photoluminescence sensing was additionally demonstrated. In this work, Cs⁺ removal was performed in a fixed-bed column, and the influence of linear velocity and mass of ion exchanger on the breakthrough curves was analyzed. The experimental data were modelled on the basis of Nernst-Planck (NP) equations and with four well-known analytic models. The analytic expressions provided low errors (root mean square deviation, RMSD, between 3.20% and 6.47%); the 2-parameter NP-based model fitted the data quite well (RMSD = 6.66% for correlation and 6.54% for prediction), yielding crucial information on both the transport mechanism within the Eu-AV-20 particles, and the intrinsic dynamic behaviour of the fixed-bed ion exchange column. Taking into account that Eu-AV-20 samples loaded with different amounts of Cs⁺ exhibited distinct photoluminescence spectra, our results reinforce the potential of AV-20 materials for Cs⁺ sensing, which raises the possibility of online monitoring the ion exchange in a fixed-bed column using an optical fiber and a spectrometer.

V.1. Cs⁺ removal and optical detection by microporous lanthanide silicate Eu-AV-20 in a fixed-bed column

V.1.1. Introduction

Nuclear wastes are complex systems containing fission products including two long-lived cesium isotopes (¹³⁵Cs and ¹³⁷Cs with a half-life of 2.3 million years and 30.17 years, respectively). The negative effects of cesium are well known and encompass medullary dystrophy, disorders of the reproductive function, and adverse effects on the liver and renal functions of mammals [1]. In soil and water environments cesium exists predominantly as a free monovalent ion (Cs⁺) since the formation of organic and inorganic cesium complexes is insignificant [2]. Several approaches may be deployed to eliminate cesium from radioactive aqueous wastes, such as chemical precipitation, evaporation, reverse osmosis, filtration, solvent extraction, ion exchange and adsorption [3]. However, ion exchange is usually preferred for water and wastewater remediation, particularly when high-purity water is required [3–5], since they allow concentrating metal ions to a level where disposal, destruction, or subsequent use are affordable.

Ion exchange can be implemented as a batch process in a stirred tank or in a continuous fixed-bed (column) operation. The last alternative is preferred from an industrial point-of-view because: (i) it is the most effective configuration for cyclic sorption-desorption stages; (ii) a nearly solute-free effluent may be obtained until the exchanger agent in the bed approaches equilibrium; (iii) the removal efficiency is usually better due to higher sorbate concentration gradients between solution and solid. Some examples of ion exchange studies in fixed-beds include the uptake of zinc by NaY zeolite [6], the removal of mercury and lead by titanosilicates ETS-4 and ETS-10, respectively [7,8], and the sorption of cesium by titanosilicate granules [9]. Most recently, the elimination of Hg(II) and Pt(IV) from aqueous solutions have been studied using fixed-beds composed of chelating resins [10–12].

Inorganic ion exchangers are well-known for their chemical, thermal, mechanical and radiation stabilities, and typically exhibit high capacity and selectivity towards a wide variety of monovalent and divalent metal cations [3,4,10–20]. Concerning the specific use of inorganic solids for Cs⁺ removal, three main families have been studied, zeolites [18,19],

hexacyanoferrates [20,21] and titanosilicates [9,22,23]. Nevertheless, their use in fixed-bed experiments is limited [9,24,25].

In the early years of this century, the synthesis of zeolite-type rare-earth or lanthanide-silicate (Ln-silicates) materials was an emerging field due to their interesting optical properties associated to transitions between 4f orbitals, which generate atomic-like emission spectra displaying characteristic sharp lines [26,27]. The existence of other species in the vicinity of the emitter lanthanide may affect the photoluminescence spectra, which raises the possibility of exploring such optical properties for sensing the presence of molecules/ions [27].

The microporous Ln-silicate Eu-AV-20 and the mineral tobermorite 11 Å [28] have a similar crystal structure, encompassing 5.8 Å x 6.8 Å channels and cavities containing exchangeable Na⁺ and K⁺ ions coordinated with framework oxygen atoms and water molecules [29]. Furthermore, the presence of stoichiometric amounts of europium affords photoluminescence properties to Eu-AV-20 [29,30]. Figueiredo et al. [31] assessed the ion-exchange capacity of Eu-AV-20 for Cs⁺ removal from aqueous solutions in a stirred batch tank, and found that indeed the photoluminescence of Eu-AV-20 does change upon Cs⁺ uptake.

Here, we study Cs⁺ removal in a fixed-bed column and evaluate the photoluminescence properties of Cs⁺-exchanged Eu-AV-20. The experimental breakthrough curves were modelled using two distinct approaches: Nernst-Planck (NP) based model, and commonly used analytic models, such as the Thomas, Bohart-Adams, Yoon-Nelson and Clark models.

V.1.2. Materials and Methods

V.1.2.1. Chemicals and materials

Extra pure sodium silicate solution (HS code 2839 19 00), potassium hydroxide (CAS number 1310-58-3) and sodium hydroxide (CAS number 1310-73-2) were supplied by Merck. Europium(III) chloride hexahydrate (CAS number 13759-92-7) and cesium nitrate (CAS number 7789-18-6) were purchased from Sigma-Aldrich. High-purity water (18.2 MΩcm) was produced in a Milli-Q Millipore water purification system and the cellulose acetate membrane disc filters were bought from Sterlitech Corporation.

V.1.2.2. Synthesis and characterization of Eu-AV-20

The hydrothermal synthesis of Eu-AV-20 was performed as previously described [29]. Briefly, an alkaline solution was prepared by mixing a sodium silicate solution ($\text{Na}_2\text{O}(\text{SiO}_2)_x \cdot x\text{H}_2\text{O}$, 5.75 g), with H_2O (16.51 g), KOH (3.25 g) and NaOH (1.07 g) followed by the addition of $\text{EuCl}_3 \cdot 6\text{H}_2\text{O}$ (1.37 g) and stirring the mixture thoroughly. The resulting gel (with molar ratios 0.79 Na_2O : 1.10 K_2O : 1.0 SiO_2 : 0.07 Eu_2O_3 : 35 H_2O) was transferred to a Teflon-lined autoclave and heated at 230 °C under autogenous pressure, during 3 days. After quenching the autoclave in cold water the off-white microcrystalline powder was filtered-off, washed at room temperature with distilled water, and dried overnight at 100 °C [29]. The relevant features of this material are summarized in Table V.1.1.

Table V.1.1 – Features of the synthesized Eu-AV-20 lanthanide silicate [28].

Formula	$\text{Na}_{1.08}\text{K}_{0.5}\text{Eu}_{1.14}\text{Si}_3\text{O}_{8.5} \cdot 1.78\text{H}_2\text{O}$
Density, ρ_s (kg m ⁻³)	3080
Cation exchange capacity, Q (eq. kg ⁻¹)	2.55
Equivalent particle diameter (10 ⁻⁶ m)	23.1
Pore diameter (10 ⁻¹⁰ m)	5.8 x 6.8

V.1.2.3. Characterization and analytic methods*Photoluminescence spectroscopy.*

The photoluminescent spectra of native and Cs⁺-exchanged Eu-AV-20 samples (oven-dried at 353.15 K during 48 h) were recorded in the visible region, at room temperature, using a Jobin Yvon-Spex spectrometer (HR 460) fitted with a 1200 grooves mm⁻¹ grating blazed at 500 nm, coupled to a R928 Hamamatsu photomultiplier. A 150 W Xenon arc lamp coupled to an excitation monochromator Jobin Yvon-Spex (TRIAX 180) fitted with a 1200 grooves mm⁻¹ grating blazed at 330 nm was used as excitation source. All spectra were corrected for the response of the detectors.

Scanning Electron Microscopy (SEM) and Energy-Dispersive X-Ray Spectroscopy (EDS).

Particle dimensions and morphology of native and Cs⁺-exchanged Eu-AV-20 samples were

assessed by SEM analysis using a Hitachi S4100 microscope. EDS was used to confirm the cesium uptake by Eu-AV-20.

Powder X-Ray Diffraction (PXRD).

PXRD was carried out on a PANalytical Empyrean diffractometer (Cu K_{α1,2}X-radiation, $\lambda_1 = 1.540598 \text{ \AA}$; $\lambda_2 = 1.544426 \text{ \AA}$) equipped with an PIXcel 1D detector and a flat-plate sample holder in a Bragg-Brentano para-focusing optics configuration (45 kV, 40 mA). Intensity data were collected by the step-counting method (step 0.04°), in continuous mode, in the range $ca. 5 \leq 2\theta \leq 50^\circ$.

Cesium concentration in solution.

The concentration of Cs⁺ in solution was measured with a Perkin Elmer AAnalyst 100 atomic absorption spectrometer, in the emission mode (with a wavelength of 852.1 nm and a slit of 0.2 nm) and using an air-acetylene flame. The ionization was controlled by the addition of 0.5% (wt.) of potassium chloride to samples and standards. Each sample was

V.1.2.4. Fixed-bed and batch ion experiments

Preparation of the fixed-bed column. The column consisted of a vertical stainless steel tube (length 10.0 cm and internal diameter 1.30 cm) containing a precise amount of Eu-AV-20 (Figure 1). The solid was placed in the tube and confined at both ends by four to six quartz wool discs (from Elemental Microanalysis), followed by one stainless steel net, and the assembly was closed with Swagelok® fittings. The bottom of the column was connected to the influent reservoir and the top of the column was connected to a sampler (Figure V.1.1).

Preparation of solutions. A Cs⁺ stock solution (10.0 mol m⁻³) was prepared by dissolving CsNO₃ (0.0980x10⁻³ kg, 5.03x10⁻⁴ mol) in high-purity water (50.0 mL). Working solutions were prepared by diluting the stock solution to the desired concentration, using high-purity water, immediately before their usage to avoid cation adsorption on the glassware and lab material.

Fixed-bed ion exchange experiments. In a typical experiment a freshly prepared solution containing a known concentration of Cs⁺ was fed to the bottom of the column (up-flow mode) at constant flow rate using a peristaltic pump (Knauer Smartline pump 100). The pH and

temperature were measured at column inlet using a pH meter (Crison Basic 20). Periodically, 15 mL samples were collected at the outlet of the column after passing an acid washed cellulose acetate membrane disc filter (0.45 µm). The concentration of Cs⁺ in the samples was measured by atomic emission spectroscopy. Operation of the column was stopped for equal influent and effluent concentrations of Cs⁺. A control experiment (i.e. without Eu-AV-20 in the column) was run to check that Cs⁺ removal occurred by ion exchange with the solid rather than by adsorption on the lab material.

A set of five experiments (Table V.1.2) was performed to assess the influence of superficial velocity ($0.40\text{--}1.03\times 10^{-3}\text{ m s}^{-1}$) and mass of ion exchanger ($0.42\text{--}0.85\times 10^{-3}\text{ kg}$) on the Cs⁺ removal efficiency. Exps. 1–3 were performed for similar cesium influent concentration (ca. 1.4 ppm) and mass of solid (ca. $0.43\times 10^{-3}\text{ kg}$) to study the influence of the superficial velocity. The effect of exchanger mass can be evaluated from Exps. 2 and 4. The last run (Exp. 5) was carried out for a shorter period, under the same conditions of Exp. 3, to obtain Eu-AV-20 with an intermediate amount of Cs⁺ (ca. 65% of the breakthrough curve, 80% of the exchange capacity) in order to assess reproducibility and the dependence of photoluminescence on the cesium content in the sorbent.

Batch ion experiments. An additional set of four batch experiments (Table V.1.3) was carried out to evaluate the selectivity of Eu-AV-20 towards Cs⁺ in the presence of Na⁺. The initial concentration of cesium was fixed around $5\times 10^{-3}\text{ mol m}^{-3}$ and the initial sodium nitrate concentrations were 0, 1.02, 10.00 and 52.42 mol m⁻³, which means the molar ratios were 0, 193, 2000 and 9456, respectively. The mass of Eu-AV-20 was always ca. $3\times 10^{-4}\text{ kg}$ and the run time 150 h to ensure system equilibration. Preparation of the solutions and cesium quantification were performed as described above.

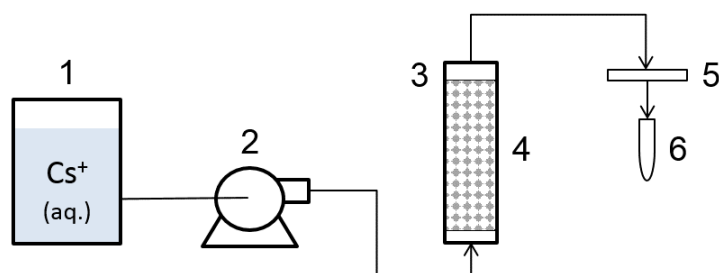


Figure V.1.1 – Experimental setup of the ion exchange unit: 1) influent reservoir tank; 2) peristaltic pump; 3) fixed-bed column in up-flow mode; 4) Eu-AV-20 powder bed; 5) membrane disc filter; and 6) sample collecting tube.

Table V.1.2 – Eu-AV-20 fixed-bed ion exchange experiments performed at 295 ± 1 K.

Experiment number	1	2	3	4	5
Inlet concentration of Cs ⁺ (mol m ⁻³)	0.0107	0.0108	0.0108	0.0111	0.0107
Inlet concentration of Cs ⁺ (ppm)	1.422	1.435	1.435	1.475	1.422
Bed height (m)	0.010	0.010	0.010	0.016	0.010
Mass of Eu-AV-20 (10 ⁻³ kg)	0.424	0.424	0.436	0.853	0.438
Superficial velocity (10 ⁻³ m s ⁻¹)	1.03	0.618	0.399	0.618	0.402
Run time (h)	50	50	50	50	15

Table V.1.3 – Eu-AV-20 competitive ion exchange in batch experiments performed at 295 ± 1 K.

Experiment number	1	2	3	4
Initial concentration of Cs ⁺ (mol m ⁻³)	0.0055	0.0050	0.0053	0.0047
Initial concentration of Na ⁺ (mol m ⁻³)	52.42	10.00	1.02	0
Initial Na ⁺ /Cs ⁺ molar ratio	9456	2000	193	0
Mass of Eu-AV-20 (10 ⁻³ kg)	0.301	0.308	0.306	0.302
Run time (h)	150			

V.1.3. Modelling isotherms and breakthrough curves

V.1.3.1. Equilibrium Isotherm

Ion exchange is often represented as a conventional chemical reaction, since it is a stoichiometric process by which two counter ions, A^{z_A} and B^{z_B} , are exchanged between an electrolyte solution and a solid exchanger [32,33]. Generically, an ion exchange process is represented by:



where z_A and z_B are the electrochemical valences of both counter ions, and the capping bar denotes the exchanger phase. According to Eq. (V.1.1), the exchanger is in B^{z_B} form and is converted into A^{z_A} form. For the particular case in analysis, $A^{z_A} = \text{Cs}^+$, $B^{z_B} = \text{Na}^+, \text{K}^+$, which, for simplicity, will be henceforth designated by A and B.

The isotherm of $\text{Cs}^+(\text{Na}^+, \text{K}^+)/\text{Eu-AV-20}$ system was determined by Figueiredo et al. [31], who represented the equilibrium data with 5.3% of error by the Langmuir equation:

$$q_{A,\text{eq}} = \frac{125048 \times C_{A,\text{eq}}}{1 + 437.5 \times C_{A,\text{eq}}} \quad (V.1.2)$$

where $C_{A,\text{eq}}$ is the equilibrium concentration of A in solution (mol m^{-3}) and $q_{A,\text{eq}}$ is the equilibrium concentration of A in the solid, here expressed in mol m^{-3} .

V.1.3.2. Nernst-Planck based model for fixed-bed ion exchange

The ion-exchange process was modelled using the Nernst-Planck equations, which state that the net intraparticle fluxes (N_i , $\text{mol m}^{-2} \text{s}^{-1}$) result from molar concentration (q_i , mol m^{-3}) gradients and electric potential gradient. For counter ion A, the flux is given by [16,17,32,33]:

$$N_A = -\frac{D_A D_B (z_A^2 q_A + z_B^2 q_B)}{D_A z_A^2 q_A + D_B z_B^2 q_B} \left(\frac{\partial q_A}{\partial r} \right) = -D_{AB} \left(\frac{\partial q_A}{\partial r} \right), \quad D_{AB} \equiv \frac{D_A D_B (z_A^2 q_A + z_B^2 q_B)}{D_A z_A^2 q_A + D_B z_B^2 q_B} \quad (V.1.3)$$

where D_A and D_B ($\text{m}^2 \text{s}^{-1}$) are the self-diffusion coefficients of both counter ions, r (m) is the radial position in the particle, and D_{AB} ($\text{m}^2 \text{s}^{-1}$) is the interdiffusion coefficient. The ion exchanger capacity is given by: $Q(\text{eq m}^{-3}) = q_A z_A + q_B z_B$.

The fixed-bed model encompasses a material balance to the column, Eq. (V.1.4), with an axial dispersion term, a convective term, and two accumulation terms for the fluid and solid phases, whose boundary conditions are given by Eqs. (V.1.5) and (V.1.6):

$$\frac{\partial C_A(l, t)}{\partial t} = D_L \frac{\partial^2 C_A(l, t)}{\partial l^2} - u \frac{\partial C_A(l, t)}{\partial l} - \frac{1 - \varepsilon}{\varepsilon} \frac{\partial \bar{q}_A(l, t)}{\partial t} \quad (\text{V.1.4})$$

$$l = 0, \quad D_L \frac{\partial C_A(l, t)}{\partial l} \Big|_{l=0^+} = -u(C_{A,0} - C_A|_{l=0^+}) \quad (\text{V.1.5})$$

$$l = L, \quad \frac{\partial C_A(l, t)}{\partial l} \Big|_{l=L} = 0 \quad (\text{V.1.6})$$

Here, C_A is the molar concentration of species A in solution (mol m^{-3}), u is the superficial velocity (m s^{-1}), l is the position along the bed length (m), L is the total length of the bed (m), t is time (s), D_L is the axial dispersion coefficient ($\text{m}^2 \text{s}^{-1}$), ε is the average bed porosity ($\varepsilon = 0.88$), \bar{q}_A is the average concentration of A in the solid (mol m^{-3}), and $C_{A,0}$ is the concentration of A at the column inlet. D_L was estimated using the following correlation [34]:

$$D_L = (20 + 0.5 \times \text{Sc} \times \text{Re}) \times \frac{D_m}{\varepsilon} \quad (\text{V.1.7})$$

where D_m is the diffusivity of Cs⁺ in water ($2.06 \times 10^{-9} \text{ m}^2 \text{s}^{-1}$ at 298.15 K [35]) and Sc and Re are the Schmidt and Reynolds numbers, respectively.

The material balance to the ion exchanger is given by Eq. (V.1.8). Eqs. (V.1.9)-(V.1.11) represent its initial and boundary conditions, and Eq. (V.1.12) translates the equality of fluxes at the interface:

$$\frac{\partial q_A}{\partial t} = -\frac{1}{r^2} \frac{\partial}{\partial r} (r^2 N_A) \quad (\text{V.1.8})$$

$$t = 0, \quad \begin{cases} q_A = 0 \\ C_A = C_{A,0} \end{cases} \quad (\text{V.1.9})$$

$$r = 0, \quad \frac{\partial q_A}{\partial r} = 0 \quad (\text{V.1.10})$$

$$r = R_p, \quad q_A = q_{A,R_p} \quad (\text{V.1.11})$$

$$N_A|_{R_p} = k_f (C_A - C_A|_{R_p}) \quad (\text{V.1.12})$$

R_p is the particle radius (m), $C_A|_{R_p}$ is the concentration at the interface, and k_f is the convective mass transfer coefficient (m s⁻¹) of counter ion A. The value of k_f was estimated by the following correlation involving classical Sherwood (Sh), Reynolds (Re) and Schmidt (Sc) numbers [8]:

$$\text{Sh} = \frac{1.13}{\varepsilon} \text{Re}^{0.21} \text{Sc}^{1/3} \quad (\text{V.1.13})$$

The average loading per unit particle volume needed in Eq. (V.1.4) is calculated by:

$$\bar{q}_A = \frac{3}{R_p^3} \int_0^{R_p} r^2 q_A dr \quad (\text{V.1.14})$$

The stoichiometric time, t_{st} (h), of a breakthrough curve can be calculated by Eq. (V.1.15) using experimental data or estimated on the basis of the solute movement theory by Eq. (V.1.16):

$$t_{st} = \int_0^\infty \left(1 - \frac{C_A(t)}{C_{A,0}} \right) dt \quad (\text{V.1.15})$$

$$t_{st} = \frac{L}{v} \left(1 + \frac{1 - \varepsilon}{\varepsilon} \frac{q_{A,0}}{C_{A,0}} \right) \quad (\text{V.1.16})$$

where $q_{A,0}$ is the solid loading in equilibrium with feed concentration, $C_{A,0}$.

V.1.3.3. Analytic breakthrough models

The equations of Clark [36], Yoon-Nelson [37], Bohart-Adams [38], and Thomas [39] were adopted in this study to model the breakthrough curves along with the Nernst-Planck based model.

The Thomas model [39] assumes Langmuir kinetics for sorption-desorption, negligible axial and radial dispersion, and a second-order reversible kinetics. The most common version of this model in environmental sorption and biosorption literature is given by:

$$\frac{C_A(t)}{C_{A,0}} = \frac{1}{1 + e^{\left[\frac{k_{Th}}{v}(Q_{Th}m - C_{A,0}vt)\right]}} \quad (V.1.17)$$

where k_{Th} is the Thomas rate constant ($m^3 \text{ mol}^{-1} \text{ s}^{-1}$), Q_{Th} is the maximum concentration of the solute in the solid phase (mol kg^{-1}), m is the mass of solid (kg), and v is the volumetric flow rate ($m^3 \text{ s}^{-1}$).

The Bohart-Adams model, initially developed to describe the adsorption of chloride on charcoal [38], assumes that the sorption rate is proportional to the residual capacity of the exchanger and to the concentration of the solute species in solution. Its equation may be expressed as:

$$\frac{C_A(t)}{C_{A,0}} = \frac{1}{1 + e^{[k_{BA}(q_{A,max} \tau - C_{A,0} t)]}} \quad (V.1.18)$$

where k_{BA} is the Bohart-Adams mass transfer coefficient ($m^3 \text{ mol}^{-1} \text{ s}^{-1}$), $q_{A,max}$ is the saturation concentration (mol m^{-3}), and $\tau = L/u$ is the space time (s).

The major difference between the Thomas and Bohart-Adams models lies in the embodied isotherms: the first one uses Langmuir and the latter adopts a rectangular or irreversible isotherm. Therefore, for highly favourable isotherms the Thomas model reduces to the Bohart-Adams equation and their parameters become interchangeable, i.e. $k_{Th} = k_{BA}$ and $Q_{Th}m/v = q_{A,max} \tau$ [40].

The Clark model [36] combines mass transfer concepts and the Freundlich isotherm, and it assumes plug flow and negligible dispersion phenomena. It is mathematically given by:

$$\frac{C_A(t)}{C_{A,0}} = \left[\frac{1}{1 + A_C e^{-\omega t}} \right]^{\frac{1}{n-1}} \quad \text{with} \quad A_C = \left(\frac{C_{A,0}^{n-1}}{C_b^{n-1}} - 1 \right) e^{\omega t_b} \quad (\text{V.1.19})$$

where n is the Freundlich constant, and C_b is the solute concentration (mol m⁻³) at breakthrough time, t_b (h), and ω is a rate parameter (h⁻¹).

The Yoon-Nelson model [37] assumes that the rate of decrease in the probability of sorption for each sorbate molecule is proportional to the probability of sorbate sorption and sorbate breakthrough on the sorbent. The model does not require detailed data concerning solute characteristics, type of sorbent and physical properties of the bed. For a single component system it is expressed by:

$$\frac{C_A(t)}{C_{A,0}} = \frac{e^{[k_{YN}(t-t_{50})]}}{1 + e^{[k_{YN}(t-t_{50})]}} \quad (\text{V.1.20})$$

where k_{YN} denotes the Yoon-Nelson rate constant (h⁻¹), and t_{50} is the time for $C_A/C_{A,0} = 0.5$.

V.1.3.4. Numerical methods and calculations approach

The Method of Lines was applied for the numerical calculation of the concentration profiles of Cs⁺, and their evolution along time in the solution and in the solid phase, for the case of the NP-based model. The required spatial discretization in the particle and bed length was accomplished by Finite Differences. The resulting initial-value problem set of ordinary differential equations was solved numerically using 51 grid points for the particle radius and 31 grid points for the bed length.

Regarding the NP-based model, the self-diffusion coefficients (D_A and D_B) were fitted to the data of Exp. 1 only, while k_f values were estimated by Eq. (V.1.13). Therefore, only two initial guesses were required to model Exp. 1, and the breakthrough curves of Exps. 2–4 were completely predicted.

In what concerns the so-called Thomas and Bohart-Adams models, Eqs. (V.1.17) and (V.1.18), the calculations involved four individual constants (k_{Th} or k_{BA}), one for each run, plus one shared parameter (Q_{Th} or $q_{A,max}$). In turn, the Clark and Yoon-Nelson models (Eqs.

(V.1.19) and (V.1.20)) were adjusted considering one pair of parameters per curve: (ω , A_C) and (k_{YN} , t_{50}). Moreover, for the Clark model the values of A_C and ω were determined by nonlinear regression of breakthrough data, using the Freundlich constant ($n = 2.368$) obtained by fitting the adsorption isotherm to published equilibrium points [31]. Although the Freundlich isotherm is not the best model to represent the Cs⁺/(Na⁺,K⁺)/Eu-AV-20 system, the fitting was acceptable (9.74% error).

The Nelder-Mead and the Marquardt-Levenberg algorithms were adopted in this work for all optimizations using the root mean square deviation (RMSD) as objective functions:

$$\text{RMSD (\%)} = 100 \times \sqrt{\sum_{i=1}^{\text{NDP}} \frac{(C_{A,\text{calc}}|_i - C_{A,\text{exp}}|_i)^2}{\text{NDP}}} \quad (\text{V.1.21})$$

where NDP is the number of data points, and the subscripts 'exp' and 'calc' denote measured and calculated concentrations, respectively. All programs were written and coded in Matlab R2013a®.

V.1.4. Results and discussion

V.1.4.1. Materials characterization

SEM images of native and Cs⁺-exchanged Eu-AV-20 crystals are similar (Figure V.1.2) and reveal microcrystalline pseudo hexagonal thin plates with a lateral dimension lower than 20×10^{-6} m, which is consistent with previous reports [31]. With respect to EDS results, Figure 3 confirms that the Cs⁺ was sorbed because cesium is absent in the native material (see Figure V.1.3.a) while it appears in the solid after ion exchange (see Figure V.1.3.b).

The experimental PXRD pattern of native Eu-AV-20 (Figure V.1.4) shows all the characteristic reflections [29] and no impurity phases are detected. The PXRD patterns of the samples collected after the fixed-bed experiments (Exps. 1–5, Table V.1.2) exhibit some changes, such as peak shifts from 14.21° to 14.36°, from 31.25° to 31.38° and from 32.27° to 32.43°, the increment of intensity of the peak at 28.95° and the presence of a new peak at 30.09°. Altogether, these results indicate slight changes in the crystalline structure of Cs⁺-

exchanged Eu-AV-20, which may result in alterations in the local Eu^{3+} environment that impact on the photoluminescence properties (to discuss in Section V.1.4.4).

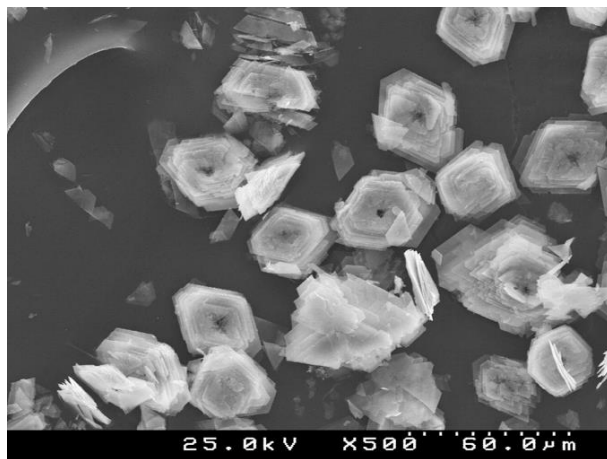


Figure V.1.2 – SEM image of Eu-AV-20 crystals.

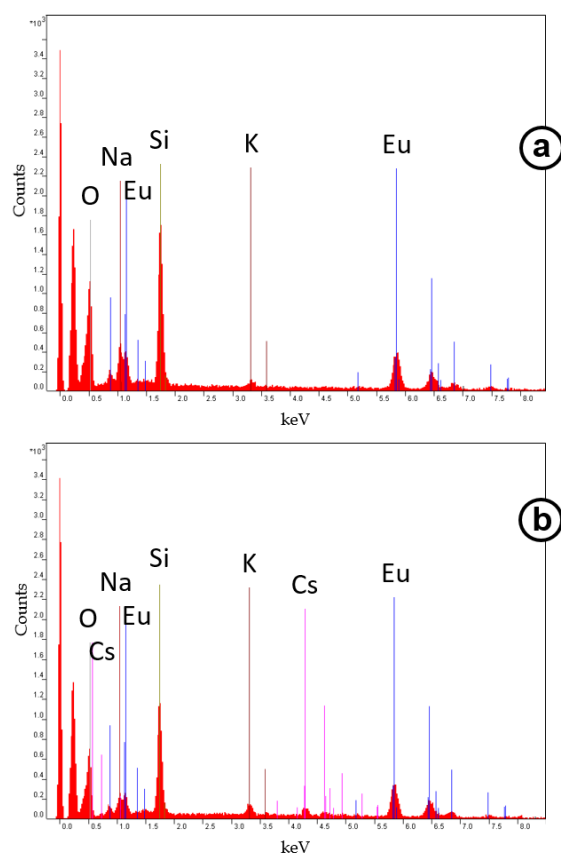


Figure V.1.3 – EDS spectra of (a) native and (b) Cs^+ -exchanged Eu-AV-20 samples.

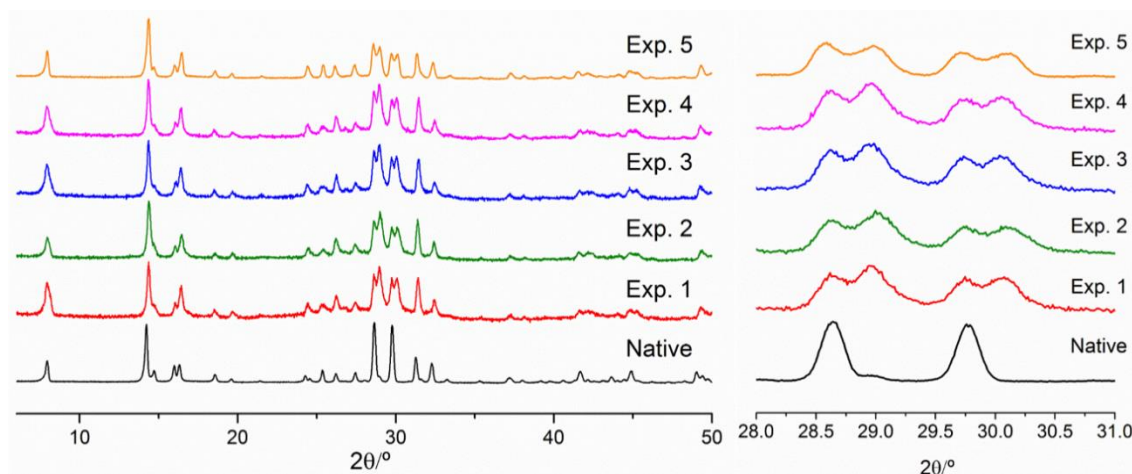


Figure V.1.4 – PXRD of native and Cs⁺-exchanged Eu-AV-20 samples collected after the fixed-bed experiments (Exps. 1–5, see Table V.1.2). Inset: PXRD on an expanded scale in the range 28–31°.

V.1.4.2. Fixed-bed experimental results and selectivity assessment

The breakthrough curves (Exps. 1–4, Table V.1.2) are plotted in Figure 5 grouped according to the different variables under study, namely, the superficial velocity (varied *via* flow rate modification) (Exps. 1–3, Figure V.1.5.a), and the mass of ion exchanger (Exps. 2 and 4, Figure V.1.5.b). The plots illustrate the evolution of the normalized cesium concentration in solution at the column outlet, $C_A(t)/C_{A,0}$.

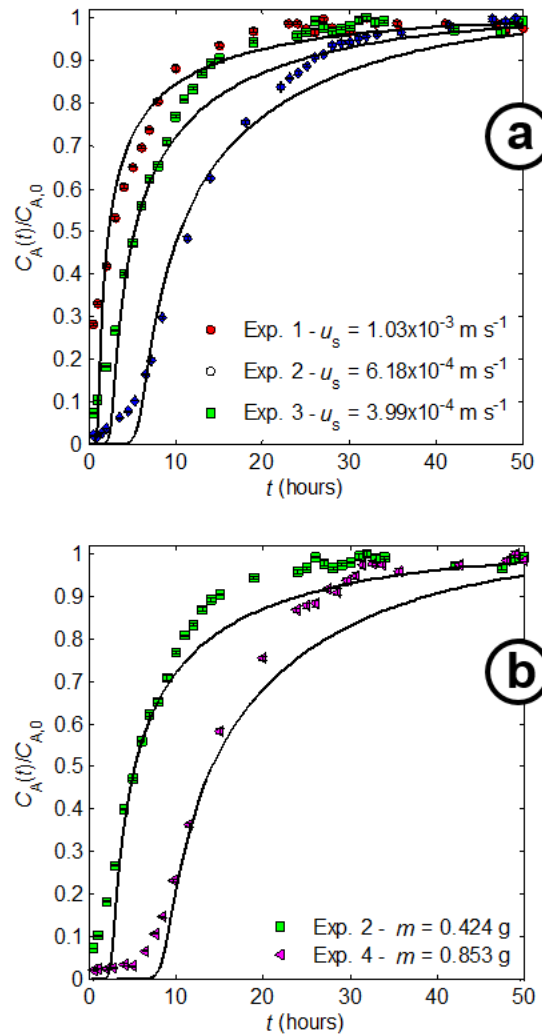


Figure V.1.5 – Normalized experimental breakthroughs for Cs^+ removal in a fixed-bed of Eu-AV-20. (a) Effect of superficial velocity (*via* flow rate variation); (b) Effect of the mass of ion exchanger. Symbols: data (experimental conditions in Table V.1.2); lines: NP-based model.

Considering that the isotherm of the $\text{Cs}^+ / (\text{Na}^+, \text{K}^+) / \text{Eu-AV-20}$ system is favourable, *i.e.*, convex upward (see Eq. (V.1.2)), in the absence of dispersive phenomena (such as axial dispersion and/or film and intraparticle resistances to mass transfer) a step-function would propagate ideally without changes along the fixed-bed and would exit the column at a precise instant, the stoichiometric time (t_{st}) given by Eqs. (V.1.15) or (V.1.16). Hence, the experimental ion exchange breakthrough curves shown in Figure 5 clearly disclose that mass transfer effects prevail in this system.

The influence of axial dispersion is certainly negligible since the calculated axial Peclet numbers ($Pe_L = uL/D_{ax}$) were 174.5, 115.1, 78.7 and 178.6 for Exps. 1–4, and the well-known relation $L > 50 d_p$ was largely obeyed ($d_p = 2.3 \times 10^{-5}$ m and L was 0.010 m (Exps. 1–3) or 0.016 m (Exp. 4)). Regarding external resistance to mass transfer, the width of the breakthrough curves changed with flow rate variation, *i.e.*, they increased with decreasing superficial velocity (Exps. 1–3), which indicates the existence of film diffusion limitations. This observation was also confirmed by simulation (to be further discussed below).

According to the breakthroughs curves (Exps. 1–3, Figure V.1.5.a), lower superficial velocities require higher operating times to exhaust the solid phase, and vice-versa. This result is in agreement with the solute movement theory, Eq. (V.1.16), since the stoichiometric time (t_{st}) is inversely proportional to superficial velocity. The t_{st} values calculated from experimental data were 4.96, 7.53 and 13.80 h (for Exps. 1, 2 and 3, respectively).

To study the impact of ion exchanger mass on the breakthrough curves, the mass of Eu-AV-20 was increased 100% (Exp. 4 *versus* Exp. 2). The two breakthrough curves (Figure V.1.5.b) are considerably different especially in what concerns the 5 h delay period observed in Exp. 4, before the consistent and visible rise of $C_A(t)$. Once again, the solute movement theory provided excellent results, since $t_{st,4}/t_{st,2} = 15.62/7.53 = 2.07$, which is almost equal to the ratio of sorbent masses, $m_4/m_2 = 0.853/0.424 = 2.0$ (calculated by Eq. (V.1.16) considering also that $L \propto m$).

A preliminary study of ion exchange competition was performed in order to analyse the influence of the presence of Na⁺ upon cesium uptake (see experimental conditions in Table V.1.3). The final uptake of Cs⁺ is plotted in Figure V.1.6 against the initial molar ratio of Na⁺ and Cs⁺, being possible to conclude that Eu-AV-20 reached Cs⁺ removals of 76.0, 70.2, 39.5 and 20.0% for 0, 193, 2000 and 9456 ratios, respectively. These values confirmed the exchanger affinity to cesium as 20% uptake was attained even when the initial sodium concentration was three orders of magnitude higher.

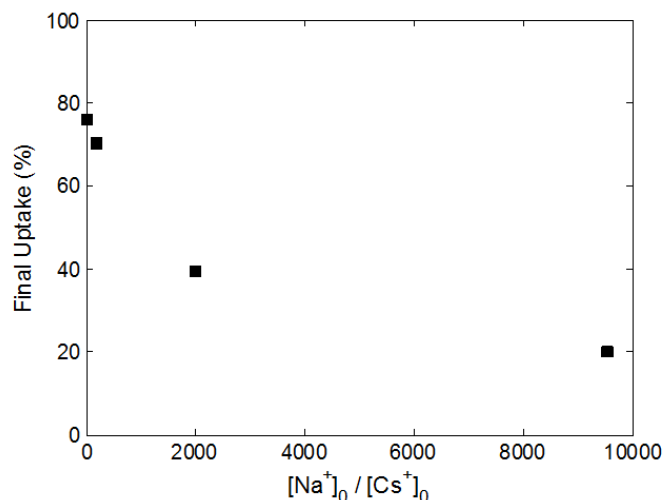


Figure V.1.6 – Final uptake of cesium as function of the initial molar ratio of Na⁺ and Cs⁺ (experimental conditions in Table V.1.3).

V.1.4.3. Fixed-bed modelling results

A model can be validated through the fitting of experimental results, but its usefulness comes mainly from its ability to predict the behaviour of a process under operating conditions different from those used to obtain its parameters [33]. In the present section, the calculated results obtained with NP-based model and by the analytic equations of Thomas, Bohart-Adams, Clark and Yoon-Nelson are presented and discussed, being demonstrated the prediction ability of the NP-based model.

Nernst-Planck based model. The results achieved in this case are plotted in Figure V.1.5 together with the experimental data (Exps. 1–4). The model parameters (D_A and D_B) were obtained by fitting the data of Exp. 1 only, with good correlation (RMSD = 6.66%), while for Exps. 2–4 pure prediction provided deviations of 6.55%, 5.24% and 7.95%, respectively (Table V.1.4) The self-diffusivities ($D_A = 2.324 \times 10^{-16} \text{ m}^2 \text{ s}^{-1}$ and $D_B = 6.134 \times 10^{-15} \text{ m}^2 \text{ s}^{-1}$) are of the same order of magnitude of those reported for the system Cd²⁺/Na⁺/ETS-10 [16], and bigger than those published for Cd²⁺/Na⁺/ETS-4 [14] and Hg²⁺/Na⁺/ETS-4 [41]. Despite the exchanged counter ions are different (Cs⁺ against of Cd²⁺ or Hg²⁺), the diffusion coefficients are consistent with the pore sizes of ETS-4 (3×4 Å), Eu-AV-20 (5.8×6.8 Å) and ETS-10 (4.9×7.6 Å). With respect to the film diffusion coefficients, their values were estimated by Eq. (V.1.13) and gave rise to 4.119×10^{-4} (Exp. 1), 3.700×10^{-4} (Exp. 2 and 4) and 3.381×10^{-4} (Exp. 3) m s⁻¹. During the

course of the simulations it was observed that k_f influences the results, meaning that the external limitation to mass transfer are not negligible.

An advantage of the Nernst-Planck based model is its breadth to understand the kinetic processes governing ion exchange in a fixed-bed column. For instance, the model describes the time evolution of the outlet cesium concentration but, above all, it discloses the concentration profiles of cesium along the column in the bulk and inside the Eu-AV-20 particles. Accordingly, the normalized Cs⁺ concentration in solution, $C_A(t)/C_{A,0}$, and the normalised average solid loading, $\bar{q}_A/q_{A,\max}$, were computed and plotted against time and longitudinal bed position for the conditions of Exp. 3, in Figure V.1.7.a and Figure V.1.7.b, respectively. The independent variables were also normalized, being $Z = l/L$ and $\theta = t/\tau$, where $\tau = L/u$ is the space time (s).

In terms of bulk solution concentration, the surface in Figure V.1.7.a illustrates both the decreasing profiles along the column (as Z goes from 0 to 1) for different exchange times, and the attenuation of these curves as time increases. As a particular case of Figure V.1.7.a, the breakthrough curve previously represented for Exp. 3 in Figure 5.a becomes visible at the column outlet ($Z = 1$).

If the focus is placed on the solid, Figure V.1.7.b evidences that Cs⁺ concentration profiles follow the same tendency as in bulk solution, displaying a delay due to the effect of mass transfer kinetics. Specifically, Cs⁺ load decreases along the column (when Z goes from 0 to 1) and increases with time, reaching 80% of the capacity established by the Langmuir isotherm, Eq. (2), for θ ca. 7000. This is expected because Eu-AV-20 particles positioned at the top of the bed contact with less concentrated solutions throughout the process and, thus, require a longer time to reach equilibrium.

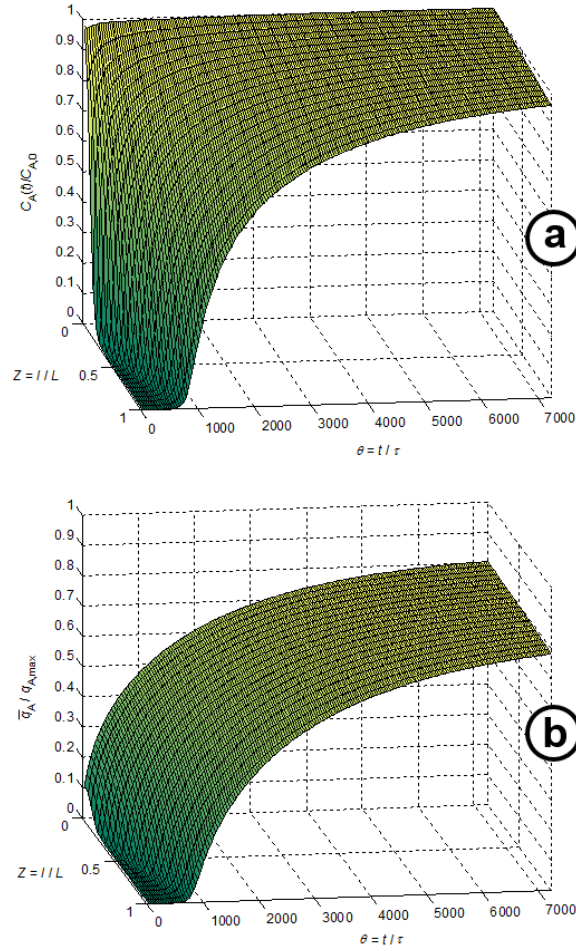


Figure V.1.7 – Normalized Cs⁺ concentration in bulk solution (a) and normalized Cs⁺ loading in the solid (b) as function of dimensionless time and longitudinal bed position. Simulations were performed for the conditions of Exp. 3 (Table V.1.2).

Analytic models. The data from Exps. 1–4 were fitted to four conventional analytic models, Eqs. (17)–(20), with good accuracy: RMSDs in the range 3.20–6.47% and R^2 between 0.962 and 0.985 (Table V.1.3). The fitting quality of the analytic models can also be assessed in Figure 8, which presents calculated *versus* experimental normalized fluid concentrations at the column outlet. In general, the four models fit the data fairly well, but consistently overestimate at low/high outlet concentrations and underestimate for intermediate concentrations, *i.e.*, in the steep rise branches of the breakthrough curves.

The smaller deviations were found for the Clark and Yoon-Nelson models (RMSD 3.64% and 3.20%, respectively) not surprisingly since both models rely on eight regressed parameters. The usefulness of such models is therefore questionable.

The other two models comprise five parameters each, with the Thomas model, which is frequently used in the literature, behaving slightly better than the Bohart-Adams model (RMSD 5.15% and 6.47%, respectively). As discussed in section V.1.3.3, a correlation between the parameters was expected in advance due to the mathematical equivalence of the models, namely $k_{\text{BA}} = k_{\text{Th}}$ and $Q_{\text{Th}}m/v = q_{\text{A,max}}L/u$. From Table V.1.3 it is possible to conclude that k_{BA} and k_{Th} are quite similar with an average absolute relative deviation of only 12.4%. Additionally, the average value of the ratio $Q_{\text{Th}}mu/(v q_{\text{A,max}} L)$ was 0.99, very close to the theoretical value of 1.

In comparison, the 2-parameter Nernst-Planck based model presents higher deviations with a RMSD of 6.53% (Table V.1.3) which is quite similar to the deviations reported in the literature for zeolite-type materials [14,16,17,41]. Despite being less expedite to implement than the four analytic models, the NP-based model presented in this work provides crucial information about the transport mechanisms inside and outside the Eu-AV-20 particles, and predicts the dynamic behaviour of the fixed-bed ion exchange column. Such potential relies on its theoretically sound assumptions.

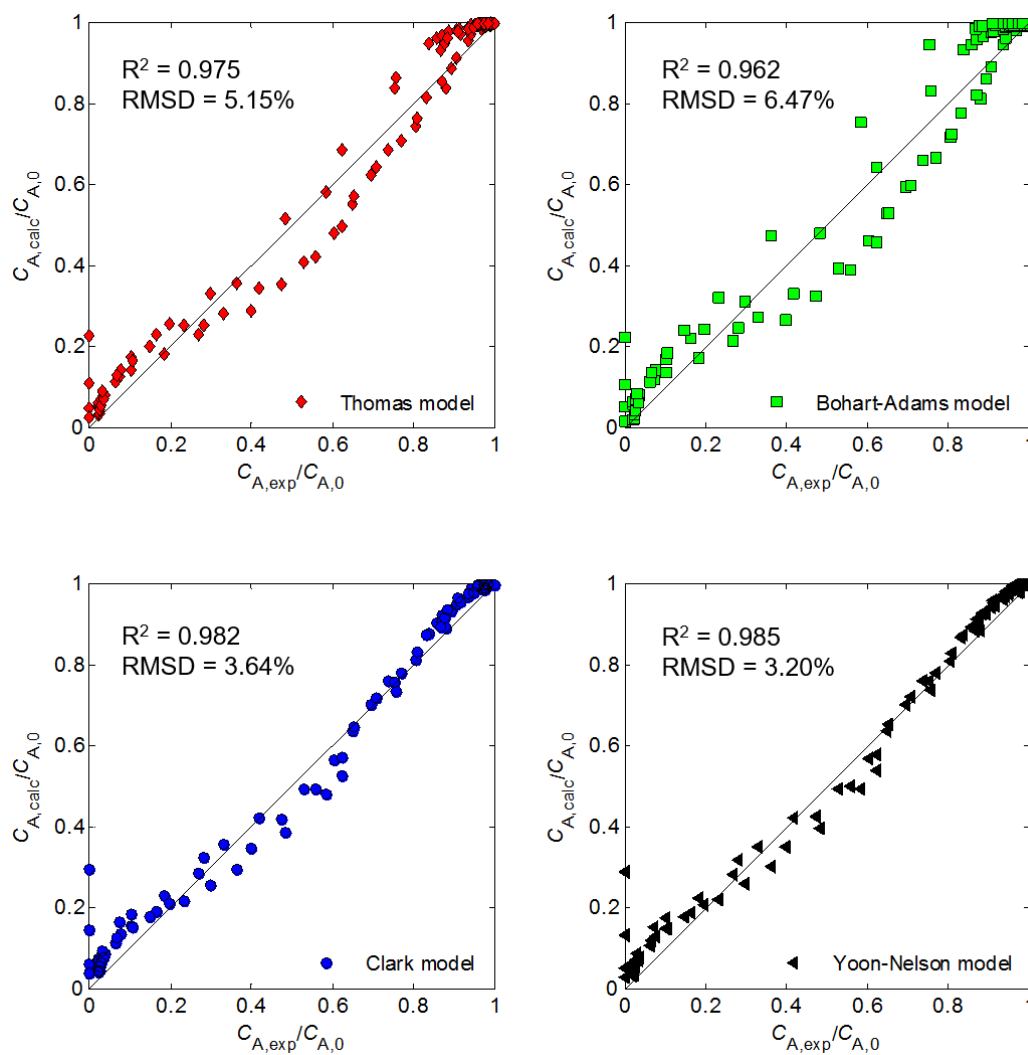


Figure V.1.8 – Comparison of the four conventional analytic models for fixed-bed ion exchange: calculated versus experimental normalized fluid concentrations at column outlet. (Experimental conditions in Table V.1.2).

Table V.1.4 – Optimized parameters and calculated deviations for the Nernst-Planck based model and for the analytic models from literature applied to the fixed-bed experiments. (Exp. conditions in Table V.1.2).

Model	Nernst-Planck based model, Eqs. (V.1.3)-(V.1.6), (V.1.8)-(V.1.12) and (V.1.14)								
Exp.	NDP	Type of calculation	D_A (m ² s ⁻¹)	D_B (m ² s ⁻¹)	RMSD (%)	Global RMSD (%)			
1	29	correlation	2.324x10 ⁻¹⁶	6.134x10 ⁻¹⁵	6.66	6.66 (correlation)			
2	32	prediction	-	-	6.55				
3	31	prediction	-	-	5.24	6.53 (prediction)			
4	28	prediction	-	-	7.95				
Model	Thomas, Eq. (V.1.17)		Bohart-Adams, Eq. (V.1.18)			Clark, Eq. (V.1.19)		Yoon-Nelson, Eq. (V.1.20)	
Exp.	NDP	k_{Th} (m ³ mol ⁻¹ s ⁻¹)	Q_{Th} (mol g ⁻¹)	k_{AB} (m ³ mol ⁻¹ s ⁻¹)	$q_{A,max}$ (mol m ⁻³)	ω (h ⁻¹)	A_C (-)	k_{YN} (s ⁻¹)	t_{50} (h)
1	29	0.0075		0.0071		0.3219	4.30	8.913x10 ⁻⁵	3.07
2	32	0.0077		0.0073		0.3461	12.91	8.708x10 ⁻⁵	5.98
3	31	0.0069	5.293x10 ⁻⁵	0.0065	18.22	0.2463	44.05	6.092x10 ⁻⁵	13.26
4	28	0.0066		0.0088		0.2642	91.14	6.508x10 ⁻⁵	15.09
		RMSD = 5.15%		RMSD = 6.47%		RMSD = 3.64%		RMSD = 3.20%	
		R ² = 0.975		R ² = 0.962		R ² = 0.982		R ² = 0.985	
RMSD = Root Mean Square Deviation; R ² = coefficient of determination									

RMSD = Root Mean Square Deviation; R^2 = coefficient of determination

V.1.4.4. Photoluminescence results

Three samples were studied, native Eu-AV-20 and two Cs⁺-exchanged materials collected after fixed-bed experiments under similar conditions, except for the time of operation (Exps. 3 and 5, Table V.1.2). Exp. 3 was performed until exhaustion of the solid's exchange capacity (ca. 50 h) while Exp. 5 was run for a shorter period (ca. 15 h) to accomplish only 80% of $q_{A,max}$ (see Figure 9.a). Therefore, in view of the different contact times the three Eu-AV-20 samples have different Cs⁺ contents. Figure V.1.9.b reveals differences in the normalized emission spectra for the non-degenerated $^5D_0 \rightarrow ^7F_0$ transitions. The native washed Eu-AV-20 possesses two distinct europium sites (Eu1 and Eu2), which give peaks at 577.9 nm and 578.9 nm. However, the replacement of sodium and potassium cations by Cs⁺ introduces small modifications in the crystalline structure, as discussed previously (section V.1.4.1 and Figure V.1.4), leading to changes in the vicinity of Eu³⁺ cations and in the photoluminescence spectra: higher Cs⁺ loads decrease the intensity of the Eu1 emission and shift the Eu2 peak to lower wavelengths (Figure V.1.9.b). Even these are preliminary results they suggest that photoluminescence may be an expedite method to assess ion exchange phenomena in Cs⁺/Eu-AV-20 systems, and in addition disclose the potential of microporous Ln-silicate Eu-AV-20 solids for cesium sensing purposes.

The fact that the Eu-AV-20 photoluminescence varies upon Cs ion exchange raises the intriguing possibility of following up this process on-line by coupling to the fixed-bed column an optical fiber and a spectrometer. In this way the solid loading can be assessed online, complementing the usual sampling of the bulk liquid along the column. This combined information is important if one takes into account that mass transfer limitations always exist which means both phases are not in equilibrium. Work along these lines is in progress.

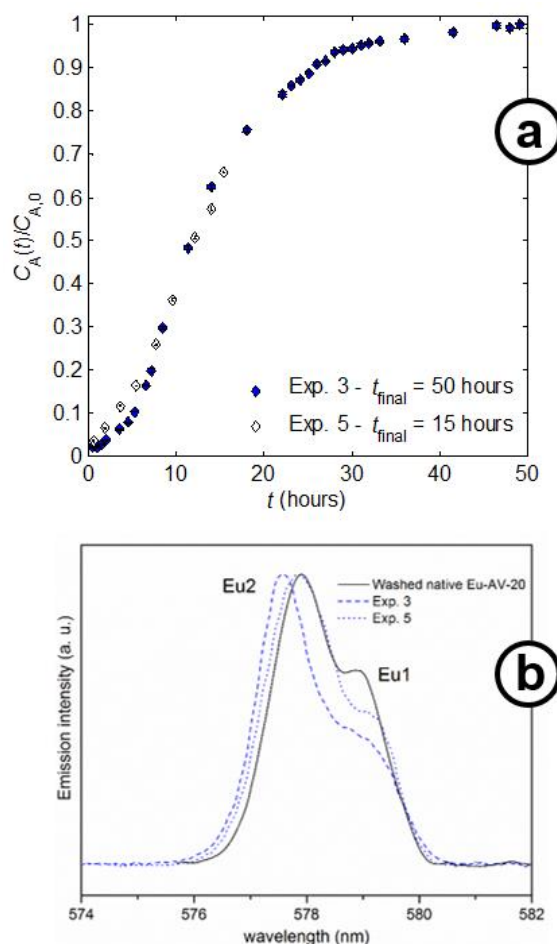


Figure V.1.9 – a) Measured breakthrough curves for two different run times (Exps. 3 and 5; experimental conditions in Table V.1.2); b) Normalized $^5\text{D}_0 \rightarrow ^7\text{F}_0$ transition of the photoluminescence emission room temperature spectra of the native and Cs^+ exchanged Eu-AV-20 with excitation at 393 nm.

V.1.5. Conclusions

The use of Eu-AV-20 for Cs^+ removal from aqueous solutions was studied in a fixed-bed column. The dynamic behaviour of the ion exchange column was in accord with theory, namely, higher solid masses and lower superficial velocities (*via* inferior flow rates) delayed the breakthrough curves. Moreover, the experimental stoichiometric times followed the solute movement theory.

The proposed Nernst-Planck based model (2 parameters) achieved $\text{RMSD} = 6.66\%$ for the correlation of one breakthrough curve, and only 6.54% for the prediction of the others. The optimized self-diffusivities were consistent with data from the literature, and followed essentially the pore size diameter of the solids. The RMSDs of Thomas, Bohart-

Adams, Clark and Yoon-Nelson models ranged between 3.20% (Yoon-Nelson, 10 parameters) and 6.47% (Bohart-Adams, 5 parameters). These reliable results are ascribed to the number of fitting parameters.

Regarding the photoluminescence of native and ion-exchanged Eu-AV-20, the uptake of Cs⁺ modifies the local environment of the Eu³⁺ emitter resulting in changes in the ⁵D₀→⁷F₀ transition intensities and line positions, indicating the potential of Eu-AV-20 for sensing purposes.

V.1.6. Nomenclature

A or A ^{z_A}	Counter ion initially in solution
A _C	Clark model parameter
B or B ^{z_B}	Counter ion initially in the exchanger
C _b	Solute concentration at breakthrough time in Clark model (mol m ⁻³)
C _A	Concentration of counter ion A in solution (mol m ⁻³)
C _{A,0}	Initial concentration of counter ion A in solution (mol m ⁻³)
D _i	Self-diffusion coefficient of counter ion <i>i</i> (m ² s ⁻¹)
D _L	Axial dispersion coefficient (m ² s ⁻¹)
D _{AB}	Interdiffusion coefficient of NP model (m ² s ⁻¹)
D _m	Diffusion coefficient of Cs ⁺ in water (m ² s ⁻¹)
Exp. j	Experiment number j
<i>i</i> and <i>j</i>	Generic counter ions
k _{BA}	Bohart-Adams mass transfer coefficient (m ³ mol ⁻¹ s ⁻¹)
k _f	Convective mass transfer coefficient (m s ⁻¹)
k _{Th}	Thomas rate constant (m ³ mol ⁻¹ s ⁻¹)
k _{YN}	Yoon-Nelson rate constant (h ⁻¹)
<i>l</i>	Column longitudinal coordinate (m)
L	Length of the fixed-bed (m)
Ln-silicate	Lanthanide silicate
<i>m</i>	Mass of ion exchanger (Eu-AV-20) (g)
<i>n</i>	Freundlich isotherm constant
NDP	Number of data points
NP	Nernst-Planck
PXRD	Powder X-ray diffraction

$q_{A,\max}$	Maximum solute concentration in the particle in Bohart-Adams model (mol m ⁻³)
$q_{A,0}$	Solid loading in equilibrium with feed concentration, $C_{A,0}$
q_i	Molar concentration of counter ion i in the particle (mol m ⁻³)
\bar{q}_i	Average concentration of counter ion i in the particle (mol m ⁻³)
Q_{Th}	Thomas model parameter: maximum solute concentration in the solid (mol kg ⁻¹)
r	Radial position in the particle (m)
R^2	Coefficient of determination
R_p	Particle radius (m)
RMSD	Root Mean Square Deviation (%)
SEM	Scanning Electron Microscopy
t_{50}	Yoon-Nelson parameter: time for $C_A/C_{A,0} = 0.5$, (h)
t	time (h or s)
t_{st}	Stoichiometric time (h)
t_b	Breakthrough time (h)
T	Absolute temperature (K)
u	Superficial velocity (m s ⁻¹)
v	Flow rate (m ³ s ⁻¹)
Z	Dimensionless longitudinal coordinate in the column
z_i	Electrochemical valence of counter ion i

Greek letters

ε	Bed void fraction
ρ_s	Density of ion exchanger
θ	Dimensionless time
τ	Space time (s)
ω	Clark model rate parameter (h ⁻¹)

Subscripts

0	Initial conditions
A	Counter ion initially present in the bulk solution (Cs ⁺)

B	Counter ions initially present in the ion exchange (K ⁺ and Na ⁺)
BA	Bohart-Adams model
calc	Calculated value
eq	Equilibrium value
exp	Experimental value
Th	Thomas
s	solid
YN	Yoon-Nelson model

Work reported in the scientific article

**Batch and fixed-bed removal of Cs⁺ from aqueous solutions using ETS-4:
Measurement and modeling of loading-regeneration cycles and equilibrium**

published on Chemical Engineering Journal 301 (2016) 276–284

Abstract

ETS-4 was prepared by hydrothermal synthesis and characterized by powder X-ray diffraction in order to assess its ion exchange capacity towards the removal of Cs⁺ from aqueous solutions in both batch and fixed-bed operation modes. Several assays were carried out to measure isotherm (8 experiments) and breakthrough curves (5 experiments); a set of loading-regeneration-loading experiments was also performed highlighting the ability of ETS-4 to be used in cyclic ion exchange. Powder X-ray diffraction showed that parent and Cs⁺-exchanged ETS-4 are isostructural. The Langmuir equation achieved good correlation results (average deviation of 6.58%), while the Nernst-Planck based model proposed for the fixed-bed assays fitted one breakthrough curve with 18.66% error, and was able to predict the remaining four experiments with 9.55% error. The Nernst-Planck parameters are the self-diffusion coefficients of Cs⁺ and Na⁺ in ETS-4, whose values ($D_{\text{Cs}^+} = 3.193 \times 10^{-16} \text{ m}^2 \text{ s}^{-1}$ and $D_{\text{Na}^+} = 6.088 \times 10^{-15} \text{ m}^2 \text{ s}^{-1}$) are consistent with the microporosity of ETS-4 framework and with the size of the counter ions.

V.2. Batch and fixed-bed removal of Cs⁺ from aqueous solutions using ETS-4: Measurement and modeling of loading-regeneration cycles and equilibrium

V.2.1. Introduction

The removal of long-lived radionuclides generated by nuclear power plants represents an important environmental aspect in nuclear waste management. For instance, the medium-lived radioisotopes strontium (⁹⁰Sr) and cesium (¹³⁷Cs), whose decay half-lives are, respectively, 28.9 and 30.1 years are responsible for most of the accumulated radiation on the produced effluents. Therefore, their removal is imperative and can be seen as an effective strategy to minimize such nuclear waste volumes [42,43]. To achieve the desired separation, various physicochemical processes may be applied, namely, co-precipitation, solvent extraction, coagulation, electrochemical, membrane processes, and adsorption/ion exchange [3,44].

In this context, inorganic ion exchangers are widely employed for the removal and safe storage of radionuclides from nuclear wastes due to their high mechanical, thermal and radiation stabilities and potential selectivity. On the other hand, due to the unique pore structure and cation exchange properties of natural and synthetic zeolites, this class of materials has attracted significant attention [33]. For instance, clinoptilolite has been used for cesium and strontium uptake before effluents discharge in the Irish Sea [45]. Mordenite and chabazite also found application in treating hazardous solutions from nuclear power plants [46,47]. Very recently, two microporous lanthanide silicates have been tested for the first time as Cs⁺ exchangers, Eu-AV-20 [31,48] (mineral tobermorite analogue) and Tb/Eu-AV-9 [49] (mineral montregianite analogue), where AV-n stands for Aveiro material number n.

Microporous titanosilicates are also a successful class of zeolite-like materials for the uptake of long- and medium-lived radionuclides from nuclear waste effluents. In this class, sitinakite [50,51] and pharmacosiderite [52,53] stand out, with the former having a synthetic counterpart commercially available from UOP [9,54,55]. Many other such materials deserve mention, such as the ETS (Engelhard Titanosilicates) [56–60] and AM (acronym of Aveiro-Manchester) [2,61–63] families. Titanosilicate ETS-4, in particular, comprises SiO₄ tetrahedra and TiO₅ and TiO₆ polyhedra, exhibiting high ion exchange capacity and, in the parent form, exchangeable Na⁺ and K⁺ cations [64]. ETS-4 has the ideal composition M₈Ti₅Si₁₂O₃₈·nH₂O (M=K,Na), essentially, the structure of zorite, comprising 8-membered rings and an effective pore size of 0.37 nm that may be fine-tuned by

progressive dehydration [64]. The Na-form of ETS-4 collapses at ca. 473 K, a limitation that may be overcome by ion exchange, for example with strontium [64].

Most of articles dealing with ion exchange focuses on batch assays for equilibrium and kinetic studies [15–17,41,45,60,65]. Nonetheless, fixed-bed experiments comprising both loading and regeneration steps are crucial for commercial/industrial applications, as their accurate design requires not only isotherms but also the knowledge of the dynamic behaviour of the system. For instance, the well-known breakthrough experiments are indispensable to measure the length of unused bed for the accurate scale-up of industrial sorption units. To accomplish this, the development of theoretically sound models for the representation of ion exchange data and subsequent simulations is also necessary for reliable optimization and scale-up. Some examples of fixed-bed assays include studies performed with titanosilicates ETS-10 [7,8] and CST [9], NaY zeolite [6], and lanthanide silicate Eu-AV-20 [31].

Here, the removal of Cs⁺ from aqueous solutions by ETS-4 is investigated using batch and fixed-bed experiments. Complete loading-regeneration cycles are performed and they are simulated using Nernst-Planck equations and Langmuir isotherm.

V.2.2. Modelling

Ion exchange is often represented as a chemical reaction because of the stoichiometric nature of the process by which two counter ions, A^{z_A} and B^{z_B} , are exchanged between an electrolyte solution and a solid sorbent according to:



where z_A and z_B are the electrochemical valences of counter ions, and the capping bar denotes the exchanger phase. In this study, A^{z_A} is Cs⁺, B^{z_B} is Na⁺, $z_A = z_B = +1$, and the exchanger (ETS-4) is converted from the $\overline{B^{z_B}}$ to the $\overline{A^{z_A}}$ form. For simplicity, A^{z_A} and B^{z_B} will be henceforth designated as A and B. To describe the fixed-bed ion exchange of the Cs⁺/Na⁺/ETS-4 system, a Nernst-Planck (NP) based model was written and coded in Matlab R2013a®.

The following equations were used successfully to represent the intraparticle mass transport of Hg²⁺/Na⁺ and Cd²⁺/Na⁺ pairs through ETS-4 [16,17]. Briefly, the NP equations state that the fluxes (N_i , mol m⁻² s⁻¹) of counter ions result from both concentration (q_i , mol

m⁻³) and electric potential gradients. For a binary A/B system, the internal flux of A is given by [16,17,32,33]:

$$N_A = -\frac{D_A D_B (z_A^2 q_A + z_B^2 q_B)}{D_A z_A^2 q_A + D_B z_B^2 q_B} \left(\frac{\partial q_A}{\partial r} \right) = -D_{AB} \left(\frac{\partial q_A}{\partial r} \right) \quad (\text{V.2.2})$$

$$D_{AB} \equiv \frac{D_A D_B (z_A^2 q_A + z_B^2 q_B)}{D_A z_A^2 q_A + D_B z_B^2 q_B} \quad (\text{V.2.3})$$

where D_A and D_B (m² s⁻¹) are the self-diffusion coefficients of A and B, r (m) is the radial coordinate in the particle, and D_{AB} (m² s⁻¹) is taken as an interdiffusion coefficient. The exchange capacity of the sorbent is calculated by Q (eq m⁻³) = $q_A z_A + q_B z_B$.

The fixed-bed model encompasses the material balance to the column (Eq. (V.2.4)), which contains the accumulation contributions in the fluid and solid phases, an axial dispersion term and a convective term. The appropriate initial and boundary conditions are given by Eqs. (V.2.5) and (V.2.6).

$$\frac{\partial C_A(l, t)}{\partial t} + \frac{1 - \varepsilon}{\varepsilon} \frac{\partial \langle q_A \rangle(l, t)}{\partial t} = D_L \frac{\partial^2 C_A(l, t)}{\partial l^2} - u \frac{\partial C_A(l, t)}{\partial l} \quad (\text{V.2.4})$$

$$t = 0, \quad C_A = C_{A, \text{in}} = 0 \quad (\text{V.2.5})$$

$$l = 0, \quad D_L \frac{\partial C_A}{\partial l} = -u(C_{A,0} - C_A) \quad (\text{V.2.6})$$

$$l = L, \quad \frac{\partial C_A}{\partial l} = 0$$

In Eqs. (V.2.4)-(V.2.6), C_A (mol m⁻³) is the molar concentration of species A in solution, u (m s⁻¹) the superficial velocity, l (m) the position along the bed, L (m) the bed length, t (s) time, ε the bed porosity ($\varepsilon = 0.88$), $\langle q_A \rangle$ (mol m⁻³) the average concentration of A in the solid, $C_{A, \text{in}}$ the initial concentration of A in the fluid inside the bed, and $C_{A,0}$ the concentration of A in the feed. The axial dispersion coefficient D_L (m² s⁻¹) was estimated here using the following correlation [34]:

$$D_L = (20 + 0.5 \times \text{Sc} \times \text{Re}) \times \frac{D_m}{\varepsilon} \quad (\text{V.2.7})$$

where D_m is the diffusivity of Cs⁺ in water ($2.06 \times 10^{-9} \text{ m}^2 \text{ s}^{-1}$ at 298.15 K [35]), and Sc and Re are the well known Schmidt and Reynolds numbers, respectively.

The material balance to the exchanger particle is given by Eq. (V.2.8), and the initial and boundary conditions for the ion exchange experiment are represented by Eqs. (V.2.9)-(V.2.11).

$$\frac{\partial q_A}{\partial t} = -\frac{1}{r^2} \frac{\partial}{\partial r} (r^2 N_A) \quad (\text{V.2.8})$$

$$t = 0, \quad q_A = q_{A,\text{in}} = 0 \quad (\text{V.2.9})$$

$$r = 0, \quad \frac{\partial q_A}{\partial r} = 0 \quad (\text{V.2.10})$$

$$r = R_p, \quad q_A = q_{A,R_p} \quad (\text{V.2.11})$$

where R_p (m) is the particle radius, $q_{A,\text{in}}$ (mol m⁻³) the initial concentration of A in the solid along the bed, and q_{A,R_p} (mol m⁻³) the concentration of A in the solid at the interface, which is in equilibrium with fluid concentration C_{A,R_p} (*i.e.*, they are related by the isotherm).

In consecutive loading-regeneration operations, the initial conditions of step n , ($C_{A,\text{in}}|_n$ and $q_{A,\text{in}}|_n$) must equal the final concentration profiles of step $n - 1$, ($C_{A,\text{final}}|_{n-1}$ and $q_{A,\text{final}}|_{n-1}$). Accordingly, Eqs. (V.2.5) and (V.2.9) should be substituted by the following conditions:

$$t = t_{\text{in}}|_n, \quad \begin{cases} C_{A,\text{in}}|_n = C_{A,\text{final}}|_{n-1} \\ q_{A,\text{in}}|_n = q_{A,\text{final}}|_{n-1} \end{cases}, \quad 2 \leq n < \infty, \quad (\text{V.2.12})$$

The equality of fluxes at the surface of the particle is expressed by Eq. (V.2.13), which involves the convective mass transfer coefficient of counter ion A, k_f (m s⁻¹), estimated here by Eq. (V.2.14) in terms of Sherwood (Sh), Reynolds and Schmidt numbers, and $d_p = 2R_p$ is the equivalent particle diameter (m) [8].

$$N_{A,R_p} = k_f (C_A - C_{A,R_p}) \quad (\text{V.2.13})$$

$$Sh = \frac{k_f d_p}{D_m} = \frac{1.13}{\varepsilon} Re^{0.21} Sc^{1/3} \quad (V.2.14)$$

The average loading per unit particle volume, included in the material balance to the column, Eq. (V.2.4), is calculated by:

$$\langle q_A \rangle = \frac{3}{R_p^3} \int_0^{R_p} r^2 q_A dr \quad (V.2.15)$$

The equilibrium isotherm of the system Cs⁺/Na⁺/ETS-4 is given by the Langmuir equation:

$$q_{A,eq} = q_{A,max} \frac{K_L C_{A,eq}}{1 + K_L C_{A,eq}} \quad (V.2.16)$$

where $q_{A,max}$ (mol m⁻³) and K_L (mol⁻¹ m³) are parameters to fit the experimental data.

The Method of Lines was selected to solve the concentration profiles of Cs⁺ and their evolution along time, in solution and in the solid phase, and the spatial discretization was accomplished by finite differences of second order. The resulting ordinary differential equations of the initial-value type were solved applying numerical differentiation formulas using 31 grid points for particle radius and bed length.

Concerning the methodology, the self-diffusion coefficients (D_A and D_B) of the NP-based model were adjusted to the experimental data (section V.2.4.4), the Nelder-Mead and the Marquardt-Levenberg algorithms were adopted for the optimizations, and the root mean square deviation (RMSD) was the objective function:

$$RMSD (\%) = 100 \times \sqrt{\frac{\sum_i^{NDP} (C_{A,calc|i} - C_{A,exp|i})^2}{NDP}} \quad (V.2.17)$$

Here NDP is the number of data points, and subscripts 'exp' and 'calc' denote measured and calculated cesium concentrations, respectively.

V.2.3. Materials and Methods

V.2.3.1. Chemicals and materials

Sodium hydroxide (CAS number 1310-73-2), potassium chloride (CAS number 7447-40-7) and titanium(III) chloride (15 wt% TiCl₃ and 10 wt% HCl) were supplied by Merck. Sodium metasilicate (CAS Number 13517-24-3) was purchased from BDH Chemicals. Cesium nitrate (CAS number 7789-18-6) and sodium nitrate (CAS Number 7631-99-4) were acquired from Sigma-Aldrich. Cellulose acetate membrane disc filters were bought from Sterlitech Corporation, and quartz wool discs were purchased from Elemental Microanalysis. The high-purity water (18.2 MΩ cm) was generated in a Milli-Q Millipore water purification system.

V.2.3.2. Synthesis and characterization

ETS-4 synthesis was performed as follows [13,15]. An alkaline solution was prepared by dissolving sodium metasilicate, NaOH and KCl in high-purity water (18.2 MΩcm). Then, TiCl₃ was added to this solution and stirred thoroughly. The resulting gel, with molar composition 5.9 Na₂O : 0.7 K₂O : 5.0 SiO₂ : 1.0 TiO₂ : 114 H₂O, was transferred to a Teflon-lined autoclave and heated at 230 °C for 17 h under autogenous pressure without agitation. The product was filtered off, washed at room temperature with distilled water, and dried at 70 °C overnight. *The sample crystallinity and purity were ascertained by powder X-Ray Diffraction (PXRD) collected on a PANalytical Empyrean diffractometer (CuK_{α1,2} X-radiation, λ₁ = 1.540598 Å; λ₂ = 1.544426 Å), equipped with an PIXcel 1D detector and a transmission-spinner sample holder in a Bragg-Brentano para-focusing optics configuration (45 kV, 40 mA). Intensity data were collected by the step-counting method (step 0.04°), in continuous mode, in the range ca. 5 ≤ 2θ ≤ 50°. Table V.2.1 summarizes the important features of this material.*

Table V.2.1 – Features of the synthesized titanosilicate ETS-4 [66].

Formula	M ₈ Ti ₅ Si ₁₂ O ₃₈ ·nH ₂ O (M=K,Na)
Density (kg m ⁻³)	2200
Theoretical cation exchange capacity (eq kg ⁻¹)	6.39
Measured equivalent particle diameter (10 ⁻⁶ m)	12
Pore diameter (10 ⁻¹⁰ m)	3.7

V.2.3.3. Fixed-bed and batch ion exchange experiments

Preparation of solutions. Measurement of Cs⁺ concentration.

A 0.01 mol L⁻¹ Cs⁺ stock solution was prepared by dissolving 0.098 g of CsNO₃ in 50 mL of high-purity water (18.2 MΩ cm). The Cs⁺ operational solutions were obtained by diluting the stock solution to the desired concentration with high-purity water, prepared immediately before use in order to reduce cation adsorption on the vessel walls and remaining glassware and lab material.

The cesium concentration of the solutions was measured by atomic emission spectroscopy (AES) with a Perkin Elmer AAnalyst 100 atomic absorption spectrometer, in the emission mode (with a wavelength of 852.1 nm and a slit of 0.2 nm) and using an air-acetylene flame. The ionization was controlled by the addition of a potassium chloride solution to all samples and standards until they all contained 0.5 wt.% of such alkali. Each sample was analysed in triplicate and the results are the average of concordant values (less than 5% variation between measurements of the same sample).

Batch ion exchange experiments

Batch experiments were performed contacting cesium solutions with known masses of powdered ETS-4 in volumetric flasks (2 dm³) under agitation (*ca.*, 300 rpm) at room temperature (295 K) and initial pH 4. The initial cesium concentrations were fixed at *ca.* 40 ppm in order to maintain constant the ionic strength of the solutions, while the masses of ETS-4 were varied as shown in Table V.2.2. The assays started when the exchanger was added to the solution and the stirring initiated. Aliquots (10 mL) were collected, (before adding the solid and at the end of the experiment), filtered through an acid washed cellulose acetate membrane disc filter of 0.45 μm, and the cesium concentration was measured by AES. A blank experiment (without ETS-4) was always run as a control to check that the removal of Cs⁺ occurred by ion exchange with the solid and not by adsorption on the lab material.

Fixed-bed ion exchange experiments

A stainless steel fixed-bed column was mounted on a support and filled with a precise amount of ETS-4 confined by four to six quartz wool discs plus two stainless steel nets, one at the bottom and other on top. Swagelock fittings were used to close the assembly and to connect the bottom and the top of the column to an influent reservoir and to a sample collector, respectively (Figure V.2.1).

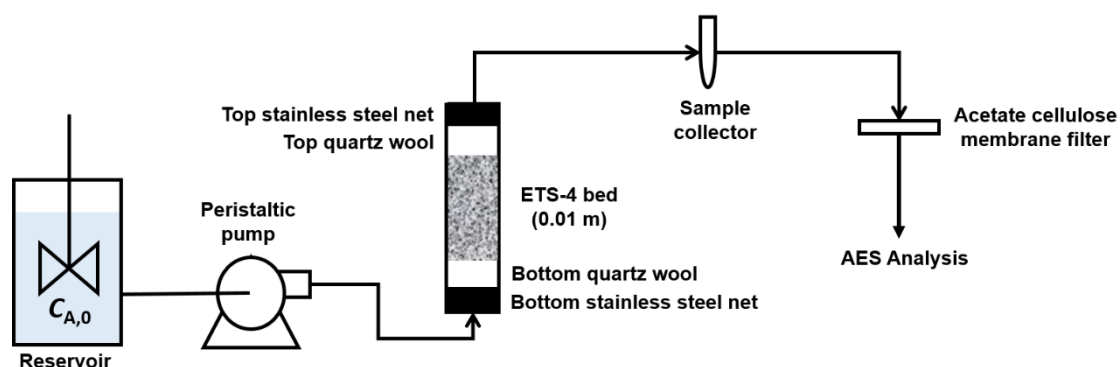


Figure V.2.1 – Experimental setup for the fixed-bed ion exchange experiments.

Three fixed-bed experiments (Exps. 9, 10 and 11 of Table V.2.3) were performed isothermally at 295 ± 1 K to study the influence of the flow rate on cesium exchange over ETS-4. The influent solution containing *ca.* 40 ppm Cs⁺ was continuously fed to the column in the up-flow mode. The pH was measured at the column inlet using a pH meter Crison Basic 20. The volumetric flow rate was regulated with a variable peristaltic pump (Knauer Smartline pump 100). Aliquots of 10 mL were collected periodically at column outlet, filtered through acid washed cellulose acetate membrane (0.45 μ m) disc filters, and then analysed for Cs⁺ concentration by AES. The experiments were stopped when the effluent and the influent Cs⁺ concentrations were equal.

To assess the regeneration capacity of ETS-4, an additional experiment was performed after Exp. 11 (Table V.2.3) using a solution of Na⁺ ($1.72 \text{ mol} \cdot \text{m}^{-3}$) continuously fed to the column for 75 hours (Exp. 12 in Table V.2.3). Then, a second cycle began using a cesium solution and operating conditions equivalent to those of Exp. 11 (Exp. 13 in Table V.2.3). The ion exchange process was always controlled through Cs⁺ measurement by AES as described above.

Table V.2.2 – Experimental conditions for batch ion exchange assays with ETS-4 to obtain isotherm data. (Fixed conditions: $T = 295 \pm 1$ K, $V_{\text{liquid}} = 2 \times 10^{-3} \text{ m}^3$, pH = 4).

Experiment No.	1	2	3	4	5	6	7	8
Mass of ETS-4 (10^{-6} kg)	8	60	157	206	314	418	524	804
Initial Cs ⁺ conc. (mol m^{-3})	0.288	0.295	0.308	0.285	0.295	0.291	0.294	0.303

Table V.2.3 - Experimental conditions for fixed-bed ion exchange assays using ETS-4. (Fixed conditions: $T = 295 \pm 1$ K, pH 4, $\varepsilon = 0.88$, $L = 0.01$ m).

Experiment No.	9	10	11	12	13
Type of experiment / cycle	Loading	Loading	Loading 1 st cycle	Regeneration 1 st cycle	Loading 2 nd cycle
Mass of ETS-4 (10^{-6} kg)	501	509	503	503	503
Initial Cs ⁺ conc. (mol m^{-3})	0.311	0.305	0.301	-	0.293
Initial Na ⁺ conc. (mol m^{-3})	-	-	-	1.720	-
Superficial velocity (m s^{-1}) 1)	6.366×10^{-4}	3.893×10^{-4}	2.567×10^{-4}	2.567×10^{-4}	2.567×10^{-4}
D_L ($\text{m}^2 \text{s}^{-1}$) by Eq. (7)	5.895×10^{-8}	5.556×10^{-8}	5.350×10^{-8}	5.350×10^{-8}	5.350×10^{-8}

V.2.4. Results and discussion

This section starts with the characterization of the synthesised ETS-4 by PXRD, before and after ion exchange. Then, the measured and modelled isotherms of the Cs⁺/Na⁺/ETS-4 system are analysed, followed by the breakthrough curves obtained under fixed-bed operation. The regeneration and the second cycle of ion exchange are also examined. Finally, the results achieved with the Nernst-Planck based model (developed in Section V.2.2) are presented and discussed in detail.

V.2.4.1. Materials characterization

The PXRD pattern of the parent sample is characteristic of ETS-4 providing no evidence for the presence of any additional impurities (Figure V.2.2). Cs⁺-exchanged ETS-4 reveals some modifications in the peaks intensities and positions, which may be ascribed not only to crystal orientation effects but also to the introduction of cesium in its framework. The major differences are found at 23.21° , where a new peak appears, and at 30.37° and 31.17° , where two peaks substituted the native 30.79° peak. Despite these differences, parent ETS-4 and the Cs⁺-exchanged solid are isostructural.

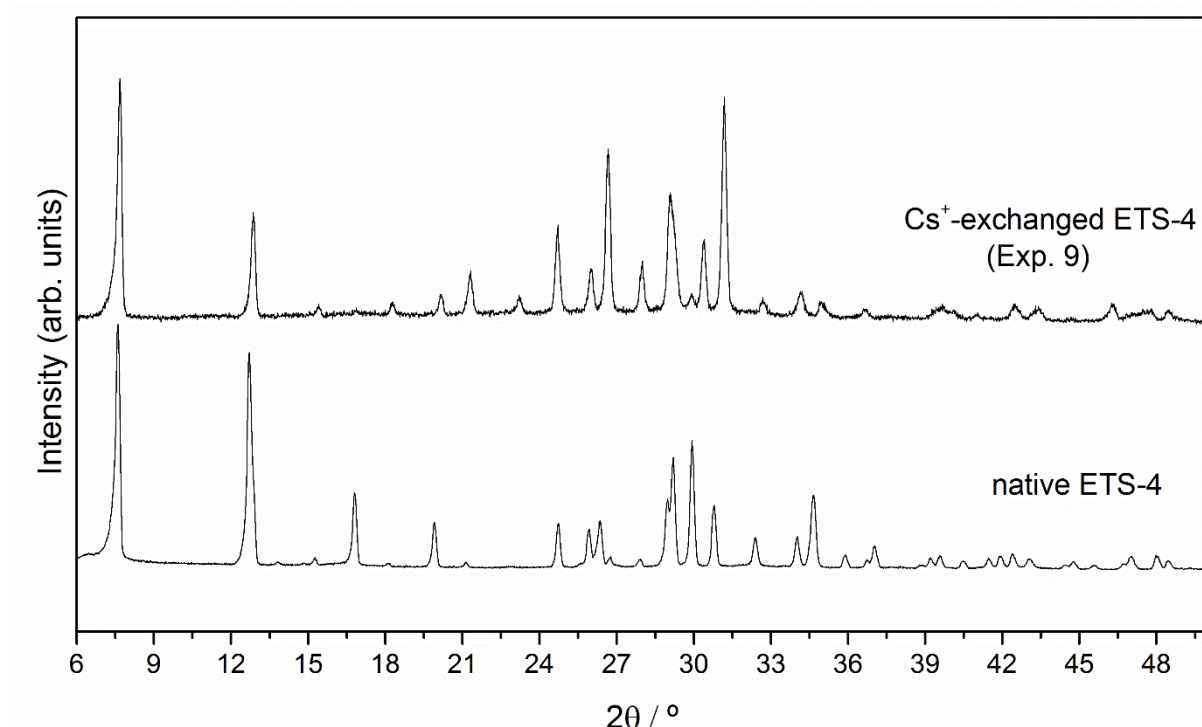


Figure V.2.2 – Normalized PXRD patterns of native and Cs⁺-exchanged ETS-4 (after Exp. 9; see experimental conditions in Table V.2.3).

V.2.4.2. Ion exchange isotherm

The equilibrium data were obtained from batch Exps. 1-8 (Table V.2.2) and fitted with the Langmuir isotherm, Eq. (V.2.16), with an average absolute relative deviation (AARD) of 6.58%. The analytical equation is depicted in Figure V.2.3 and exhibits the Langmuir parameters $q_{A,\max} = 1.86 \text{ mol kg}^{-1}$ and $K_L = 43.46 \text{ m}^3 \text{ mol}^{-1}$, similar to previously published data [57]. Freundlich and Langmuir-Freundlich isotherms were also considered, but the former fails to represent the experimental points, while the latter adds an additional parameter but no substantial gain.

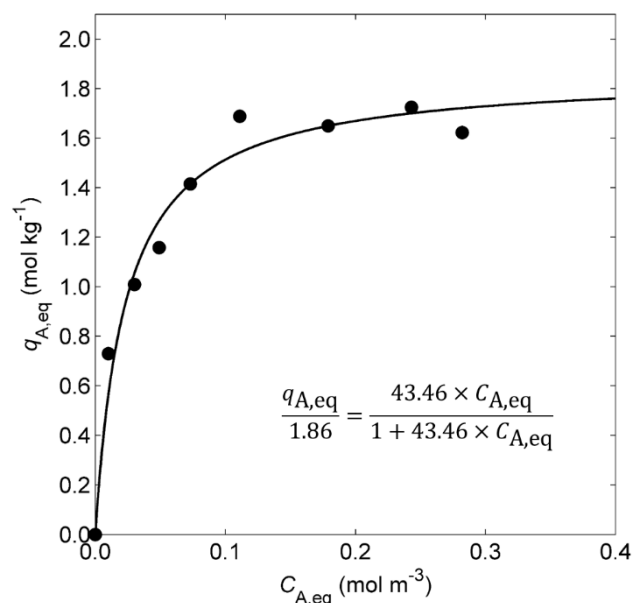


Figure V.2.3 – Measured (solid circles) and calculated (line) Langmuir isotherms of Cs⁺/Na⁺/ETS-4 system at 295 K.

V.2.4.3. Fixed-bed experimental results

The breakthrough curves obtained from Exps. 9-11 were evaluated at different superficial velocities in the range $(2.5\text{--}6.4) \times 10^{-4}$ m s⁻¹ for 75 hours (Table V.2.3). The experimental data plotted in Figure V.2.4 represent the time evolution of the normalized cesium concentration in solution at column outlet, *i.e.*, $C_A(t, L)/C_{A,0}$. Because the three breakthrough curves deviate significantly from (displaced) Heaviside functions, these results reveal mass transfer limitations in the system.

When equilibrium is favourable (which is the case for the Langmuir isotherm) and dispersive phenomena (*e.g.*, axial dispersion, film and intraparticle resistances to mass transfer) are negligible, an ideal wave front propagates unchanged along the bed and exits the column at the stoichiometric time, t_{st} . On the other hand, the occurrence of transport-rate resistances broadens the traveling wave front, which reaches a constant pattern flow due to the simultaneous effect of the self-sharpening favourable isotherm [67,68]. The stoichiometric time can be calculated from the experimental breakthrough curve using Eq. (V.2.18) or estimated from Eq. (V.2.19) on the basis of the solute movement theory:

$$t_{st} = \int_0^\infty \left(1 - \frac{C_A(t)}{C_{A,0}} \right) dt \quad (V.2.1)$$

$$t_{st} = \frac{L}{u} \left(1 + \frac{1 - \varepsilon}{\varepsilon} \frac{q_{A,0}}{C_{A,0}} \right) \quad (V.2.2)$$

where $q_{A,0}$ is the solid loading in equilibrium with feed concentration, $C_{A,0}$. For the regeneration step, the concept of stoichiometric time was extended with the objective of computing the process efficiency using:

$$t_{st} = \int_0^\infty \frac{C_A(t)}{C_{A,0}} dt \quad (V.2.3)$$

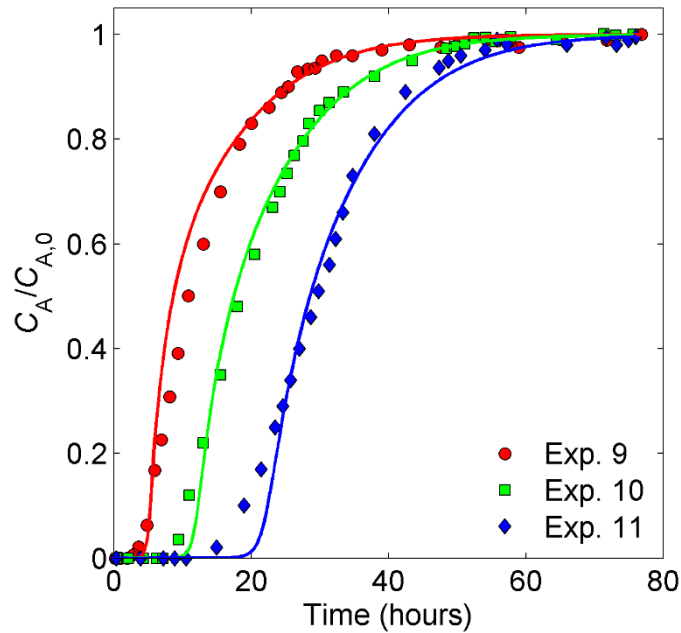


Figure V.2.4 – Effect of the feed flow rate on the normalized breakthrough curves for Cs⁺ removal in a fixed-bed of ETS-4. Symbols: data (experimental conditions in Table V.2.3); lines: NP-based model (parameters in Table V.2.4).

According to the breakthrough curves (Exps. 9, 10 and 11 in Figure 4), lower superficial velocities require higher operating times to deplete the solid phase, and vice-versa, in agreement with the solute movement theory, Eq. (V.2.19), since t_{st} is inversely proportional to the superficial velocity, u . The experimental values obtained were $t_{st} = 13.9$, 21.9 and 30.8 h, for $u = 6.366 \times 10^{-4}$ (Exp. 9), 3.893×10^{-4} (Exp. 10) and $2.567 \times 10^{-4} \text{ m s}^{-1}$ (Exp. 11), respectively.

Concerning axial dispersion, its influence was negligible because the L/d_p ratio was 833, clearly obeying the well-known relation $L > 50 d_p$, and the axial Peclet numbers ($Pe = uL/D_L$) attained were 108.0, 70.1 and 48.0, for Exps. 9, 10 and 11, respectively. Nonetheless, external mass transfer limitations were confirmed, experimentally and theoretically (further discussion in Section V.2.4.4) because the spreading of the breakthrough curves increased with decreasing superficial velocities. For example, the widths of the mass transfer zone (MTZ) based on 0.01 and 0.99 limits (*i.e.*, $0.01 \leq C_A(t, L)/C_{A,0} \leq 0.99$) were 42.4, 46.3 and 48.1 h for Exps. 9, 10 and 11, respectively; for the more flexible limits 0.05 and 0.95, the corresponding MTZ widths were 27.2, 30.1 and 31.5 h.

The regeneration experiment (Exp. 12) was subsequently performed using a Na^+ solution (*ca.* 40 ppm) to convert the ETS-4 bed at the end of Exp. 11 into its original Na -form, in order to evaluate the Cs^+ uptake capacity after regeneration (Exp. 13). The results for the normalized cesium concentration at column outlet are shown in Figure V.2.5, where time was measured continuously, without interruption, with the successive regeneration and loading experiments (Exps. 12 and 13, respectively) having the same time extension of Exp. 11. As expected, the regeneration curve is highly dispersed ($75 < t(\text{h}) < 150$) because a favourable isotherm broadens the wave front during a desorbing step and the mass transfer limitations reinforces even more this thermodynamic behaviour along the bed.

Since all experimental conditions were preserved during Exps. 11, 12 and 13, except the Cs^+ concentration of the feed, the efficiency of the regeneration and second loading steps may be unveiled by the ratio between their stoichiometric times and that of Exp. 11. With respect to this, Figure V.2.5 encompasses three different areas (A1, AR and A2) whose values correspond to the experimental stoichiometric times, $t_{\text{st}} = 31.0, 23.8$ and 23.0 h, respectively. Thus, the ratio $\text{AR}/\text{A1}$ indicates that the regeneration process (Exp. 12) attained *ca.* 76.8% of efficiency, a value confirmed by the experimental $\text{A2}/\text{A1}$ ratio that attained 74.2%. It is worth mentioning that after *ca.* 150 h (*i.e.*, at the end of *ca.* 75 h of regeneration) the Cs^+ concentration of the effluent was *ca.* 20% of its initial concentration, *i.e.*, the regeneration was incomplete. To convert all ETS-4 in its Na -form, long ion exchange runs would be necessary under the same experimental conditions. Alternatively, to accelerate the regeneration process, the inlet counter ion (Na^+) concentration and flow rate could be increased. In both cases, the mass transfer driving force would be increased, while the second possibility would also to reduce the external film thickness with advantage. In industrial applications the residual loading after regeneration is usually finite and frequently non-uniform, constituting the well-known delta loading of steady state cyclic processes.

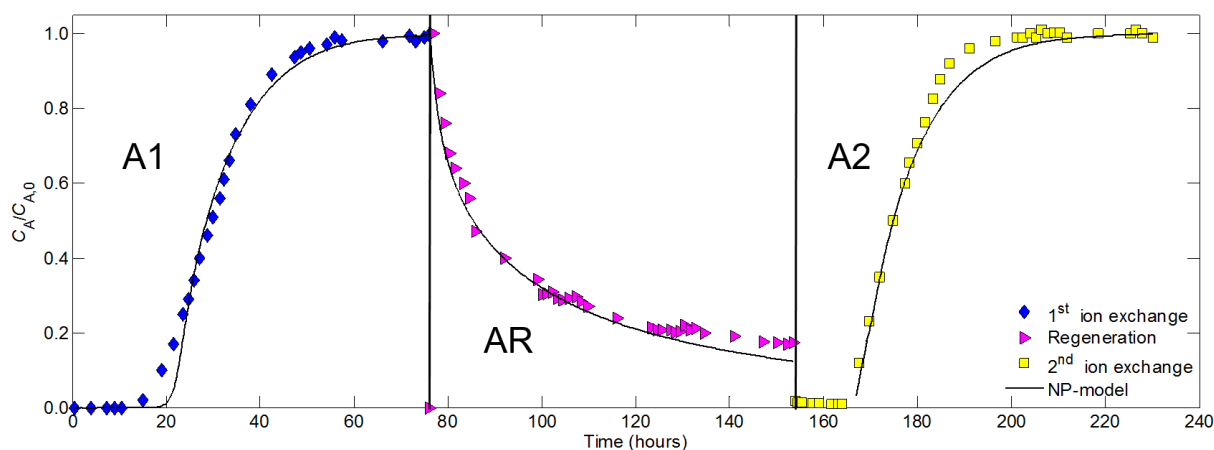


Figure V.2.5 – Normalized cesium concentration at column outlet for Exps. 11, 12 and 13 in a loading-regeneration operation. Symbols: data (experimental conditions in Table V.2.3); lines: NP-based model (parameters in Table V.2.4); A1 = area above the breakthrough of the 1st ion exchange cycle; AR = area below the regeneration curve of the 1st cycle; A2 = area above breakthrough of the 2nd cycle.

The ability of spent ETS-4 to enter a second ion exchange cycle after intermediate regeneration is a valuable outcome of this essay. ETS materials have been much studied for the removal of several hazardous metals [4] but their regeneration and utilization in subsequent ion exchange cycles is scarcely assessed. Lopes *et al.*, [7] studied the uptake of Hg²⁺ from aqueous solutions on a packed-bed of ETS-4, and the regeneration was carried out with a chelating agent, namely a concentration gradient EDTA-Na₂ solution (0.05–0.25 mol dm⁻³), attaining an elution efficiency of 98% only after 50 hours. If, alternatively, a simple aqueous solution of a counter ion had been used the fixed-bed cleaning would be impractical. This is in accord with the large selectivity of titanosilicates towards divalent cations such as Hg²⁺ and Cd²⁺ [13–15,41,65,69]. In our case the counter ions Cs⁺ and Na⁺ possess the same valence (+1) and, as mentioned above, the PXRD patterns of parent and Cs⁺-exchanged ETS-4 show that the solids are isostructural. Hence, both loading and regeneration steps were expected in advance to be essentially and effectively reversible despite the differences imparted by the distinct ionic radius of Cs⁺ and Na⁺ (170 *versus* 102 pm [70], respectively).

V.2.4.4. Fixed-bed modelling results – Nernst-Planck based model

Modelling results for the fixed-bed operation are plotted together with data for Exps. 9-11 in Figure V.2.4, and Exps. 11 (loading, 1st cycle), 12 (regeneration, 1st cycle) and 13 (loading, 2nd cycle) in Figure V.2.5. The axial dispersion (D_L) and convective mass transfer coefficients (k_f) were estimated by Eqs. (7) and (14), respectively, and the model parameters (D_A and D_B) were fitted to the data of Exp. 11 only, with RMSD = 18.66 %. The remaining four curves were predicted, providing deviations of 15.20% (Exp. 9), 13.27% (Exp. 10), 4.17% (Exp. 12) and 5.88% (Exp.13), and global RMSD of 9.55% (see Table V.2.4). Globally, these are reliable results for an ion exchange process embodying several runs with different operating conditions and distinct cycle steps.

Considering that the system's counter ions are monoatomic and monovalent, the adjusted self-diffusivities for Cs⁺ ($D_A = 3.193 \times 10^{-16} \text{ m}^2 \text{ s}^{-1}$) and Na⁺ ($D_B = 6.088 \times 10^{-15} \text{ m}^2 \text{ s}^{-1}$) must reflect their ionic radius, *i.e.*, $D_A < D_B$ because $r_{\text{ion}}(\text{Cs}^+) = 170 \text{ pm} > r_{\text{ion}}(\text{Na}^+) = 102 \text{ pm}$ [70]. Furthermore, D_A and D_B are of the same order of magnitude of those published recently for the system Cs⁺/Na⁺/Eu-AV-20 [48] and three times larger than the values for Cd²⁺/Na⁺/ETS-4 [14] and Hg²⁺/Na⁺/ETS-4 [41] systems. In all cases, the small magnitudes of the diffusion coefficients are consistent with the presence of small micropores [14,71–73], since the cations never escape from the force field of the matrix co-ions, mainly due to the strong and long-range nature of the electrostatic interactions, which imply the intraparticle transport mechanism is surface diffusion.

As mentioned above, the self-diffusivity found for Cs⁺ is approximately three times higher than those reported for Cd²⁺ and Hg²⁺ in ETS-4 [14,41]. Despite the ionic radius of cadmium(II) and mercury(II), respectively, 95 and 102 pm [70], their double charge originates stronger interactions with the solid surface, increasing their activation energy for diffusing through the channels (remember that the ionic radius of Cs⁺ is 170 pm). An additional feature that penalizes Cd²⁺ and Hg²⁺ in comparison to Cs⁺ is the magnitude of their molar Gibbs free energy of dehydration: $\Delta_{\text{dehyd}}G = 1755$, 1760 and 250 kJ mol⁻¹ [70], respectively, which means the energy required by the divalent cations for accessing the microporosity of ETS-4 is *ca.*, seven times higher than that of monovalent cesium ion, just for the dehydration step.

The convective mass transfer coefficients estimated by Eq. (V.2.14) are $3.775 \times 10^{-4} \text{ m s}^{-1}$ (Exp. 9), $3.416 \times 10^{-4} \text{ m s}^{-1}$ (Exp. 10) and $3.122 \times 10^{-4} \text{ m s}^{-1}$ (Exps. 11-13), following the decreasing superficial velocity of the fluid (*i.e.*, 6.366×10^{-4} , 3.893×10^{-4} and $2.567 \times 10^{-4} \text{ m s}^{-1}$, respectively). These values are consistent with the increasing widths of the mass transfer

zones (cited in Section V.2.4.3) for Exps. 9-11, because the film contribution to the second moment (*i.e.*, dispersion) of a pulse response of a chromatographic model is proportional to R_p/k_f [67,68]. It is interesting to confront the following ratios for qualitative but theoretically sound purposes: $k_f(\text{Exp. 10})/k_f(\text{Exp. 9})=0.905$ and $k_f(\text{Exp. 11})/k_f(\text{Exp. 10})=0.914$, *versus* $\text{MTZ}(\text{Exp. 9})/\text{MTZ}(\text{Exp. 10})=0.904$ and $\text{MTZ}(\text{Exp. 10})/\text{MTZ}(\text{Exp. 11})=0.956$.

To access the performance of the NP-based model, the calculated *versus* experimental normalized cesium concentrations at column outlet are plotted in Figure V.2.6. As expected from the RMSD values listed in Table V.2.4, the rough linearity observed between both sets of data highlights the model's ability to correlate and predict the ion exchange behaviour of the Cs⁺/Na⁺/ETS-4 system under the various experimental conditions, in particular, different superficial velocities and loading-regeneration steps. Despite the reliable results achieved, the model overestimates Exp. 9, while the points of the remaining experiments are well distributed near the diagonal. Figure V.2.6 also reveals that the proposed model is less reliable at the beginning of the breakthrough curves, where errors are more likely to occur due to the detection limits of the analytical method (AES). The fact that the proposed NP-based model can be used to study the different stages of a cyclic ion exchange operation is of major importance, since it is a fundamental tool for the accurate scale-up and optimization of a fixed-bed unit.

Table V.2.4 – Optimized parameters and calculated deviations for the Nernst-Planck based model applied to the fixed-bed assays. (Experimental conditions in Table V.2.3).

Exp.	NDP	Type of calculation	D_A (m ² s ⁻¹)	D_B (m ² s ⁻¹)	RMSD (%)	Global RMSD (%)
9	35	Prediction	-	-	15.20	9.55 (prediction)*
10	34	Prediction	-	-	13.27	
11	31	Correlation	3.193x10 ⁻¹⁶	6.088x10 ⁻¹⁵	18.66	18.66 (correlation)
12	35	Prediction	-	-	4.17	
13	35	Prediction	-	-	5.88	

* 9.55% is the calculated RMSD for the set of Exps. 9,10,12 and 13.

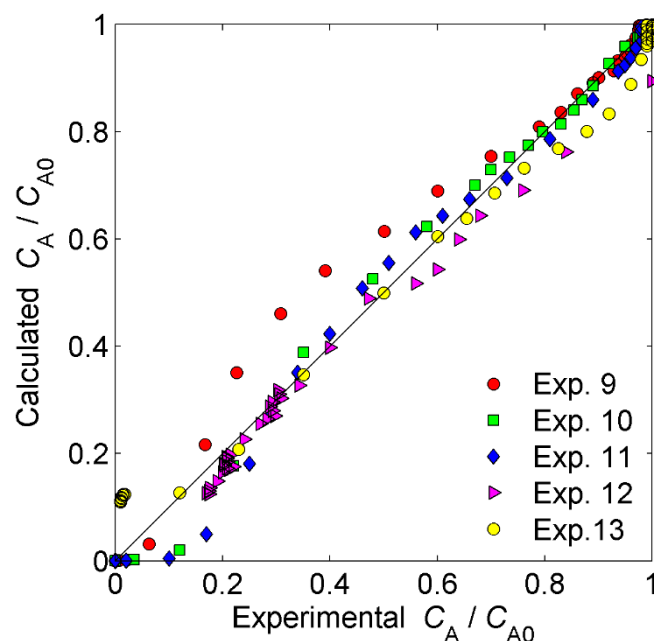


Figure V.2.6 – Calculated *versus* experimental normalized Cs⁺ concentration in solution (experimental conditions in Table V.2.3).

V.2.5. Conclusions

The cesium exchange capacity of ETS-4 was assessed in batch and fixed-bed experiments aiming at: measuring the isotherm of the system Cs⁺/Na⁺/ETS-4, assessing the influence of the superficial velocity on the fixed-bed operation (*via* breakthrough curves), and evaluating the regeneration ability of ETS-4 for future cyclic operation. The Langmuir isotherm fitted the equilibrium data reliably (AARD = 6.58%), while the experimental breakthrough curves exhibited the expected trend characterized by a sigmoidal shape. The proposed Nernst-Planck based model achieved global deviations of 18.66% and 9.55%, respectively, for correlation (1 curve) and prediction (4 curves) of cesium concentration in the fluid at column outlet. The correlated parameters were the NP self-diffusivities of Cs⁺ and Na⁺ in ETS-4, and the determined values ($D_{Cs^+} = 3.193 \times 10^{-16} \text{ m}^2 \text{ s}^{-1}$ and $D_{Na^+} = 6.088 \times 10^{-15} \text{ m}^2 \text{ s}^{-1}$) were consistent with the microporosity of ETS-4 and the size of the exchanged cations. The embodied axial dispersion and convective mass transfer coefficients (estimated by dimensionless correlations) confirmed external limitations and ruled out axial dispersion phenomena. The good results obtained in consecutive loading-regeneration steps evidence the ability of ETS-4 to be used in cyclic ion exchange operations, while the NP-based model proved to be reliable for process design and optimization.

V.2.6. Nomenclature

A^{Z_A}	Counter ion initially in solution (Cs ⁺)
A1, A2	Areas above breakthrough curves in Figure V.2.5 (h)
AARD	$= \frac{100}{\text{NDP}} \sum_{i=1}^{\text{NDP}} C_{A,i,\text{calc}} - C_{A,i,\text{exp}} / C_{A,i,\text{exp}}$, Average absolute relative deviation (%)
AES	Atomic emission spectroscopy
AR	Area below regeneration curve in Figure V.2.5 (h)
B^{Z_B}	Counter ion initially in the exchanger (Na ⁺)
C_A	Concentration of counter ion A in solution (mol m ⁻³)
$C_{A,0}$	Concentration of counter ion A in the feed (mol m ⁻³)
$C_{A,\text{in}}$	Initial concentration of counter ion A in solution (mol m ⁻³)
$C_{A,\text{eq}}$	Concentration of counter ion A in solution in equilibrium with solid loading concentration, $q_{A,\text{eq}}$ (mol m ⁻³)
C_{A,R_p}	Concentration of counter ion A in solution at the interface (mol m ⁻³)
d_p	Equivalent particle diameter (m)
D_i	Nernst-Planck self-diffusion coefficient of counter ion i in the exchanger (m ² s ⁻¹)
D_L	Axial dispersion coefficient (m ² s ⁻¹)
D_{AB}	Interdiffusion coefficient of Nernst-Planck model (m ² s ⁻¹)
D_m	Diffusion coefficient of Cs ⁺ in water (m ² s ⁻¹)
ETS-4	Engelhard titanosilicate number 4
Exp. n	Experiment number n
i and j	Generic counter ions
k_f	Convective mass transfer coefficient (m s ⁻¹)
K_L	Langmuir parameter (m ³ mol ⁻¹)
l	Column longitudinal coordinate (m)
L	Length of the fixed-bed (m)
MTZ	Mass transfer zone
N_{A,R_p}	Net intraparticle flux of counter ion A at the interface (mol m ⁻² s ⁻¹)
NDP	Number of data points
N_i	Intraparticle flux of counter ion i (mol m ⁻² s ⁻¹)
NP	Nernst-Planck
Pe	Peclet number

PXRD	Powder X-ray diffraction
q_{\max}	Langmuir parameter (mol kg ⁻¹)
$q_{A,0}$	Solid loading in equilibrium with feed concentration, $C_{A,0}$
$q_{A,\text{eq}}$	Solid loading in equilibrium with concentration of counter ion A in solution, $C_{A,\text{eq}}$ (mol kg ⁻¹)
q_i	Molar concentration of counter ion i in the particle (mol m ⁻³)
$\langle q \rangle_i$	Average concentration of counter ion i in the particle (mol m ⁻³)
Q	Total amount of sorbed species per unit mass of exchanger (eq m ⁻³)
r	Radial coordinate in the particle (m)
Re	Reynolds number
RMSD	Root mean square deviation (%)
R_p	Particle radius (m)
Sc	Schmidt number
Sh	Sherwood number
t	Time (h or s)
t_{st}	Stoichiometric time (h)
T	Absolute temperature (K)
u	Superficial velocity (m s ⁻¹)
V_s	Volume of exchanger (m ³)
z_i	Electrochemical valence of counter ion i

Greek letters

$\Delta_{\text{dehyd}}G$	Molar Gibbs free energy of dehydration (kcal mol ⁻¹)
ε	Bed void fraction

Subscripts

0	Feed condition
A	Counter ion initially present in the bulk solution (Cs ⁺)
B	Counter ion initially present in the exchanger particle (Na ⁺)
calc	Calculated
eq	Equilibrium
exp	Experimental

- in Initial condition
- n Step n in a loading-regeneration setup

V.3. References

- [1] X. Liu, G.R. Chen, D.J. Lee, T. Kawamoto, H. Tanaka, M.L. Chen, Y.K. Luo, Adsorption removal of cesium from drinking waters: A mini review on use of biosorbents and other adsorbents, *Bioresour. Technol.* 160 (2014) 142–149.
- [2] G. Lujaniene, J. Šapolaite, A. Amulevičius, K. Mažeika, S. Motiejunas, Retention of cesium, plutonium and americium by engineered and natural barriers, *Czechoslov. J. Phys.* 56 (2006) D103–D110.
- [3] K. Popa, C.C. Pavel, Radioactive wastewaters purification using titanosilicates materials: State of the art and perspectives, *Desalination* 293 (2012) 78–86.
- [4] C.B. Lopes, P.F. Lito, S.P. Cardoso, E. Pereira, A.C. Duarte, C.M. Silva, Metal Recovery, Separation and/or Pre-concentration, in: Inamuddin, M. Luqman (Eds.), *Ion Exchange Technology II - Applications*, Springer Netherlands, Dordrecht, 2012.
- [5] P.F. Lito, J.P.S. Aniceto, C.M. Silva, Removal of Anionic Pollutants from Waters and Wastewaters and Materials Perspective for Their Selective Sorption, *Water, Air, Soil Pollut.* 223 (2012) 6133–6155.
- [6] I.C. Ostroski, C.E. Borba, E.A. Silva, P.A. Arroyo, R. Guirardello, M.A.S.D. Barros, Mass Transfer Mechanism of Ion Exchange in Fixed Bed Columns, *J. Chem. Eng. Data* 56 (2011) 375–382.
- [7] C.B. Lopes, E. Pereira, Z. Lin, P. Pato, M. Otero, C.M. Silva, J. Rocha, A.C. Duarte, Fixed-bed removal of Hg²⁺ from contaminated water by microporous titanosilicate ETS-4: Experimental and theoretical breakthrough curves, *Microporous Mesoporous Mater.* 145 (2011) 32–40.
- [8] L. Lv, Y. Zhang, K. Wang, A.K. Ray, X.S. Zhao, Modeling of the adsorption breakthrough behaviors of Pb²⁺ in a fixed bed of ETS-10 adsorbent, *J. Colloid Interface Sci.* 325 (2008) 57–63.
- [9] I.M. Latheef, M.E. Huckman, R.G. Anthony, Modeling Cesium Ion Exchange on Fixed-Bed Columns of Crystalline Silicotitanate Granules, *Ind. Eng. Chem. Res.* 39 (2000) 1356–1363.
- [10] C. Xiong, Q. Jia, X. Chen, G. Wang, C. Yao, Optimization of Polyacrylonitrile-2-aminothiazole Resin Synthesis, Characterization, and Its Adsorption Performance and Mechanism for Removal of Hg(II) from Aqueous Solutions, *Ind. Eng. Chem. Res.* 52 (2013) 4978–4986.
- [11] C. Xiong, Y. Zheng, Y. Feng, C. Yao, C. Ma, X. Zheng, J. Jiang, Preparation of a novel chloromethylated polystyrene-2-amino-1,3,4-thiadiazole chelating resin and its adsorption properties and mechanism for separation and recovery of Pt(IV) from aqueous solutions, *J. Mater. Chem. A* 2 (2014) 5379–5386.
- [12] C. Xiong, Y. Li, G. Wang, L. Fang, S. Zhou, C. Yao, Q. Chen, X. Zheng, D. Qi, Y. Fu, Y. Zhu, Selective removal of Hg(II) with polyacrylonitrile-2-amino-1,3,4-thiadiazole chelating resin: Batch and column study, *Chem. Eng. J.* 259 (2015) 257–265.

- [13] S.P. Cardoso, C.B. Lopes, E. Pereira, A.C. Duarte, C.M. Silva, Competitive Removal of Cd²⁺ and Hg²⁺ Ions from Water Using Titanosilicate ETS-4: Kinetic Behaviour and Selectivity, *Water, Air, Soil Pollut.* 224 (2013) 1535–1541.
- [14] T.R. Ferreira, C.B. Lopes, P.F. Lito, M. Otero, Z. Lin, J. Rocha, E. Pereira, C.M. Silva, A. Duarte, Cadmium(II) removal from aqueous solution using microporous titanosilicate ETS-4, *Chem. Eng. J.* 147 (2009) 173–179.
- [15] C.B. Lopes, M. Otero, Z. Lin, C.M. Silva, J. Rocha, E. Pereira, A.C. Duarte, Removal of Hg²⁺ ions from aqueous solution by ETS-4 microporous titanosilicate - Kinetic and equilibrium studies, *Chem. Eng. J.* 151 (2009) 247–254.
- [16] E.D. Camarinha, P.F. Lito, B.M. Antunes, M. Otero, Z. Lin, J. Rocha, E. Pereira, A.C. Duarte, C.M. Silva, Cadmium(II) removal from aqueous solution using microporous titanosilicate ETS-10, *Chem. Eng. J.* 155 (2009) 108–114.
- [17] L.D. Barreira, P.F. Lito, B.M. Antunes, M. Otero, Z. Lin, J. Rocha, E. Pereira, A.C. Duarte, C.M. Silva, Effect of pH on cadmium (II) removal from aqueous solution using titanosilicate ETS-4, *Chem. Eng. J.* 155 (2009) 728–735.
- [18] M. Endo, E. Yoshikawa, N. Muramatsu, N. Takizawa, T. Kawai, H. Unuma, A. Sasaki, A. Masano, Y. Takeyama, T. Kahara, The removal of cesium ion with natural Itaya zeolite and the ion exchange characteristics, *J. Chem. Technol. Biotechnol.* 88 (2013) 1597–1602.
- [19] J. Mon, Y. Deng, M. Flury, J.B. Harsh, Cesium incorporation and diffusion in cancrinite, sodalite, zeolite, and allophane, *Microporous Mesoporous Mater.* 86 (2005) 277–286.
- [20] Z. Du, M. Jia, X. Wang, Cesium removal from solution using PAN-based potassium nickel hexacyanoferrate(II) composite spheres, *J. Radioanal. Nucl. Chem.* 298 (2012) 167–177.
- [21] J. Lehto, S. Haukka, R. Harjula, M. Blomberg, Mechanism of caesium ion exchange on potassium cobalt hexacyanoferrates(II), *J. Chem. Soc. Dalt. Trans.* (1990) 1007–1011.
- [22] A.J. Celestian, J.D. Kubicki, J. Hanson, A. Clearfield, J.B. Parise, The mechanism responsible for extraordinary Cs ion selectivity in crystalline silicotitanate, *J. Am. Chem. Soc.* 130 (2008) 11689–11694.
- [23] A. Clearfield, D.G. Medvedev, S. Kerlegon, T. Bosser, J.D. Burns, M. Jackson, Rates of Exchange of Cs⁺ and Sr²⁺ for Poorly Crystalline Sodium Titanium Silicate (CST) in Nuclear Waste Systems, *Solvent Extr. Ion Exch.* 30 (2012) 229–243.
- [24] A.M. El-Kamash, Evaluation of zeolite A for the sorptive removal of Cs⁺ and Sr²⁺ ions from aqueous solutions using batch and fixed bed column operations, *J. Hazard. Mater.* 151 (2008) 432–445.
- [25] R. Cortés-Martínez, M.T. Olguín, M. Solache-Ríos, Cesium sorption by clinoptilolite-rich tuffs in batch and fixed-bed systems, *Desalination* 258 (2010) 164–170.
- [26] J. Rocha, Z. Lin, Microporous mixed octahedral-pentahedral-tetrahedral framework

- silicates, *Micro- Mesoporous Miner. Phases* 57 (2005) 173–201.
- [27] J. Rocha, L.D. Carlos, Microporous materials containing lanthanide metals, *Curr. Opin. Solid State Mater. Sci.* 7 (2003) 199–205.
- [28] S. Komarneni, D.M. Roy, Tobermorites - A New Family of Cation Exchangers, *Sci. Class.* 221 (1983) 647–648.
- [29] A. Ferreira, D. Ananias, L.D. Carlos, C.M. Morais, J. Rocha, Novel microporous lanthanide silicates with tobermorite-like structure, *J. Am. Chem. Soc.* 125 (2003) 14573–14579.
- [30] R.C. Evans, L.D. Carlos, P. Douglas, J. Rocha, Tuning the emission colour in mixed lanthanide microporous silicates: energy transfer, composition and chromaticity, *J. Mater. Chem.* 18 (2008) 1100–1107.
- [31] B.R. Figueiredo, D. Ananias, J. Rocha, C.M. Silva, Cs⁺ ion exchange over lanthanide silicate Eu-AV-20: Experimental measurement and modelling, *Chem. Eng. J.* 268 (2015) 208–218.
- [32] F. Helfferich, *Ion Exchange*, Courier Dover Publications, New York, 1995.
- [33] P.F. Lito, S.P. Cardoso, J.M. Loureiro, C.M. Silva, Ion Exchange Equilibria and Kinetics, in: Inamuddin, M. Luqman (Eds.), *Ion Exchange Technology I - Theory and Materials*, Springer Netherlands, Dordrecht, 2012.
- [34] N. Wakao, T. Funazkri, Effect of fluid dispersion coefficients on particle-to-fluid mass transfer coefficients in packed beds, *Chem. Eng. Sci.* 33 (1978) 1375–1384.
- [35] H. Sato, M. Yui, H. Yoshikawa, Ionic Diffusion Coefficients of Cs⁺, Pb²⁺, Sm³⁺, Ni²⁺, SeO₂⁻⁴ and TcO₂⁻⁴ in Free Water Determined from Conductivity Measurements, *J. Nucl. Sci. Technol.* 33 (1996) 950–955.
- [36] R.M. Clark, Evaluating the cost and performance of field-scale granular activated carbon systems, *Environ. Sci. Technol.* 21 (1987) 573–580.
- [37] Y.H. Yoon, J.H. Nelson, Application of Gas Adsorption Kinetics I. A Theoretical Model for Respirator Cartridge Service Life, *Am. Ind. Hyg. Assoc. J.* 45 (1984) 509–510.
- [38] G.S. Bohart, E.Q. Adams, Some aspects of the behavior of charcoal with respect to chlorine, *J. Am. Chem. Soc.* 42 (1920) 523–544.
- [39] H.C. Thomas, Heterogeneous ion exchange in a flowing system, *J. Am. Chem. Soc.* 66 (1944) 1664–1666.
- [40] K.H. Chu, Fixed bed sorption: setting the record straight on the Bohart-Adams and Thomas models., *J. Hazard. Mater.* 177 (2010) 1006–1012.
- [41] C.B. Lopes, P.F. Lito, M. Otero, Z. Lin, J. Rocha, C.M. Silva, E. Pereira, A.C. Duarte, Mercury removal with titanosilicate ETS-4: Batch experiments and modelling, *Microporous Mesoporous Mater.* 115 (2008) 98–105.
- [42] E.A. Behrens, P. Sylvester, A. Clearfield, Assessment of a sodium nonatitanate and

- pharmacosiderite-type ion exchangers for strontium and cesium removal from DOE waste simulants, *Environ. Sci. Technol.* 32 (1998) 101–107.
- [43] A. Clearfield, Ion-exchange materials: seizing the caesium, *Nat. Chem.* 2 (2010) 161–162.
- [44] R.O.A. Rahman, H.A. Ibrahim, Y.T. Hung, Liquid Radioactive Wastes Treatment: A Review, *Water* 3 (2011) 551–565.
- [45] C.C. Pavel, M. Walter, P. Pöml, D. Bouëxière, K. Popa, Contrasting immobilization behavior of Cs⁺ and Sr²⁺ cations in a titanosilicate matrix, *J. Mater. Chem.* 21 (2011) 3831–3837.
- [46] H. Mimura, T. Kobayashi, K. Akiba, Chromatographic Separation of Strontium and Cesium with Mixed Zeolite, Column, *J. Nucl. Sci. Technol.* 32 (1995) 60–67.
- [47] E.H. Borai, R. Harjula, L. Malinen, A. Paajanen, Efficient removal of cesium from low-level radioactive liquid waste using natural and impregnated zeolite minerals, *J. Hazard. Mater.* 172 (2009) 416–422.
- [48] B.R. Figueiredo, M.M.R. de Melo, I. Portugal, D. Ananias, J. Rocha, C.M. Silva, Cs⁺ removal and optical detection by microporous lanthanide silicate Eu-AV-20 in a fixed-bed column, *Chem. Eng. J.* 286 (2016) 48–58.
- [49] B.R. Figueiredo, D. Ananias, I. Portugal, J. Rocha, C.M. Silva, Tb/Eu-AV-9: A lanthanide silicate for the sensing and removal of cesium ions from aqueous solutions, *Chem. Eng. J.* 286 (2016) 679–688.
- [50] A.I. Bortun, L.N. Bortun, A. Clearfield, Ion exchange properties of a cesium ion selective titanosilicate, *Solvent Extr. Ion Exch.* 14 (1996) 341–354.
- [51] D.M. Poojary, R.A. Cahill, A. Clearfield, Synthesis, Crystal-Structures, and Ion-Exchange Properties of a Novel Porous Titanosilicate, *Chem. Mater.* 6 (1994) 2364–2368.
- [52] A.M. Puziy, Cesium and strontium exchange by the framework potassium titanium silicate K₃HTi₄O₄(SiO₄)₃·4H₂O, *J. Radioanal. Nucl. Chem.* 237 (1998) 73–79.
- [53] E.A. Behrens, A. Clearfield, Titanium silicates, M₃HTi₄O₄(SiO₄)₃·4H₂O (M=Na⁺,K⁺), with three-dimensional tunnel structures for the selective removal of strontium and cesium from wastewat, *Microporous Mater.* 11 (1997) 65–75.
- [54] C. V. Philip, S.H. Kim, M. Philip, R.G. Anthony, The Effect of Hydrogen Peroxide on a CST Under Cesium Ion Exchange Conditions, *Sep. Sci. Technol.* 38 (2003) 3009–3029.
- [55] T.A. Todd, K.N. Brewer, D.J. Wood, P.A. Tullock, N.R. Mann, L.G. Olson, Evaluation and testing of inorganic ion exchange sorbents for the removal of cesium-137 from actual Idaho nuclear technology and engineering center acidic tank waste, *Sep. Sci. Technol.* 36 (2001) 999–1016.
- [56] K.P. C. Borcia, Sorption of thalious ion from acidic aqueous solutions onto as-made and modified ETS-10, *J. Radioanal. Nucl. Chem.* 288 (2011) 25–30.

- [57] H. Liu, A. Yonezawa, K. Kumagai, M. Sano, T. Miyake, Cs and Sr removal over highly effective adsorbents ETS-1 and ETS-2, *J. Mater. Chem. A* 3 (2015) 1562–1568.
- [58] K. Popa, C.C. Pavel, N. Bilba, A. Cecal, Purification of waste waters containing ⁶⁰Co²⁺, ^{115m}Cd²⁺ and ²⁰³Hg²⁺ radioactive ions by ETS-4 titanosilicate, *J. Radioanal. Nucl. Chem.* 269 (2006) 155–160.
- [59] L. Al-Attar, A. Dyer, R. Blackburn, Uptake of Uranium on ETS-10 Microporous Titanosilicate, *J. Radioanal. Nucl. Chem.* 246 (2000) 451–455.
- [60] C.C. Pavel, K. Popa, Investigations on the ion exchange process of Cs⁺ and Sr²⁺ cations by ETS materials, *Chem. Eng. J.* 245 (2014) 288–294.
- [61] N. Döbelin, T. Armbruster, N. Dobelin, T. Armbruster, Microporous titanosilicate AM-2: Rb-exchange and thermal behaviour, *Mater. Res. Bull.* 42 (2007) 113–125.
- [62] N. Dobelin, T. Armbruster, Microporous titanosilicate AM-2: Ion-exchange and thermal stability, *Microporous Mesoporous Mater.* 99 (2007) 279–287.
- [63] L. Al-Attar, A. Dyer, R. Harjula, Uptake of radionuclides on microporous and layered ion exchange materials, *J. Mater. Chem.* 13 (2003) 2963–2968.
- [64] S.M. Kuznicki, V.A. Bell, S. Nair, H.W. Hillhouse, R.M. Jacubinas, C.M. Braunbarth, B.H. Toby, M. Tsapatsis, A titanosilicate molecular sieve with adjustable pores for size-selective adsorption of molecules, *Nature* 412 (2001) 720–724.
- [65] M. Otero, C.B. Lopes, J. Coimbra, T.R. Ferreira, C.M. Silva, Z. Lin, J. Rocha, E. Pereira, A.C. Duarte, Priority pollutants (Hg²⁺ and Cd²⁺) removal from water by ETS-4 titanosilicate, *Desalination* 249 (2009) 742–747.
- [66] L. Liu, W. Tan, P. Xiao, Y. Zhai, A novel synthesis process of ETS-4 titanosilicate using commercial anatase in the absence of fluoride ions, *Int. J. Miner. Metall. Mater.* 19 (2012) 675–678.
- [67] D.M. Ruthven, *Principles of Adsorption and Adsorption Processes*, John Wiley & Sons, New York, 1984.
- [68] J.P.S. Aniceto, C.M. Silva, Preparative Chromatography: Batch and Continuous, In: J. L. Anderson, A. Berthod, V. Pino, A. Stalcup (Eds.), *Analytical Separation Science* (Vol. 5) Wiley-VCH, 2015.
- [69] C.B. Lopes, M. Otero, Z. Lin, C.M. Silva, E. Pereira, J. Rocha, A.C. Duarte, Effect of pH and temperature on Hg²⁺ water decontamination using ETS-4 titanosilicate, *J. Hazard. Mater.* 175 (2010) 439–444.
- [70] Y. Marcus, Thermodynamics of solvation of ions. Part 5.-Gibbs free energy of hydration at 298.15 K, *J. Chem. Soc. Faraday Trans.* 87 (1991) 2995–2999.
- [71] P.F. Lito, J.P.S. Aniceto, C.M. Silva, Modelling ion exchange kinetics in zeolyte-type materials using Maxwell-Stefan approach, *Desalin. Water Treat.* (2013) 1–10.
- [72] C.M. Silva, P.F. Lito, Application of the Maxwell–Stefan approach to ion exchange in microporous materials. Batch process modelling, *Chem. Eng. Sci.* 62 (2007) 6939–

6946.

- [73] P.F. Lito, J.P.S. Aniceto, C.M. Silva, Maxwell–Stefan based modelling of ion exchange systems containing common species (Cd²⁺, Na⁺) and distinct sorbents (ETS-4, ETS-10), *Int. J. Environ. Sci. Technol.* 12 (2015) 183–192.

VI

General conclusions
and future work

VI.1. General conclusions

1) Cs^+ removal from aqueous solutions was carried out by ion exchange carrying out batch and fixed-bed experiments.

Batch ion exchange

The ion exchange of Cs^+ from aqueous solutions was studied in batch room-temperature experiments, for equilibrium and kinetic measurements, using the luminescent microporous lanthanide silicates Eu-AV-20 [1] and Tb/Eu-AV-9 [2]. The main conclusions of these studies are:

- The Langmuir and Langmuir-Freundlich equations provide a good representation of the equilibrium data, attaining average absolute relative deviations of 5.3% and 13.1% for $\text{Cs}^+/(Na^+,K^+)/\text{Eu-AV-20}$ and $\text{Cs}^+/K^+/\text{(Tb,Eu)-AV-9}$, respectively;
- Tb/Eu-AV-9 is more advantageous than Eu-AV-20 for Cs^+ removal, considering the time needed for reaching equilibrium. Although the experiments carried out with AV-9 solids have higher mass of exchange *per* cesium concentration than the Eu-AV-20 experiments, the time to the uptake of cesium is significantly lower (2 hours vs. 80 hours). Regardless of the uptake time, the results indicated that Eu-AV-20 and Tb/Eu-AV-9 used only 3.7% ($0.093 \text{ eq}\cdot\text{kg}^{-1}$ in $2.550 \text{ eq}\cdot\text{kg}^{-1}$) and all the theoretical cation exchange capacity, respectively;
- A kinetic model based on the Maxwell-Stefan equations was developed and adjusted to the cesium removal curves of both materials. For Eu-AV-20, the model achieved an average error of 19.0%, while the Tb/Eu-AV-9 kinetic curves were well-fitted, with an error of 8.4%;
- The optimized Maxwell-Stefan diffusivities obtained for both solids are five to six orders of magnitude smaller than the Cs^+ diffusion coefficient in aqueous solutions, consistent with their small micropores and similar microporosity;
- Photoluminescence spectroscopy revealed that both materials may play an important role as qualitative or even quantitative Cs^+ sensors. Our work using Eu-

AV-20 as exchanger [1] has proved that the emission spectrum is modified upon cesium uptake as a consequence of changes in the local Eu^{3+} environment. In the case of Tb/Eu-AV-9, the average lifetimes corroborated the influence of Cs^+ on the solids emission, namely, higher metal loads led to lower lifetimes. Much more important was the linear relationship found between the average lifetimes and Cs^+ concentration in the solid.

Fixed-bed ion exchange

Fixed-bed cesium(I) ion exchange experiments were carried out using Eu-AV-20 [3] and the microporous titanosilicate ETS-4. The influence of the superficial velocity on the breakthrough curves behaviour was assessed. The influence of the mass of exchanger on the continuous Cs^+ uptake by Eu-AV-20 was also discussed in detail, while for $\text{Cs}^+/\text{Na}^+/\text{ETS-4}$ loading-regeneration-loading assays were performed. The main conclusions are:

- ETS-4 equilibrium data is well-fitted by the Langmuir isotherm with an average absolute relative deviation of 6.6%;
- In both solids, the broadening of the breakthrough curves observed after decreasing the superficial velocity of the solution (in the absence of axial dispersion, confirmed from calculated axial Peclet number) disclosed film diffusion limitations.
- All curves were modelled using a Nernst-Planck based model and takes into account the internal and external mass transfer limitations, which provided accurate results: average deviations of 6.5% (three curves; prediction) and 6.7% (one curve; correlation) for Eu-AV-20, and 9.6% (four curves; prediction) and 18.7% (one curve; correlation) for ETS-4, respectively;
- The measured Eu-AV-20 breakthrough curves were also modelled by simplified analytic models taken from the literature, such as Thomas, Bohart-Adams, Clark and Yoon-Nelson providing errors between 3.2 and 6.5%;
- The optimized Nernst-Planck diffusivities of both solids are consistent with the relative sizes of the counter ions and the small micropores of the sorbents. The

same was observed in the modelling of the batch ion exchange using the Maxwell-Stefan equations;

- The good results obtained for ETS-4 in consecutive loading-regeneration-loading steps evidenced the ability of this material to be used in cyclic ion exchange operations;
- Since the Eu-AV-20 photoluminescence varies upon Cs^+ exchange, two different experiments were carried out in similar conditions, except for the time of operation (15 vs. 50 hours), in order to obtain Eu-AV-20 samples with different cesium loadings. The results (differences in the normalised emission spectra for the non-degenerated $^5\text{D}_0 \rightarrow ^7\text{F}_0$ transitions) suggested that luminescence may be an easy and fast method to assess ion exchange phenomena in $\text{Cs}^+ / (\text{Na}^+, \text{K}^+) / \text{Eu-AV-20}$ systems.

2) The uptake of Cs^+ and Na^+ results in changes in the emission spectrum of Eu-AV-20, due to slight variations in the local environment of the Eu^{3+} emitter. In fact, when the solid was used in ion exchange experiments using only sodium or cesium in increasing concentrations, the Eu1/Eu2 intensity ratio of the non-degenerated $^5\text{D}_0 \rightarrow ^7\text{F}_0$ transition of the Eu septet increased. However when an equimolar solution of both cations was used, the Eu1/Eu2 ratio remained essentially the same. Thus, these results suggest that Eu-AV-20 materials have potential for being used as luminescence sensors for Cs^+ (and Na^+) cations in aqueous solutions, even if further work is required.

VI.2. Future work

Although the realm of inorganic exchangers is well established, there is much room for growing. The quest for novel materials must endure, in order to enhance the selectivity and efficiency of the uptake of radioactive wastes, particularly Cs^+ , one of the main species of concern. Most existing solids have application limitations, mainly due to their low efficiency in certain conditions. In general, the common exchangers perform better at neutral pH and in the absence of competing cations. New materials should deal with the fact that radionuclides are present in a complex phase, where the solution pH and the salt content (typically from the sea water cooling system) have to be considered. In addition, the majority of the radioactive wastewaters present extreme conditions of pH (acidic or

alkaline) and contain large amounts of other elements, such as alkali, alkaline-earth metals, transition metals, lanthanides, and actinides, in variable concentrations that may participate in the exchange. The ion exchangers used must be resistant to chemical, thermal and, mainly, radiation attack. The latter deserves special attention since elevated doses of radiation may reduce the selectivity and/or capacity of the exchangers as consequence of total or partial collapse of the solid. In this context, and when this thesis comes to an end, there is much scope for the following studies.

- Synthesis of new exchangers. Synthesising materials with transition metals or lanthanides other than those used so far may bring to light new molecular architectures with interesting properties, such as enhanced selectivity or capacity, by achieving the best compromise between the sorbed ion and the size of the micropores.
- Influence of pellet and particle size. The preparation of pellets and nanoparticles with well-defined sizes and their use in batch and fixed-bed experiments should be addressed. Regardless of the anisotropy observed in the material's microporosity, the size of the particles fundamentally affects the kinetics of the ion exchange process, since it determines the length of the internal diffusion path. In the case of nanoparticles, the increment of specific surface area is the dominant factor.
- Effect of the pH, salt content and competing ions. The cesium exchange with Eu-AV-20, Tb/Eu-AV-9 and ETS-4 should be accomplished in the presence of salts, acids and bases, in order to assess their selectivity towards cesium, and chemical resistance in extreme environments. In the case of acids, the ion exchange with H^+ must be taken into account, while the material's structural integrity may also be affected. The existence of divalent cations (e.g., Ca^{2+} , Mg^{2+} , Ba^{2+} , Pb^{2+} , Hg^{2+} and Cd^{2+}) in solution is of particular concern, due to the well-recognized materials preference towards them.
- Effect of temperature. Assays at several temperatures should be performed as this was not covered in this dissertation.

- Capability of undergoing ion exchange cycles. It is important to understand the ability of the prepared materials of undergoing sorption-desorption cycles without losing selectivity and capacity towards a specific cation. This study is fundamental from an industrial point-of-view where, typically, trim beds or parallel beds arrangements are implemented.

In this thesis ETS-4 revealed a considerable ability for being used in loading-regeneration tests. Eu-AV-20 and, particularly, Tb/Eu-AV-9 due to its fast kinetics and cation exchange capacity, should be tested for the same purpose.

- Equilibrium modelling. An accurate modelling of the equilibrium encompassing the determination of the activity coefficients of ions in the liquid and in the exchanger phases should be undertaken, as the deviations from ideality are important in electrolyte solutions. Accordingly, equilibrium may be rigorously described using mass action law expressed with activities, and the thermodynamic methods of Gains and Thomas [5] or Ioannidis *et al.*, [6] should be adopted for fitting the equilibrium constants independently of the parameters of the activity coefficients model selected for the solid phase. The exchanger heterogeneity can also be taken into account by considering distinct active sites (co-ions) in the solid, which may be particularly important in the case of Eu-AV-20.
- Online monitoring of the photoluminescence spectra. During this thesis, all the photoluminescence spectra were measured using the same amount of (parent or exchanged) sample in the form of pellets compressed at ca. 2 ton cm⁻². In terms of batch experiments and since Tb/Eu-AV-9 possesses a fast cesium exchange kinetics [2], an experimental apparatus comprising a small reservoir under agitation, coupled to the Jobin Yvon-Spex spectrometer in order to record several photoluminescence spectra online, can be proposed. In turn, the fixed-bed experiments carried out with Eu-AV-20 [3] raised the possibility of online monitoring the ion exchange in a fixed-bed column using an optical fibre and a spectrometer.

VI.3. References

- [1] B.R. Figueiredo, D. Ananias, J. Rocha, C.M. Silva, Cs⁺ ion exchange over lanthanide silicate Eu-AV-20: Experimental measurement and modelling, *Chem. Eng. J.* 268 (2015) 208–218.
- [2] B.R. Figueiredo, D. Ananias, I. Portugal, J. Rocha, C.M. Silva, Tb/Eu-AV-9: A lanthanide silicate for the sensing and removal of cesium ions from aqueous solutions, *Chem. Eng. J.* 286 (2016) 679–688.
- [3] B.R. Figueiredo, M.M.R. de Melo, I. Portugal, D. Ananias, J. Rocha, C.M. Silva, Cs⁺ removal and optical detection by microporous lanthanide silicate Eu-AV-20 in a fixed-bed column, *Chem. Eng. J.* 286 (2016) 48–58.
- [5] G.L. Gaines, H.C. Thomas, Adsorption Studies on Clay Minerals. II. A Formulation of the Thermodynamics of Exchange Adsorption, *J. Chem. Phys.* 21 (1953) 714.
- [6] S. Ioannidis, A. Anderko, S.J. Sanders, Internally consistent representation of binary ion exchange equilibria, *Chem. Eng. Sci.* 55 (2000) 2687–2698.